Dissertation

Vibrational Spectroscopy of Macroscopic and Liquid-Phase Exfoliated Organic Crystals

---

Vaishnavi J. Rao

2021

Dissertation

zur
Erlangung der Doktorwürde (Dr. rer. nat.)
der
Gesamtfakultät für Mathematik, Ingenieur- und Naturwissenschaften
der
Ruprecht-Karls-Universität Heidelberg

vorgelegt von

Vaishnavi Jayathirtha Rao

aus Bangalore

Tag der mündlichen Prüfung

10. Dezember 2021

Vibrational Spectroscopy of Macroscopic and Liquid-Phase Exfoliated Organic Crystals

Gutachter

Prof. Dr. Jana Zaumseil

Prof. Dr. Petra Tegeder

Abstract

Single crystals of organic semiconductors are chemically pristine and exhibit nearly perfect long-range structural order. As such, they provide an ideal platform to investigate intrinsic properties. Vibrational spectroscopy techniques, such as Raman and Fourier-transform infrared spectroscopy (FT-IR), are widely employed techniques for the characterization of organic materials. They are versatile tools that can be used to study molecular packing and polymorphism in crystalline organic semiconductors, albeit with poor spatial resolution. Two fundamentally different scanning probe techniques with infrared spectroscopy and imaging capabilities offer a spatial resolution below 100 nm — atomic force microscopy-infrared spectroscopy (AFM-IR) and scattering-type infrared scanning near-field optical microscopy (IR-SNOM).

This thesis compares the AFM-IR and the IR-SNOM with each other and to the conventional FT-IR spectroscopy with regard to their applicability to small-molecule organic semiconductors. To this end, single crystals of TIPS-pentacene, TIPS-tetraazapentacene, rubrene and perfluorobutyldicyanoperylene carboxydiimide (PDIF-CN_2) are used as the testbed. Significant differences are observed in the spectra of the crystals depending on the technique and polarization of incident light that are associated with the intrinsic molecular structure and packing as well as the different working principles of the applied methods. Furthermore, the imaging mode of the AFM-IR and the IR-SNOM is tested on solution-deposited microcrystals of PDIF-CN_2.

Micro- and nanostructures of layered organic materials can also be created by liquid-phase exfoliation (LPE), a popular technique used to produce two-dimensional nanosheets from layered inorganic crystals. The orthorhombic and the triclinic polymorphs of rubrene are dispersed in aqueous surfactant solution by ultrasonication. Distinct nanostructures of rubrene, referred to as nanorods and nanobelts, are formed that are isolated via liquid cascade centrifugation. Their crystalline nature is confirmed through electron diffraction measurements and Raman spectroscopy. Absorbance and photoluminescence (PL) of the dispersions are found to be similar to rubrene solutions due to random orientations of the nanostructures, however, their PL lifetimes are comparable to the macroscopic crystals. The likely arrangement of rubrene molecules within the nanorods and the nanobelts is deduced from AFM images, electron diffraction patterns, and IR-SNOM spectra.

Kurzfassung

Einkristalle organischer Halbleiter zeichnen sich durch chemische Reinheit und nahezu perfekte, langreichweitige Ordnung aus, wodurch sie ideale Modellsysteme für die Untersuchung intrinsischer Eigenschaften darstellen. Schwingungsspektroskopische Techniken wie Raman- und Fourier-Transformations-Infrarot-Spektroskopie (FT-IR) finden breite Anwendung in der Charakterisierung organischer Materialien. Sie sind vielseitige Werkzeuge für die Untersuchung der molekularen Packung und der verschiedenen Polymorphe kristalliner organischer Halbleiter, bieten jedoch nur begrenzte räumliche Auflösung. Zwei fundamental verschiedene Rastersondentechniken ermöglichen hingegen Infrarot-Spektroskopie mit einer räumlichen Auflösung von unter 100 nm — die Rasterkraft-Infrarot-Spektroskopie (AFM-IR) und die Infrarot-Rasternahfeldmikroskopie (IR-SNOM).

Diese Arbeit vergleicht AFM-IR, IR-SNOM und die konventionelle FT-IR-Spektroskopie untereinander im Hinblick auf ihre Anwendbarkeit auf molekulare organische Halbleiter. Diese Untersuchungen werden an Einkristallen von TIPS-Pentacen, TIPS-Tetraazapentacen, Rubren und Perfluorbutyldicyanoperylen-Carboxydiimid (PDIF-CN_2) durchgeführt. Abhängig von der Messmethode und der Polarisation des einfallenden Lichtes zeigen sich bedeutende spektrale Unterschiede, welche die intrinsische Molekülstruktur und molekulare Packung ebenso wie die Charakteristika der Messmethode widerspiegeln. Darüberhinaus wurde der Mikroskopie-Modus von AFM-IR und IR-SNOM anhand von lösungsabgeschiedenen PDIF-CN_2 Mikrokristallen getestet.

Mikro- und Nanostrukturen organischer Schichtmaterialien lassen sich ebenfalls durch die Flüssigphasen-Exfolierung (LPE) erzeugen – eine weitverbreitete Methode zur Produktion zweidimensionaler Nanolagen ausgehend von anorganischen Schichtkristallen. Orthorhombische und trikline Polymorphe von Rubren werden in wässriger Tensidlösung durch Ultraschall dispergiert. Dabei bilden sich charakteristische Nanostrukturen von Rubren, die als Nanostäbe und Nanobänder bezeichnet werden und durch Flüssigphasen-Kaskadenzentrifugation isoliert werden können. Elektronenbeugung und Raman-Spektroskopie bestätigen ihre kristalline Natur. Die Absorption und Photolumineszenz (PL) der Dispersionen ähneln denen von Rubrenlösungen aufgrund der ungeordneten Orientierung der Nanostrukturen. Im Gegensatz dazu sind ihre PL-Lebensdauern vergleichbar zu denen makroskopischer Kristalle. Auf Basis von AFM, Elektronenbeugung und IR-SNOM-Spektren wird die wahrscheinliche Anordnung der Rubrenmoleküle innerhalb der Nanostäbe und Nanobänder aufgeklärt.

Acknowledgements

It is my belief that a sense of gratitude is what makes any accomplishment, big or small, truly fulfilling. The work that I have presented here was only possible because of the opportunities, help, and support that were offered by many people who are invaluable to me. I would like to use this platform to thank them all.

I would like to begin by expressing my utmost gratitude to *Prof. Jana Zaumseil* for giving me the opportunity to explore new scientific territories within her research group. Her constant guidance and unconditional support were indispensable for the completion of my thesis. Thank you, *Jana*, for inspiring me to be a better academic through your immaculate scientific standards and practices. Your trust in my abilities and interest in my work were strong motivating factors for me to do my best. Thank you, especially, for fostering a good learning experience through collaborations, students and equipment responsibilities, and conference participations.

I had the distinct opportunity of having *Prof. Claudia Backes* co-supervise one of the projects. Thank you, *Claudia*, for not only training me in the lab and helping me with data analysis but also for your kind advices and appreciation. You have shown me that it is possible and important to have fun while doing what you must.

I would like to extend my sincere thanks to *Prof. Petra Tegeder* for her willingness to review this thesis.

My colleagues from the *Nanomaterials for Optoelectronics* and *PhysChem2D* groups were an integral part of my PhD life. From training me to use various equipment to getting stuff for me when I couldn't physically reach them, help was offered generously. Thank you, guys, for providing great company, entertainment, and snacks. A very special thanks goes to *Team SFB 1249 — Dr. Katelyn Goetz* for being a patient tutor during my early days in the lab and a wonderful friend later, *Maik Matthiesen* for readily helping me with so many things equipment-related and for his eggnog cake, and *Severin Schneider* for all things chemistry and for being an amazing office mate. It was such a pleasure hanging out with you all both at and outside the institute. Thanks also to my other office mates, *Jan Gotthardt* and *Nicolas Zorn*, for their pleasant company and the much-needed chit-chat. My girls — *Dr. Beata Szydłowska*, *Farnia Rashvand*, *Sonja Wieland*, and *Merve Balcı* definitely deserve a 'thank you' for their strong positive presence and support.

I give my heartfelt thanks to *Jan*, *Beata*, and *Dr. Felix Berger* for proofreading my thesis,

with special thanks to *Felix* for translating the abstract into German.
I am particularly grateful to all my collaborators — *Dr. Haoyuan Qi*, *Dr. Christian Huck*, *Dr. Chanyoung Yim*, *Dr. Jie Han*, *Dr. Sebastian Hahn*, *Rita Siris*, *Sebastian Grieger*, *Felix*, *Katelyn*, and *Maik* without whom my projects would have been a lot less interesting or even non-existent. Your cooperation and promptness are much appreciated.
In addition, I am also very thankful to my students, *Jian Yin*, *Naomi Harris*, and *Sarah Lembke*, for their contributions to my work. Thank you for being kind when I made mistakes and for helping me (perhaps unknowingly) be a better supervisor.
A big 'thank you' to the administrative and the technical staff at the *Institute of Applied Physical Chemistry* as well as the *Center for Advanced Materials* for their timely help.

I would also like to say many thanks to my family and friends for being an endless source of strength and positivity. I owe the biggest debt of gratitude to my mother who has always been my greatest support system. Thank you, *Amma*, for your unparalleled love and encouragement which give me wings. Last but not the least, I would like to express my deepest appreciation of my fiancé for partaking in this journey of mine and extending his warm support throughout. Thank you, *Avi*, for being the wind beneath my wings.

This work is dedicated to my father who strived to provide me with a holistic education.
Thank you for everything, Appa!

List of Abbreviations

2D	Two-Dimensional
3D	Three-Dimensional
AFM	Atomic Force Microscopy
AFM-IR	Atomic Force Microscopy-Infrared
AOI	Angle of Incidence
BTBT	Benzothienobenzothiophene
cRED	Continuous Rotation Electron Diffraction
CTE	Coefficient of Thermal Expansion
DFT	Density Functional Theory
FET	Field-Effect Transistor
FPA	Focal Plane Array
FT-IR	Fourier Transform-Infrared
h-BN	Hexagonal-Boron Nitride
HOMO	Highest Occupied Molecular Orbital
IR	Infrared
IR-SNOM	Infrared-Scanning Near-Field Optical Microscopy
LCC	Liquid Cascade Centrifugation
LPE	Liquid-Phase Exfoliation
LUMO	Lowest Unoccupied Molecular Orbital
NA	Numerical Aperture
OFET	Organic Field-Effect Transistor
OLED	Organic Light-Emitting Diode
OPV	Organic Photovoltaic
OSC	Organic Semiconductor
OSSC	Organic Semiconducting Single Crystal
PDIF-CN_2	Perfluorobutyldicyanoperylene carboxydiimide
PL	Photoluminescence
PLE	Photoluminescence Excitation-Emission

PVT	Physical Vapour Transport
SAED	Selected-Area Electron Diffraction
SEM	Scanning Electron Microscopy
TAPP	Tetraazaperopyrene
TEM	Transmission Electron Microscopy
TFT	Thin-Film Transistor
TIPS-PEN	Triisopropylsilyl-pentacene
TIPS-TAP	Triisopropylsilyl-tetraazapentacene
UV/VIS	Ultraviolet/Visible
XRD	X-ray Diffraction

Contents

Chapter 1

Introduction

Organic electronics, a multidisciplinary research field that focuses on the development of (opto)electronics centred around organic semiconductors has exponentially grown from its infancy just a few decades ago to being the backbone of a multi-billion dollar industry today. Much of its advancement can be attributed to consistent scientific work that has been carried out towards designing, synthesizing, and characterizing novel organic materials to improve their structure-(opto-)electronic property relationship, stability, and processability.

Semiconductors are those materials whose electrical conductivity, σ, lies between that of conductors ($\sigma > 10^3$ S m^{-1}) and insulators ($\sigma < 10^{-8}$ S m^{-1}), and can be controlled via an external stimulus. Organic semiconductors, in particular, constitute a class of semiconductors composed of carbon-rich molecules. The fundamental property of these molecules that enable them to conduct electronic charge is molecular conjugation, or in other words, the presence of alternating single and double bonds between carbon atoms that are covalently bound together. Such an arrangement is often referred to as π-conjugation because it results in the delocalization of one of the four valence electrons, called the π electron, of each carbon atom within the conjugated system. It is these π electrons which are responsible for electronic charge transport in organic semiconductors.

There are three device categories that are central to both scientific research as well as technological applications in the context of organic electronics — organic field-effect transistors (OFETs), organic light-emitting diodes (OLEDs), and organic photovoltaic cells (OPVs). Although each of their underlying operational mechanism and functionality are very different, what is common to them is the important role that charge transport and energy transfer play in determining the device performance. Molecular structure and packing are two intrinsic factors that strongly influence these phenomena since small changes to the structure can alter the packing and therefore the extent of π-orbital overlap between adjacent molecules that determines charge transport and energy transfer efficiencies.[1,2] It is, therefore, imperative to characterize the arrangement of molecules in organic solids.

Although X-ray diffraction (XRD) is generally the method of choice to gain insights into molecular packing, alternative techniques that can locally probe the orientation of molecules and resolve spatial inhomogeneities in films without destroying the samples are often necessary. Vibrational spectroscopy techniques, such as Raman and Fourier-transform infrared spectroscopy (FT-IR) are powerful tools that provide good a understanding of both structure of individual molecules as well as their orientation, albeit with low spatial resolution. To examine the innate long-range arrangement of molecules, single crystals of organic semiconductors would be ideal as they are chemically pristine, free of grain boundaries, and have nearly perfect structural order. However, for most practical purposes, polycrystalline films are used which warrants the investigation of molecular orientation with high spatial resolution. Two scanning probe based techniques combined with infrared spectroscopy, called atomic force microscopy-infrared spectroscopy (AFM-IR) and infrared scanning near-field optical microscopy (IR-SNOM), offer the advantage of good chemical specificity along with superior spatial resolution. Their applicability to highly ordered molecular crystals is explored in this thesis.

Besides molecular structure and packing which have a clear effect on the properties of solid-state organic materials, reducing the dimensions of a system also dramatically changes the properties as established since long, for example, with the help of graphene[3] and single-walled carbon nanotube.[4] Usually, bottom-up solution- or vapour-based methods are employed to generate low dimensional materials. However, an increasingly popular top-down technique called liquid-phase exfoliation (LPE) has been used to produce 2D counterparts of a range of predominantly inorganic crystals in the last decade.[5] In all the cases so far, the exfoliated materials have strong in-plane covalent or coordination bonds. It is not understood whether molecular crystals with only non-covalent in-plane π-π interactions can also be exfoliated via LPE. In this thesis, the application of LPE to non-covalently bound organic single crystals of rubrene is investigated. Furthermore, the local orientation of molecules in the resulting nanostructures is deduced by comparing their IR-SNOM signals with those of the corresponding macroscopic crystals of rubrene.

The organization of this thesis is as follows. **Chapter 2** summarizes the properties and current knowledge of the research on small-molecule organic semiconductors with a special focus on rubrene. The employed vibrational spectroscopies and the related state-of-the-art techniques are described. The chapter ends with a discussion about liquid exfoliation and size selection.

Chapter 3 details the materials and protocols used in the preparation of samples. It also presents the characterization techniques employed in this work.

Chapter 4 examines the far-field absorbance spectra acquired from a selection of organic single crystals and compares them with the amplitude and phase signals obtained from the spectroscopy mode of the AFM-IR and the IR-SNOM, respectively. Furthermore, the nanoimaging and nanospectroscopy capabilities of the two techniques were tested on a polycrystalline film. The resulting amplitude and phase maps were compared with the height images and correlated to the spectra.

Chapter 5 demonstrates liquid-phase exfoliation of two different polymorphs of rubrene single crystals. Microscopic as well as spectroscopic characterization of thus derived nanostructures are performed and the results are compared with those of the corresponding macroscopic crystals and rubrene solution. Additionally, the local orientation of the molecules within the nanostructures is deduced from their IR-SNOM signals and the proposed molecular packing is presented as an illustration.

Finally, in **Chapter 6**, the main insights drawn from the entire study are revisited and perspectives on the course of further research are offered.

Chapter 2

Background

2.1 Small-Molecule Organic Semiconductors

The rapidly emerging field of organic electronics is supported mainly by two classes of materials: conjugated polymers and conjugated small-molecules. Although the earliest accounts of photovoltage and photoconductivity measurements on organic materials date back to the late 19th and early 20th centuries,[6] it was not until the 1980s that organic electronics came into being as a distinct field of research following the works of Heeger et al. on polyacetylene, and Warta and Karl on naphthalene crystals.[7,8] A wealth of organic materials have since then been developed whose electrical properties are of metallic, semiconducting and even superconducting nature.[9–11] Small-molecule organic semiconductors (OSCs), comprising of polyarenes and polyacenes with typically 2 to 10 benzene rings, are the focus of this thesis. These materials have not only been successfully implemented in organic field-effect transistors (OFETs), organic light-emitting diodes (OLEDs) and organic photovoltaic cells (OPVs) but have also allowed for fundamental studies on charge transport and energy transfer that govern the operation and reliability of organic electronic devices.

A key difference between organic semiconductors and the traditional inorganic ones (e.g., silicon) that impacts their properties and processing is that organic crystals are characterized by weak van der Waals bonding, whereas inorganic semiconductors are held together by covalent bonds in their solid-state. Based on the current understanding, a direct consequence of the weak intermolecular interactions is the presence of large thermal molecular motions that limits charge transport in crystalline OSCs.[12] These thermal motions cause a localization of charge carriers because of which the charge transport mechanism in molecular crystals is neither band-like nor hopping but something in between.

The HOMO (highest occupied molecular orbital) and the LUMO (lowest occupied molecular orbital) are discrete energy levels in OSCs that are analogous to the valence and conduction bands, respectively, of inorganic semiconductors. In small-molecule organic semiconductors, it is well-established that their opto-electronic properties, such as the energy gap between the HOMO and the LUMO, and the charge carrier mobility, are primarily determined by the structure of an isolated molecule and the intermolecular packing.[13] For instance, a weak intermolecular overlap of the orbitals results in a small bandwidth ($\sim$ 0.1 eV) and low mobility of charge carriers ($<$ 1 cm^2 V^{-1} s^{-1}).[13] Therefore, materials with favourable molecular structures exhibiting desirable molecular arrangements in the solid state that can also be processed easily and integrated readily in devices are necessary. Although this seems very challenging, with judicious molecular design strategies high performing OSC materials have been realized.

2.1.1 Organic Field-Effect Transistors

A common approach to probe the electronic properties of organic semiconductors is by incorporating them into field-effect transistors which are then called organic field-effect transistors (OFETs). Based on the electric field effect,[14] OFETs enable a systematic study of charge transport on the surface of OSCs by allowing for continuous tuning of charge density induced by the external electric field. An OFET consists of several components — the organic semiconductor, the gate dielectric, the gate electrode, and the source and drain electrodes, all deposited on a substrate as shown in **Figure 2.1**. A single crystal or a thin film of the OSC may be used. In the latter case, an OFET is more specifically called as a thin-film transistor (TFT).[10]

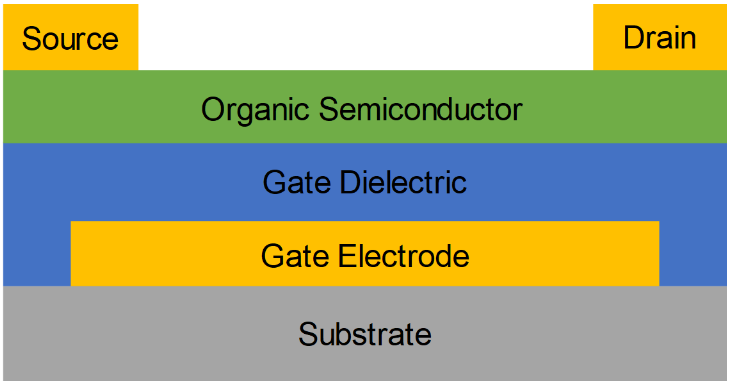

Figure 2.1: Schematic of the cross-section of a standard organic field-effect transistor.

OFETs operate as voltage-controlled current sources.[15] When a voltage is applied between the gate electrode and the semiconductor (the gate-source voltage), a thin sheet of mobile charge carriers of opposite polarity to that at the gate electrode is induced in the vicinity of the semiconductor-dielectric interface. These charges constitute the drain current that flows through the semiconductor when a voltage between the drain and the source electrodes is applied. Since the charge carrier density in the semiconductor is a function of the gate-source voltage, the drain current can be modulated by altering the gate-source voltage. A parameter called field-effect mobility, which is a measure of how quickly charge carriers can move in response to an external electric field, is of paramount importance to assess device performance.[16] In general, higher the mobility, more efficient is the device. Field-effect mobility is, therefore, also used as a metric to compare different OSCs, and materials research focuses on strategies to improve it.

2.1.2 General Molecular Design Strategies

Theoretically, organic semiconductors cannot be strictly categorised as p- or n-type materials since they are not usually doped. Hence, they are in principle ambipolar. However, transport of either the electrons or the holes can be suppressed by traps,[17] and predominantly p- or n-type behaviour is observed depending on whether charges can be injected. Therefore, in extended π-conjugated systems with HOMO lying close to the Fermi energy level of the injecting electrode, E_F, the hole injection barrier (ϕ_h) is smaller which results in preferential hole injection and hence hole transport.[10] On the other hand, if the LUMO is situated closer to the E_F, injection of electrons into the LUMO of the semiconductor is facilitated due to low electron injection barrier (ϕ_e), leading to n-type behaviour. Here, it is very important that the LUMO of the OSC is below the trap level of molecular oxygen[18] and water-oxygen complexes.[19] In a third scenario, when the band gaps of the OSCs are small, both ϕ_h and ϕ_e are small, resulting in hole as well as electron injection leading to ambipolar behaviour.[20]

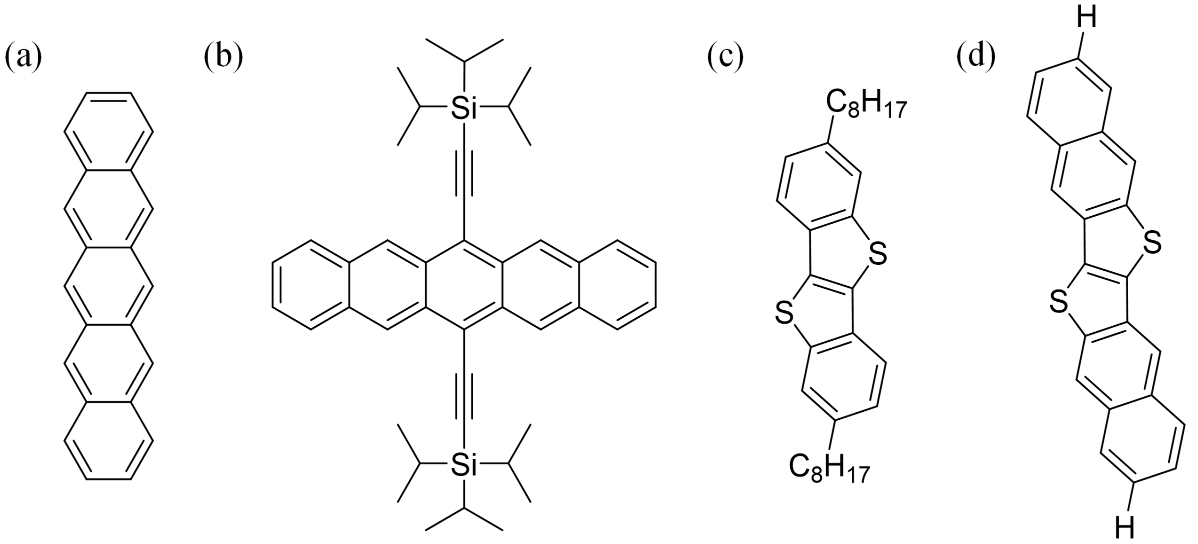

Figure 2.2: Molecular structures of a few well-known p-type organic semiconductors: (a) pentacene, (b) TIPS-PEN, (c) C8-BTBT, and (d) DNTT.

Acenes and their derivatives are prominent candidates among small-molecule OSCs. Pentacene (see **Figure 2.2(a)**), for example, is a benchmark p-type OSC whose remarkable charge transport properties[21–24] are attributed to the electron rich aromatic core with strong intermolecular overlaps in the solid state, as well as perfect alignment of the HOMO (-5.1 eV) with the Fermi energy level of gold (-5.1 eV) that is conducive to hole injection and transport.[25] However, pentacene (and higher order acenes) are barely soluble in common organic solvents and also suffer from poor environmental stability due to photo-oxidation. To overcome these issues, Anthony et al. incorporated triisopropylsilylethynyl (TIPS) groups at the C-6 and C-13 positions of the pentacene core.[26] This molecule, called TIPS-pentacene (TIPS-PEN, **Figure 2.2(b)**), was a game changer for acene chemistry. It has been shown that the insertion of the TIPS group stabilizes the electron rich pentacene backbone by lowering the LUMO energy level. It also reduces the triplet energy and thus prevents singlet oxygen sensitization leading to minimization of photo-oxidation.[27] Furthermore, the alkyl groups of the TIPS moiety drastically improves the solubility of the molecule and also forces the acene backbones to adopt face-to-face π-stacking in spin-coated films.[26] Hole mobilities of > 1 cm^2 V^{-1} s^{-1} were reported in early studies,[28] however, various TIPS substituted acenes have been synthesized and their structure-property relationships have been studied. In particular, heteroacenes (where one or more carbon atoms of the acene skeleton are replaced with nitrogen, oxygen, sulphur or phosphorus) with the TIPS groups, such as triethylsilylethynyl anthradithiophene (TESADT),[29] difluorinated (di-F) TESADT[30] and their derivatives[31] are found to be promising.

Thiophene-based heterocycles form an important sub-class of p-type small-molecule semiconductors that are highly stable under ambient conditions owing to the low lying HOMO levels (-5.0 eV to -5.5 eV) arising from the electron-rich sulphur.[15] Bao and co-workers were the first to report heteroacenes with a single thiophene ring and they showed that by increasing the number of fused rings they could raise the HOMO level and therefore, lower the band gap.[32,33] They also observed that when the benzene/thiophene rings were not linearly fused, the HOMO energy level was lowered and the HOMO/LUMO gap increased.[34] Thin film mobilities of these molecules were found to be in the range of 0.1-0.6 cm^2 V^{-1} s^{-1}. The group of Takimiya is credited with the invention of a series of thiophene, selenophene and thiazine fused ring systems with or without end-substitutions that have performed exceedingly well as p-type semiconductors.[35,36] Going from mono- to dialkyl end-substituted benzothienobenzothiophene (C$_n$-BTBT), the mobility was seen to improve, as was the effect of increasing the length of the side chain.[37] Various other alkylated phenylene-thiophene oligomers, such as dithienothiophene (DTT)[38] and dinaphthothienothiophene (DNTT)[39,40] also show above average performance in OFETs. Molecular structures of C8-BTBT and DNTT are provided in **Figure 2.2(c),(d)**. Rubrene, a tetracene derivative, is regarded as a touchstone of all small-molecular OSCs. Its features and properties are discussed in detail in **Section 2.2**. For a more complete picture of all the available p-type semiconductors and their structure-property relationship, the reader is directed to several comprehensive reviews.[1,10,25,41]

When it comes to n-type OSCs, the LUMO energy level of the molecule plays a significant role in its performance. For efficient electron injection, the energy barrier between the work function of the injecting electrode and the LUMO should be as small as possible. One of the reasons why a vast majority of OSCs show poor n-type behaviour is because this energy difference is rather high when gold or silver (the prototypical electrode materials with a large work function) are used. An easy solution is to use electrodes with low work function, such as calcium or magnesium; however, these materials are extremely susceptible to moisture and air. Other reasons why OSCs show suppressed electron mobility is because of their own instability in air and electron trapping at the semiconductor-dielectric interface due to the presence of residual impurities and hydroxyl groups existing as silanols in the case of the typically used SiO_2 dielectric.[20,42]

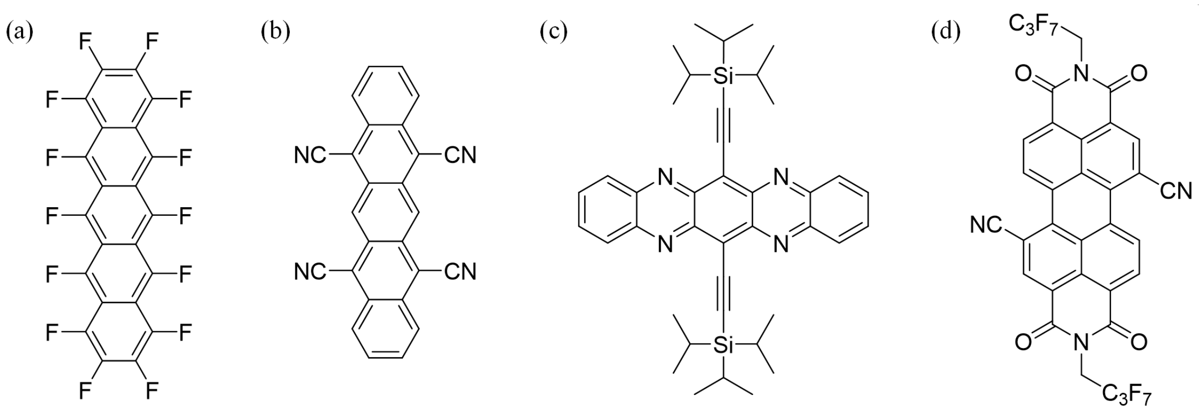

Figure 2.3: Molecular structures of a few well-known n-type organic semiconductors: (a) perfluoropentacene, (b) TIPS-TAP, (c) tetracyanopentacene, and (d) PDIF-CN_2.

The general idea to improve electron transport is to lower the LUMO energy level of the semiconductor while ensuring that the orbital overlap between adjacent molecules is good. It has been determined theoretically and demonstrated empirically that a LUMO level of -3.6 eV or lower is necessary to realize stable electron transport in OSCs.[17] The strategy that is adopted to preferentially lower the energy of the LUMO is to induce electron deficiency in the π-system by introducing electron withdrawing functionalities.[43] Perfluorination(**Figure 2.3(a)**) has been found to significantly increase the electron affinities of acenes. Perfluoropentacene, for example, has a LUMO energy level at around -3.67 eV that is lower than that of pentacene at -3.0 eV and shows an electron mobility of 0.22 cm^2 V^{-1} s^{-1}.[44] Cyanated acenes are known to have significantly low LUMO energy levels because of the highly electron withdrawing cyano group. Glöcklhofer et al. reported a one pot synthesis of 6,13-dicyanopentacene and 5,7,12,14-tetracyanopentacene, both which have a deep LUMO of -4.16 eV and -4.54 eV.[45] While the former exhibits ambipolar behaviour, tetracyanopentacene transports electrons with a mobility of around 2.2 x 10^{-4} cm^2 V^{-1} s^{-1}. It is therefore, important to note that even a material with low LUMO level can show poor electron transport if the orbital overlap is suboptimal. A common issue with cyanated acenes is that they are not solution-processable. The molecular structure of tetracyanopentacene is shown in **Figure 2.3(b)**

N-heteroacenes, otherwise known as azaacenes, present a very promising class of n-type OSCs. Although not tested for their semiconducting properties until two decades ago, N-heteroacenes have been a subject of interest for synthetic organic chemists for a long time.[46,47] They are ideal candidates to test structure-property relationships since their molecular packing and electronic properties can be tailored by changing the number of nitrogen atoms, their positions in the acene backbone, as well as their valency. Simple N-heteroacenes like tetraazatetracene and tetraazapentacene already show a considerable lowering of their LUMO energy levels (-4 eV and -4.14 eV, respectively) that renders them as n-type materials albeit with very low mobilities (8.9 x 10^{-5} cm^2 V^{-1} s^{-1} and 3.8 x 10^{-4} cm^2 V^{-1} s^{-1}, respectively).[48] However, they are insoluble in common organic solvents which restricts them to vapour-based deposition techniques. Following the success of TIPS-PEN, Miao et al. synthesized 6,13-bis(triisopropylsilylethynyl)-tetraazapentacene (TIPS-TAP, **Figure 2.3(c)**)[49]that showed a LUMO of -4.01 eV. The bulky TIPS groups not only make the molecule soluble but also shield the nitrogen atoms from the environment, thus slowing down the degradation of TIPS-TAP drastically.[50] Xue and co-workers published an electron mobility of 13.3 cm^2 V^{-1} s^{-1} in solution-grown single crystals of TIPS-TAP,[51] one of the highest values of electron mobility reported till date, although this value is highly unreliable and probably overestimated due to non-ideal device characteristics. Liang et al. synthesised a silylethynylated N-heteropentacene with nitrogen atoms on the end rings that showed ambipolar transport, thus indicating that the position of the nitrogen atoms on the conjugated backbone strongly influences its properties.[50] Other notable molecules in this class include halogenated and cyanated N-heteroacenes which are known to further increase the electron affinity and improve charge transport.[52–54]

Imide groups are excellent inducers of high electron affinity and providers of thermal stability, and as such they have been incorporated into acenes to generate n-type OSCs. Perlyene diimide and its derivatives, in particular, have gained ample attention for their electron deficient π-conjugated cores and more importantly, for the ease with which they can be functionalized at the imide nitrogen atom and within the core to tune their properties.[55,56] A distinguished member of this family of molecules is N,N'-1H,1H-perfluorobutyl-dicyanoperylene carboxydiimide (see **Figure 2.3(d)**), commonly known as PDIF-CN_2. Core-cyanation enhances the air-stability of the material by lowering the LUMO and the fluoroalkyl chains at the imide nitrogen act as kinetic barriers against atmospheric water and oxygen by inducing close packing of the molecules, thus further increasing the material's resistance to degradation.[55] PDIF-CN_2 is, therefore, a highly stable molecule whose electron mobility in its single crystal form was measured to be 6 cm^2 V^{-1} s^{-1} in vacuum and ranges between 0.8 and 3 cm^2 V^{-1} s^{-1} in ambient conditions.[57]

The pursuit of better n-type OSCs which not only have higher mobilities but also show increased stability and solution-processability has always been a priority within the organic electronics community. There has been significant progress, as discussed, since the early reports on fullerene, copper phthalocyanine, TCNQ and their derivatives. Many reviews over the years have closely tracked the development of n-type materials and offer thoughtful insights on the synthetic strategies, properties and functionalities.[10,20,27,41,43,47]

2.1.3 Organic Semiconducting Single Crystals

Thin films of small-molecule organic semiconductors used in device fabrication enable quick characterization of the material but do not facilitate a systematic study of its intrinsic properties owing to chemical and structural imperfections. Single crystals, on the other hand, have high chemical purity, are free of grain boundaries, and show long range structural order with minimal traps and defects. As such, organic semiconducting single crystals (OSSCs) of small-molecules provide a better platform to investigate the intrinsic electronic and optical properties. Following the report by Podzorov et al. on single crystal OFET[58] based on rubrene, a number of studies examining the nature of charge accumulation and transport in single crystals were published.[59–64] What these studies also revealed was that the charge carrier mobilities measured in single crystal OFETs were at least an order of magnitude higher than their TFT counterparts. Another important observation was that of anisotropic charge carrier mobility which reflects the low symmetry of molecular packing in OSSCs,[60] although this had been previously reported by Warta and Karl for naphthalene single crystals.[8] As a consequence, single crystals became the testbed for carrying out fundamental studies.

2.1.4 Growth of OSSCs

Single crystal OFETs initially constituted only crystals of rubrene,[58] tetracene[65] or pentacene,[62] all of which were grown from the vapour phase. There are two growth methods — vacuum sublimation and physical vapour transport (PVT).[66,67] The former involves sublimation of a small quantity of the semiconductor powder under vacuum in a clean quartz tube provided with a temperature gradient. Due to convection currents, the sublimed material recrystallizes in the cooler regions of the tube. In the PVT setup there is no vacuum, instead an inert gas under ambient pressure transports the vapours to cooler regions (see **Chapter 3.2.1** for more details). Crystals grown by these methods are found to be pristine both chemically and structurally. There are, however, a few drawbacks — i) the dimensions of the crystals cannot be controlled, ii) crystals are prone to scratches and breakage as they have to be picked up by hand and placed suitably on substrates, and iii) not all materials sublime easily, thermal decomposition is not uncommon. To tackle these problems, several solution-based techniques have been developed. Although most of them yield thin films, there are a few with which single crystals can be obtained.

Drop-casting, for example, involves covering a substrate with the solution of the OSC and letting the solvent evaporate spontaneously, leaving behind well-faceted single crystals (see **Chapter 3.2.1**). Again, specific dimensions are hard to achieve but it is a simple technique with no material wastage. Another straightforward method to access single crystals is by reprecipitation. A supersaturated solution of the OSC is injected into an antisolvent following which single crystals of the OSC precipitate out (more information about this can be found in **Chapter 3.2.1**). The droplet pinning strategy is an effective way to grow dense arrays of single crystals[68] or large crystalline domains.[69,70] Here, a directional growth of crystals is promoted by pinning the solution to a piece of silicon wafer called the pin. Nucleation occurs at the edge of the droplet and as the contact line of the droplet recedes towards the pin, the solute molecules deposited on the initial seed crystals crystallize. In another method developed by Nakayama et al., an inclined solid substrate was used to spatially confine the OSC solution droplets and limit the solvent evaporation only to the exposed sides resulting in large areas of single crystals.[71] The method was also extended to produce crystal arrays by using a stamp with arrays of inclined protrusions.

Solution-shearing, blading, and zone-casting, all of which fall under the umbrella term "meniscus-guided coating" are popular methods to obtain films with large crystalline domains.[72] All of them involve a blade or a bar that is either moved over a solution reservoir or holds a drop of the solution over a substrate placed on a movable heating stage. As the blade or the stage is moved, the meniscus is dragged leaving behind a thin film of the solution which crystallizes as the solvent evaporates. Highly oriented single crystalline ribbons of TIPS-TAP were prepared using zone-casting.[73] Although solution-grown single crystals are not as immaculate as vapour-grown ones due to trapped solvent molecules or other impurities, they are still high performing as evidenced by many reports.[51,68,74] Several excellent reviews provide a good overview of all the available solution-processing techniques, compatible materials, and challenges.[72,75–77]

2.1.5 Molecular Packing in OSSCs

An organic crystal is composed of identical molecules stacked together closely and regularly that are bound by weak intermolecular forces, such as hydrogen bonds or van der Waals interactions. Therefore, the properties of the crystal are strongly dependent on the arrangement of the molecules with respect to each other. The organization of individual molecules inside a crystal lattice and the resulting intermolecular interactions are determined by the chemical structure of the molecule. Its shape, size, and steric factors are all consequential in the formation of molecular crystals. Ultimately, the energetically favourable packing of the molecules is regulated by the balance between the exchange repulsion and the attractive forces (dispersion, electrostatic, and induction terms).[2,78,79]

From previous discussions, it is clear that the field-effect mobility in small-molecule OSCs is sensitively dependent on the molecule itself. For charge transport to take place, the charge (hole or electron) has to hop from one molecule to another which can be described in the simplest way by Marcus theory,[80] although more suitable models have been developed over the past few years such as transient localization.[12,81] Molecular structure and packing together determine the charge transfer integral and the reorganization energy both of which eventually govern charge transport.[82] The charge transfer integral, otherwise known as electronic coupling, is defined as the splitting of the HOMO or the LUMO energy levels between adjacent molecules which in turn reflects the strength of the intermolecular interaction. And, the reorganization energy is a measure of the strength of electron-phonon coupling. To achieve high mobility, the reorganization energy should be minimized and the transfer integral maximized. In general, this can be realized by tuning the intermolecular distance and the π-π overlap.

Organic semiconducting molecules typically arrange themselves in one of the four packing motifs shown in **Figure 2.4**.[41] Although strict face-to-face packing would result in the strongest π-π overlap, molecules do not arrange themselves in such a pattern because of the large electrostatic repulsion that would then exist.[77] As a result, the molecules are either translated or rotated relative to one another. When molecules are rotated about the plane of their conjugated core from their strictly cofacial configuration to minimize the exchange repulsion, the herringbone packing motif is observed. Within this motif there are two types — herringbone (face-to-edge) without π-π overlap between adjacent molecules (**Figure 2.4(a)**), and herringbone with π-π (face-to-face) overlap between adjacent molecules (**Figure 2.4(b)**). By default most acenes and heteroacenes, in the solid state, arrange themselves into the former type.[1] Rubrene, on the other hand, adopts a cofacial herringbone packing in an orthorhombic lattice. There also exists mixed herringbone motif, called sandwiched herringbone, where a pair of molecules interact face-to-face, but then interact in an face-to-edge fashion with adjacent pairs. This was first observed by Bao and co-workers in certain mono-halogenated tetracene derivatives.[83] In the same study, they also report that a dihalogenated tetracene derivative shows a linear face-to-face π-stacking.

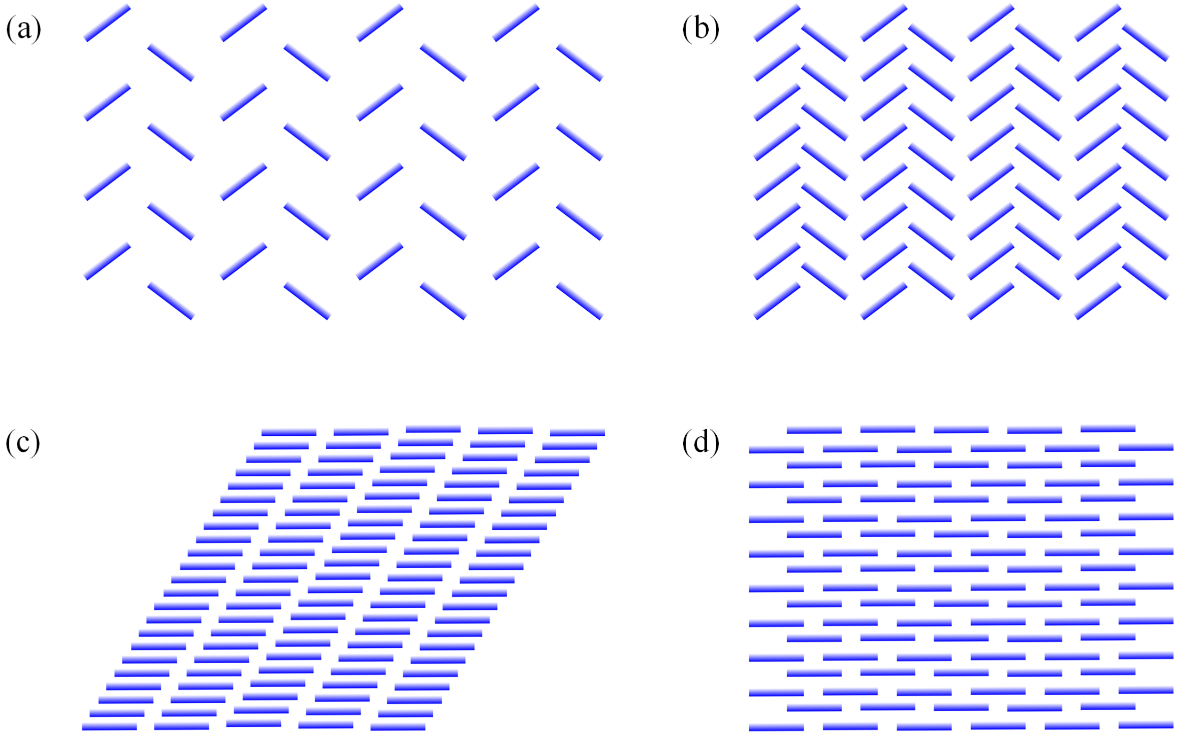

Figure 2.4: Schematic representation of the typical molecular packing motifs adopted by small-molecule organic semiconductors. (a) Herringbone (face-to-edge), (b) herringbone (face-to-face), (c) 1D face-to-face, and (d) 2D brick-wall packing.

When molecules are translated by a short distance along their long or short axis from a strictly cofacial configuration, it results in 1D π-stacking (**Figure 2.4(c)**) and 2D brick-wall (**Figure 2.4(d)**) assembly, respectively. They are sometimes also referred to as the 1D/2D slipped cofacial stacking or 1D/2D lamellar π-stacking motifs. Usually, molecules which are 2D disc-shaped, such as hexabenzocoronene (HBC) or have peripheral substituents that can lead to steric hindrance like dichlorotetracene, conform to the 1D face-to-face motif. In the latter case interactions between the substituents and the aromatic rings tend to stabilize the cofacial packing.[84] For this reason, most of the n-type and ambipolar materials which have electron-withdrawing groups show strong intrastack and poor interstack (between laterally placed stacks) interactions leading to 1D packing. In 2D slipped stacking arrangement, each molecule interacts with four neighbouring molecules and therefore, presents 2D electronic coupling. TIPS-PEN and TIPS-TAP are exemplary molecules in this category which also show very high mobilities. In general, acenes and heteroacenes with bulky trialkylsilyl side groups are known to adopt this motif.[1] The TIPS groups act as steric directors inhibiting face-to-edge alignment while at the same time forcing the aromatic backbones to adopt a face-to-face packing, resulting in a 2D slipped stacking arrangement. However, it is interesting to note that the packing is dependent on the size of the substituent with respect to the acene length.[85] When the diameter of the roughly spherical substituent is less than half the length of the acene, 1D slipped stacking of the molecules is observed. If the diameter is approximately the same as half the acene length, the molecules assume 2D brick-wall packing. As the size of the subsituent is increased, the packing reverts to 1D and with further increment to face-to-edge herringbone arrangement, as the volume of the substituent will then be able to completely cover the acene backbone. Perylene diimide derivatives like PDIF-CN_2 with long fluoroalkyl side-chains also show 2D slipped stacking. It can be inferred that the cyano groups on the aromatic core promote a side-by-side interaction between stacks and the alkyl side-chain prevents edge-to-face stacking simultaneously. Alkylation, in general, is observed to increase intermolecular interactions due to large dispersion forces which brings the molecules closer, leading to a dense packing.[55,86] This effect is very prominent in the case of C_n-BTBT where longer the alkyl chains, more enhanced is the conjugated molecular overlap.[87]

It is common for organic crystals to show polymorphism (that is, the existence of a material in multiple crystal structures) and phase transitions between the different polymorphs (each individual form of a material). Several acenes, like tetracene, pentacene, α-sexithiophene,[88] show a low temperature and a high temperature polymorph. Rubrene, on the other hand, exhibits three different polymorphs based on the growth method.[89] The molecules arrange themselves very differently within the different crystal structures resulting in distinct characteristics. Rubrene in its orthorhombic polymorph adopts a face-to-face herringbone motif, whereas in its triclinic polymorph assumes a 2D slipped stacking motif. More information about rubrene's polymorphs and their properties can be found in the next section.

The packing motif that an OSC molecule adopts also determines the morphology of the bulk crystal. Massaro et al. provide computational results that indicate that in acenes and thiophenes where molecules are packed in face-to-edge herringbone motif, the equilibrium morphologies are barrel shaped with several facets governed by the point group.[90,91] Molecules in 1D cofacial stacking show very little interstack interactions which result in narrow, needle-like crystals. On the other hand, molecules conforming to 2D slipped stacking motif interact strongly across and within stacks which results in a faceted, platelet-like crystal morphology.

In summary, small-molecule semiconductors offer great flexibility in tailoring their properties through careful molecular design. Various synthetic strategies have enabled the tuning of (i) HOMO/LUMO levels, (ii) packing and hence charge transport, and (iii) processability, however with a very complex interplay of all. Single crystals of small-molecule OSCs are ideal systems to investigate intrinsic behaviour and structure-property relationships owing to their near-perfect chemical purity and structure. Molecular packing within the crystals, in addition to molecular structure, influences charge transport. Of the different motifs that the molecules typically arrange themselves into, 2D π-π stacking facilitates the most efficient charge transport with rubrene being an exception.

2.2 Rubrene

Rubrene, a tetraphenyl derivative of tetracene, is an evergreen material that has held the attention of scientists for decades since its first synthesis in 1936.[92] Outstanding photophysical and semiconducting properties, such as fluorescence quantum yield of unity in molecular rubrene[93] and a contact-free intrinsic hole mobility of 40 cm^2 V^{-1} s^{-1} in crystalline rubrene,[94] have provided the impetus for sustained research on this material.

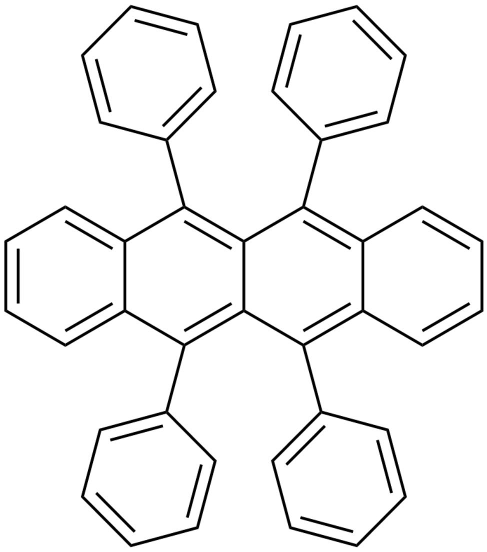

Figure 2.5: Molecular structure of rubrene showing the tetracene backbone with four phenyl groups substituted at the 5,6,11,12 positions.

As a result, rubrene has made its way into a number of applications — as a laser dye,[95] in organic field-effect transistors (OFETs) as the charge transport layer,[59–61,96] as a host or dopant in organic light-emitting diodes (OLEDs)[97–100] and organic photovoltaic (OPV) devices,[101–103] and as a spacer in organic spin-valves (OSVs).[104,105] The molecular structure of rubrene is shown in **Figure 2.5**.

2.2.1 Polymorphs

In order to access intrinsic properties, a vast majority of research on rubrene is performed on its single crystals owing to their defect-free and high purity attributes in addition to superior structural order. To date, three different polymorphs of rubrene — orthorhombic, triclinic, and monoclinic, have been reported.[106] A quick and reliable identification is possible via lattice phonon Raman spectroscopy.[89]

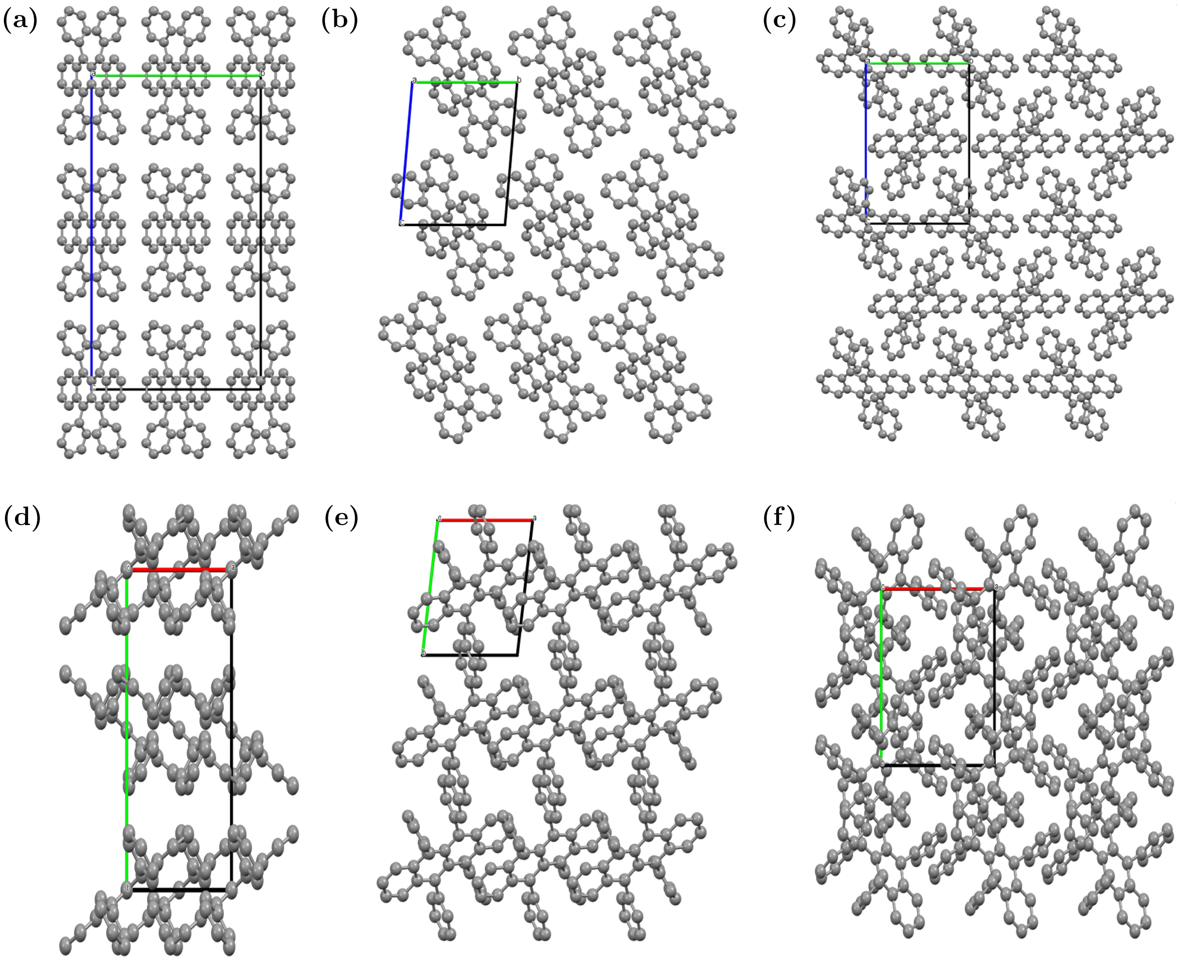

Figure 2.6: Packing of rubrene molecules in the (a) orthorhombic lattice, (b) triclinic lattice, and (c) monoclinic lattice, as viewed along the *a*-axis. (d, e, f) Corresponding view along the *c*-axis. The respective unit cells are indicated with the crystallographic *a*-axis shown in red, *b*-axis in green, and *c*-axis in blue. Hydrogen atoms are omitted for the sake of clarity.

Single crystals of rubrene with the orthorhombic lattice are grown via the physical vapour transport (PVT) method (see **Chapter 3.2.1**),[67] where the molecules arrange themselves into a herringbone packing motif as shown in **Figure 2.6(a)**.[107] The most commonly observed morphologies of the orthorhombic polymorphs of rubrene are platelets and needle-like crystals among others such as thin foils and cotton-wool-like structures.[108] The triclinic polymorph of rubrene is seen in 1D ribbon-shaped crystals, with the molecules adopting a 2D face-to-face slipped-stacking motif (see **Figure 2.6(b)**). Finally, the monoclinic polymorph of rubrene is observed in 2D hexagonal or rhombic plate-like crystals where molecules in consecutive layers are arranged almost perpendicularly to each other, as shown in **Figure 2.6(c)**. Both triclinic as well as monoclinic single crystals of rubrene are grown from solution following a reprecipitation technique.[106] In all three polymorphs, the π-stacking occurs along the a-axis (red-coloured axis) as shown in **Figure 2.6(d),(e),(f)**.

Besides single crystals, polymorphism in thin films of rubrene has also been explored. Thermal evaporation of rubrene followed by abrupt heating is known to produce crystalline rubrene films exhibiting either the orthorhombic or the triclinc phase.[109–111] Spin-coated and annealed rubrene films also show the same two crystal structures depending on the polymer binders used, as demonstrated by Jo and co-workers.[112]

2.2.2 Electronic Properties

Although π-stacking is observed in all three polymorphs of rubrene, the degree of π-π overlap between adjacent molecules is vastly different. The orthorhombic form shows maximum overlap, resulting in very efficient electron coupling[80] while the monoclinic phase exhibits minimal interactions between neighbouring molecules. As a result, the orthorhombic polymorph has been widely studied as a p-type semiconductor in OFETs. Podzorov et al. fabricated single crystal OFETs using rubrene and achieved a hole mobility of 8 cm^2 V^{-1} s^{-1}.[59] Subsequently, a vast amount of research efforts was directed towards understanding charge transport and improving field-effect mobility in rubrene single crystals. Investigation of its intrinsic properties using air-gap transistors revealed anisotropy of carrier mobility and increase of mobility with decreasing temperature.[60] Mobility along the π-stacking axis (a-axis, see **Figure 2.3(d)**) was found to be significantly higher at 15.4 cm^2 V^{-1} s^{-1} in comparison to the mobility along the b-axis (4.4 cm^2 V^{-1} s^{-1}).[60] A study on the influence of different dielectrics on the mobility of rubrene single crystal demonstrated that crystal/dielectric interface plays a crucial role, with high-k dielectrics leading to increased polaron-induced self-trapping of charge carriers.[113,114] Takeya and co-workers minimized interface trap density by laminating rubrene crystals on SiO_2 substrates pre-treated with high density self-assembled monolayers (SAMs) and determined the contact resistance-free intrinsic hole mobility of rubrene to be 40 cm^2 V^{-1} s^{-1}.[115] The Hall effect has also been observed in rubrene single crystals, which together with high mobilities and the negative temperature dependence of mobility, provides unambiguous proof of band-like transport in rubrene,[64,116] and contradicts the assumptions of the hopping model.[12,81]

With the use of appropriate gate dielectrics, electrode materials and design, ambipolar transport has been realized in rubrene single crystals.[117–123] Takahashi et al. first reported ambipolar OFETs of rubrene crystals consisting of a hydroxyl-free poly(methyl methacrylate) (PMMA). Reduced electron traps at the semiconductor-metal interface results in enhanced electron transport. The hole and electron mobilities were found to be 1.8 and 0.011 cm^2 V^{-1} s^{-1}, respectively.[117] More recently, Kanagasekaran et al. have improved these values to 22 cm^2 V^{-1} s^{-1} (hole mobility) and 5 cm^2 V^{-1} s^{-1} (electron mobility) by incorporating a staggered electrode structure comprising of Au or Ca, polycrystalline rubrene and tetratetracontane.[123] The ambipolar behaviour in rubrene crystals has been exploited to construct complementary metal oxide semiconductor (CMOS) inverters and light-emitting FETs.[119,121,123] Additionally, owing to rubrene's high hole mobilities, single crystals of rubrene have been used in combination with inorganic n-type 2D materials such as MoS_2, to generate van der Waals heterostructures that show ambipolar behaviour.[124–126] Ambipolar FETs thus fabricated have been further used as phototransistors or as building blocks in CMOS inverters.

It is not only single crystals but also thin-films of rubrene whose field-effect mobilities have been examined.[109,112,127] Fusella et al. have prepared highly crystalline films of rubrene by using a suitable underlayer between the substrate and thermally evaporated rubrene. Post-deposition annealing results in orthorhombic crystalline film with grains as large as 500 µm showing hole mobilities as high as 3.5 cm^2 V^{-1} s^{-1}.[127]

Most importantly, due to the high reproducibility of single crystals of rubrene, it is the benchmark semiconductor for testing transport theories. Several interesting experiments such as the measurement of Seebeck coefficient,[128] anisotropy of charge transport,[129] and negative isotope effect on charge transport have been carried out on rubrene crystals.

2.2.3 Optical Properties

Rubrene can be purchased as an orange powder with a strong absorption in the blue and green regions of the visible spectrum. Its most striking feature is a photoluminescence quantum yield (PLQY) of unity in solution,[93] that has inspired considerable amount of research on rubrene's optical properties. Although the PLQY of single crystals of rubrene is low, other properties such as long exciton diffusion lengths, high photoconductivity, waveguiding, and good singlet fission efficiencies are beneficial for optoelectronic applications. It has been experimentally observed that unlike in rubrene solution where only singlet state absorption takes place with low quantum yield of intersystem crossing, in orthorhombic rubrene crystals triplet formation takes place via singlet fission.[130] It is these triplet excitons that are responsible for high surface photocurrents in rubrene crystals because of their long lifetime ($\sim$ 1 µs) and large diffusion length ($\sim$ 5 µm).[131] Irkhin and

Biaggio have further shown that the exciton mobility in the crystals is highly anisotropic with the long-range diffusion present only in the direction of the π-stacking.[132] Furthermore, experimental results are consistent with theoretical calculations that show that the red component of rubrene's PL originates from triplet-triplet fusion process, whereas the yellow-green PL is associated with charge-transfer singlet excitons.[131]

An interesting characteristic of rubrene crystals is their strong absorption and emission anisotropy. The twofold axis of rotation (M axis) of a rubrene molecule as it is found in orthorhombic rubrene crystals lies parallel to the short axis of the backbone (or parallel to c-axis, see **Figure 2.6(a)**) and the transition dipole moment corresponding to the strongest low-energy electronic transition is along this axis.[133] Such a combination results in strong absorption and emission anisotropy which in turn have a large impact on the spectra obtained from rubrene crystals under different illumination and detection geometries. The strongest absorption band of orthorhombic rubrene for c-polarized light is observed at 2.32 eV and is followed by a higher-energy vibronic progression with a band separation of 0.17 eV. The absorption band observed at 2.8 eV distinguishes the orthorhombic rubrene crystal from rubrene solution and amorphous solid. Interestingly, majority of the PL of orthorhombic rubrene crystal is emitted with c-polarization with the main emission peak at 2.2 eV. However, this is redshifted from the intrinsic PL due to self-absorption since the strongest absorption is in the same direction. The intrinsic c-polarized emission has the main band centred at 2.22 eV followed by lower-energy vibronic progression with a separation of 0.15 eV. Different polymorphs of rubrene are expected to show a different degree of self-absorption determined by the extent of overlap of their absorption and emission spectra as well as the surface quality of the crystals.

In orthorhombic crystals, the reabsorbed light along the c-axis (perpendicular to the ab facet) is self-guided towards the edge.[134] Similar waveguiding effects are also seen in the 1D triclinic ribbons and the 2D monoclinic plates.[106] With regard to the lifetimes, all solid samples of rubrene are characterized by a multi-exponential decay with the monoclinic crystal displaying the longest lifetime, followed by the triclinic form and lastly the orthorhombic phase with the shortest lifetime.[106] The short lifetime component of each polymorph is attributed to the self-quenching phenomena in solid-state aggregates of red-emissive materials.[135] Rubrene in solution, on the other hand, shows a single exponential decay with a lifetime as long as 13 ns.[106]

Absorbance and emission of an amorphous film of rubrene are slightly redshifted with respect to the solution due to the combined effect of higher polarizability and static disorder in its environment.[136] It is, however, crucial to note that as with the crystals and solutions of rubrene, reabsorption effects may have an influence on the PL position of films as well.

The occurrence of singlet fission as well as triplet fusion leading to delayed fluorescence[137] in addition to the formation of polaron pairs from the singlet excited state[138] has been investigated in disordered films of rubrene.

2.3 Vibrational Spectroscopy of Organic Molecules

2.3.1 Infrared Spectroscopy

One of the most important and widely used techniques of analytical chemistry is infrared (IR) spectroscopy. Although the infrared region of the electromagnetic spectrum encompasses the near-infrared (13000-4000 cm^{-1}), the mid-infrared (4000-400 cm^{-1}) and the far-infrared ($<$ 400 cm^{-1}) sub-regions,[139] the term 'infrared' in this thesis only refers to the mid-infrared section. When photons of this energy are absorbed by molecules they are excited to higher vibrational states, and the spectroscopy technique that measures these vibrational transitions of molecules is termed IR spectroscopy. A material's IR absorption properties is described by its complex refractive index (N) at the macroscale by,[140]

$$N(\lambda) = n(\lambda) + i \cdot \kappa \tag{2.1}$$

where, λ is the wavelength of light, n and κ are the real and imaginary components of the complex refractive index that are related to scattering and absorption, respectively. In the case of non-magnetic materials, N is related to the dielectric permittivity (ϵ) by,

$$N(\lambda) = \sqrt{\epsilon(\lambda)} \tag{2.2}$$

The real and imaginary parts of the dielectric permittivity are therefore,

$$Re[\epsilon] = n^2 - \kappa^2 \tag{2.3}$$

$$Im[\epsilon] = 2 \cdot n \cdot \kappa \tag{2.4}$$

The vibrational energy levels (E_v) according to the harmonic oscillator model is given by,[141]

$$E_v = \Big(v + \frac{1}{2}\Big)\hbar\omega \tag{2.5}$$

where, the vibrational quantum number v = 0, 1, 2,..., $\hbar$ is the reduced Planck constant, and frequency $\omega = (k/m)^{1/2}$ with k being the force constant that characterizes the stiffness of the bond and m the effective mass. The vibrational levels of a harmonic oscillator are schematically shown in **Figure 2.7(a)**.

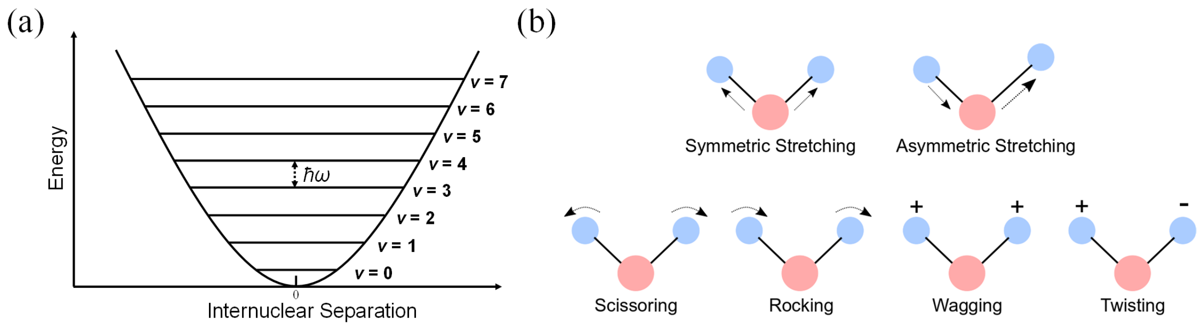

Figure 2.7: (a) Schematic of the vibrational energy levels of a harmonic oscillator evenly separated by $\hbar\omega$. Even in its lowest state the oscillator has a non-zero energy. (b) Illustration of the different types of stretching (top) and bending (bottom) molecular vibrations. The arrows indicate the direction of simultaneous change of either bond length or bond angle in the plane of the paper. The '+' and '-' indicate bending of the bonds out of and into the plane of the paper, respectively.

The selection rule for a change in the vibrational state caused by the absorption or emission of radiation is that there must be a change in the electric dipole moment of the molecule when its atoms are displaced relative to one another. Only such vibrations are said to be IR active. Mathematically this is denoted as,

$$\left(\frac{\partial \boldsymbol{\mu}}{\partial Q}\right)_0 \neq 0 \tag{2.6}$$

where, $\boldsymbol{\mu}$ is electric dipole moment and Q is the normal coordinate of a normal mode. Normal coordinates are theoretically determined set of coordinates that describe the motion of all atoms (called the normal modes) by approximating the intramolecular potential with a harmonic function.[142] A non-linear molecule with X number of atoms will have 3X-6 vibrational degrees of freedom, otherwise known as vibrational modes. Even for a fairly simple molecule, there are several vibrational modes that couple together to give rise to a complex spectrum. The intensity of an absorption peak is proportional to the square of the derivative of the electric dipole moment with respect to the normal coordinate, and the position is determined by the stiffness of the bond along with the masses of the atoms at each end. The resonance frequency expressed in wavenumbers follows from **Equation 2.5** as,

$$\tilde{\nu} = \left(\frac{1}{2\pi c}\right)\sqrt{\frac{k}{m}} \tag{2.7}$$

where, $\tilde{\nu}$ is the wavenumber of an absorption maximum in cm^{-1} and c is the speed of light. Molecular vibrations either involve a change in bond length leading to stretching vibrations (symmetric or asymmetric) or a change in bond angle resulting in bending vibrations (scissoring, rocking, wagging, or twisting), as shown in **Figure 2.7(b)**.

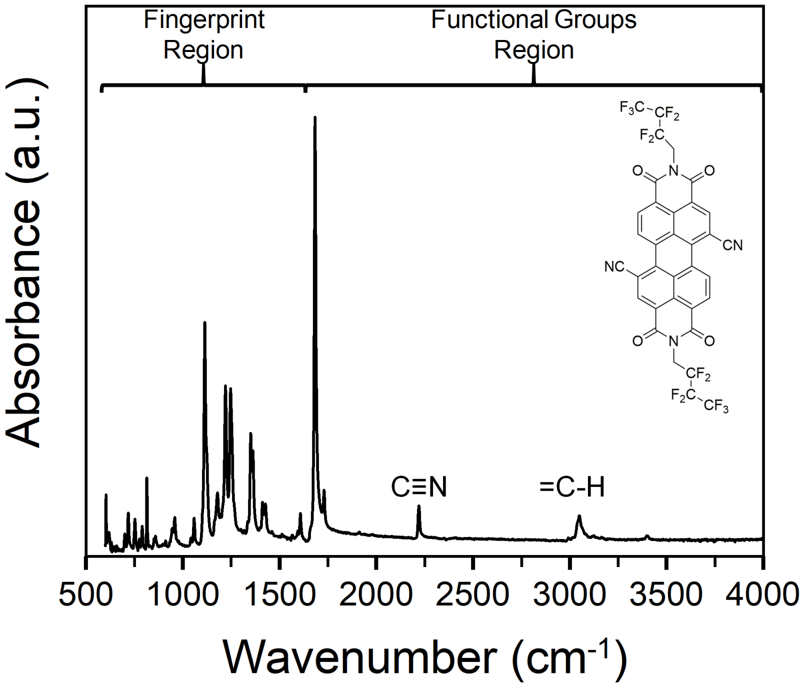

Figure 2.8: Unpolarized IR absorbance spectrum of PDIF-CN_2 (inset). The skeletal vibrations of the molecule are observed between 600 and 1700 cm^{-1}, whereas vibrations localized to its functional groups can be seen above 2000 cm^{-1}. Here, the peaks at 2220 cm^{-1} and 3040 cm^{-1} correspond to C≡N and =C-H stretching vibrations, respectively.

An example of IR absorbance spectrum of an organic molecule is shown in **Figure 2.8**. Some vibrations are localized to the functional groups and the corresponding absorption peaks appear in the 1700-4000 cm^{-1} range, while others called skeletal vibrations involve atoms from a large part of the molecule or the entire molecule. The absorption bands associated with skeletal vibrations are observed between 600 and 1700 cm^{-1} and are regarded as the “fingerprint” of the molecule. It is important to note that several factors such as intramolecular conformations,[143,144] intermolecular interactions,[145,146] combination and overtone bands, and Fermi resonance[139] can cause shifts in position and intensity of the absorption peaks. These perturbations hold crucial chemical and structural information which can be extracted by using advanced IR techniques and performing theoretical calculations followed by rigorous analysis.

With polarized IR light the absorbance of a sample along specific directions can be probed. From this the orientation of the molecules can be deduced as only those vibrational modes with the transition dipole moment vector (i.e., electric dipole moment that is associated with the transition between two states) or its component aligned parallel to the incident electric field are excited.

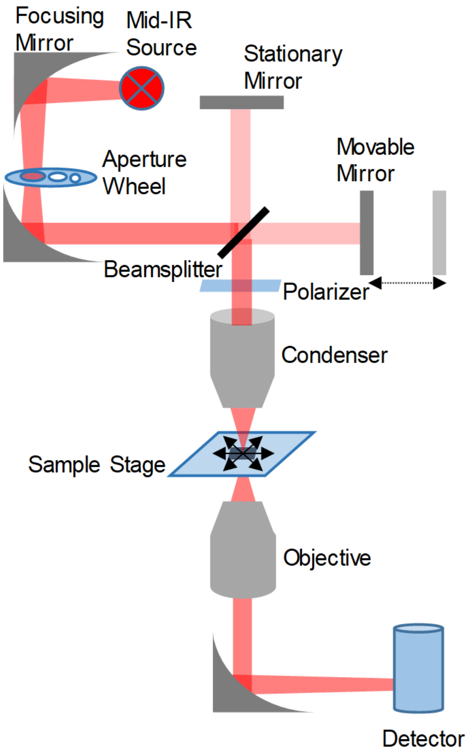

Figure 2.9: Schematic of an FT-IR microscope with a Michelson interferometer in the transmission mode. Adapted with permission from Ref.[147]. Copyright 2020 American Chemical Society.

To record high quality IR spectra and perform chemical imaging within reasonable timeframes, a Fourier-transform infrared spectrometer (FT-IR) coupled with IR microscope is predominantly used. The basic components of an IR microimaging setup are shown in **Figure 2.9** — a broadband thermal source, a Michelson interferometer, an optical microscope, and a focal plane array (FPA) detector. The polychromatic light that emerges from the source (Globar or Nernst) is directed into the interferometer where the moving mirror introduces an optical path difference between the two arms resulting in a modulated exit beam that is incident on the sample. In the transmission mode, assuming the losses from reflection are negligible, the transmittance (T) is defined as the ratio of the intensity of the transmitted beam (I) to the intensity of the incident beam (I_0) and is further related to the absorption coefficient (α_{abs}) and the path length of light inside the sample (l) by,

$$T = \left(\frac{I}{I_0}\right) = e^{-\alpha_{abs} \cdot l} \tag{2.8}$$

It follows from **Equation 2.8** that the absorbance (A) of the sample is

$$A = -log(T) = \gamma \cdot c \cdot l \tag{2.9}$$

where, γ the molar absorptivity and c the molar concentration of the sample are related to α_{abs} through $\alpha_{abs} = \gamma \cdot c$. The transmitted signal then reaches the detector (mercury cadmium telluride) following which it is amplified, converted to a digital form by an analog-to-digital converter and transferred to a computer. Here, the raw data (called an interferogram) which contains information about the transmission of light at each mirror position is converted to an actual spectrum of transmittance as a function of wavenumber by the mathematical method of Fourier transformation. The Fourier transform essentially converts the distance domain (here, the displacement of the mirror) to its inverse domain (wavenumber in cm^{-1}).

The lateral resolution of IR microscopes like optical microscopes is limited by the diffraction of light. It is approximated by the Rayleigh criterion,

$$r = \left(\frac{0.61 \cdot \lambda}{NA} \right) \tag{2.10}$$

where, r is the lateral resolution, λ is the wavelength of light, and NA is the numerical aperture of the objective. Clearly, from **Equation 2.10** the lateral resolution of an IR microscope tends to be several micrometers which is too low to resolve nanoscale features. Although successful attempts have been made to improve image quality by employing FPAs with small pixel sizes,[148,149] and compensate for the resulting poor signal-to-noise ratio by using synchrotrons[150] and quantum cascade lasers,[151,152] IR microscopes are still deficient in lateral resolution for utility in nanoscale science and technology.

2.3.2 Raman Spectroscopy

A complementary technique to IR spectroscopy is Raman spectroscopy, also a non-invasive and non-destructive technique that provides information about molecular structure and interactions, crystallinity, phase, and polymorphism. It is based on the Raman effect which, classically speaking, describes the inelastic scattering of light that occurs when electromagnetic radiation interacts with matter. When an electric field is incident on a sample, it disturbs the electronic charge distribution in the molecule thus inducing a dipole moment even in an otherwise non-polar molecule. This induced dipole moment ($\mathbf{p}$) is related to the electric field ($\mathbf{E}$) by,

$$\mathbf{p} = \alpha \cdot \mathbf{E} \tag{2.11}$$

where, α, the proportionality factor, is the molecular polarizability that determines the extent to which the external field is able to distort the sample's electron density out of its equilibrium configuration.[153]

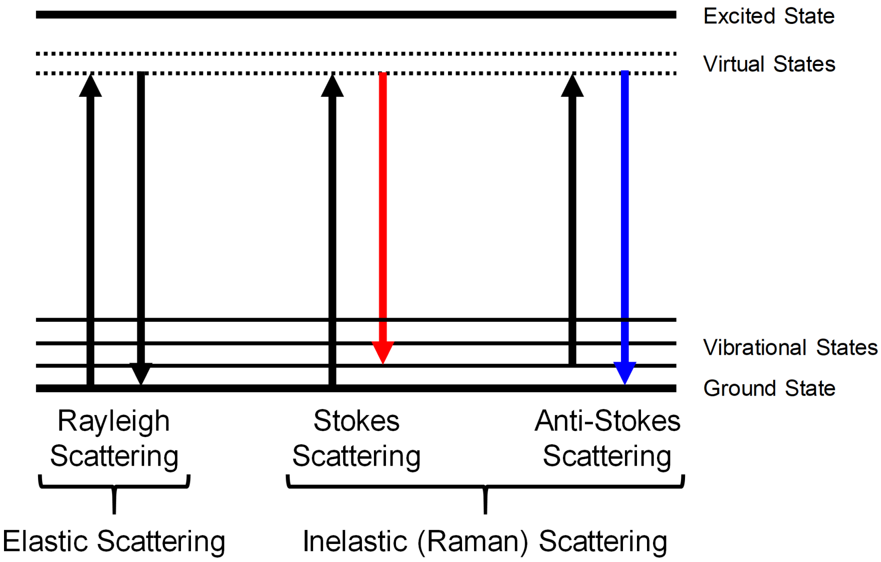

Figure 2.10: Energy level diagram of the different states involved in elastic and inelastic scattering of light.

Depending on the nature of interaction between the excitation radiation and the sample, there are two types of scattering — (i) elastic and (ii) inelastic, as shown in **Figure 2.10**. Elastic or Rayleigh scattering occurs when the incident light and the scattered light have the same energy resulting in zero frequency shift. Whereas, inelastic or Raman scattering is further sub-divided into (i) inelastic Stokes scattering where the scattered light is red-shifted with respect to the excitation frequency and (ii) inelastic anti-Stokes scattering where the scattered light is blueshifted with respect to the incident light. As with IR spectroscopy, there exists a selection rule for Raman spectroscopy as well which states that the inelastic scattering of light results from the non-zero derivative of the electronic polarizability along the Q-th normal coordinate at equilibrium geometry, that is,

$$\left(\frac{\partial \alpha}{\partial Q}\right)_0 \neq 0 \tag{2.12}$$

This implies that the vibrations observed with Raman spectroscopy are different from those seen with IR spectroscopy. It is important to note that the intensity of a signal from Raman scattering cross-sections is proportional to the square of (i) the gradient of the polarizability and (ii) the electric field, and (iii) to the fourth power of frequency of the excitation laser. The Raman intensity, is however, typically six orders of magnitude smaller than the signal from IR absorptivity.[148] Technological developments have not only enabled signal enhancement via resonant Raman scattering or surface enhanced Raman scattering (SERS), but also combined the chemical specificity and sensitivity of Raman spectroscopy with the high spatial resolution of confocal microscopy leading to imaging of samples. The main components of a Raman microscope include a monochromatic laser excitation source, an optical microscope, stray light filtering system, a spectrometer (dispersive or interferometric) and a detection system (typically a charge-coupled device). The spatial resolution is still limited by the wavelength of the laser (e.g., 532 nm) but is much better than that of an IR microscope.

Raman spectroscopy is usually employed to identify molecules and understand their conformation based on their intramolecular vibrations. However, when certain molecular crystals show polymorphism, the chemical identity of the different polymorphs being the same implies that their intramolecular vibrational modes are similar or even identical. In this case, it would be beneficial to study their intermolecular modes. These modes which are composed of collective translational or rotational motions of the molecules in the unit cell produce dynamical deformations of the crystal lattice called lattice vibrations or lattice phonons that cause Raman shifts in the range 10-150 cm^{-1}. Since lattice phonons involve intermolecular interactions, they are very sensitive to molecular packing and hence the lattice phonon Raman spectra serve as fingerprints of individual crystal structures. Polymorphs of several well-known OSCs such as pentacene, tetracene, α-sexithiophene and rubrene have been identified from their lattice phonon pattern which has further enabled in-situ characterization of phase purity.[88,89,154,155] As such, lattice phonon Raman spectroscopy is a powerful tool to probe structural information in a fast, reliable manner and acts as a complementary technique to X-ray diffraction (XRD) by providing access to lattice dynamics.

In recent years, it has been established that the interaction between a charge carrier and the inter- and intramolecular vibrations of an organic semiconducting molecule, called electron-phonon interactions, leads to charge localization that results in less efficient hopping transport.[12,81,156–160] These electron-phonon interactions comprise of two components — the local component that corresponds to changes in the vibrational levels of the molecule and is associated with high-wavenumber ($\tilde{\nu} > 200$ cm^{-1}) intramolecular vibrations, and the non-local component that arises from changes to the transfer integral and is mainly related to the low-wavenumber ($\tilde{\nu} < 200$ cm^{-1}) intermolecular vibrations or lattice phonons.[158] Low-wavenumber Raman spectroscopy is one of the techniques used to analyse the impact of these lattice phonons on charge transport.

2.4 AFM-IR

It is well-established that while FT-IR provides rich chemical information it is limited in lateral resolution to several micrometers because of the diffraction of long-wavelength

(2.5-25 µm) mid-IR radiation. To circumvent this constraint imposed by diffraction of light, a few advanced methods involving scanning probe techniques have been developed. The AFM-IR, originally known as photothermal induced resonance (PTIR), is one such method that combines the high lateral resolution of atomic force microscopy (AFM) and the high chemical specificity of IR spectroscopy.[140,161,162] It operates by employing an AFM tip to locally and instantaneously detect thermal expansion of the sample resulting from the absorption of mid-IR radiation. Unlike FT-IR, the spatial resolution of AFM-IR does not depend on the wavelength of light but only on the radius of the apex of the AFM tip which is typically only a few nanometers.[163–166] As a result, IR spectra and chemical images with nanoscale resolution are achievable. Alexandre Dazzi and co-workers are credited with the development of the state-of-the-art AFM-IR[167] which has been used for the chemical characterization of a range of materials and samples such as polymers, proteins, cells and tissues, quantum dots, solar cells, etc.

2.4.1 Working Principle

The top-side illumination setup of an AFM-IR is shown in **Figure 2.11**. It consists of a tunable laser that produces pulsed mid-IR radiation, which when incident on a sample excites the molecules to higher vibrational states. As and when the molecules return to their ground state, a part of the vibrational energy is dissipated as heat. It is this heat that causes a rise in temperature and subsequently, thermal expansion of the sample.

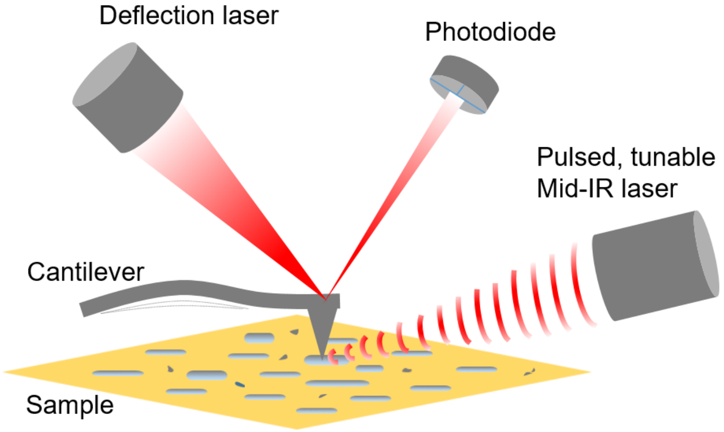

Figure 2.11: Schematic of an AFM-IR setup with top-side illumination. Adapted with permission from Ref.[147]. Copyright 2020 American Chemical Society.

Assuming that the electric field is uniform inside the sample and $n^2 >> \kappa^2$ (see **Equation 2.1**), the power absorbed by the sample (P_{abs}) is given by,[167]

$$P_{abs} = I_0 \cdot \alpha_{opt} \cdot V \cdot \tilde{\nu} \cdot \kappa(\tilde{\nu}) \tag{2.13}$$

where, α_{opt} contains all the optical constants and parameters and V is the volume of the sample. The maximum temperature increase (ΔT_{max}) inside the sample when the duration of the laser pulse (t_p) is shorter than the thermal diffusion time is derived from the Fourier heat equation and is,

$$\Delta T_{max}(t) = \left(\frac{P_{abs} \cdot t_p}{V \cdot \rho \cdot C_p}\right) exp\left(\frac{t - t_p}{\tau}\right) \tag{2.14}$$

where, ρ is the density of the sample, C_p is the heat capacity of the material, and $\tau = (\rho \cdot C_p \cdot a^2)/k$ with k being the thermal conductivity of the environment and a the size of the sample (e.g., radius of a sphere or length of a cube). The resulting thermal expansion ($u(t)$) due to increase in temperature of the sample is then,

$$u(t) = a \cdot G \cdot \alpha_{exp} \cdot \Delta T_{max}(t) \tag{2.15}$$

where, G is a geometric constant, and α_{exp} is the thermal expansion coefficient of the sample. From **Equations 2.13, 2.14** and **2.15** it is clear that there exists a linear relationship between the power absorbed and the product of wavenumber and optical absorption coefficient, the temperature increase and the power absorbed, and finally the thermal expansion and the temperature increase. Consequently, the thermal expansion is also proportional to the the wavenumber multiplied by the optical absorption coefficient. Therefore, by measuring the thermal expansion as a function of wavenumber, the absorption spectra of the sample is obtained in the AFM-IR.

The AFM tip itself detects the thermal expansion of the sample as it induces a force impulse on the cantilever that drives it into oscillations. It has been found that in most cases the cantilever's oscillation amplitude is directly proportional to the power absorbed, which in turn is linearly dependent on the optical absorption coefficient.[166,168] Thus, by measuring the oscillation amplitude of the cantilever either as a function of wavenumber or of sample position, the AFM-IR enables acquisition of both IR absorption spectra as well as chemical maps of the sample.

Typically, a quantum cascade laser is used in AFM-IR for its high repetition rate (1 MHz and higher) which allows synchronization with different resonance frequencies of the cantilever. As such, the cantilever can be made to oscillate continuously at a specific frequency by matching the repetition rate of the quantum cascade laser and therefore eliminate the damping of the photodetector signal. This is called "resonance enhanced AFM-IR" which enables efficient excitation of the cantilever into continuous wave oscillations and thus improves the sensitivity of the detection of IR absorption. Using metal-coated tips and substrates is shown to further enhance the sensitivity.[169] However, as demonstrated recently by Morsch et al., the specular reflectance and thermal response of the substrate as well as the resulting interference effects have an influence on the local absorption spectra and maps. These factors along with the non-uniformities in specimen thickness should be considered while interpreting data from the AFM-IR.[170]

Until recently, the AFM-IR was used in contact mode which prevented its application to soft and loosely adhered samples. In order to overcome this limitation, tapping AFM-IR mode has been developed which is based on heterodyne detection.[171] Using this novel mode, structure and composition of drug-carrying nanoparticles of size less than 200 nm have been unravelled,[172] drug-metal nanoparticle interactions have been investigated,[173] and drug partitioning at lipid-polymer phase boundaries has been demonstrated.[174]

2.4.2 Applications

The AFM-IR has shown great versatility in the analytical characterization of various materials and samples where conventional FT-IR microspectroscopy has failed. Studies on polymers, polymer blends and composites have especially benefited from this technique, gaining crucial insights into composition, distribution, crystallinity and orientation. In multilayer polymer films, for instance, ensuring uniformity and compatibility of different layers is of great importance. By tuning the laser to a specific absorption band that is strongly excited in one of the layers, variations in uniformity were recorded.[167] The AFM-IR has also been employed to reverse engineer the composition of multilayer films by comparing spectra from the AFM-IR to reference FT-IR spectra.[175,176] A study showed phase segregation of acrylonitrile butadiene into regions rich in polybutadiene and domains mainly composed of polystyrene based on characteristic peaks of polystyrene.[177] In another study, different polymeric components in high impact polypropylene could be quantified and their distribution was identified by analysing relative peak intensities.[178] In addition to thin films, polymeric fibres have also been investigated using the AFM-IR. The presence of two distinct phases — crystalline and amorphous, of electrospun fibres of a biodegradable polymer were determined based on different spectroscopic features. With the help of the imaging mode, it was revealed that the crystalline and amorphous phases separated into a core and shell structure, respectively.[179] Molecular orientation in certain polymer fibres was examined by changing the polarization of incoming light. As the incident electric field was aligned with a specific molecular bond, the absorption increases which results in a stronger AFM-IR signal.[165]

Life sciences have also exploited the AFM-IR for a number of purposes. Cell studies that measure its physiological state, ageing and disease have used the AFM-IR.[180,181] Marcott et al. mapped human tissue like skin and hair to understand their chemical composition in order to optimize skincare and haircare products and treatments.[182] Furthermore, insights into the process of protein aggregation that results in certain neurodegenerative diseases have been gained because of the AFM-IR which can resolve intermediate and secondary structures of proteins.[183]

Other areas where the AFM-IR has been utilized include perovskite solar cells where electromigration was visualized,[184] in plasmonics to study localized surface plasmon resonances in InAs nanostructures,[185] and in the semiconductor field for the investigation of quantum dots, phonon absorption, interlayers and interfaces.[186–189] Finally, the AFM-IR has also been used to examine the material composition of artworks in an effort to understand their degradation and formulate better preservation and restoration methods.[190]

Surprisingly, samples composed of small-molecule organic semiconductors have so far not been studied with the AFM-IR. This is likely because of their low coefficients of thermal expansion (CTE) that range between 10 and 170 ppm/K and may result in poor quality of the AFM-IR signals.[191] Polymeric semiconductors, on the other hand, have a significantly higher CTE that vary from 50 to 500 ppm/K.

2.5 IR-SNOM

Scanning near-field optical microscopy (SNOM) is another advanced technique that circumvents the diffraction limit by coupling radiation to an optical antenna placed at a distance less than the wavelength of light, in the so-called “near-field” of the sample. The IR-SNOM, much like the AFM-IR, also exploits the superior lateral resolution of an AFM and merges it with the very good chemical specificity of IR spectroscopy. It works by focusing light at the apex of a metallic, scanning probe tip and measuring the modified amplitude and phase of scattered light resulting from tip-mediated light-sample interactions.[192–194] The AFM tip enables electric field confinement and enhancement, and thus offers high spatial resolution and surface sensitivity. The IR-SNOM has shown great potential in characterizing layered materials such as graphene and hexagonal boron nitride (h-BN), plasmonic nanostructures, polymers as well as biological samples.[195,196]

2.5.1 Working Principle

A schematic of the IR-SNOM setup is shown in **Figure 2.12**. It is a complex system consisting of an atomic force microscope integrated with a broadband mid-IR laser unit and a Michelson interferometer-based asymmetric Fourier-transform spectrometer.[194] The AFM tip which not only provides topographic information of the sample but is responsible for the electric field confinement and enhancement that is necessary for achieving subwavelength resolution ($\approx$20 nm)[197] is central to the IR-SNOM. Typically, platinum/iridium coated probes that enable spectrally flat enhancement are used. A metallic substrate such as gold-coated silicon can further improve the local field enhancement.[140]

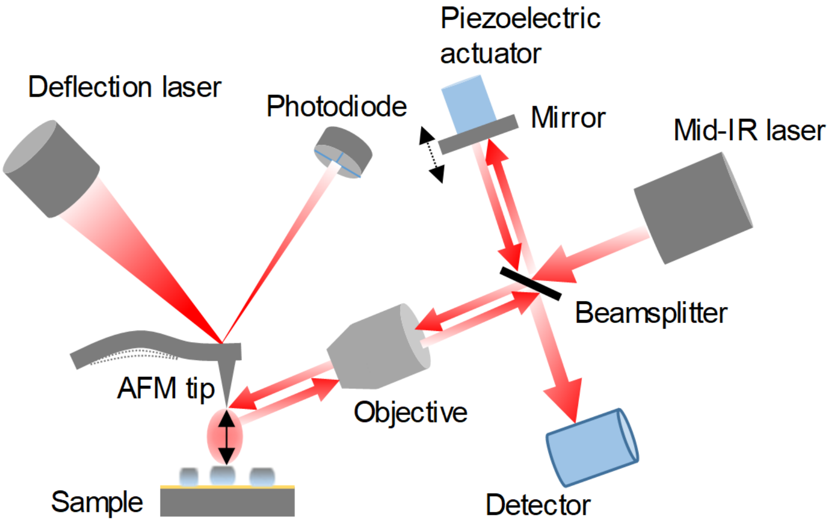

Figure 2.12: Schematic of an IR-SNOM setup with an asymmetric Michelson interferometer. Adapted with permission from Ref.[147]. Copyright 2020 American Chemical Society.

The near-field interaction between the tip and the sample is described by the complex-valued, frequency-dependent scattering coefficient $\sigma(\omega)$. It carries information about the local dielectric properties (and therefore the local refractive indices) of the tip and the sample, and is related to the measured amplitude $s(\omega)$ and phase $\phi(\omega)$ signals of the backscattered light as follows:[197,198]

$$\sigma(\omega) = s(\omega) \cdot e^{i\phi(\omega)} \tag{2.16}$$

A relationship between the scattered electric field E_{sca} and the incident electric field E_{inc} is then established through the scattering coefficient by,

$$E_{sca}(\omega) = \sigma(\omega) \cdot E_{inc}(\omega) \tag{2.17}$$

In order to eliminate the background contributions, a “pseudoheterodyne” detection technique is adopted.[199] Here, the detector signal is demodulated at higher harmonics of the vibrational frequency of the tip (Ω) and the near-field interferogram of the demodulated signal is obtained by vibrating the reference mirror in the Michelson interferometer using a piezoelectric actuator. Fourier transformation of this near-field interferogram yields near-field spectra given by,[199]

$$E_n(\omega) = \sigma_n(\omega) \cdot R(\omega) \cdot E_{inc}(\omega) \tag{2.18}$$

where, n is the demodulation order and $R(\omega)$ is the spectral response of the instrument. Analogous to classical FT-IR measurements, the near-field spectra are normalized to reference spectra ($E_{n,ref}(\omega)$) recorded from a spectrally flat (that is, $\sigma_n(\omega)$ = constant) substrate such as gold-coated silicon. The scattering coefficient of the tip-sample is therefore,

$$\sigma_n(\omega) = \frac{E_n(\omega)}{E_{n,ref}(\omega)} \tag{2.19}$$

It has been established that the imaginary part of the scattering coefficient ($\mathrm{Im}[\sigma(\omega)] = s(\omega) \cdot sin[\phi(\omega)]$) is associated with local absorption in the case of organic materials.[200,201] That is, $a_n \equiv \mathrm{Im}[\sigma(\omega)]$.

From an accurate mathematical description of the scattering coefficient extracted from the point-dipole model[192] or the finite-dipole model,[202] it is known that $\sigma(\omega)$ depends on the surface response function, $\beta(\omega)$, such that,

$$\beta(\omega) = \frac{\epsilon(\omega) - 1}{\epsilon(\omega) + 1} \tag{2.20}$$

and where, $\epsilon(\omega)$ is the complex-valued dielectric function of the sample. Under specific conditions for thin films of weak molecular oscillators (e.g., organic molecules) where the sample thickness $<< \lambda$ and the substrate is spectrally flat,

$$\sigma_n(\omega) \propto \beta(\omega) \tag{2.21}$$

Hence, it follows that the scattering coefficient depends exclusively on the local dielectric function of the sample and by measuring it, it is possible to determine the real and imaginary parts of $\epsilon(\omega)$ and thus, $\kappa(\omega)$ (see **Equations 2.1** and **2.2**). For molecular vibrations of organic materials $\kappa(\omega)$ can be approximated to $\mathrm{Im}[\beta(\omega)]$.[197] Given that the far-field absorbance A of the sample is proportional to $\kappa(\omega)$, a linear chain of dependencies is established: $a_n \propto \mathrm{Im}[\beta(\omega)] \propto \kappa(\omega) \propto A$. From this, the connection between the near-field and the far-field absorption can be approximated to,

$$a_n(\omega) \propto A \tag{2.22}$$

Therefore, mid-IR spectroscopy performed using the IR-SNOM (also known as nano-FTIR) enables chemical identification of any material exhibiting vibrational resonances at very high spatial resolution by correlating with the corresponding spectra from conventional FT-IR measurements. To this end, the phase ($\phi(\omega)$) as a function of wavenumber is compared with the standard FT-IR absorbance spectrum of a material. Additionally, with a tunable laser such as a quantum cascade laser, the IR-SNOM is capable of acquiring IR-maps by scanning the AFM tip over a specified area of the sample at a fixed wavelength. This allows for direct visualization of nanoscale changes in, for example, material composition, molecular packing, stresses and strains across the sample. Sometimes, however, the interpretation of signals from the IR-SNOM can be challenging, especially for thicker samples (i.e., thickness $\geq \lambda$) because of complex tip-sample interactions. In this case, tip and sample specific modelling would be necessary to be able to extract information about the sample's local absorption. Moreover, the signals are also sensitive to substrate effects[203] which can further complicate the analysis of IR-SNOM data.

2.5.2 Applications

The capabilities of the IR-SNOM have been tested to a great extent on low dimensional materials. Visualization of grain boundaries and defects in graphene, the most widely studied van der Waals material, was made possible by the IR-SNOM.[204,205] The interference between surface plasmon waves launched by the AFM tip and the reflected waves from the grain boundaries and defects is what revealed their presence. In h-BN, surface phonon polaritons were imaged using the IR-SNOM.[206] The technique has also enabled the examination of plasmon-phonon coupling and plasmon delocalization in heterostructures of graphene and h-BN.[207] This study also showed that the IR-SNOM can effectively distinguish between different heterostructures and can accurately distinguish graphene stacks with different layer numbers. Plasmonic nature of other 2D materials, such as MoS_2 and its interactions with graphene and SiO_2 have also been investigated with the IR-SNOM.[208–210] In the study of single-walled carbon nanotubes, the IR-SNOM could differentiate between metallic and semiconducting species, and image Luttinger-liquid plasmons.[211–213]

The application of IR-SNOM has also been extended to polymers and biological materials. For example, using the carbonyl resonance as a vibrational probe, local concentration of PMMA in disordered quasi-lamellar structures of the block copolymer — PMMA-*b*-PS, was provided by the IR-SNOM.[214] Although very challenging, nanoimaging and nanospectroscopy of certain dried biological samples, such as melanin granule in human hair and collagen fibrils in damaged human tendons, and tobaccomosaic virus in aqueous environments have also been carried out.[215–217]

Various bulk materials and thin films of small-molecule organic semiconductors have also been probed with the IR-SNOM to obtain insights into molecular orientation, phase mixing and lattice strains. Raschke et al. imaged and quantified molecular orientation and crystallinity in aggregates and polycrystalline films of perylene tetracarboxylic dianhydride (PTCDA), an organic semiconductor, with the combination of single wavelength imaging and broadband spectroscopy that the IR-SNOM provides.[218] In a study by Westermeier et al., structural inhomogeneity in pentacene thin films was uncovered. Coexistence of two different phases — the bulk phase and the thin film phase of pentacene was documented by measuring a shift in one of the vibrational resonances using the nano-FTIR mode, and their morphological difference was imaged in the nanoimaging mode.[219]

2.6 Comparison of AFM-IR and IR-SNOM

While both the AFM-IR and the IR-SNOM fulfil the objective of spectroscopic mapping with high spatial resolution, they are not equivalent techniques, but complementary. The key difference is that the AFM-IR measures light that is absorbed by the sample, whereas the IR-SNOM detects scattered light. The signal recorded by the AFM-IR is a direct measurement of the sample's absorption coefficient; on the other hand, the IR-SNOM is the result of a complex interaction between the tip, the sample and the substrate with the phase component connected to the sample's absorption. Another significant difference is that the IR-SNOM is primarily a surface sensitive technique,[192] while the signal in the AFM-IR comes from a greater depth of the sample.[166] Although both techniques are capable of providing useful information about inorganic, organic, as well as biological samples, the AFM-IR is preferred for the latter two. This suggests that materials with large thermal expansion coefficient and small refractive index are better suited for measurements with the AFM-IR and vice versa for the IR-SNOM. Therefore, discreet selection of the method for the material is imperative to harness the full potential of these two versatile IR techniques. The case of small-molecule organic semiconductors is, however, not as clear. They exhibit low CTEs as well as low refractive indices, which makes it unclear if one technique is preferred to the other. Other intrinsic properties such as the structure of an individual molecule or the packing in the solid state may also have an influence on the signals detected in the AFM-IR and the IR-SNOM, but are not yet not well understood.

2.7 Liquid Exfoliation and Stabilization

The successful isolation of atomically thin layers of graphene from graphite by Geim and Novoselov using an adhesive tape[220] initiated a new field of research on the process of exfoliating layered materials as well as on the layer dependent properties of the exfoliated structures. Besides graphene, a number of materials with strong in-plane (intralayer) covalent bonds and simultaneously weak out-of-plane (inter-layer) van der Waals interactions such as transition metal dichalcogenides (e.g., WS_2 and MoS_2), hexagonal boron nitride (h-BN), black phosphorus, metal oxides and hydroxides (e.g., MnO_2 and $Mg_6Al_2(OH)_{16}$) have been investigated.[221–225] Exfoliation of these materials results in high-aspect-ratio nanosheets with large surface areas ideal for surface chemistry.

In recent years, liquid-phase exfoliation (LPE), pioneered by Coleman et al.,[226] has become the method of choice to produce 2D nanosheets from their bulk 3D counterparts mainly owing to its simplicity, affordability, and potential scalability. The process is fairly straightforward — a layered crystal immersed in a stabilizing liquid such as a solvent, an aqueous surfactant or polymer solution is exfoliated into 2D nanosheets by imparting either shear or ultrasonic energy. Provided the surface energy of the solvent/aqueous solution matches that of the layered material, the net exfoliation energy is reduced and the nanosheets are stabilized electrostatically or sterically against reaggregation.[227] Apart from graphite[228] and h-BN,[229] LPE has been successfully applied to a wide variety of layered materials like transition metal dichalcogenides,[230] pnictogens (e.g., black phosphorus),[225] metal oxides,[231,232] hydroxides[233,234] and sulfides[235] as well as III-VI[236,237] and IV-VI semiconductors.[238,239] More recently, its applicability has been further extended to synthetic organic layered materials such as 2D polymers,[240] 2D covalent organic frameworks[241] and metal organic frameworks.[242] The as-produced dispersions from this method are highly polydisperse with lateral sizes of the nanosheets ranging from 40 to 400 nm and thicknesses of 1 to 10 monolayers, with the tendency of small sheets being thinner and large sheets being thicker by nature.[243] As a result, size selection becomes a requisite for effective examination of size and thickness dependent material properties and for applications. A centrifugation-based method called “liquid cascade centrifugation” (LCC), developed by Backes and co-workers, has not only proven to be an efficient strategy to access dispersions that are separated by size of the nanosheets but has also facilitated controlled dispersion enrichment in monolayer ensembles.[244]

Exfoliation of novel layered materials and formulation of functional inks via LPE requires careful selection and fine-tuning of several process parameters starting with how the energy required to break interlayer forces is provided. One of the well-established methods is ultrasonication either by using sonic baths or tip sonicators. The principle strategy here is that the ultrasonic waves generate cavitation bubbles which turn into high-energy jets as they collapse, thus delaminating and fragmenting the material with tensile and shear forces.[245] Between bath and tip sonication, the former delivers lower intensities to the sample and the position of the sample-containing vial in the tank is crucial to avoid non-uniform distribution of sonic energy. In the latter case, energy is imparted directly to the sample in its dispersed medium. It has been found that for inorganic layered materials, tip sonication results in larger amounts of exfoliated material in shorter periods of time.[246] A major concern in both the methods is the heating of samples which affects quality and quantity of exfoliated materials. It can be prevented by periodically replacing the water in the sonication bath or by using a chiller. Although ultrasonication is the preferred method for its ease of use and cost-effectiveness, issues with regard to reproducibility and scalability persist. A good alternative is shear exfoliation in rotor/stator mixers or rotating blade blenders where high yields of exfoliated material with comparatively larger nanosheets are achievable simply by increasing the volume.[247]

The second prominent factor that strongly influences the efficiency of exfoliation via LPE is the choice of the dispersion medium or stabilizer. The role of a stabilizer is two-fold: it reduces the net exfoliation energy while also preventing the aggregation of exfoliated nanostructures. The question of what is an appropriate stabilizer is largely dependent on the material that is to be exfoliated. Organic solvents such as *N*-methyl-2-pyrrolidone (NMP) and dimethylformamide (DMF) have been regularly used[226,230,248] to stabilize graphene and h-BN. They offer the advantages of protection against degradation of chemically unstable materials like black phosphorus[225] and adjustable rheological properties, but at the same time are extremely toxic and have high boiling points. For these reasons, aqueous surfactant solutions have been in use to obtain colloidally stable dispersions.[249,250]

A fundamental principle of thermodynamics is that a system maintained at a constant temperature will tend to spontaneously change in the direction which will lower its free energy. Hence, in a colloidal dispersion where particles (dispersed phase) are suspended in a medium (continuous phase), aggregation is expected occur over time. The stability of a colloidal dispersion is, therefore, the tendency of the dispersed phase to continue to remain discrete (or avoid agglomeration) in the continuous phase. It is defined by the interaction between the particles, mainly the van der Waals attraction and the electrostatic repulsion, both of which contribute to the overall free energy of the system.

The DLVO theory (named after Derjaguin, Landau, Verwey and Overbeek)[251,252] classically describes the balance between the two opposing forces — van der Waals attraction and electrostatic repulsion to characterize the stability of a colloidal dispersion. The colloidal particle develops a net surface charge due to the surfactant and as a result, there is an effective surface potential which leads to the formation of an electric double layer consisting of a layer of immobile charges (Stern layer) followed by diffuse charges (diffuse layer), as shown in **Figure 2.13(a)**. When two such charged particles approach each other, the long-range electrostatic repulsive forces come into play. For the two particles to aggregate, certain energy is required to overcome the repulsion which is indicated by the electrostatic repulsion curve (see **Figure 2.13(b)**). As the particles get closer, the short-range van der Waals attractive forces which is a combination of different dipole-dipole interactions (i.e., Keesom, London, and Debye forces)[141] have to be surpassed if the particles are to remain discrete. This is indicated by the van der Waals attraction curve. The DLVO theory combines the repulsive and attractive energies to obtain a net interaction energy, as shown in **Figure 2.13(b)**. If the net interaction energy is present in the repulsive regime, then its maximum is called the energy barrier which indicates the stability of a dispersion. Provided the energy of the interacting particles is high enough to clear this barrier, they will cross over to the attractive regime where they are "trapped" together.

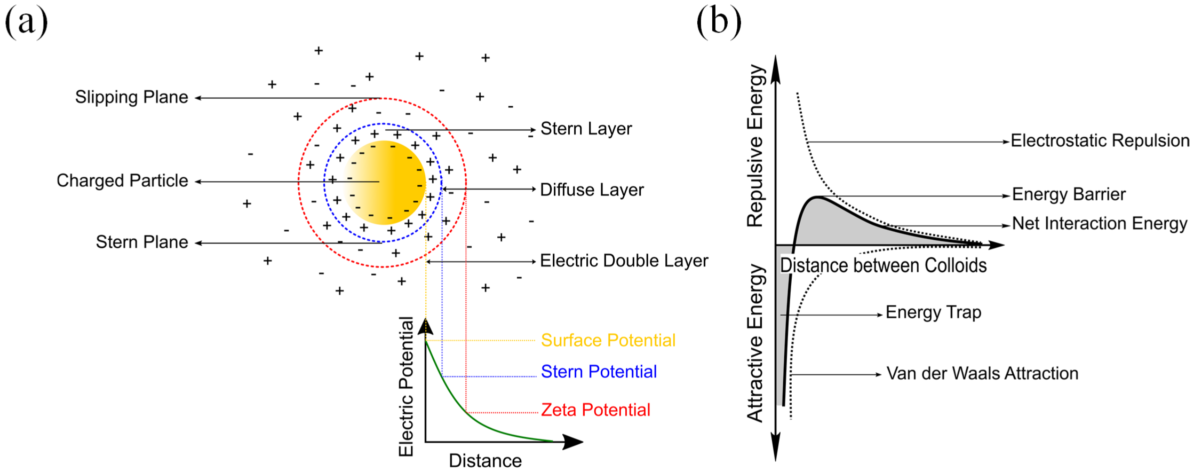

Figure 2.13: (a) Illustration of a charged colloidal particle and the electric double layer surrounding it. (b) The net interaction energy curve of two charged colloidal particles in close proximity.

The environment of the dispersed phase can be altered to change the height of the energy barrier with the help of surfactants, as mentioned above. Surfactants are usually organic molecules that are amphiphilic, that is, both hydrophobic (or non-polar) as well as hydrophilic (or polar) groups are present.[253] In the case of aqueous dispersions, these amphiphilic surfactants adsorb onto the surfaces of the hydrophobic dispersed phase through their non-polar group via non-covalent forces while the polar group interacts with the surrounding water (see **Figure 2.14**). Depending on the type of surfactant — cationic, anionic, zwitterionic, or non-ionic, re-aggregation is blocked by electrostatic and/or steric repulsion. Typically, ionic surfactants promote electrostatic stabilization where attractive van der Waals are counterbalanced by repulsive forces between charged colloidal particles. Whereas, non-ionic surfactants facilitate stabilization through steric effects.[254]

A quantitative indicator of the stability of a dispersion is its zeta potential whose magnitude reflects the degree of electrostatic repulsion between two closely spaced, similarly charged particles. It is strictly equal to the electric potential at the slipping plane (see

Figure 2.13(a)) and not the surface potential or the Stern potential which are defined at different positions. Values of ±30 mV or higher indicate very stable dispersions.[255]

A number of surfactants have been tested to stabilize nanomaterial dispersions of which sodium cholate (SC), sodium deoxycholate (SDC) and sodium dodecylbenzenesulfonate (SDBS) are among the ones employed often. An illustration of stabilization of a dispersion with varying nanosheet sizes and thicknesses achieved with the help of sodium cholate is shown in **Figure 2.14**.

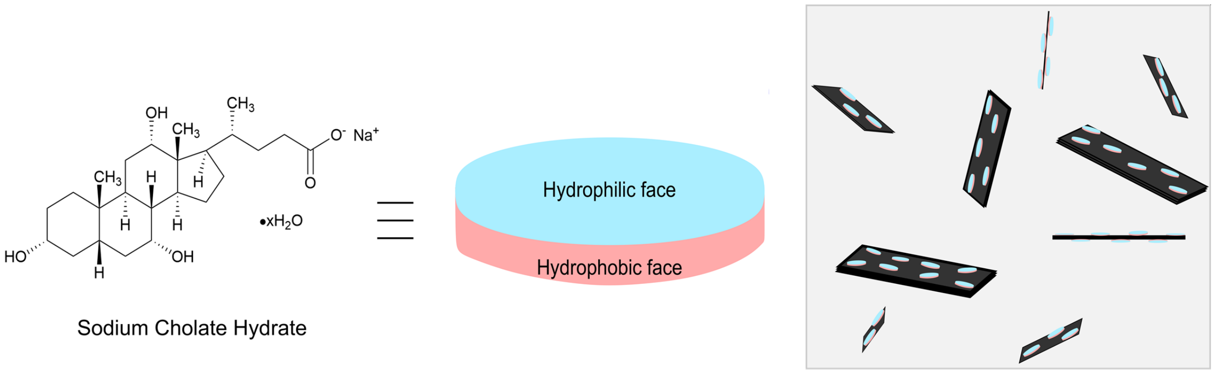

Figure 2.14: Molecular structure of sodium cholate hydrate and an illustration of its adsorption on nanosheets of different sizes and thicknesses in a dispersion. Note that the surfactant molecules are adsorbed on both faces of the nanosheets.

As mentioned above, the LPE technique suffers an inherent bottleneck in that the resulting dispersion following exfoliation is a heterogeneous mixture of nanosheets of different lateral sizes and thicknesses. This is neither ideal for studying intrinsic, size-dependent properties nor for exploiting the full potential of the exfoliated material in applications. Therefore, different separation strategies involving centrifugation, such as density gradient ultracentrifugation[256–258] and liquid cascade centrifugation,[244,259] have been explored. Of these, the latter is less complex and is used in this thesis (see Chapter 5), hence it is described below.

2.8 Sedimentation and Size Selection

As mentioned above, centrifugation-based techniques have been employed to effectively separate nanomaterials based on their lateral size. Centrifugation involves the use of centrifugal force to separate particles by way of sedimentation. However, two other forces, namely the buoyant force and the frictional force also act on the particle. It is only when the centrifugal force exceeds the sum of these two counteracting forces that the particles sediment at a constant rate.

Stokes' law which describes the motion of a spherical particle in a gravitational field can be used to describe sedimentation of particles.[260] It relates the terminal velocity of a particle (v, also referred to as settling velocity or rate of sedimentation) to a number of factors — the radius of the particle (r), density of the particle (ρ_p), density of the surrounding medium (ρ_m), viscosity of the medium (µ), and the gravitational acceleration (g), as follows:

$$v = \left(\frac{2r^2(\rho_p - \rho_m)g}{9\mu} \right) \tag{2.23}$$

Because of the very weak gravitational field of Earth, the sedimentation rate of especially small particles can be very slow which why a centrifuge is used to produce high accelerations. In this case, the gravitation acceleration in Equation 2.23 is replaced with the centrifugal acceleration which is the product of the square of the angular velocity (ω) and the radius of the rotor (R), resulting in

$$v = \left(\frac{2r^2(\rho_p - \rho_m)R\omega^2}{9\mu} \right) \tag{2.24}$$

Hence, the sedimentation rate is higher for larger particles with bigger difference in density between the dispersed and continuous phases. It can be maximized by increasing the speed and/or the radius of the rotor and by using a low-viscosity medium for dispersion. Note that the acceleration applied to a dispersion in a centrifuge is expressed as "relative centrifugal force" (RCF) in units of g. It takes into account both rotational speed as well as the radius of the rotor. An important parameter that is used to characterize the sedimentation of a particle is the sedimentation coefficient (s).[261] It is defined as the ratio of the sedimentation rate of a particle to the applied acceleration and expressed in units of Svedberg (1 S = 10^{-13} s). Therefore,

$$s = \frac{v}{R\omega^2} \tag{2.25}$$

Therefore, from **Equations 2.24** and **2.25**,

$$s = \frac{m}{6\pi\mu r} \tag{2.26}$$

where, m is the difference in mass between the particle and the surrounding fluid of equal volume. The sedimentation coefficient thus only depends on the properties of the particle and the medium in which it is dispersed. Even for non-spherical particles, it still depends only on the mass and any one of its dimensions. As a result, in a polydisperse mixture, the heavier and larger particles sediment faster compared to the lighter and smaller ones.

Liquid cascade centrifugation (LCC) is an established method that allows size selection following LPE. It is a multi-step process where the dispersion containing exfoliated material is subjected to several consecutive centrifugation steps, each at a higher rotation speed than the previous one. After each run, the supernatant is collected and passed down the "cascade" while the sediment is retained and redispersed in fresh solvent/solution. A fraction of the starting dispersion containing nanomaterials of a particular size distribution is thus trapped between two centrifugation steps, and with each increasing step smaller particles are collected.[246] What is critical for efficient size selection is the careful and complete decantation of the supernatant after each step. Other factors include duration of centrifugation and centrifugal acceleration, one or both of which need optimization depending on the density of the material as well as the density and the viscosity of the stabilizing liquid, as discussed above. The two big advantages of LCC are low material wastage and high concentration of nanomaterials in the sediment fractions. On the downside, layer-dependent selection is hard to achieve, that is, small and thick structures cannot be separated from the large and thin ones with LCC. However, this problem can be partially overcome by the so-called secondary cascades.[244] Nevertheless, the LCC technique has been successfully demonstrated on a large number of materials suspended in different solvent and surfactant solutions.[225,233,236,244,259]

Liquid-phase exfoliation in combination with liquid cascade centrifugation is a powerful approach to access tunable properties of layered materials for real-world applications.

Chapter 3

Materials and Experimental Methods

3.1 Semiconducting Materials

The four materials used in this thesis are 6,13-bis((triisopropylsilyl)ethynyl)pentacene (TIPS-PEN), 6,13-bis((triisopropylsilyl)ethynyl)-5,7,12,14-tetraazapentacene (TIPS-TAP), 5,6,11,12-tetraphenyltetracene (rubrene), and N,N'-1H,1H-perfluorobutyl-dicyanoperylene carboxydiimide (PDIF-CN_2). Their molecular structures are shown in **Figure 3.1** and information about their source and purity are provided in **Table 3.1**.

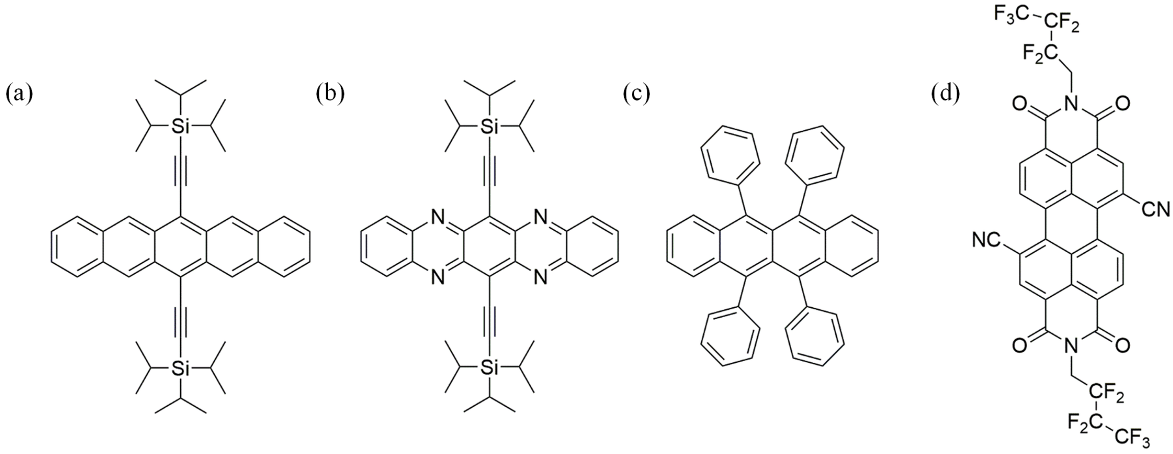

Figure 3.1: Molecular structures of (a) TIPS-PEN, (b) TIPS-TAP, (c) rubrene, (d) PDIF-CN_2.

Table 3.1: Organic semiconducting materials used in this thesis, their source and purity.

Organic Semiconductor	Source	Purity
TIPS-PEN	Sigma-Aldrich	≥ 99% (HPLC)
TIPS-TAP	In-house*	N/A
Rubrene	Sigma-Aldrich	N/A, further purified**
PDIF-CN_2	Polyera Corporation	N/A, further purified**

* TIPS-TAP was synthesized by Dr. Sebastian Hahn in the Bunz group at the Institute of Organic Chemistry, Heidelberg University, Germany, according to Ref. [49].

** Further purification of rubrene and PDIF-CN_2 was achieved by the physical vapour transport method (see below).

3.2 Preparation of Samples

3.2.1 Single Crystals

Single crystals of TIPS-PEN and TIPS-TAP were grown by the drop-casting method, where a small volume of the solution is pipetted onto a substrate placed inside a glass Petri dish, as shown in **Figure 3.2(a)**. A solvent-rich atmosphere is provided by placing a few drops of the solvent around the substrate, to ensure slow crystallization. The Petri dish is then covered and left undisturbed until the solvent completely evaporates, leaving behind crystals of the material on the substrate.. With chlorobenzene as the solvent (99.8%, Sigma-Aldrich), solutions of 0.5 wt% TIPS-PEN and TIPS-TAP were prepared. A double-side polished silicon wafer with a native oxide layer was cut into 1 cm sided square substrates and subjected to sonication in deionised water, acetone and isopropanol for 10 min each. Following this preliminary cleaning procedure, the substrates were blow-dried with a nitrogen gun and placed in the UV/ozone cleaner for 15 min. The solutions were then drop-cast onto these ultraclean substrates placed in pre-cleaned Petri dishes, under ambient conditions. After $\sim$24 hours of crystallization, well-faceted, micrometer-sized single crystals of TIPS-PEN and TIPS-TAP were obtained (see **Figure 3.2(b)**).

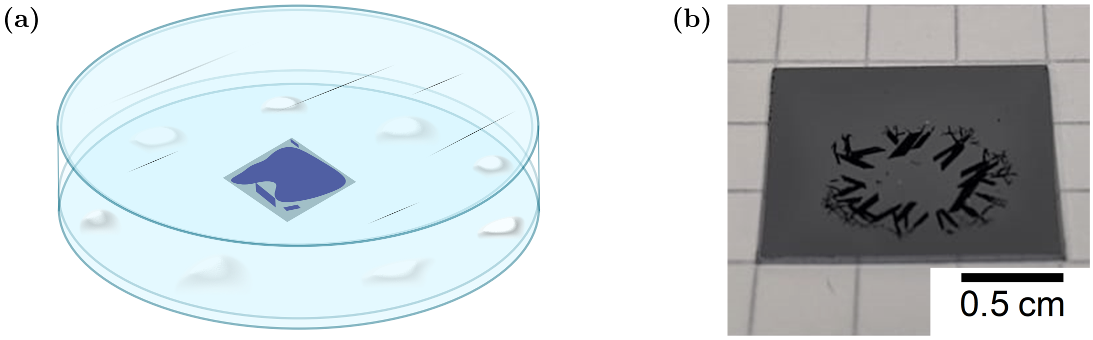

Figure 3.2: (a) Schematic of single crystal growth by the drop-casting method. (b) Photograph of a sample showing crystals grown by the drop-casting method.

A vapour-based method called physical vapour transport (PVT)[67] was employed to grow single crystals of orthorhombic rubrene and triclinic PDIF-CN$_2$. A long, pre-cleaned quartz tube that housed five smaller glass tubes was placed inside a horizontal growth furnace such as the one in **Figure 3.3(a)**. Resistance wire wound around an outer glass casing provided a temperature gradient and thus determined the three different zones — source zone, crystal growth zone, and impurity deposition zone.

Using a temperature controller and a gas-flow meter (to control the flow rate of argon, the

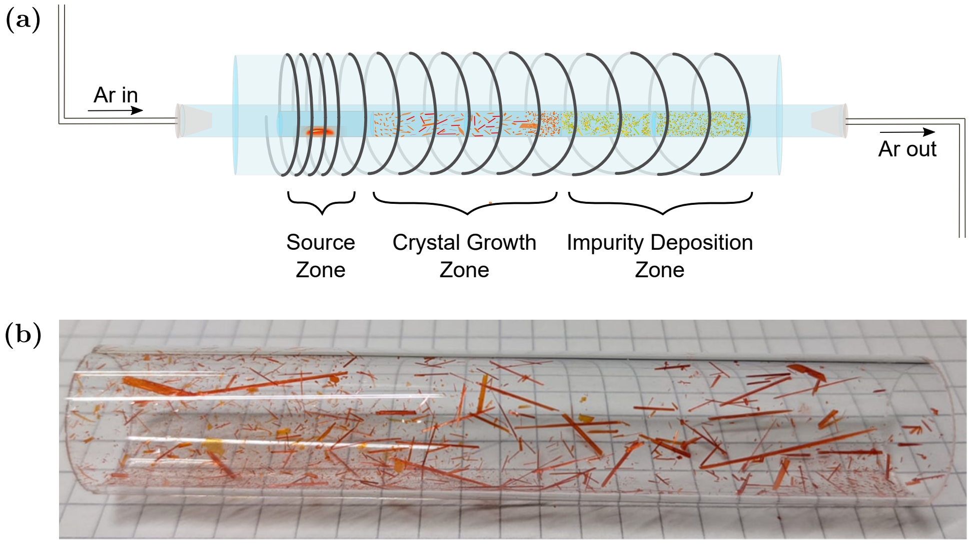

Figure 3.3: (a) Schematic of the physical vapour transport (PVT) method. (b) Photograph of rubrene crystals grown by the PVT method.

carrier gas), the tubes were baked for a few hours to eliminate any residual moisture. Once the furnace was brought back to room temperature, the starting material was introduced into the source zone and baked again at 150 °C. After a couple of hours, the temperature of the furnace was slowly increased in steps of 10 °C until the sublimation temperature of the material was reached. The setup was then left undisturbed until all of the starting material sublimed and deposited as crystals in the growth zone. The tubes containing the impurities (if any) were cleaned while those with the crystals were stored for use. To obtain higher quality crystals, a tube containing the crystals from the first round of sublimation was used as the starting material in the subsequent re-sublimation step.

Rubrene and PDIF-CN$_2$ were sublimed at 290 °C under an argon flow rate of 50 and 75 sccm, respectively. Crystals from twice-purified rubrene (see **Figure 3.3(b)**) and once-purified PDIF-CN$_2$ were then laminated onto pre-cleaned double-side polished native silicon substrates.

The triclinic polymorph of rubrene, used for exfoliation experiments, was prepared by a solution-based method. The procedure established by Huang et al.,[106] yields needle-like crystals of rubrene via a simple reprecipitation technique and was adapted here. A small amount of rubrene ($\sim$50 mg) was first purified in the PVT furnace by placing it in the source zone and heating it to around 260 °C overnight until only the impurities sublimed. Clean rubrene powder was retrieved and used to prepare a 30 mM solution in choloform ($\geq$99%, Sigma-Aldrich) that was sonicated for 5 min to ensure complete dissolution of rubrene. 50 µL of this solution was quickly injected into a vial containing 2.5 mL of methanol ($\geq$99.8%, Sigma Aldrich), after which it was allowed to rest at 25 °C overnight. Several micrometer-sized rubrene crystals with jagged edges precipitated from the turbulent mixing of the good and poor solvents (here, chloroform and methanol, respectively) as shown in **Figure 3.4**. The crystals were then collected via centrifugation.

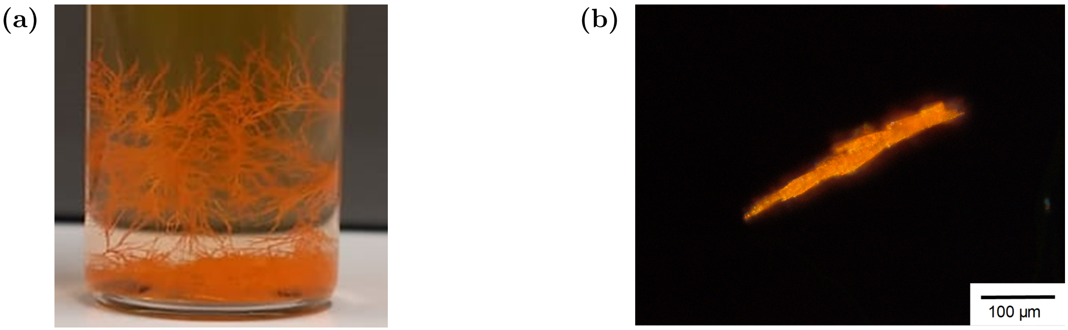

Figure 3.4: (a) Photograph of triclinic crystals of rubrene grown via the reprecipitation method. (b) Dark-field optical micrograph of a single needle-like triclinc rubrene crystal.

3.2.2 Polycrystalline Film

A discontinuous film of PDIF-CN_2 was fabricated by spin-coating, another solution-based technique. Here, a substrate centred on a vacuum chuck is covered with a solution of a material and spun at high speeds. The combined effect of the resulting centripetal force and surface tension of the liquid causes a thin, uniform layer of the solution to form on the substrate. The solvent then quickly evaporates because of the airflow within the spin-coater, leaving behind a film of the material on the substrate. **Figure 3.5(a)** illustrates the different steps involved in spin-coating and **Figure 3.5(b)** shows an optical micrograph of the spin-coated PDIF-CN_2 film.

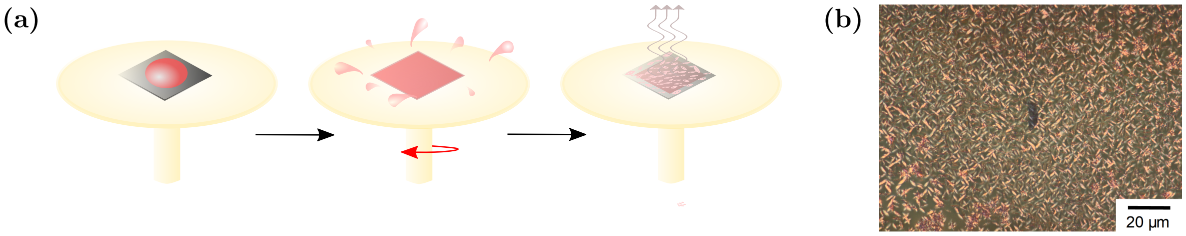

Figure 3.5: (a) Schematic of the spin-coating process. Deposition of the solution is followed by spinning and thereafter, formation of the film as the solvent evaporates. (b) Optical micrograph of a discontinuous film of PDIF-CN_2 crystallites.

A concentrated solution of 5 mg of PDIF-CN_2 in 1 mL of anhydrous chloroform (99.0-99.4%, Sigma Aldrich) was prepared by heating the mixture at 110 °C for 15 min. Upon filtering the ink through a 0.2 µm PTFE filter, it was spin-coated onto a pre-cleaned native silicon substrate coated with gold at 2000 rpm for 30 s. Subsequently, the sample which consisted of a discontinuous, polycrystalline film of PDIF-CN_2 was annealed for an hour at 110 °C. All the processing steps were carried out inside a dry nitrogen glove-box (MB-200B, MBRAUN).

3.3 Liquid-Phase Exfoliation and Size Selection

3.3.1 Exfoliation by Bath Sonication

Orthorhombic rubrene crystals, grown by the PVT method, were collected in 15 mL of aqueous sodium cholate ($\geq$99%, Sigma-Aldrich) solution of 2 g L^{-1} concentration in a 50 mL centrifuge tube (from VWR). Subsequently, the centrifuge tube was immersed in a Branson 2800 water bath sonicator at one of the two hotspots. The ultrasonication bath was then operated at full power for 4 h to exfoliate the crystals. The water in the bath was exchanged with ice-cold water every 30 min to prevent heating of the dispersion.

The triclinic rubrene crystals, which were grown in solution, were first subjected to centrifugation at 1000 *g* for 1 h using a Hettich Mikro 220R centrifuge equipped with a 1195A fixed-angle rotor. The supernatant — a mixture of methanol and chloroform, was discarded. The sedimented crystals were re-dispersed in 2 g L^{-1} aqueous sodium cholate and sonicated, as before. The schematic in **Figure 3.6** shows rubrene crystals dispersed in aqueous surfactant solution and the resulting stock dispersion after exfoliation.

Figure 3.6: Rubrene crystals dispersed in an aqueous solution of sodium cholate (2 g L^{-1}) undergo exfoliation by bath sonication, resulting in a stock dispersion of exfoliated and stabilized rubrene, and a sediment comprising of unexfoliated rubrene crystals.

3.3.2 Size Selection via Liquid Cascade Centrifugation

The selection of exfoliated rubrene by size was achieved through liquid cascade centrifugation as developed by Backes et al.[244] Stock dispersion of exfoliated rubrene in sodium cholate solution was distributed equally into several 1.5 mL Eppendorf tubes and centrifuged at 100 *g* for 1 h at 15 °C in a Hettich Mikro 220R centrifuge equipped with a 1195A fixed-angle rotor. The supernatant was transferred to fresh tubes and the sediment, which consisted of unexfoliated rubrene, was discarded. Subsequently, the centrifugation was continued at 100 *g* for 2 h followed by 1000 *g* and finally at 30,000 *g*, for 1.5 h each. The sediment after each centrifugation step was collected in 0.1 g L^{-1} aqueous sodium cholate solution, thus yielding three dispersions (see **Figure 3.7**) which were used for UV/VIS, fluorescence, lifetime and zeta potential measurements. Each dispersion was labelled according to the lower and upper relative centrifugal force applied at each step.

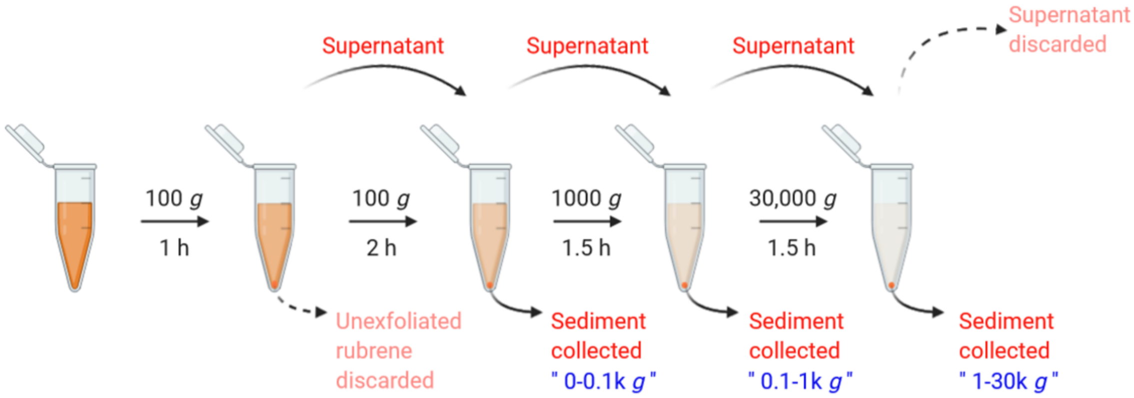

Figure 3.7: Schematic of size-selection by liquid cascade centrifugation. Labels given to the three collected dispersions are within quotes.

3.4 Characterization Techniques

3.4.1 Optical Microscopy

An Olympus BX51 microscope with an in-built camera was employed to acquire optical micrographs of the samples either in the bright-field or the dark-field mode. Different objectives from Olympus (5x, 10x, 20x, 100x) were used to obtain images of different magnifications. The scale bar and other parameters such as brightness and contrast were adjusted on the Stream Essentials software.

3.4.2 Atomic Force Microscopy (AFM)

Samples of exfoliated rubrene crystals were prepared for AFM by pipetting about 15 µL of diluted sediments (with deionised water) onto pre-cleaned 0.5 x 0.5 cm^2 $\mathrm{Si/SiO_2}$ substrates at 150°C. Topography images of samples were collected using Bruker's Dimension Icon Atomic Force Microscope in the ScanAsyst® mode with either the ScanAsyst-Air or the OLTESPA-R3 tips. Surfaces were scanned typically at a rate of 0.2-1 Hz with a resolution of 512 or 1024 samples/line. Processing of images was performed using Gwyddion 2.48.

3.4.3 Scanning Electron Microscopy (SEM)

Scanning electron micrographs of samples were recorded using a JEOL JSM-7610F field emission scanning electron microscope. Both the in-lens detector (for good material contrast) as well as the in-chamber detector (for good topographic contrast) were employed to acquire secondary electron images. Low acceleration voltages of 0.5-1 kV and short working distances of 6-12 mm were used. For better topographic contrast of the crystallites of PDIF-$\mathrm{CN_2}$, this sample was imaged with a tilt of 8.6°. To minimize charging effects, gold-coated native silicon was used as a substrate.

3.4.4 Transmission Electron Microscopy (TEM)

TEM imaging and selected-area electron diffraction (SAED) measurements on exfoliated rubrene crystals were carried out by Dr. Haoyuan Qi at the Electron Microscopy Group of Materials Science, Ulm University, Germany. A FEI Titan 80-300 with image-side spherical-aberration-correction operated under 300 kV was employed. A low dose rate of 0.15 $\mathrm{e^-/Å^2 s}$ and an exposure time of 15-20 s for SAED acquisition were used in order to minimize electron radiation induced damage of samples. Continuous rotation electron diffraction (cRED) was performed by Dr. Tatiana Gorelik (same affiliation as above) on a triclinic crystal of rubrene using a Thermo Fisher Talos TEM operated under 200 kV. Diffraction patterns were recorded by rotating the specimen stage from -40° to 40° at a rate of about 1°/s and with 1° step size.[262] The 3D reconstruction of the unit cell and analysis were executed using EDT Process and PETS2 software.

3.4.5 UV/VIS

Extinction spectra of exfoliated rubrene dispersions as well as that of rubrene solution were measured using Agilent's Cary 6000i UV-Vis-NIR spectrophotometer. A baseline was first collected using either 0.1 g L^{-1} aqueous solution of sodium cholate or chloroform, which was then automatically used by the acquisition software, Scan 4.2, to correct the baselines of the samples. An integrating sphere (also from Agilent), which is a hollow spherical cavity with highly reflective white coating on the interior surface, was used to collect the absorbance spectra of the dispersions by detecting diffuse scattered and transmitted light. A sample placed at the center of the sphere is illuminated through a narrow entrance slit after which both scattered and transmitted light undergo multiple reflections before reaching the photodetector (attached to the integrating sphere) without any spatial information. A baseline correction is applied by measuring the absolute scattered and transmitted light using a reference sample (0.1 g L^{-1} aqueous sodium cholate solution or chloroform). All measurements were carried out with a quartz cuvette of 4 mm path length, with a spectral resolution of 0.5 nm and an integration time of 0.1 s.

3.4.6 Fluorescence and Lifetime Measurements

Photoluminescence (PL) spectra of the rubrene dispersions as well as that of its solution were measured with a Horiba Fluorolog®-3 fluorescence spectrometer equipped with a 450 W xenon excitation lamp. Double monochromators were used for both excitation (1200 lines/mm grating blazed at 330 nm) and emission (1200 lines/mm grating blazed at 500 nm). The dispersions or solutions were placed in a 4 x 10 mm^2 quartz cuvette and the emission was collected perpendicular to the excitation direction. That is, the excitation light passed through the 10 mm side of the cuvette and the emission was recorded from the 4 mm side. The emission spectra of triclinic rubrene dispersions and rubrene solution were acquired by exciting the samples at 495 nm, while that of orthorhombic rubrene dispersions at 500 nm. The excitation spectra of triclinic rubrene dispersions and rubrene solution were obtained for emission at 550 nm and 560 nm, respectively, and that of orthorhombic rubrene dispersions at 600 nm. The photoluminescence excitation/emission (PLE) maps of all the samples were acquired for an excitation range of 350 to 570 nm and an emission range of 500 to 750 nm. A bandwidth of 5 nm on both the excitation and emission sides and an integration time of 0.1 s were used for all measurements.

PL of orthorhombic and triclinic rubrene crystals was measured by the spectrally filtered output of a Fianium WhiteLase SC400 supercontinuum laser with a repetition rate of 20 MHz and ~10 ps pulse duration. With the use of appropriate long pass filters, the samples were excited and the emitted PL was collected through the same 50x objective from Olympus (NA = 0.7). The spectra were acquired by exciting the samples at 450 nm and dispersing the emitted light in an Acton SpectaPro SP 2358 grating spectrograph (150 lines/mm) before being detected by a liquid nitrogen cooled InGaAs line camera from Princeton Instruments (OMA V:1024-1.7 LN). All spectra were corrected to account for the wavelength-dependent detector sensitivity by employing a broadband calibration light source of known spectral power distribution from Thorlabs (SLS201L/M). The PLE maps of crystals were obtained for an excitation range of 400 to 495 nm and an emission range of 450 to 800 nm.

Time-correlated single-photon counting (TCSPC) was performed by directing the PL of rubrene dispersions, solution and crystals excited at 493 nm using the same supercontinuum laser as above to a fibre-coupled silicon avalanche photodiode from Micro Photon devices and the histograms of photon arrival times were constructed using a PicoQuant PicoHarp 300 counting module. The instrument response function (IRF) was recorded on the attenuated laser signal. Finally, PL lifetimes were derived from reconvolution fits using SymPhoTime 64 software.

3.4.7 Raman

Samples of exfoliated rubrene were prepared by depositing ~ 5 µL of the collected sediments onto pre-cleaned 0.5 x 0.5 cm^2 Si/SiO$_2$ substrates at 150°C. Orthorhombic crystals of rubrene were laminated onto a pre-cleaned native silicon substrate, while the triclinic crystals were drop-cast. Low-wavenumber vibrational Raman modes of crystals and exfoliated crystals of rubrene were measured using inVia™ confocal Raman microscope from Renishaw. To avoid photoluminescence, all samples were excited by a 785 nm edge laser through a 50x objective (Olympus, NA 0.5) with a long working distance. The Raman emission was collected using the same objective and dispersed by a 1200 lines/mm grating. The spectra of exfoliated rubrene were acquired with an integration time of 10 s at 10% laser power, while the spectra of single crystals are an average of 100 accumulations recorded with 1 s integration time and 5% laser power.

3.4.8 FT-IR

FT-IR spectra of single crystals were recorded with Bruker's Hyperion 1000 infrared microscope connected to a Tensor 27 FT-IR spectrometer. Light was incident normally on the *ab* facet of the crystals with the electric field oriented in the plane of the crystal facet for both polarized as well as unpolarized IR spectroscopy. Polarized-IR spectra were acquired by inserting a linear polarizer into the beam path and manually rotating it to change the direction of the incident electric field. Spectra of the samples were automatically normalized to the background spectrum collected from a bare double-side polished native silicon substrate using the OPUS software (Bruker). All measurements were performed in the transmission mode with a spectral resolution of 2 cm^{-1}.

3.4.9 AFM-IR

A nanoIR2-s™ system from Bruker at Bundeswehr University Munich, Germany, was used to acquire AFM-IR spectra and maps of samples. The required mid-IR wavelengths were provided by tunable pulsed quantum cascade laser chips that covered a a spectral range of 910 to 1722 cm^{-1} with a gap from 1482 to 1510 cm^{-1}. All measurements were performed with a gold-plated AFM tip (PR-EX-nIR-10) in contact mode. Spectroscopic data was obtained by fixing the position of the tip on the sample and scanning the wavenumber range. The absorbance spectrum thus collected is a measure of the cantilever's oscillation amplitude normalized by the laser power, as a function of wavenumber. The spectral resolution was kept constant at 2 cm^{-1}. Polarization-dependent spectra of single crystal samples were recorded by manually rotating the crystal. The incident laser light was linearly polarized with a vertical polarization axis (see **Figure 2.11**) and had an angle of incidence of 70°. Topography and amplitude images were simultaneously acquired by scanning the tip across a section of the sample, keeping the wavenumber fixed.

3.4.10 IR-SNOM

Single crystals for IR-SNOM measurements were either grown or laminated on pre-cleaned double-side polished native silicon substrates. Crystallites of PDIF-CN$_2$ and exfoliated rubrene were deposited on gold-coated native silicon substrates via spin-coating and drop-casting, respectively. The Nano-FT-IR and the imaging modules of neaSNOM, a product of Neapec GmbH, were employed to gather IR-SNOM data of the samples. Platinum/iridium coated tips from Neaspec, optimized for spectroscopy as well as imaging, were used in the tapping mode for all measurements. A mid-IR broadband laser spanning a spectral range of 900 to 1700 cm^{-1} was part of the spectroscopy module. Before measuring the sample's amplitude and phase spectra, a reference signal was recorded from a highly reflective, spectrally flat substrate such as gold-coated silicon. This was used by the software (neaSCAN) to normalize the sample's spectra, thereby eliminating the instrument's influence. A good signal-to-noise ratio and a spectral resolution of 5-10 cm^{-1} were achieved by adjusting the interferometer center and distance, respectively. The imaging module was connected to a tunable quantum cascade laser with a wavenumber range of 1020 to 1097 cm^{-1} from Daylight Solutions. Near-field amplitude and phase images together with topography of a section of the sample were acquired by tuning the laser to the required wavenumber and a power setting of 1.5 mW. Background removal was performed automatically following a pseudoheterodyne detection scheme.[199]

3.4.11 Zeta Potential

Zeta potential measurements were carried out using a Malvern Panalytical Zetasizer Nano ZSP equipped with a 633 nm Helium-Neon laser together with a DTS1070 folded capillary cell. Prior to each measurement, the capillary cell was equilibrated with the aqueous sodium cholate solution. The sample viscosity was assumed to be the same as the viscosity of water at 20 °C (1.0031 mPa s) and the Smoluchowski approximation was employed. Each of the six dispersions was measured five times with ten runs per measurement, with no delay in between the measurements. A Gaussian function was used to fit the distribution data of each measurement, following which the center of the Gaussian were extracted and averaged.

3.4.12 Computational Methods

Density functional theory (DFT) calculations were performed by Dr. Jie Han in the Theoretical and Computational Chemistry group (Interdisziplinäres Zentrum für Wissenschaftliches Rechnen), Heidelberg University, Germany. The Gaussian 09 (Revision D.01) program package was utilized to carry out gas-phase calculations. At the DFT/B3LYP/6-31+G* level of theory, the ground state equilibrium structures of TIPS-PEN, TIPS-TAP, rubrene and PDIF-CN_2 were optimized, and subsequently, their IR and Raman modes were calculated.

Chapter 4

AFM-IR and IR-SNOM for the Characterization of Crystalline Organic Semiconductors

The results of the study presented in this chapter were published in reference [147]: V. J. Rao, M. Matthiesen, K. P. Goetz, C. Huck, C. Yim, R. Siris, J. Han, S. Hahn, U.H.F. Bunz, A. Dreuw, G. S. Duesberg, A. Pucci, J. Zaumseil, "AFM-IR and IR-SNOM for the Characterization of Small Molecule Organic Semiconductors", The Journal of Physical Chemistry C 2020, 124, 5331-5344. Single crystals of rubrene and PDIF-CN_2 were grown by Maik Matthiesen and DFT calculations were performed by Dr. Jie Han.

4.1 Motivation

As discussed in **Chapter 2**, both the AFM-IR and the IR-SNOM, although fundamentally different techniques, provide nanoscale spatial resolution as well as rich chemical information using an AFM tip in combination with IR spectroscopy. Both techniques show great versatility in investigating a range of samples. The AFM-IR is favourable for the study of polymer blends, composites and biological materials such as proteins, cells and tissues,[178,182,263–266] while the IR-SNOM has been used more often for molecular crystals, inorganic monolayers as well as some polymeric and biological materials.[267–271]

The functionality of small organic molecules with extended π-conjugation, as described in **Chapter 2**, depends strongly on their molecular structure and packing and therefore, a better understanding of the structure-property relationship on the micro- and nanoscale is desirable. Surprisingly, there are very few studies where AFM-IR or IR-SNOM have been employed to investigate these materials which raises the question about the applicability of the two techniques.[167,171,174,196,218,219,272] Furthermore, the lack of a comprehensive study comparing both the techniques on the same material system makes it hard to establish the advantages and disadvantages of each.

Single crystals of small-molecule organic semiconductors provide an ideal platform to examine intrinsic properties of materials. The absence of grain boundaries, low density of defects and very high purity make them ideal candidates to ascertain the applicability of novel techniques such as the AFM-IR and the IR-SNOM. For this purpose, single crystals of TIPS-PEN, TIPS-TAP, rubrene and PDIF-CN$_2$ have been employed here. TIPS-PEN and TIPS-TAP are p- and n-type semiconductors, respectively, with similar molecular structure and packing in their single crystal lattice. Hence, comparing the spectra acquired from them using the AFM-IR and the IR-SNOM will help to understand the influence of small compositional differences to the observed spectral features. Rubrene differs largely from TIPS-PEN and TIPS-TAP in both structure and packing, and here the orthorhombic polymorph will be used to shed light on the effect of molecular packing on spectral information gain. Lastly, the significance of the orientation of the π-conjugated core is explored through a single crystal of the n-type PDIF-CN$_2$. The spectra acquired from the single crystals of the four molecular semiconductors using AFM-IR and IR-SNOM are compared with one another and to the classical FT-IR. Unpolarized FT-IR spectrum provides access to all the intramolecular vibrational modes of a material and thus serves as the perfect reference. Linearly polarized FT-IR measurements, on the other hand, excite only specific modes depending on the arrangement of the molecules in a crystal and as a result, assist in determining the molecular packing.

To explore the spatial resolution and accessible local spectral information, the nanoimaging and the nanospectroscopy capabilities of the AFM-IR and the IR-SNOM are tested with a polycrystalline film of PDIF-CN$_2$.

4.2 Infrared Spectroscopy on Single Crystals

In this section, the amplitude and the phase signals of the single crystals of the four molecules obtained through the AFM-IR and the IR-SNOM, respectively, are compared with one another and to the absorption spectra from the FT-IR. Polarized IR spectroscopy is performed where possible to determine and/or corroborate the molecular orientation in each of the well-faceted crystals.

4.2.1 TIPS-PEN

A single crystal of TIPS-PEN grown from solution as described in **Chapter 3.2.1** was first investigated using the FT-IR. An absorbance spectrum with non-polarized light served as a reference. Following this, the absorbance spectra for different in-plane orientations of the electric field with respect to the long edge of the crystal (see **Figure 4.1(b)**) were acquired.

Figure 4.2 (top) shows the FT-IR reference spectrum (x) of TIPS-PEN with several absorption peaks, as expected for an organic molecule. Under polarized illumination, the position, shape and intensity of the peaks change depending on the direction of the electric field of the incident light. As an example, consider the peak at 1176 cm^{-1}. At 0°, where the in-plane electric field is parallel to the long axis of the crystal, it is strong. At 45°, the peak disappears; but, reappears even stronger at 135°. Studying the vibrational mode corresponding to this peak helps to elucidate the observed behaviour. As shown in figure **Figure 4.3**, the peak at 1176 cm^{-1} originates from exciting rocking vibrations restricted to the pentacene core. The associated dipole derivative unit vector (red arrow) and the displacement vectors (blue arrows) lie in the plane of the backbone of TIPS-PEN. The orientation of the electric field with respect to the dipole derivative unit vector (also known as transition dipole moment vector) directly influences the excitation of this mode. Therefore, the peak is most intense when the electric field is parallel to the π-conjugated core of TIPS-PEN oriented at 135° with respect to the long edge of the single crystal.

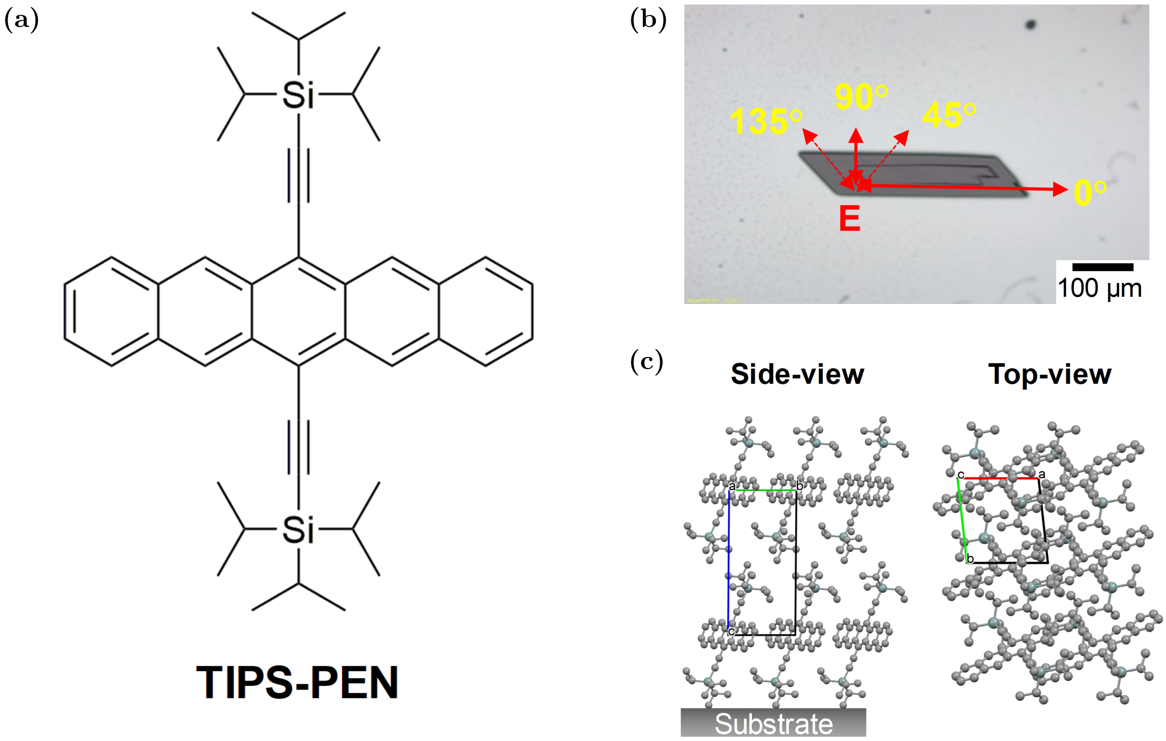

Figure 4.1: (a) Molecular structure of TIPS-PEN. (b) Optical micrograph of a single crystal of TIPS-PEN with the in-plane orientations of the electric field indicated. (c) Packing of the TIPS-PEN molecules in the crystal lattice (unit cell indicated) as seen from the side and the top. Hydrogen atoms are omitted for the sake of clarity. Adapted with permission from Ref.[147]. Copyright 2020 American Chemical Society.

It is known that in a free-standing single crystal of TIPS-PEN, the molecules stand on one of the TIPS groups, arranging themselves in a 2D slipped-stacking motif with a small tilt angle as shown in **Figure 4.1(c)**.[273] The same molecular orientation is observed in crystals grown on a substrate, corroborated by the polarization dependence of several other absorption peaks. For example, the strong mode at 1461 cm^{-1} has the transition dipole moment vector lying in the plane of the backbone but pointing downwards (see **Figure 4.3**). For all orientations of the electric field, the intensity of the peak remains the same, as expected for the molecular arrangement shown in **Figure 4.1(c)**.

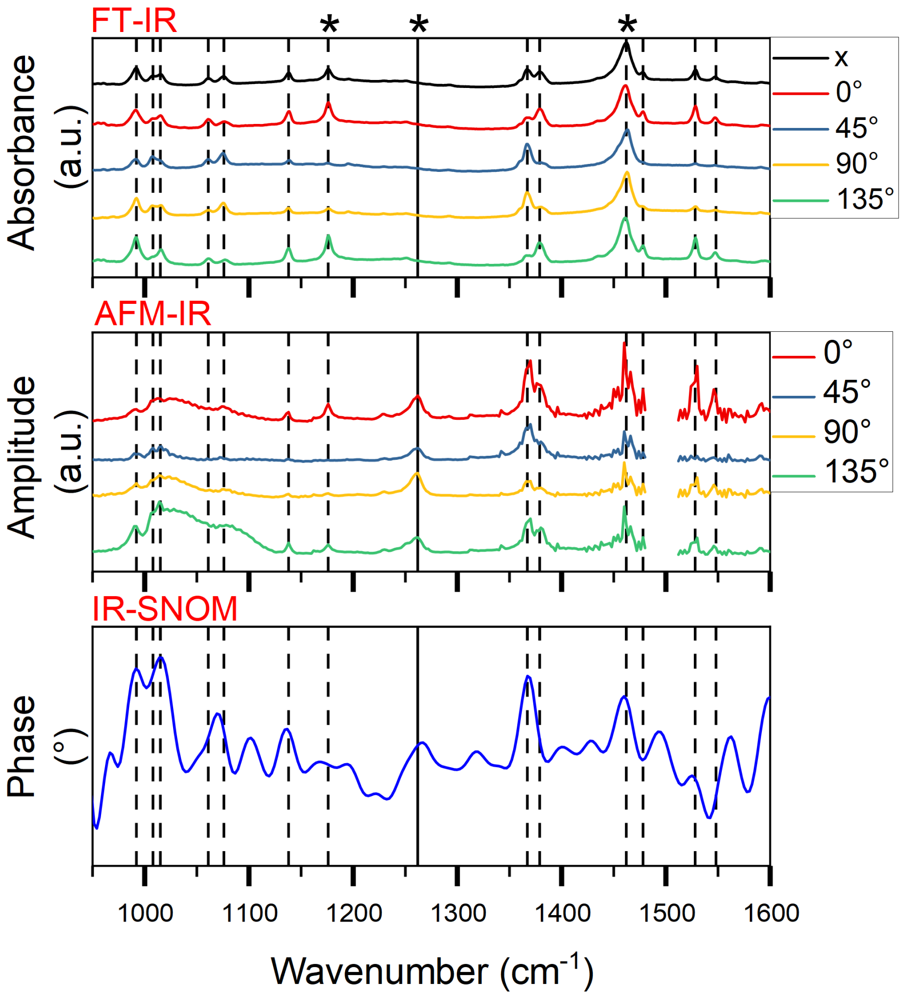

Figure 4.2: Polarization-dependent absorbance spectra from FT-IR and amplitude spectra from AFM-IR, and phase spectrum from IR-SNOM of a single crystal of TIPS-PEN. Absorbance spectrum with non-polarized light (x) is shown for reference. Dashed lines correspond to the modes seen in the FT-IR spectra, solid lines indicate modes which are present only in the AFM-IR and IR-SNOM spectra and the asterisks mark those peaks whose vibrational modes are presented below. Adapted with permission from Ref.[147]. Copyright 2020 American Chemical Society.

IR-spectra acquired with the AFM-IR are shown in **Figure 4.2** (middle). The different angles, here, again indicate the angle between the electric field and the long edge of the crystal which was achieved by rotating the crystal with respect to the AFM tip.

Almost all the modes seen in the FT-IR spectra are also observed with the AFM-IR, although noisier. Peak position, shape and intensity are nearly identical, especially above 1100 cm^{-1}.

Changing polarization has the same effect on peaks at 1176 cm^{-1} and 1460 cm^{-1}. There is, however, a peak at 1262 cm^{-1} in all the AFM-IR spectra that is completely absent in the FT-IR spectra. The presence of this medium-intensity peak can be explained by considering the relative orientation of the transition dipole moment vector of the corresponding mode and the direction of the incident electric field. One of the differences between the two techniques is the angle of incidence of light (AOI). In the case of the FT-IR, light is incident nearly perpendicular to the substrate which, for s-polarized light, means the electric field vector lies in the plane of the substrate. Therefore, only those modes with an in-plane component of the transition dipole moment vector are excited by FT-IR. The AFM-IR, on the other hand, has an AOI of 70° and as a result the vertically polarized incident light excites those modes with an out-of-plane component as well. **Figure 4.3** shows the vibrational mode corresponding to the peak at 1262 cm^{-1}. Its transition dipole moment vector lies out-of-plane of the backbone with a strong component normal to the substrate given the tilt angle of the TIPS-PEN molecules (see **Figure 4.1(c)**), hence this mode becomes visible in the AFM-IR spectrum.

Finally, the phase signal of a single crystal of TIPS-PEN was acquired with the nanospectroscopy module of the IR-SNOM, as shown in **Figure 4.2** (bottom). There are no polarization dependent spectra here because the incident laser polarization is enhanced only in the direction perpendicular to the sample by the metallic tip and the refractive index of the substrate. Therefore, measuring spectra for electric field directions parallel to the sample yields nothing meaningful. The corresponding amplitude signal is provided in **Figure A.2** of the Appendix. The modes observed with the IR-SNOM are not directly comparable to those from the FT-IR. The peaks are slightly shifted, their shapes and relative intensities are different. Moreover, there are several additional peaks, at 1102 cm^{-1}, 1267 cm^{-1} and 1320 cm^{-1} that were not observed with the FT-IR. In comparison to the AFM-IR, the mode at 1267 cm^{-1} in the IR-SNOM corresponds to the mode at 1262 cm^{-1} in the former. In the IR-SNOM, where the enhanced electric field is parallel to the tip and therefore perpendicular to the sample, all those modes with an out-of-plane component of the dipole derivative unit vectors become visible. The mode at 1267 cm^{-1}, with its out-of-plane transition dipole moment (see **Figure 4.3**) is therefore seen here as well. Other strong excitations, at 1367 cm^{-1} and 1462 cm^{-1}, appear as a single peak in the phase signal, whereas, in the FT-IR and AFM-IR spectra they are split into two peaks of varying intensities dependent on the orientation of the electric field. This is due to the lower spectral resolution of the IR-SNOM spectrum.

Table 4.1 gives the position and intensity of selected modes at different polarizations for the three techniques. For a full list, refer to **Table A.1** of the Appendix.

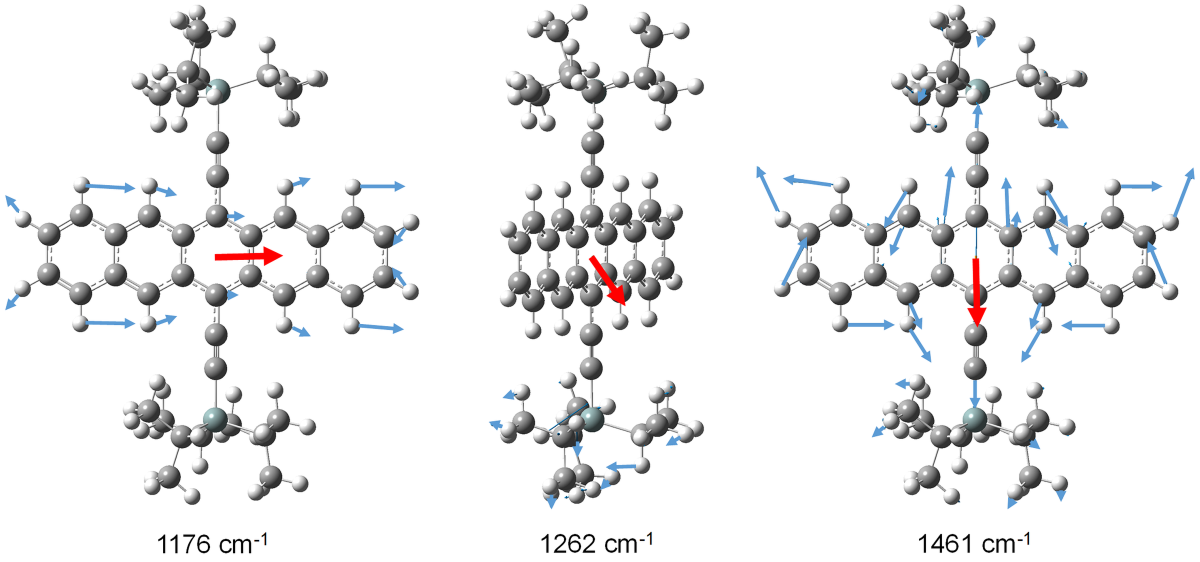

Figure 4.3: Visualisation of the vibrational modes corresponding to selected absorption peaks of TIPS-PEN. Blue and red arrows (lying in the plane of the paper and scaled to improve visibility) indicate the displacement vectors and the dipole derivative unit vectors, respectively. Atoms of hydrogen are shown in white, carbon in gray and silicon in gray-green. Adapted with permission from Ref.[147]. Copyright 2020 American Chemical Society.

Table 4.1: Comparison of position and intensity[*] of the most prominent absorption peaks of a single crystal of TIPS-PEN for different polarizations and IR spectroscopic techniques. This table was adapted with permission from Ref.[147]. Copyright 2020 American Chemical Society.

TIPS-PEN	FT-IR (cm^{-1})	AFM-IR (cm^{-1})	IR-SNOM (cm^{-1})
0°	**1176**	1176	
		1262	**1267**
	1461	**1460**	**1460**
45°			
		1262	
	1463	**1460**	
90°	(1176)		
		1262	
	1463	**1460**	
135°	**1176**	(1176)	
		1262	
	1461	**1460**	

[*] Intensity of the peaks is indicated as: bold font - strong; regular font - medium; within brackets - weak.

4.2.2 TIPS-TAP

A molecule very similar to TIPS-PEN in molecular structure, except for the four nitrogen atoms in the π-conjugated core, is TIPS-TAP as shown in **Figure 4.4(a)**. A free-standing single crystal of TIPS-TAP shows the same 2D slipped-stacking arrangement of molecules standing on one of the TIPS groups at an angle, (see **Figure 4.4(c)**).

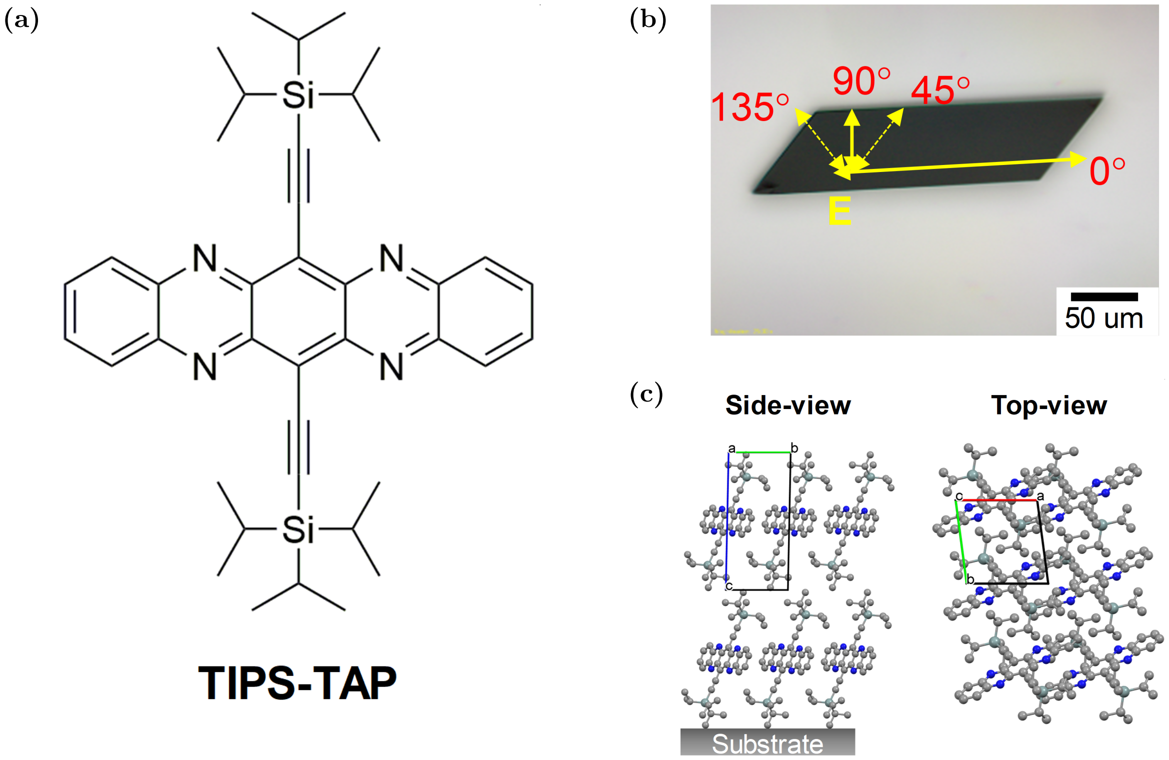

Figure 4.4: (a) Molecular structure of TIPS-TAP. (b) Optical micrograph of a single crystal of TIPS-TAP with the in-plane orientations of the electric field indicated. (c) Packing of the TIPS-TAP molecules in the crystal lattice (unit cell indicated) as seen from the side and the top. Hydrogen atoms are omitted for the sake of clarity. Adapted with permission from Ref.[147]. Copyright 2020 American Chemical Society.

A single crystal of TIPS-TAP grown on a substrate from solution (see **Chapter 3.2.1**), as shown in **Figure 4.4(b)**, was used to measure the absorbance, amplitude and phase spectra with the FT-IR, AFM-IR and the IR-SNOM, respectively. As with TIPS-PEN, several absorption peaks are observed (see **Figure 4.5**) as well. Change in intensity with polarization of some of the peaks, for example, at 1315 cm^{-1}, bears a strong correlation to the molecular orientation within the crystal. This mode, which arises from coupled stretching and rocking modes restricted to the backbone of the molecule (see **Figure 4.6**), shows high intensity at 0° and 45° but is completely absent at 135°. Its transition dipole moment vector lies in the plane of the π-conjugated core. Another mode, the one at

1460 cm^{-1}, does not change with polarization. It is the same mode as seen in TIPS-PEN where vibrations are from all over the molecule with the transition dipole moment vector lying in the plane of the backbone but pointing downwards. Correlating the direction of the incident electric field to the orientation of the transition dipole moment vector and the corresponding intensities confirms that molecules in single crystals of TIPS-TAP grown by the drop-casting method adopt the same molecular packing shown in **Figure 4.4(c)**.

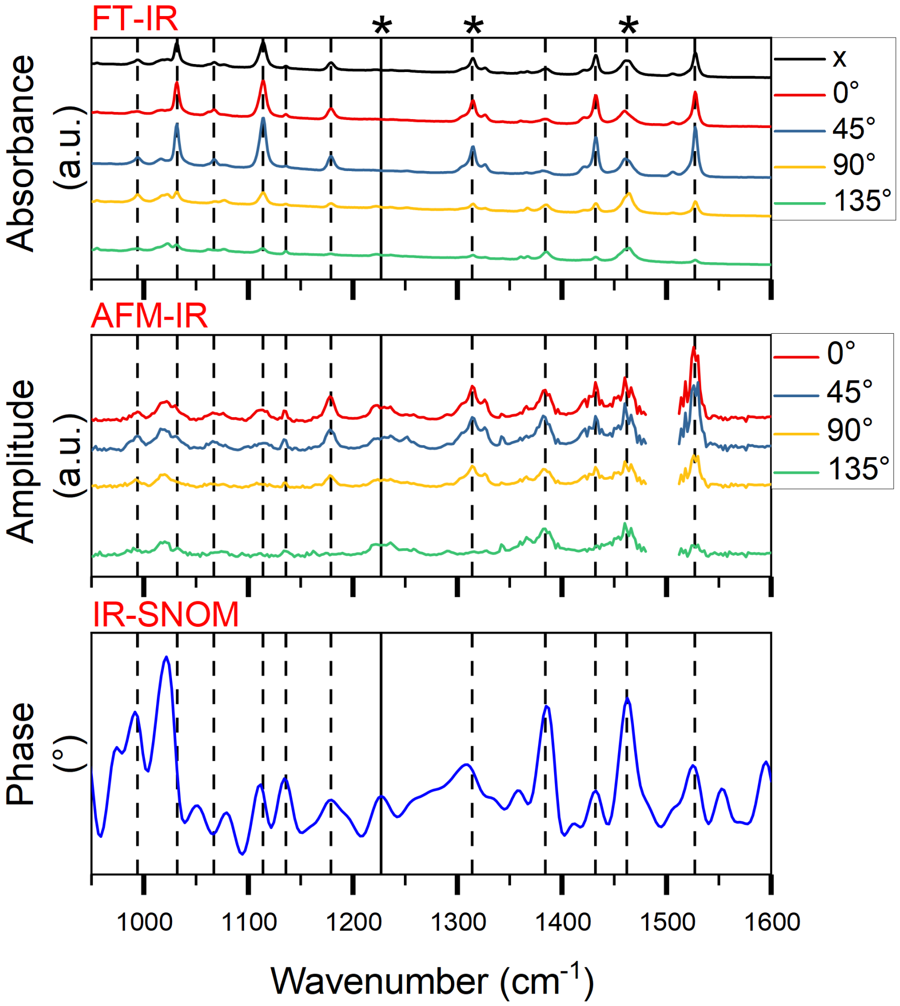

Figure 4.5: Polarization-dependent absorbance spectra from FT-IR and amplitude spectra from AFM-IR, and phase spectrum from IR-SNOM of a single crystal of TIPS-TAP. Absorbance spectrum with non-polarized light (x) is shown for reference. Dashed lines correspond to the modes seen in the FT-IR spectra, solid lines indicate modes which are present only in the AFM-IR and IR-SNOM spectra and the asterisks mark those peaks whose vibrational modes are presented below. Adapted with permission from Ref.[147]. Copyright 2020 American Chemical Society.

Polarization-dependent AFM-IR spectra (see **Figure 4.5** (middle)) show a good correspondence to the FT-IR spectra in terms of peak position, shape and intensity. Similar to what was observed with TIPS-PEN, all modes above 1100 cm^{-1} are better resolved.

Intensities of peaks at 1315 and 1460 cm^{-1} also show the same polarization-dependent behaviour as with FT-IR. Analogous to the 1262 cm^{-1} mode seen for the TIPS-PEN crystal, there is a peak at 1228 cm^{-1} for the TIPS-TAP crystal, although not as well resolved. This additional mode results from vibrations on the TIPS groups, as shown in **Figure 4.6**, with the dipole derivative unit vector pointing out of the molecule's backbone. The strong out-of-plane (of the substrate) component of this vector leads to its visibility in the AFM-IR spectra but not in the FT-IR spectra because of the difference in AOI, as discussed above.

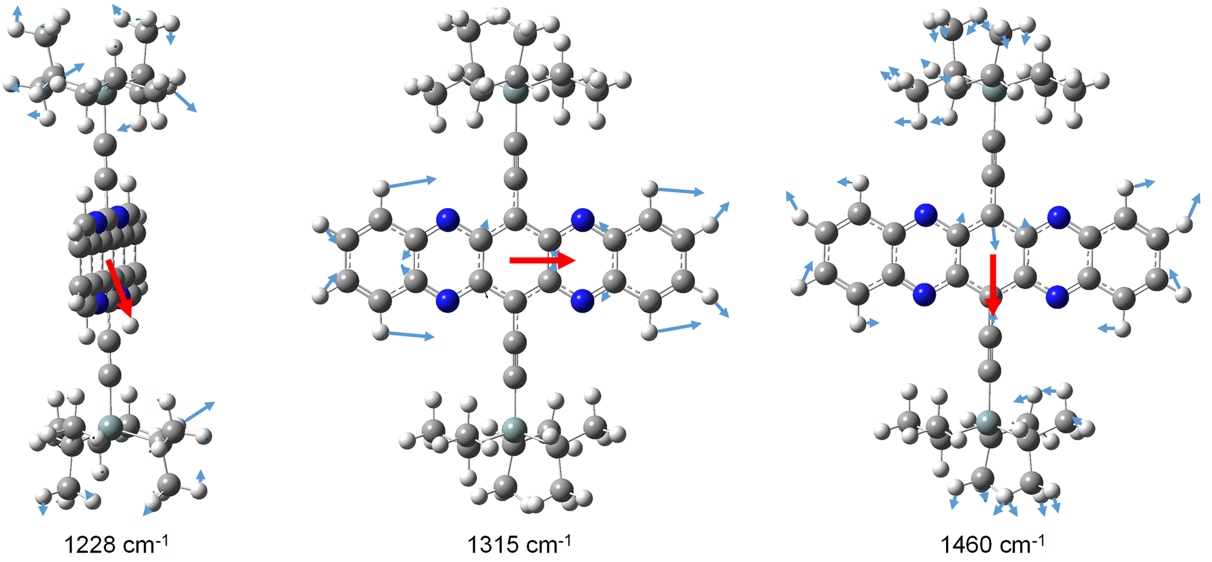

Figure 4.6: Visualisation of the vibrational modes corresponding to selected absorption peaks of TIPS-TAP. Blue and red arrows (lying in the plane of the paper and scaled to improve visibility) indicate the displacement vectors and the dipole derivative unit vectors, respectively. Atoms of hydrogen are shown in white, carbon in gray, nitrogen in blue and silicon in gray-green. Adapted with permission from Ref.[147]. Copyright 2020 American Chemical Society.

The IR-SNOM phase spectrum of a single crystal of TIPS-TAP is shown in **Figure 4.5** (bottom) and the corresponding amplitude spectrum can be found in **Figure A.2** of the Appendix. Nearly all the modes observed in the absorbance and amplitude spectra from the FT-IR and the AFM-IR, respectively, are also seen in the phase signal of TIPS-TAP, with some peaks shifted by a maximum of 5 cm^{-1}. All modes with an out-of-plane component are also observed with the IR-SNOM. As such, a weak mode at 1227 cm^{-1} is seen which corresponds to the peak at 1228 cm^{-1} in the AFM-IR spectra. Since the component of the transition dipole moment vector of this mode parallel to the enhanced polarization direction of the IR-SNOM is small, the mode is not strong. The mode at 1462 cm^{-1} is, however, strong even in comparison to that in the FT-IR and the AFM-IR spectra. This can be attributed to the large out-of plane component of the dipole derivative unit vector. A comparison of the modes in **Figure 4.6** in terms of position and intensity for the three techniques is given in **Table 4.2**. For a full list of all the modes, see **Table A.2** of the Appendix.

Table 4.2: Comparison of position and intensity* of the most prominent absorption peaks of a single crystal of TIPS-TAP for different polarizations and IR spectroscopic techniques. Adapted with permission from Ref.[147]. Copyright 2020 American Chemical Society.

TIPS-TAP	FT-IR (cm^{-1})	AFM-IR (cm^{-1})	IR-SNOM (cm^{-1})
0°		1228	1227
	1315	**1314**	1310
	1460	**1460**	**1462**
45°		1228	
	1464	**1460**	
90°		1228	
	(1315)	1314	
	1464	**1460**	
135°		1228	
	1315	**1314**	
	1461	**1460**	

* Intensity of the peaks is indicated as: bold font - strong; regular font - medium; within brackets - weak.

4.2.3 Rubrene

Rubrene single crystals grown by the PVT method (see **Chapter 3.2.1**) are typically platelet-like with well-defined facets, as shown in **Figure 4.7**. As in the previous two cases, polarization-dependent absorbance spectra for different in-plane orientations of the electric field (see **Figure 4.7(b)**) with respect to the long edge of the crystal were acquired. Rubrene molecules in PVT-grown crystals assume a layered herringbone packing in an orthorhombic lattice, as shown in **Figure 4.7(c)**. Because the molecules in each layer are arranged in a zig-zag pattern, excitation of the same modes for different polarizations can be expected.

FT-IR measurements (**Figure 4.8**, top) reveal several absorption peaks, of which only two medium-intensity peaks at 1031 and 1069 cm^{-1} exhibit a small variation in intensity with change in electric field orientation (see **Figure 4.7(b)**) but neither of which disappears completely. The C-H bending vibration on the four phenyl substituents, as shown in **Figure 4.9**, gives rise to these two modes.

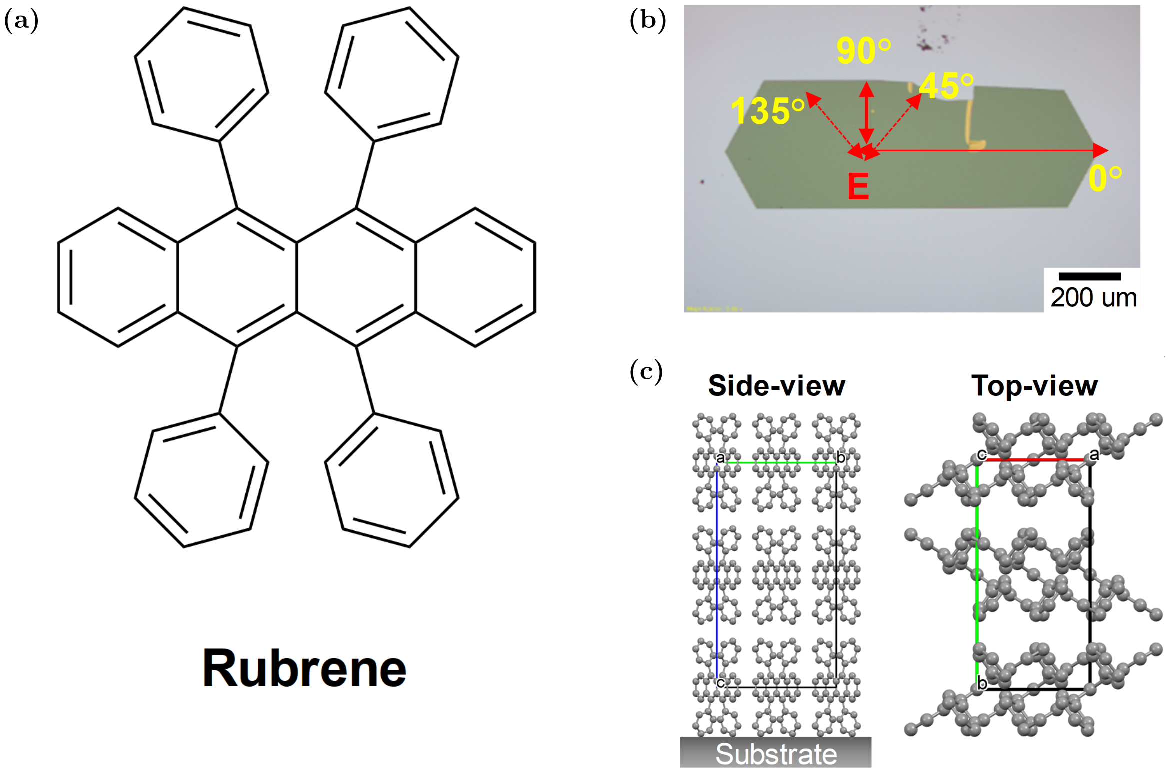

Figure 4.7: (a) Molecular structure of rubrene. (b) Optical micrograph of a single crystal of rubrene with the in-plane orientations of the electric-field indicated. (c) Packing of the rubrene molecules in the crystal lattice (unit cell indicated) as seen from the side and the top. Hydrogen atoms are omitted for the sake of clarity. Adapted with permission from Ref.[147]. Copyright 2020 American Chemical Society.

Polarization-dependent amplitude spectra of a single crystal of rubrene (**Figure 4.8**, middle) acquired with the AFM-IR show the best correspondence to the FT-IR spectra so far. In comparison to the AFM-IR spectra of the previous two crystals, the signal-to-noise ratio is much better and even the peaks below 1100 cm^{-1} are well resolved. Since the PVT-grown rubrene crystal was thinner than the solution-grown TIPS-PEN and TIPS-TAP crystals, the improved signal-to-noise ratio cannot be attributed to the thickness of the crystal; instead, it could be a result of a higher thermal expansion coefficient. An additional mode at 1394 cm^{-1} is excited because of the oblique incidence of polarized light. It is a strong mode that originates from coupled vibrations from the entire molecule, and whose intensity is polarization independent. As shown in **Figure 4.9**, the transition dipole moment vector of this mode lies in the plane of the π-conjugated core, orientated along the c-axis. Therefore, it is expected to be visible in the IR-SNOM signal as well.

Indeed, the phase signal of rubrene single crystal (**Figure 4.8**, bottom) has two strong modes — at 1031 cm^{-1} and 1394 cm^{-1} — both of which have the transition dipole moment vector oriented along the enhanced electric field direction (**Figure 4.9**). The corresponding amplitude spectrum from the IR-SNOM is shown in **Figure A.2** of the Appendix.

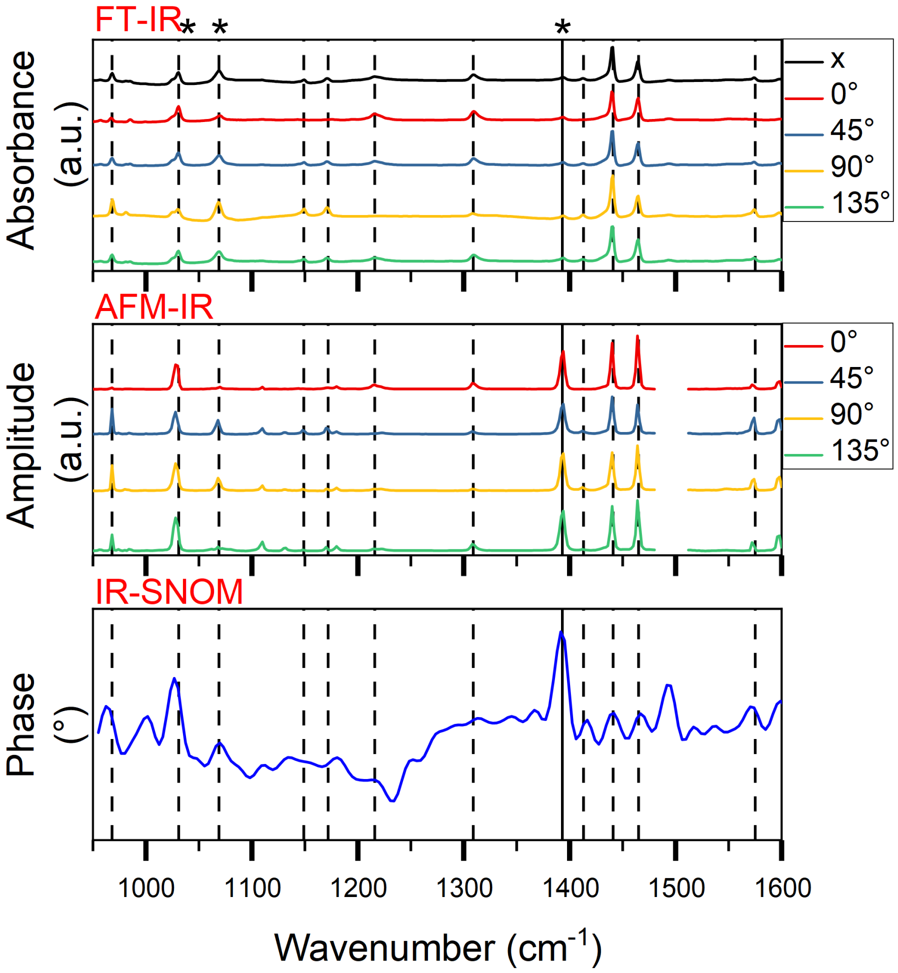

Figure 4.8: Polarization-dependent absorbance spectra from FT-IR and amplitude spectra from AFM-IR, and phase spectrum from IR-SNOM of a single crystal of rubrene. Absorbance spectrum with non-polarized light (x) is shown for reference. Dashed lines correspond to the modes seen in the FT-IR spectra, solid lines indicate modes which are present only in the AFM-IR and IR-SNOM spectra and the asterisks mark those peaks whose vibrational modes are presented below. Adapted with permission from Ref.[147]. Copyright 2020 American Chemical Society.

Table 4.3 provides a comparison of the position and intensity of the most prominent modes of rubrene at different polarizations for the three techniques. A complete list of all IR modes of rubrene is given in **Table A.3** of the Appendix.

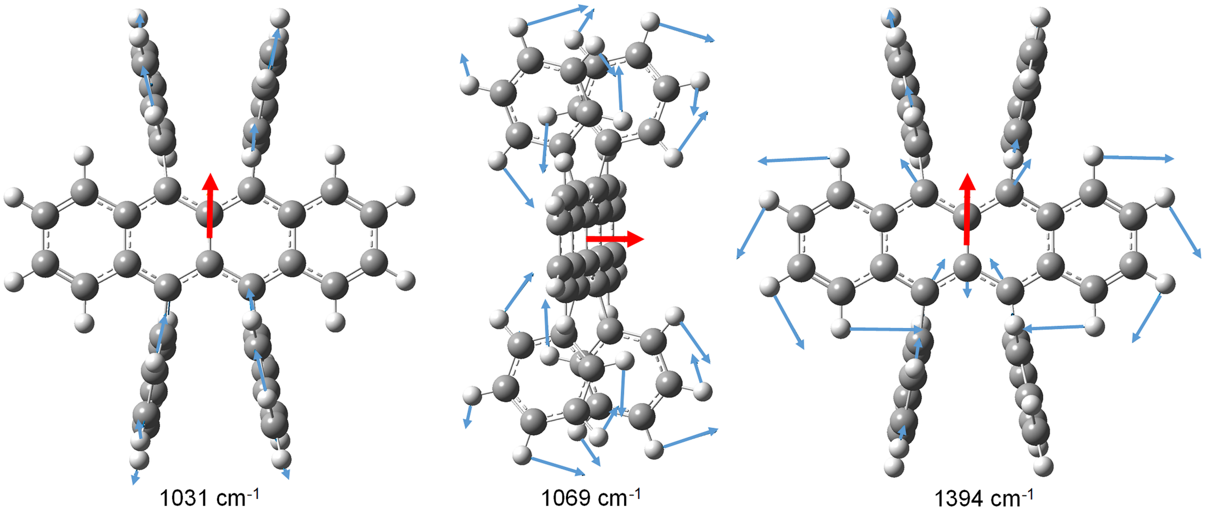

Figure 4.9: Visualisation of the vibrational modes corresponding to selected absorption peaks of rubrene. Blue and red arrows (lying in the plane of the paper and scaled to improve visibility) indicate the displacement vectors and the dipole derivative unit vectors, respectively. Atoms of hydrogen are shown in white and carbon in gray. Adapted with permission from Ref.[147]. Copyright 2020 American Chemical Society.

Table 4.3: Comparison of position and intensity* of the most prominent absorption peaks of a single crystal of rubrene for different polarizations and IR spectroscopic techniques. This table was adapted with permission from Ref.[147]. Copyright 2020 American Chemical Society.

Rubrene	FT-IR (cm^{-1})	AFM-IR (cm^{-1})	IR-SNOM (cm^{-1})
0°	1031 (1069)	**1028** (1068) **1394**	**1027** 1070 **1392**
45°	1031 1069	**1028** 1068 **1394**	
90°	1030 1069	**1028** 1068 **1394**	
135°	1031 1069	**1028** (1068) **1394**	

* Intensity of the peaks is indicated as: bold font - strong; regular font - medium; within brackets - weak.

4.2.4 PDIF-CN$_2$

To study the effect of the orientation of the π-conjugated core on the different IR spectra, a single PVT-grown crystal of PDIF-CN$_2$ was employed (see **Chapter 3.2.1**). Although the molecules of PDIF-CN$_2$ assume a 2D slipped-stacking arrangement in the single crystal (**Figure 4.10**), like TIPS-PEN and TIPS-TAP, the long-axis of the core is oriented differently with respect to the substrate. It is nearly upright unlike the other two crystals where it is parallel to the substrate. This leads to a much stronger out-of-plane polarizability that should mainly become visible in the IR-SNOM spectra.

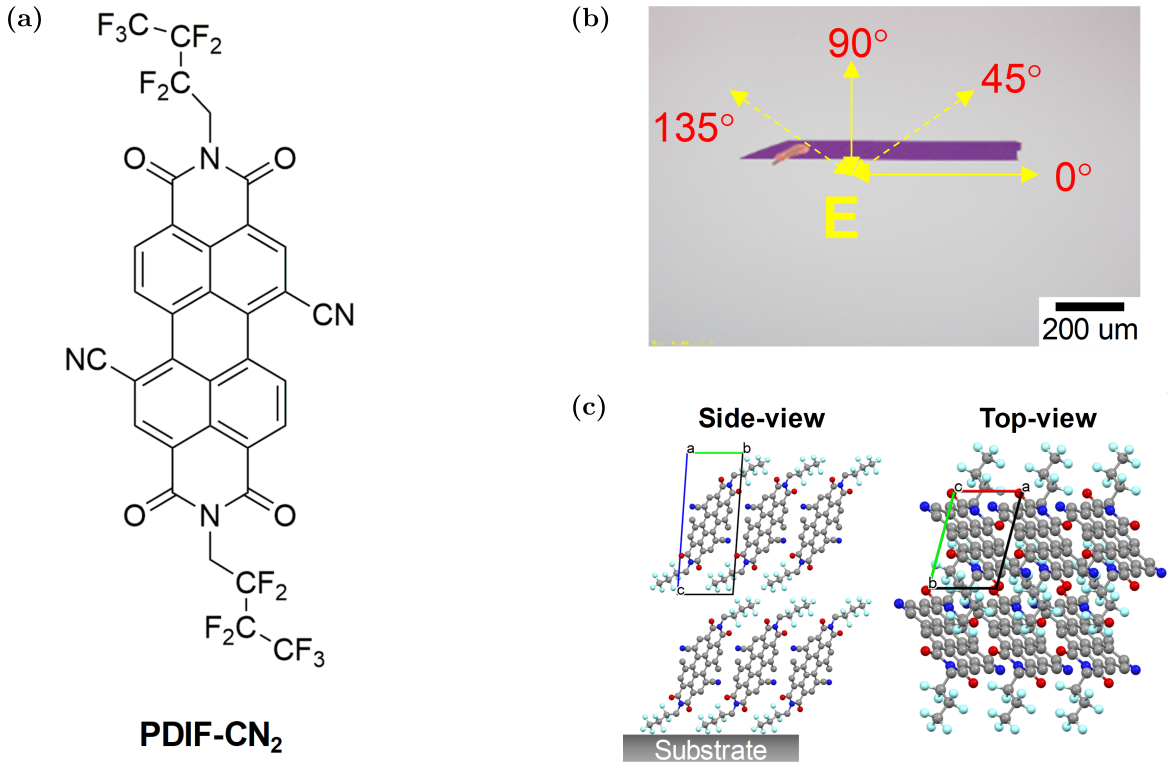

Figure 4.10: (a) Molecular structure of PDIF-CN$_2$. (b) Optical micrograph of a single crystal of PDIF-CN$_2$ with the in-plane orientations of the electric field indicated. (c) Packing of the PDIF-CN$_2$ molecules in the crystal lattice (unit cell indicated) as seen from the side and the top. Hydrogen atoms are omitted for the sake of clarity. Adapted with permission from Ref.[147]. Copyright 2020 American Chemical Society.

Figure 4.11 (top) shows the IR spectrum of a single crystal of PDIF-CN$_2$ for different linear polarizations of the incident light (see **Figure 4.10(b)**). Three main sets of doublets at 1114/1124 cm^{-1}, 1221/1247 cm^{-1}, and 1351/1362 cm^{-1} make up the spectra, wherein, the intensity of each peak within a doublet varies with change in polarization. For example, the modes at 1114 and 1124 cm^{-1} are a result of coupled vibrations from all over the molecule, as shown in **Figure 4.12**. However, each peak within this doublet shows a different polarization dependence because their total transition dipole moment vectors are oriented differently. Intensity of the peak at 1114 cm^{-1} is maximum at 0°, whereas the peak at 1124 cm^{-1} is most intense at 90°.

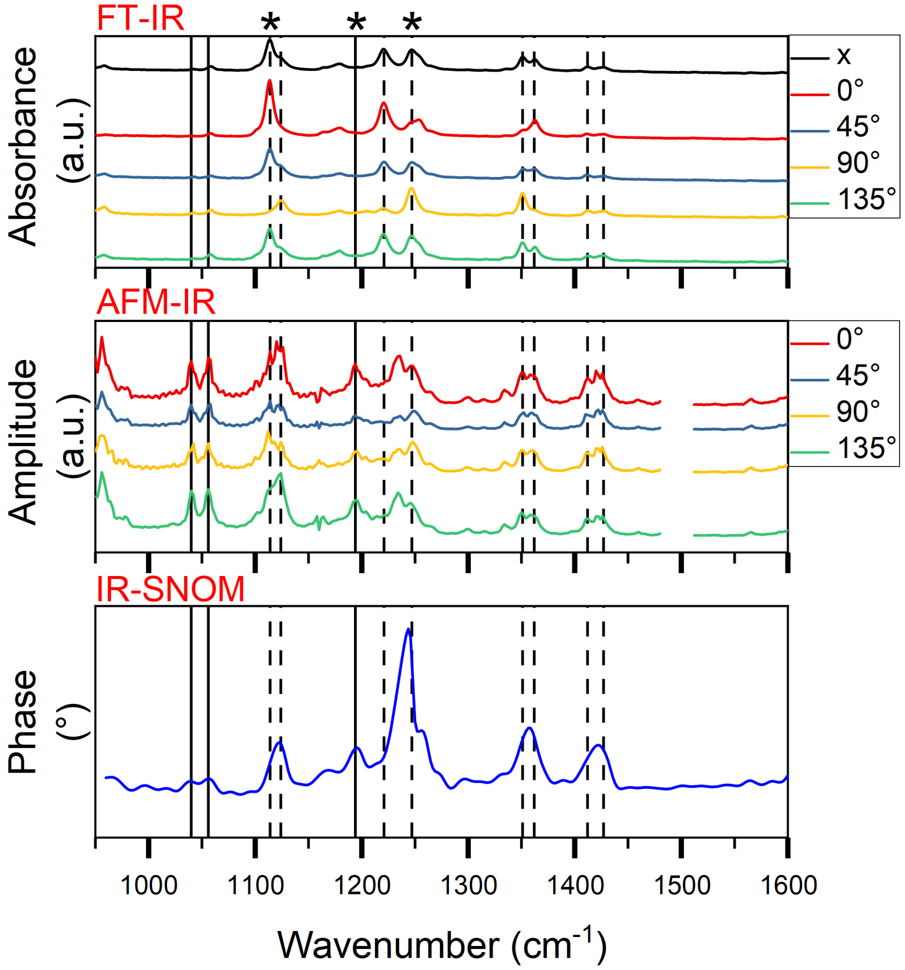

Figure 4.11: Polarization-dependent absorbance spectra from FT-IR and amplitude spectra from AFM-IR, and phase spectrum from IR-SNOM of a single crystal of PDIF-CN$_2$. Absorbance spectrum with non-polarized light (x) is shown for reference. Dashed lines correspond to the modes seen in the FT-IR spectra, solid lines indicate modes which are present only in the AFM-IR and IR-SNOM spectra and the asterisks mark those peaks whose vibrational modes are presented below. Adapted with permission from Ref.[147]. Copyright 2020 American Chemical Society.

In addition to the doublets observed in the FT-IR spectra, the AFM-IR spectra of PDIF-CN$_2$ single crystal (**Figure 4.11**, middle) show two strong doublets at 1040/1056 cm^{-1} and 1412/1422 cm^{-1}, and two individual peaks at 956 cm^{-1} and 1194 cm^{-1}. These new modes, which have an out-of-plane component of the transition dipole moment vector (see **Figure 4.12** and **Figure A.3** of the Appendix), become accessible with the AFM-IR and should be visible in the IR-SNOM signal as well.

Interestingly, the phase signal from a single crystal of PDIF-CN$_2$ acquired by the IR-SNOM, shown in **Figure 4.11** (bottom), is very distinct compared to the previously investigated molecular crystals. The corresponding amplitude signal is given in **Figure A.2** of the Appendix. The doublets seen in the FT-IR and/or AFM-IR spectra appear as single, broad peaks (except for the 1040/1056 cm^{-1} doublet) in the IR-SNOM signal, revealing no splitting even at better spectral resolutions (3-5 cm^{-1}). See **Table 4.4** for a comparison of positions and intensities of selected doublets and a singlet for different orientations of the electric field, as observed by the three different techniques. For a full list, see **Table A.4** of the Appendix.

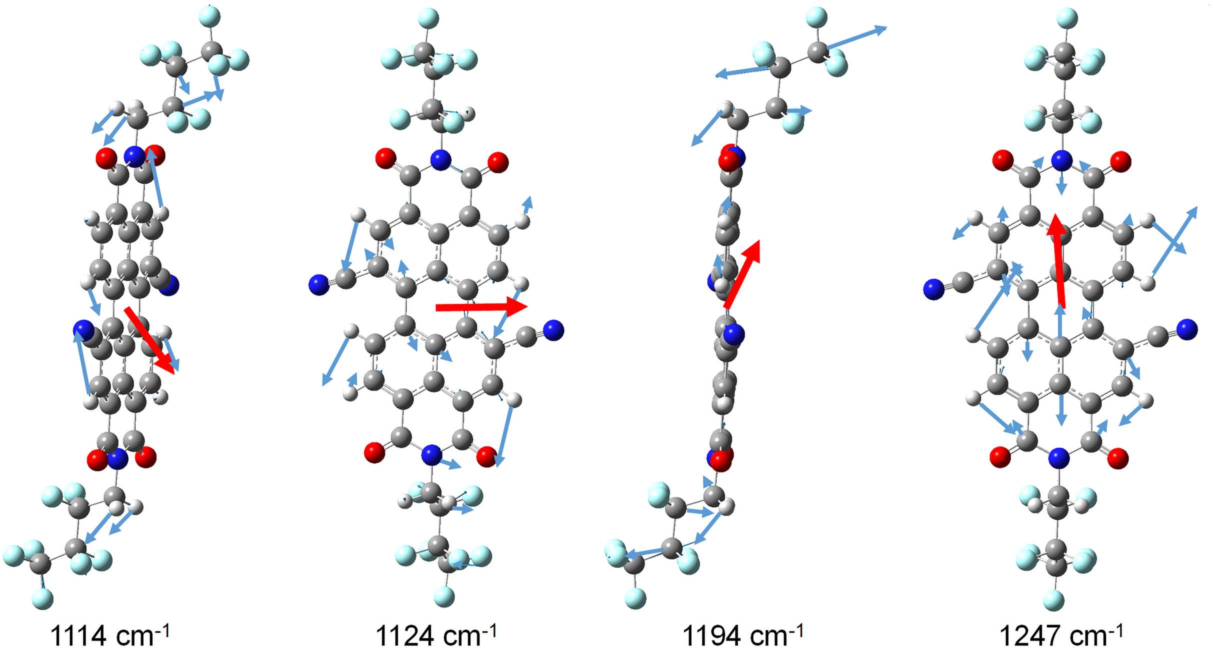

Figure 4.12: Visualisation of the vibrational modes corresponding to selected absorption peaks of PDIF-CN$_2$. Blue and red arrows (lying in the plane of the paper and scaled to improve visibility) indicate the displacement vectors and the dipole derivative unit vectors, respectively. Atoms of hydrogen are shown in white, carbon in gray, oxygen in red, nitrogen in blue and fluorine in cyan. Adapted with permission from Ref.[147]. Copyright 2020 American Chemical Society.

The peak at 1244 cm^{-1} is unusually strong, which is a result of vibrations restricted to the backbone of the PDIF-CN$_2$ molecule. The transition dipole moment vector of this mode lies in the plane of the π-conjugated core, oriented parallel to the long-axis of the molecule, as shown in **Figure 4.12**. The polarizability of a molecule increases when its transition dipole moment aligns with the direction of the field enhancement of the metallic SNOM tip (that is, parallel to the tip axis) which leads to better scattering of the incident electric field by the sample. Since PDIF-CN$_2$ molecules in a single crystal exhibit a nearly vertical arrangement of the π-conjugated core (see **Figure 4.10(c)**), the transition dipole vector of the mode at 1244 cm^{-1} is almost parallel to the tip and therefore strongly excited.

Table 4.4: Comparison of position and intensity* of the most prominent absorption peaks of a single crystal of PDIF-CN$_2$ for different polarizations and IR spectroscopic techniques. Adapted with permission from Ref.[147]. Copyright 2020 American Chemical Society.

PDIF-CN$_2$	FT-IR (cm^{-1})	AFM-IR (cm^{-1})	IR-SNOM (cm^{-1})
0°	1221/1247	**1040/1056** 1194 1236/1248	(1039)/(1056) 1196 **1244**
45°	1221/1247	**1040/1056** (1194) 1236/1248	
90°	1221/1247	**1040/1056** (1194) 1236/1248	
135°	1221/1247	**1040/1056** 1194 1236/1248	

* Intensity of the peaks is indicated as: bold font - strong; regular font - medium; within brackets - weak.

4.2.5 Conclusions from Single Crystal Measurements

Infrared spectroscopy performed on the four organic single crystals using three different techniques emphasizes the influence of molecular packing and orientation on the excitation of specific vibrational modes for each method and crystal. The direction and polarization of the incident light determines accessibility and visibility of certain modes. As demonstrated by the AFM-IR, oblique incidence of vertically polarized light excites modes with in-plane and out-of-plane components. The IR-SNOM, on the other hand, excites only those modes which have a component perpendicular to the substrate. The signal-to-noise ratio of the spectra recorded by the different techniques appears to be strongly dependent on the molecular packing.

The AFM-IR has made its mark with polymer samples by providing high quality spectra. However, the spectral quality are not as impressive with organic molecular crystals which could be because of lower thermal expansion coefficients (small molecules: 10-170 ppm/K, polymers: 50-500 ppm/K).[191] An exception to this observation was rubrene. The AFM-IR spectra of its single crystal is distinctive with sharp absorption peaks, as shown in **Figure 4.8**. Precise thermal expansion coefficient along the *c*-axis of rubrene and other investigated single crystals were, unfortunately, not available. One could, however, assume that the bulky, interlocking TIPS groups on TIPS-PEN and TIPS-TAP, and the alkyl side-chains on PDIF-CN_2 might hinder expansion in the direction perpendicular to the substrate (along *c*-axis), as observed with polymorphs of 2,6-dichloronaphthalene tetracarboxylic diimide.[274] Rubrene on the other hand has four phenyl substituents that do not interlock, and has well-separated layers in the *c*-axis direction (see **Figure 4.7(c)**). This would imply that the thermal expansion of rubrene in the vertical direction is less constrained and as a result the AFM-IR signals are stronger. This example suggests that the applicability of the AFM-IR depends strongly on the intrinsic structure of the system under investigation. It nevertheless shows the versatility of the technique in performing polarization spectroscopy with exceptional spectral resolution and quality while still enabling access to both in-plane and out-of-plane modes. The easy-to-use setup and easy-to-interpret data further make the AFM-IR a promising tool to characterize novel organic materials.

The IR-SNOM depends not on thermal expansion but on scattering of incident light by the sample. The higher the polarizability of the molecule, the better scatterer it is. Since polarizability depends on the molecule's internal structure and its orientation with respect to the external electric field (i.e., vertical to the substrate and parallel to the tip's axis), the outstanding signal quality of PDIF-CN_2 single crystal can be assumed to result from the orientation of the molecules with respect to the substrate (see **Figure 4.10(c)**). The well-resolved peaks have transition dipole moment vectors oriented along the π-conjugated core which is nearly parallel to the tip-axis or, in other words, parallel to the direction of electric field enhancement. The other investigated crystals also show some strong peaks but their spectra are not quite like that of PDIF-CN_2 perhaps due to lower overall polarizability resulting from the parallel orientation of the π-conjugated core with respect to the substrate. Studies involving the IR-SNOM and molecular thin films (pentacene[218] and perylene tetracarboxylic dianhydride (PTCDA)[218]) also benefited from the fact that the molecules stood upright on the substrate. The IR-SNOM, like the AFM-IR, appears to be suitable for certain organic materials, typically limited by their out-of-plane oscillator strength. Furthermore, the interpretation of IR-SNOM spectra is not straightforward since the amplitude and phase signals are a result of complex tip-sample interactions, which therefore requires system specific modelling.[140] Moreover, the signals are also sensitive to the thickness of the sample as this can alter the extent of interference of the substrate with tip-sample interactions.[203]

Both techniques might be interesting for other classes of organic single crystals, such as phenyl-containing linearly fused oligothiophenes such as [1]benzothieno[3,2-b][1]benzothiophenes (BTBT), and dibenzo[d,d']thieno[3,2-b;4,5-b']dithiophene (DBTDT) which are another important class of small-molecule organic semiconductors. Large aspect ratios of these thiophene derivatives leads them to organize into columns along the *c*-axis in their crystal lattice (see **Figure 4.13(a),(e)**) while forming a herringbone pattern in the *ab* plane.[275,276] Such an orientation increases the polarizability of the molecule in the IR-SNOM configuration and therefore, good signals could be expected. Other members of the peropyrene family like diaza- and tetraazaperopyrenes (TAPP) along with their polyheterocyclic derivatives are known to exhibit a slip-stacked face-to-face assembly in their single crystals,[277,278] very similar to PDIF-CN$_2$ molecules as shown in **Figure 4.13(b),(f)**. Hence, characterizing them with the IR-SNOM may provide valuable information. However, long alkyl sidechains in both thiophene and peropyrene derivatives increase the intermolecular interactions across consecutive layers and as such, may not perform so well under the AFM-IR. On the other hand, 2D disc-like molecules such as porphyrin and hexabenzocoronene (HBC), which stack into 1D face-to-face or cofacial herringbone motifs,[84] are worth investigating with the AFM-IR (see **Figure 4.13(c),(d),(g),(h)**).

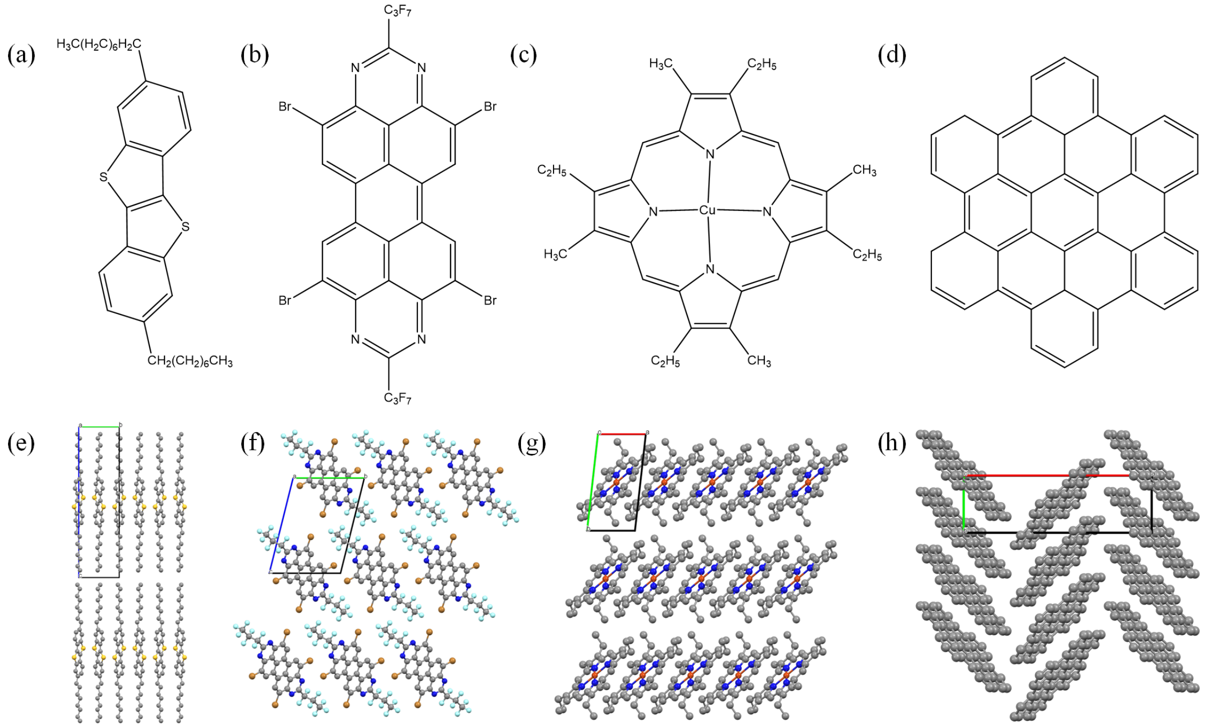

Figure 4.13: Molecular structure of (a) C8-BTBT, (b) TAPP-Br, (c) Cu-porphyrin, and (d) HBC. The columnar packing of C8-BTBT molecules is shown in (e), the slipped-stacking motif of TAPP-Br in (f), the 1D face-to-face arrangement of Cu-porphyrin in (g), and the cofacial herringbone motif of HBC in (h). The unit cell in each case is indicated with the crystallographic *a*-axis in red, *b*-axis in green, and *c*-axis in blue. The colours of atoms are as follows: carbon - gray, sulphur - yellow, nitrogen - blue, fluorine - cyan, bromine - brown, copper - orange. Hydrogen atoms are omitted for the sake of clarity. Molecular packing structures are taken from crystal data published by Ref. [275], [279], [280], [281].

4.3 Infrared Nanospectroscopy and Imaging

The capabilities of the advanced vibrational spectroscopy techniques, AFM-IR and IR-SNOM, go beyond simple spectroscopy to enable nanospectroscopy and nanoimaging. Information about the presence of polymorphs, micro- and nanocrystalline features, local strains and doping in thin films, which is otherwise inaccessible, can be detected qualitatively through imaging and quantitatively through spatially resolved IR spectra. In order to demonstrate these useful features, a polycrystalline film of PDIF-CN_2 was investigated since single crystals of this material provided well-resolved AFM-IR and IR-SNOM spectra as a reference.

A discontinuous film of PDIF-CN_2 prepared by spin-coating a solution of the material in chloroform onto a gold-coated silicon wafer (see **Chapter 3.2.2**) is shown in **Figure 4.14**. The two SEM micrographs show randomly distributed leaf-shaped crystallites with lengths of 3-4 µm, widths of around 1.5 µm and thickness between 50 and 150 nm. **Figure 4.14(a)** was acquired with the secondary electron in-lens detector which provides good material contrast between the semiconducting organic crystallites and the conductive gold substrate. Topographic contrast of the same section of the film was simultaneously obtained with the in-chamber detector, shown in **Figure 4.14(b)**. This image reveals that the edges of the crystallites are corrugated and buckled upwards, thereby partially detaching themselves from the substrate.

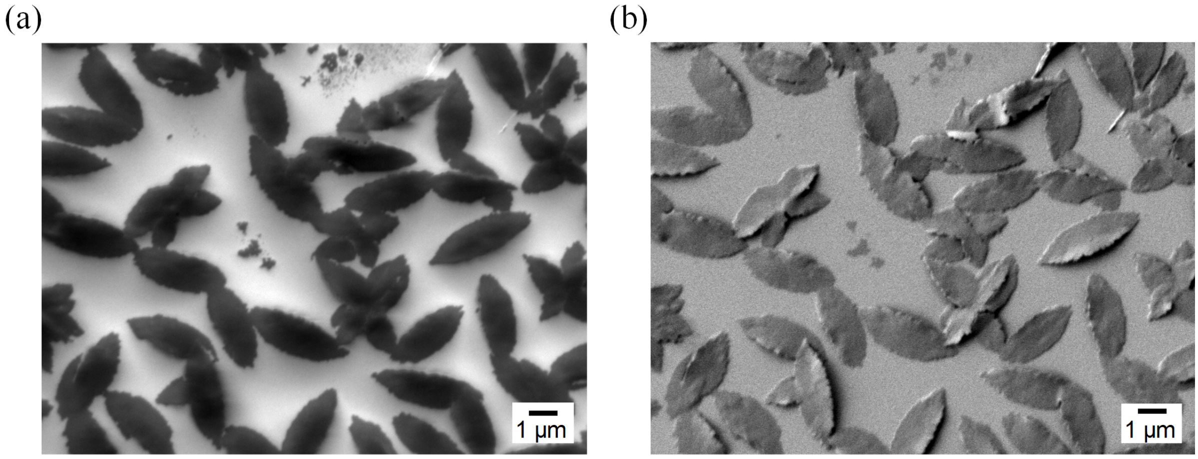

Figure 4.14: Secondary electron micrographs of a spin-coated film of PDIF-CN_2 on gold-coated Si substrate. (a) Shows the material contrast and (b) the topographic contrast of a section of the film, recorded with the in-lens and the in-chamber detectors, respectively. Adapted with permission from Ref.[147]. Copyright 2020 American Chemical Society.

A far-field absorbance spectrum of the PDIF-CN_2 film, was first measured with the FT-IR and is shown in **Figure 4.15**. Following this, local IR spectra were acquired with the AFM-IR from the buckled edges and flat-lying center of the crystallites.

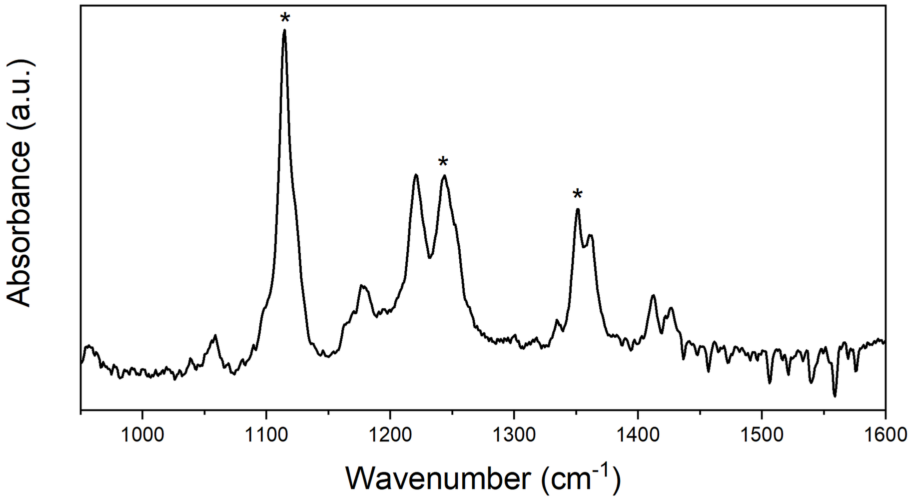

Figure 4.15: Far-field (FT-IR) absorbance spectrum of a polycrystalline film of PDIF-CN$_2$. Peaks that show a noticeable difference in the AFM-IR and IR-SNOM spectra between the edge and the center are indicated with asterisks. Adapted with permission from Ref.[147]. Copyright 2020 American Chemical Society.

Figure 4.16 shows individual AFM-IR spectra from the center and the edges, and the corresponding points on a topography image from where they were acquired. Spectra marked as 'Center' and 'Edge' were then averaged separately (see **Figure 4.17**) to determine changes in relative peak intensities and positions.

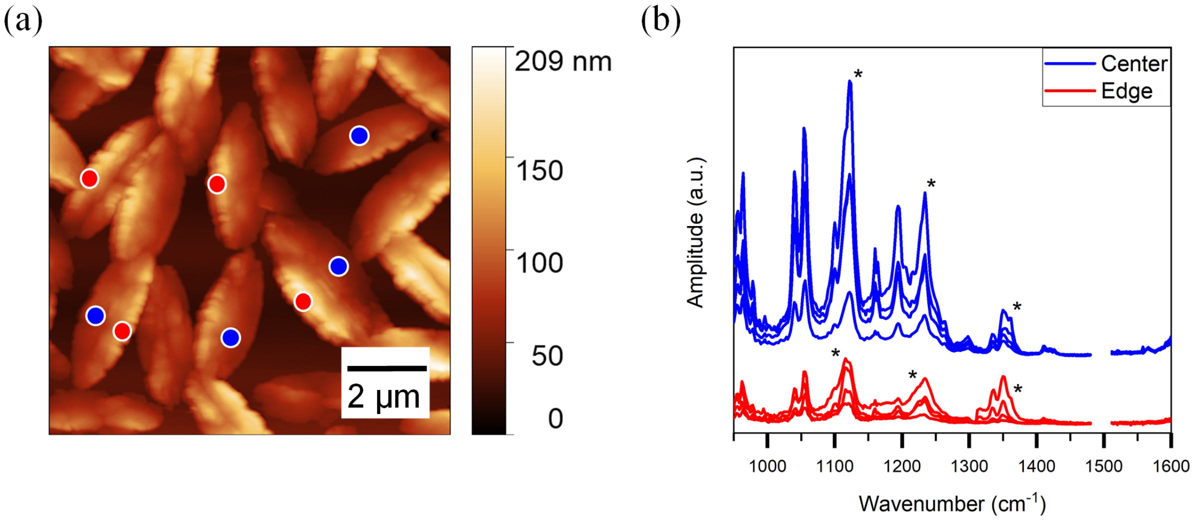

Figure 4.16: (a) Topography image of a polycrystalline PDIF-CN$_2$ film with blue (center) and red (edge) dots indicating the positions from where (b) AFM-IR spectra (blue and red lines, respectively) were measured. Adapted with permission from Ref.[147]. Copyright 2020 American Chemical Society.

Some obvious differences are present between the spectra from the center and those from the edge. First of all, amplitude signal from the buckled edges is much lower than that from the flat-lying center of the crystallites. The peak seen at 1122 cm^{-1} in the spectra from the center is redshifted by 6 cm^{-1} to 1116 cm^{-1} in the spectra from the edge. The mode at 1234 cm^{-1} develops a low-energy shoulder, and the high-energy shoulder of the 1350 cm^{-1} peak shows reduced intensity.

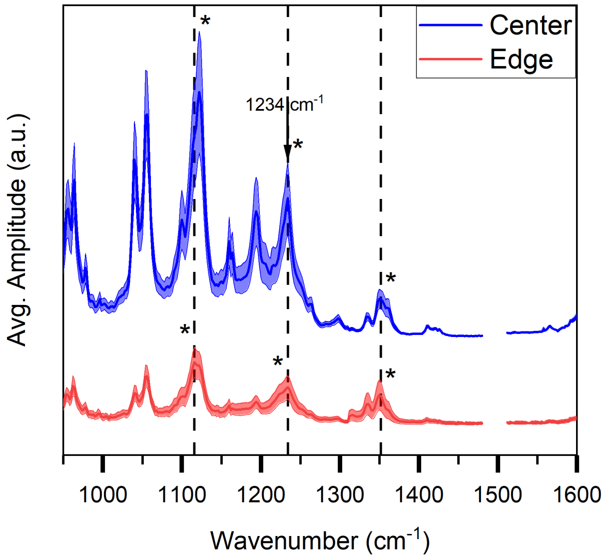

Figure 4.17: Average of the spectra shown in **Figure 4.16** (center - blue, edge - red). Shaded area indicates the deviation from the average. Arrow indicates the wavenumber with which mapping was done. Asterisks indicate those peaks that show a noticeable difference. Adapted with permission from Ref.[147]. Copyright 2020 American Chemical Society.

Tensile strains usually manifest as redshifts in vibrational modes, and change of relative intensities (between modes at 1122 cm^{-1} and 1234 cm^{-1} with in-plane and out-of-plane transition dipole moments, respectively) may indicate a change in molecular orientation between the center of a crystallite and its buckled edge.

The imaging module of the AFM-IR was then used to record the height and amplitude images of a section of the polycrystalline film of PDIF-CN_2. **Figure 4.18** shows the topography and amplitude images of a 10 x 10 μm^2 area of the film mapped at 1234 cm^{-1}. Since the sample strongly absorbs at this wavenumber and a change in the shape of the peak is observed between the center and the edge of the crystallite, it was chosen for mapping. In the topography map, some sections of the crystallites appear to be higher where it can be assumed the crystallites are bent upwards, as the SEM image shows. However, strangely, the corresponding sections of the amplitude map appear discontinuous. While some regions of the edges show a strong contrast against the background gold, others show no contrast at all. However, a significant area of each crystallite has large amplitudes, thus indicating higher absorbance.

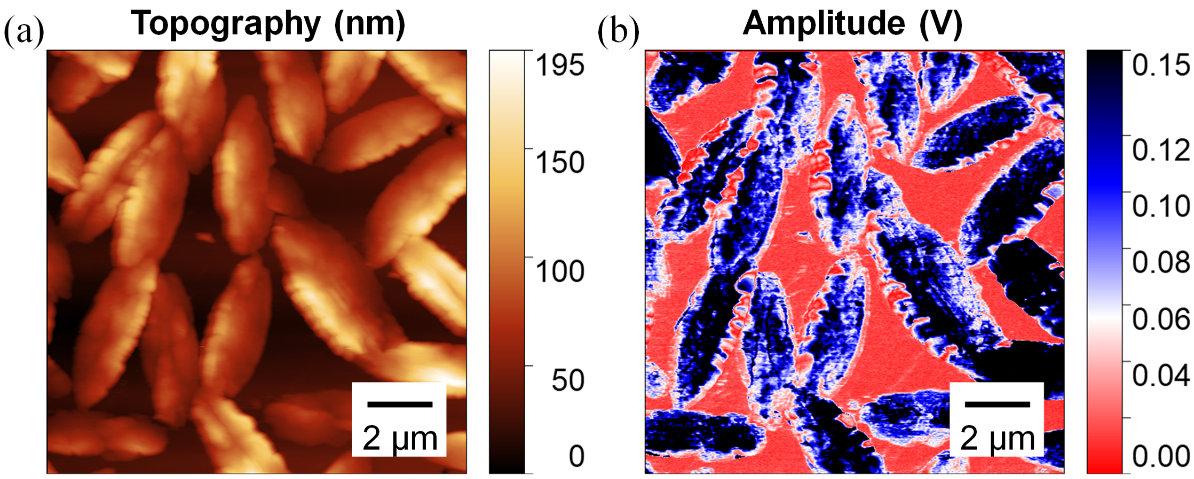

Figure 4.18: (a) Topography and (b) amplitude images of a spin-coated film of PDIF-CN_2 on gold-coated Si substrate mapped simultaneously with an AFM-IR at 1234 cm^{-1}. Adapted with permission from Ref.[147]. Copyright 2020 American Chemical Society.

An overlay image of height and amplitude maps provided in **Figure 4.19** highlights the local variations in the two signals. It further confirms that some areas appear with low amplitudes even though PDIF-CN_2 is present and elevated height is observed. The origin of these non-uniformities in contrast along the edges could be due to one or more of the following factors: differences in thermal expansion, lower thermal conductance, and changes in molecular orientation. Thermal expansion of a material is a function of the geometry and the volumetric size of the sample in addition to other parameters.[167] The crystallites are not uniformly thick at the edges, which could bring about local differences in thermal expansion, leading to uneven contrast. A material's effective thermal conductance is again dependent on the sample's dimensions and contact to the substrate. Therefore, small changes in thickness, for example, eventually affects the observed amplitude contrast. It is clear from the SEM image (**Figure 4.14(b)**) that the crystallites do not lie flat on the substrate but are buckled upwards and are corrugated at the edges. This would force the molecules to distort themselves and shift their orientation with respect to the incident electric field, thus becoming evident in the observed contrast. The partial delamination and wrinkling would further cause a build-up of strain in different regions of the crystallites, indicated by variations in contrast in the amplitude map. Decoupling these various factors is not straightforward and perhaps impossible without the help of some complementary techniques.

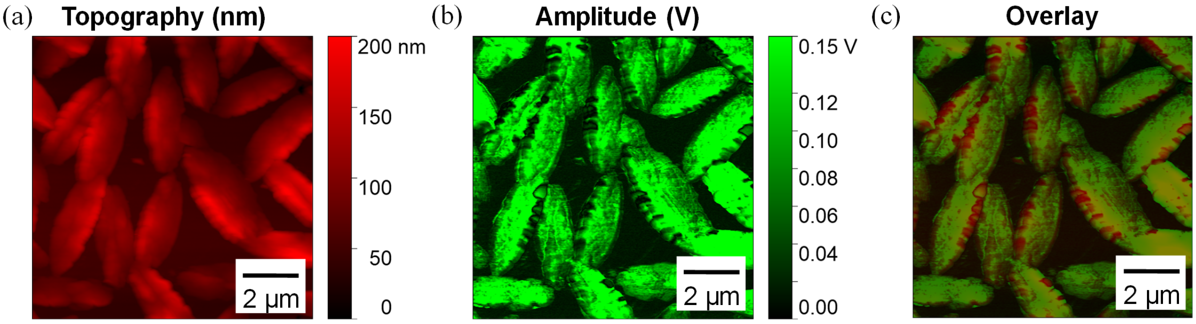

Figure 4.19: An overlay of the topography (red) and amplitude (green) images of a polycrystalline film of PDIF-CN_2 recorded with the AFM-IR at 1234 cm^{-1}. The overlay image highlights the presence of material at the edges of the crystallites where the amplitude image shows little to no signal. Adapted with permission from Ref.[147]. Copyright 2020 American Chemical Society.

Next, the IR-SNOM was used to acquire spectra from different positions on the same sample of PDIF-CN_2. Phase spectra, of the second demodulation order, from the center and edges of crystallites and the corresponding measurement spots are shown in **Figure 4.20**. The averaged spectra, in **Figure 4.21**, show some differences in peak positions and intensities between the center and the edge. Modes at 1124 and 1425 cm^{-1} in the signal from the center are redshifted by a few wavenumbers to 1122 and 1422 cm^{-1}, respectively, in the spectrum from the edge. Also, the relative intensities of the modes at 1245 and 1422 cm^{-1}, both of which have out-of-plane transition dipole moment vectors, vary slightly. These subtle but non-negligible differences could be an indication of differences in the orientation of molecules within the crystallites.

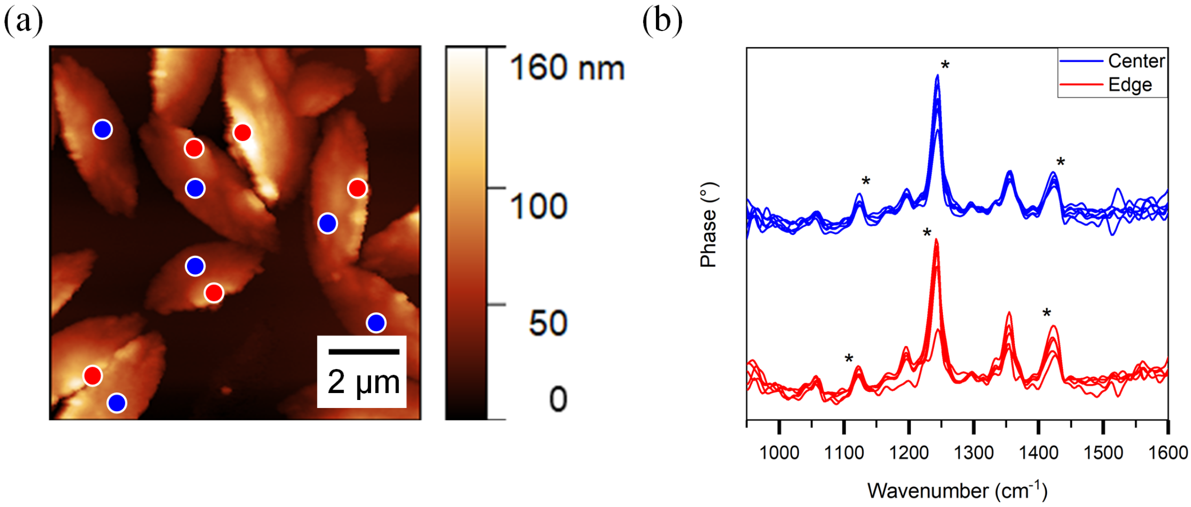

Figure 4.20: Topography image of a polycrystalline PDIF-CN_2 film with blue (center) and red (edge) dots indicating the positions from where IR-SNOM spectra (blue and red lines, respectively) were measured. Adapted with permission from Ref.[147]. Copyright 2020 American Chemical Society.

A 10 x 10 µm^2 section of the film was then mapped with the laser tuned to 1058 cm^{-1}, where an absorption peak is present. The resulting near-field amplitude and phase images (of the second demodulation order) along with topography is shown in **Figure 4.22**.

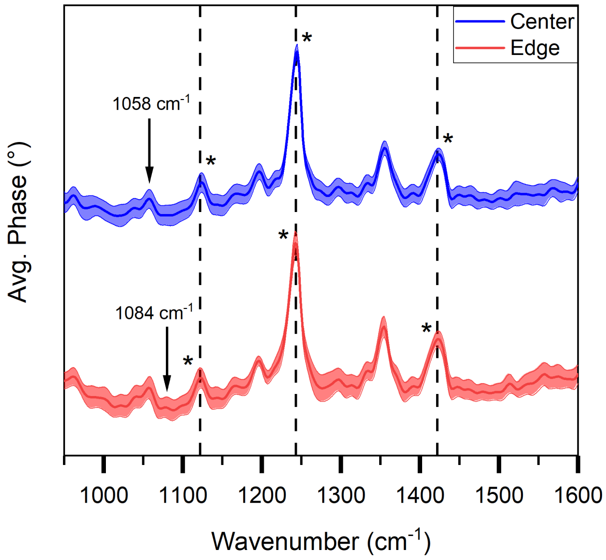

Figure 4.21: Averaged near-field phase spectra (second demodulation order) obtained with the IR-SNOM from center (blue) and edge (red) positions of different crystallites. Shaded area indicates the deviation from the average. Arrow indicates the wavenumber with which mapping was done. Asterisks indicate those peaks that show a noticeable difference. Adapted with permission from Ref.[147]. Copyright 2020 American Chemical Society.

As expected, the topography image shows protruding features along the edges where the crystallites are presumably bent upward. The corresponding areas in the amplitude and phase images display a clear contrast with respect to the gold substrate as well as to the center of the crystallites. This contrast is often significantly correlated with the height but not everywhere.

When mapped at 1084 cm^{-1}, where a weak mode appears only in the spectra from the edge, similar correlations can be made between the crystalline edges and the observed contrast. Mapping at other wavenumbers where stronger modes are excited could not be done because of the limited range of the available quantum cascade laser (1020-1097 cm^{-1}).

Interpretation of these IR-SNOM maps is difficult on the one hand, as near-field amplitude and phase signals are indirectly related to the local complex refractive index through the local complex polarizability of the sample. Variations in contrast in the amplitude and phase maps from the IR-SNOM indicate differences in the near-field resonances which could be a result of changes in molecular orientation at the buckled edges of the PDIF-CN$_2$ crystallites. It is clear from the previous section that the IR-SNOM probes only those vibrations whose dipole moment is (nearly) perpendicular to the substrate. Therefore, the appearance of any new peak and/or alterations in the intensity of a peak from one region to another translates to dissimilar arrangement of molecules between those regions, which is reflected in the amplitude and phase contrasts. Perhaps by mapping at 1245 cm^{-1}, where a strong mode is observed, this difference would become more obvious. However, the edges of crystallites also act as boundaries which could cause spectral changes due to disorder. Another reason for the changing contrast from the edges to the center could simply be that the former is partially delaminated from the substrate. Since the substrate effect is strong in IR-SNOM measurements,[203] whether the sample lies flat on it or not would influence the resulting contrast. The smooth transition in contrast from the edge to the center in the maps from the IR-SNOM is quite unlike what is observed with the AFM-IR. This difference likely stems from the fact that in the case of the AFM-IR, the mechanical motion of the cantilever induced by the thermal expansion of the partially free-standing edges is significantly different from that induced by other areas of the crystallites whose expansion is constrained by the substrate on one side. Furthermore, the AFM-IR and the IR-SNOM are operated in contact and tapping modes, respectively, which might lead to some unaccountable differences especially when the sample is a rather thin and flexible, free-standing organic layer. Nevertheless, the ability of both the IR techniques to acquire local IR spectra and create IR maps simultaneously with topographic images is demonstrated clearly with the help of these thin PDIF-CN$_2$ microcrystals.

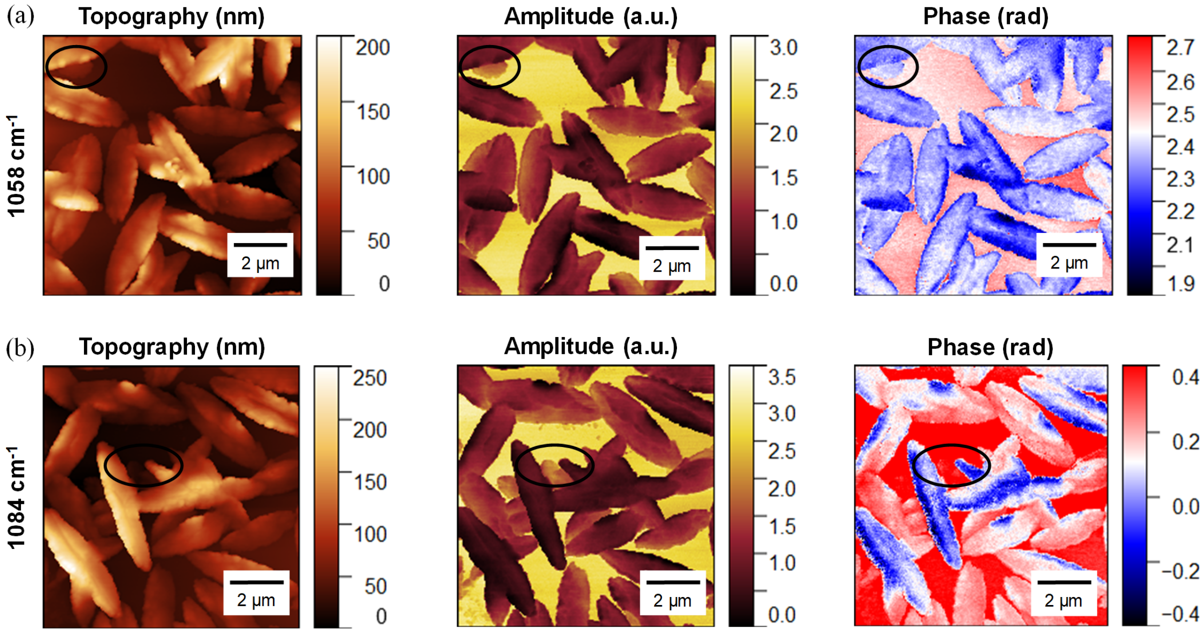

Figure 4.22: Topography, near-field amplitude and phase images (second-order) of a spin-coated film of PDIF-CN$_2$ on gold-coated silicon wafer mapped at (a) 1058 cm^{-1} and at (b) 1084 cm^{-1} with the imaging module of the IR-SNOM. Regions in the amplitude and phase images where there is less correlation to topography are circled. Adapted with permission from Ref.[147]. Copyright 2020 American Chemical Society.

4.4 Conclusion

The study presented in this chapter tests the versatility of two advanced nano-IR spectroscopy techniques: AFM-IR and IR-SNOM, with the help of four well-known small-molecule organic semiconducting single crystals of TIPS-PEN, TIPS-TAP, rubrene and PDIF-CN_2, and a polycrytalline film of the last. Standard FT-IR spectroscopy was also performed on the same samples with both polarized and unpolarized light. Spectra of each molecular crystal acquired with the different techniques display significantly different features. Certain in-plane and out-of-plane vibrational modes were either enhanced or suppressed, which was attributed to differences in the angle of incidence and the orientation of molecules inside the crystal. The quality of the spectra from the AFM-IR and the IR-SNOM was found to be largely dependent on the intrinsic molecular structure and packing within the crystal. For the AFM-IR, it was supposed that differences in thermal expansion coefficients along the vertical crystal axis and/or the presence of interlocking side-chains/groups caused variations in signal quality. For IR-SNOM, the orientation of the π-conjugated core of the molecules with respect to the enhanced electric field direction plays an important role. When aligned with the field (parallel to the tip), the polarizability of the molecule increases which results in a better overall signal. Nanoscale spatial resolution of both AFM-IR and IR-SNOM was demonstrated with a polycrystalline film of PDIF-CN_2. Features within a single micron-sized crystallite could be spectrally distinguished. When imaged with specific wavenumbers, a clear contrast was observed with good spatial resolution. The precise origin of the contrast and what the differences represent remain very challenging to interpret.

As demonstrated here, AFM-IR and IR-SNOM could be exploited to examine the presence of foreign particles, structural disorder and even build-up of strain in the active layer of organic opto-electronic devices. For example, Mrkyvkova et al. have reported the presence of defective crystallites showing a different orientation of the π-conjugated core in thin films of diindenoperylene (DIP, a small-molecule organic semiconductor) which was detected using the IR-SNOM.[272] In thin-film transistors of TAPP-Br, charge carrier mobility is found to be lower in solution-grown films in comparison to vacuum-deposited films.[279] This difference could be because of solvent molecules trapped locally within the crystal lattice, which distort the molecular packing and the π-π overlap. Or, as shown by Tzschoppe et al.,[282] the molecules of TAPP-Br are perhaps arranged differently in the two films depending on the deposition method. All these characteristics could be thoroughly investigated by combining nanospectroscopy with nanoimaging as offered by the AFM-IR and the IR-SNOM. In any case, access to calculated IR spectra and vibrational modes is crucial to interpret and assign the observed IR modes. Additional experimental and theoretical studies on model systems (e.g., see **Figure 4.13**) may enable clearer correlations between the observed spectral features and the structure and property of organic crystals and thin films.

Chapter 5

Liquid-Phase Exfoliation of Rubrene Single Crystals

The results of the study presented in this chapter were published in reference [283]: V. J. Rao, H. Qi, F. J. Berger, S. Grieger, U. Kaiser, C. Backes, J. Zaumseil, "Liquid Phase Exfoliation of Rubrene Single Crystals into Nanorods and Nanobelts". Electron diffraction experiments using transmission electron microscopy and related analysis were carried out by Dr. Haoyuan Qi. Rotation electron diffraction experiments were performed by Dr. Tatiana Gorelik.

5.1 Motivation

Liquid-phase exfoliation (LPE) has emerged as a popular top-down technique to produce nanomaterials with size-dependent properties in large quantities. As discussed in **Chapter 2.7**, individual layers of crystals are delaminated with the help of sonication or shear, and the resulting nanomaterials are stabilized against re-aggregation by using appropriate solvents or aqueous surfactant solutions. The initial dispersions are usually highly polydisperse[284] and are therefore subjected to size selection via band sedimentation or liquid cascade centrifugation (LCC, see **Chapter 2.8**) in order to investigate size-dependent properties. The current understanding is that the shape of the nanomaterial obtained with LPE is dictated by the ratio of in-plane and out-of-plane binding strength of the bulk material.[243] As a consequence, scission in addition to delamination occurs which implies that not only layered crystals but also non-layered materials[285,286] can be exfoliated via LPE. However, so far the layers of the exfoliated materials are found to have strong in-plane covalent or coordination bonds.

In crystals of π-conjugated organic semiconductors, strong non-covalent π-π interactions often exist within one crystalline plane while weaker forces act in other directions. This anisotropy of intermolecular interactions in small-molecule organic crystals, such as pentacene[287] and rubrene,[107] is known to influence charge carrier mobilities,[60] coefficients of thermal expansion,[288] and Young's moduli.[289] Low dimensional structures of organic semiconductors in the form of self-assembled monolayers and nanowires have been demonstrated,[290,291] however, they were fabricated bottom-up from solution or gas phase but not top-down from a macroscopic crystal. It would, therefore, be interesting to find out whether the offset between in-plane and out-of-plane intermolecular forces in molecular crystals facilitates exfoliation of mono- or multilayered nanomaterials from bulk crystals via LPE.

Here, single crystals of rubrene were chosen as the model system to test LPE on organic molecular crystals. As presented in **Chapter 2.2**, rubrene is one of the most extensively studied organic semiconductor that has led to its application in OFETs, OLEDs, and OPVs. Depending on the growth method and conditions, three different polymorphs of rubrene have been discovered — orthorhombic, triclinic, and monoclinic. The molecular packing within each of these lattices is distinct resulting in different degrees of π-orbital overlap along the three crystallographic axes. In this study, LPE was applied only to the orthorhombic and the triclinic rubrene single crystals.

5.2 Exfoliation and Size Selection of Rubrene Single Crystals

The orthorhombic crystals of rubrene, grown by the PVT method (see **Chapter 3.2.1**), with lattice parameters a = 7.18 Å, b = 14.43 Å, c = 26.81 Å, α = 90°, β = 90°, γ = 90°, and the triclinic crystals, grown by the reprecipitation method[106] with lattice parameters a = 7.02 Å, b = 8.54 Å, c = 11.95 Å, α = 93.04°, β = 105.58°, γ = 96.28°, are shown in **Figure 5.1** alongside their crystal packing as seen from the side and the top. Note that the standard crystallographic assignment for rubrene was followed here,[106,292] whereas in the literature the a- and b-axis of orthorhombic rubrene are often interchanged. Liquid-phase exfoliation of these two polymorphs were carried out via bath-sonication in aqueous sodium cholate solution (see **Chapter 3.3** for experimental details).

The resulting orange-coloured stock dispersion was then subjected to size selection via liquid cascade centrifugation (**Chapter 3.3**) following which three fractions each of milky pink-orange dispersions of orthorhombic and triclinic rubrene were obtained, as shown in **Figure 5.2**. Under ultraviolet (UV) light illumination, the dispersions showed a yellow-green fluorescence. The three fractions were labelled according to the applied relative centrifugal forces — 0-0.1k g (lowest), 0.1-1k g (intermediate), and 1-30k g (highest). The stability of the dispersions was confirmed by zeta potential measurements that yielded values between -15 and -30 mV. **Table 5.1** provides the average zeta potentials of the different rubrene dispersions. The values are consistent with anionic cholate as the surfactant.

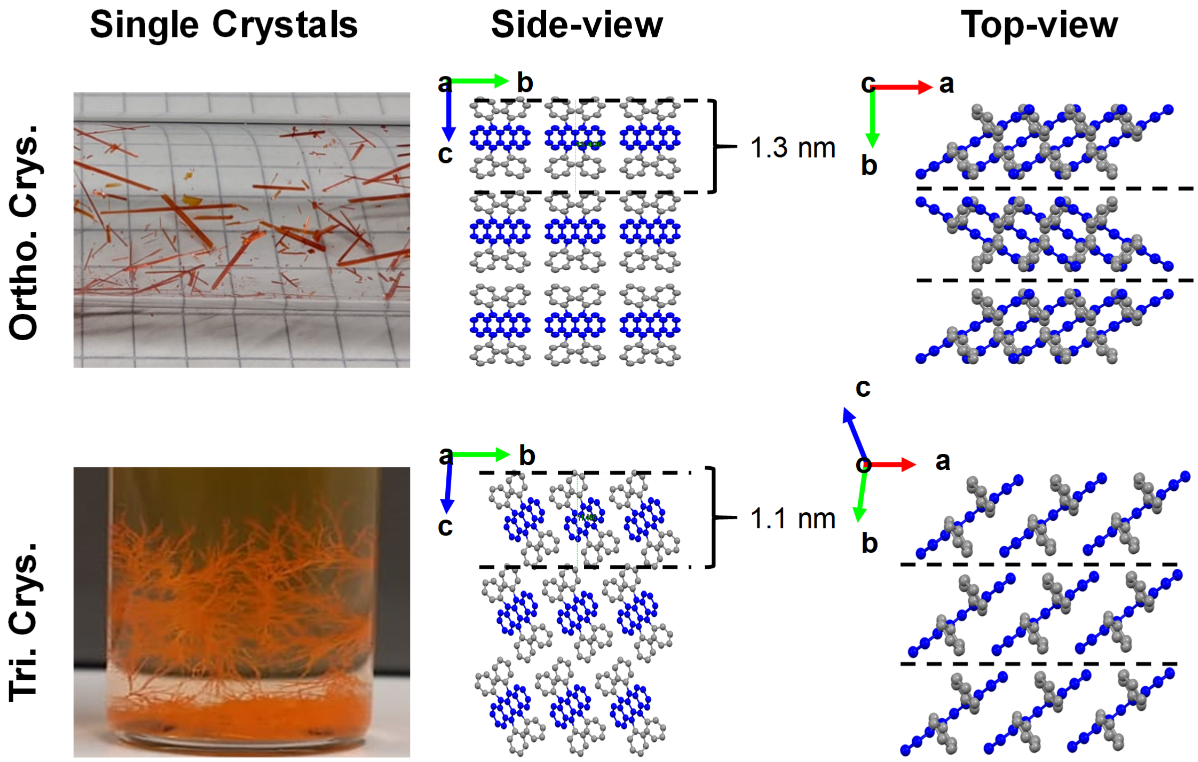

Figure 5.1: Photographs of orthorhombic (Ortho.) and triclinic (Tri.) rubrene crystals (Crys.) and the molecular packing within their corresponding lattices. The *b*- and the *c*-axis are parallel to the short axis and the thickness of the crystals, respectively. The interlayer spacing of 1.3 nm in orthorhombic lattice and 1.1 nm in triclinic lattice is shown in the side-view images. The π-conjugated tetracene core is highlighted in blue and its stacking direction, which is along the *a*-axis, is shown in the top-view images. Hydrogen atoms are omitted for clarity. Adapted with permission from Ref.[283]. Copyright 2021 American Chemical Society.

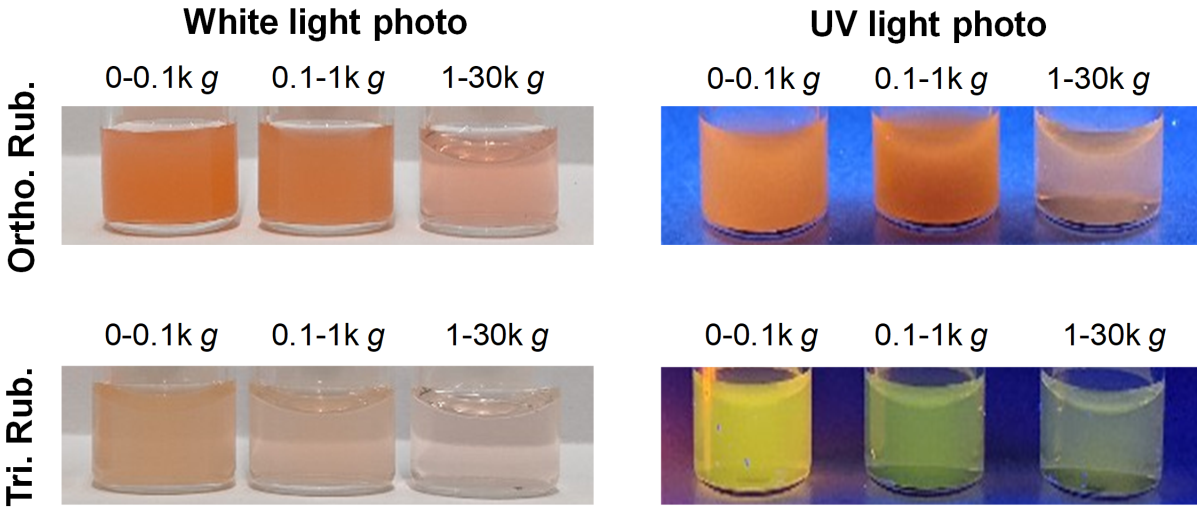

Figure 5.2: Photographs of the liquid-phase exfoliated and size-selected dispersions of orthorhombic rubrene crystals (Ortho. Rub.) and triclinic rubrene crystals (Tri. Rub.) under white light as well as UV light illumination. Adapted with permission from Ref.[283]. Copyright 2021 American Chemical Society.

Table 5.1: Average zeta potential values of three different fractions of LPE rubrene dispersions in 0.1 g L^{-1} aqueous sodium cholate solution. Adapted with permission from Ref.[283]. Copyright 2021 American Chemical Society.

	LPE Orthorhombic Rubrene			LPE Triclinic Rubrene		
	0-0.1k *g*	0.1-1k *g*	1-30k *g*	0-0.1k *g*	0.1-1k *g*	1-30k *g*
Zeta Potential (mV)	-30.6	-21.1	-15.9	-22.3	-26.2	-19.4

5.3 Rubrene Nanorods and Nanobelts

The morphology of nanostructures resulting from the exfoliation of rubrene single crystals was studied with the help of an AFM. **Figure 5.3(a),(b)** show the topography images of the intermediate and the highest fractions of orthorhombic rubrene dispersion, respectively. Apart from expected residual chunks of crystals, flakes, and platelets, distinct rod-like structures were first observed in the intermediate fraction. The highest fraction (1-30 k *g*) was further enriched with these nanorods, as seen in **Figure 5.3(b)**. Their thickness was found to be between 30 and 50 nm (**Figure 5.3(c)**), their length ranges from 0.5 to 1 µm, while their width varies between 100 and 200 nm.

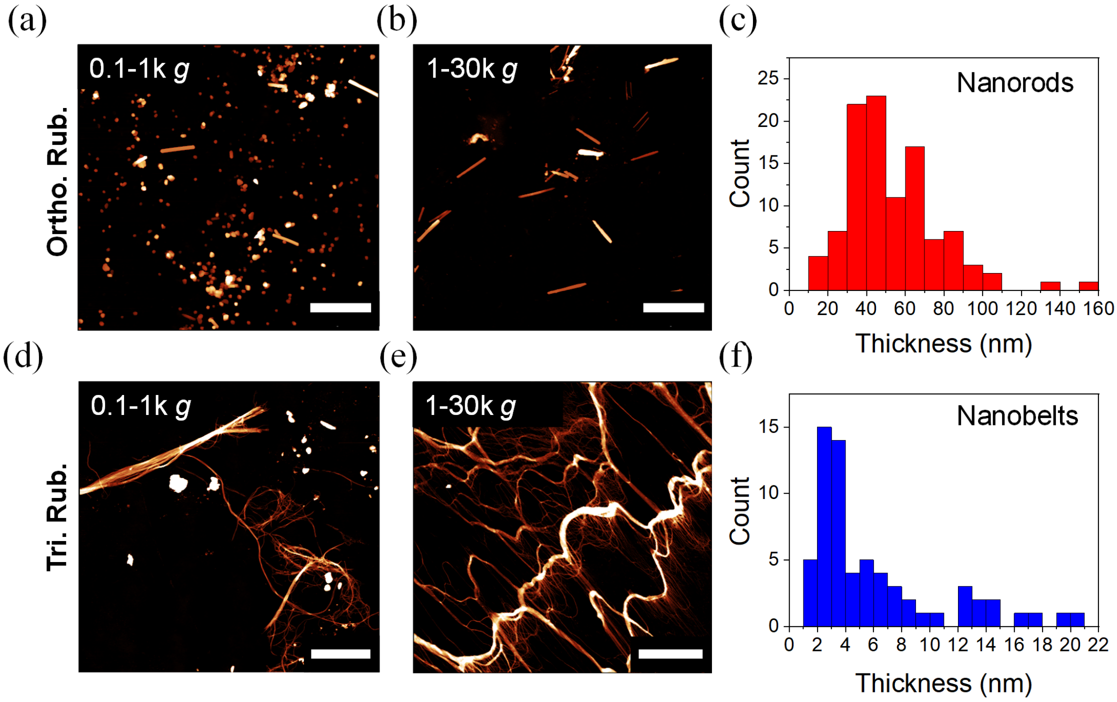

Figure 5.3: AFM height images of the intermediate (0.1-1k *g*) and the highest (1-30k *g*) fractions of exfoliated orthorhombic rubrene (Ortho. Rub.) (a, b) showing nanorods, and triclinic rubrene (Tri. Rub.) (d, e) showing nanobelts/bundles (scale bar: 2 µm). The corresponding thickness histograms are shown in (c, f). Adapted with permission from Ref.[283]. Copyright 2021 American Chemical Society.

In the case of triclinic rubrene dispersions, the size and aspect ratios of the nanostructures were vastly different. **Figure 5.3(d),(e)** show the intermediate and highest fractions of exfoliated triclinic rubrene, respectively, where thin and long belt- and bundle-like structures are observed. A height histogram of single strands of the nanobelts (**Figure 5.3(f)**) reveals that they are only about 3 nm thick. Their length could not be precisely determined due to the overlapping and entangled nature of the belts and belt bundles, but it appears to be several micrometers with widths between 30 and 50 nm.

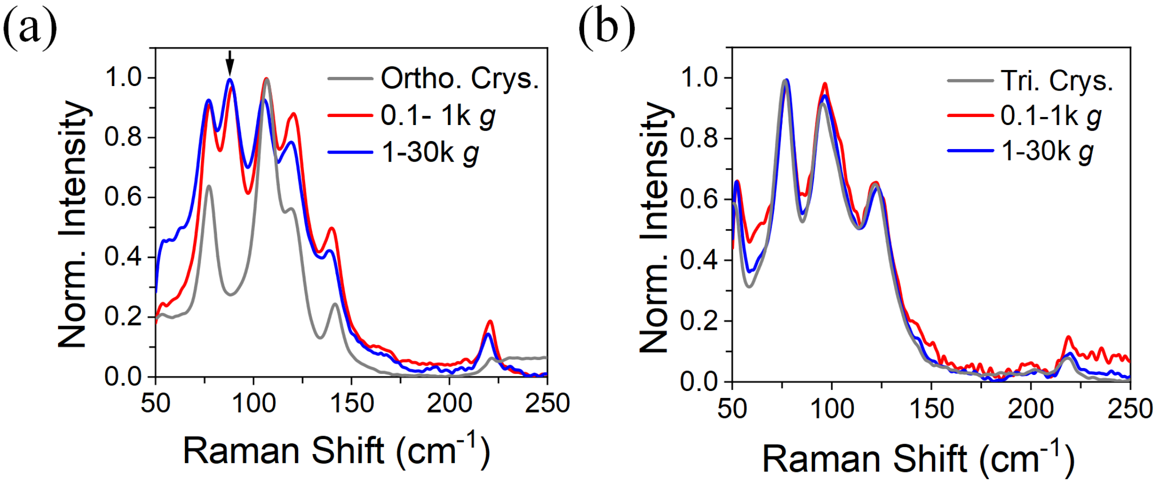

Figure 5.4: Normalized low-wavenumber Raman spectra of the intermediate (0.1-1k *g*) and the highest (1-30k *g*) fractions of (a) orthorhombic and (b) triclinic rubrene dispersions in comparison to the corresponding bulk crystals. The arrow in (a) indicates the peak at 88 cm^{-1} that is present only in the spectra of the two fractions. Adapted with permission from Ref.[283]. Copyright 2021 American Chemical Society.

To determine whether the original crystallinity is retained in the nanorods and nanobelts post exfoliation of orthorhombic and triclinic crystals, respectively, low-wavenumber Raman spectroscopy was performed. Since Raman active lattice phonons of different polymorphs of rubrene are distinct,[89] acquiring the low-wavenumber Raman spectra of the drop-cast dispersions and comparing them with the fingerprint of the parent crystal would enable a fast and reliable identification of their crystallinity. The excited modes of the intermediate and the highest fractions of exfoliated orthorhombic rubrene in comparison to the bulk crystal are shown in **Figure 5.4(a)**. All peaks (see **Table 5.2** for a complete list) except for the one at 88 cm^{-1} correspond well to the Raman modes of the bulk orthorhombic crystal. This suggests that the nanorods are crystalline and the crystal structure of the original crystal is preserved. The additional peak at 88 cm^{-1} (indicated with an arrow in **Figure 5.4(a)**), that is observed only in the 0.1-1k *g* and 1-30k *g* samples, was found to be a result of randomly oriented drop-cast nanorods. Whereas, the spectrum of the bulk crystal was measured strictly from the *ab* facet, lying parallel to the substrate. The mode is seen in the spectrum of a differently oriented bulk orthorhombic crystal as well as in powdered rubrene, as shown in **Figure A.4** of the Appendix. Additionally, the peak at 220 cm^{-1} is more prominent in the spectra of the two fractions compared to the bulk crystal. Since this mode is associated with a surface active mode along the c-axis,[293] it is perhaps stronger in exfoliated rubrene because of the larger surface area.

As for exfoliated triclinic rubrene, the low-wavenumber Raman modes are identical in shape, position, and relative intensity to those of the bulk triclinic crystal, as shown in **Figure 5.4(b)**. This is suggestive of the crystallinity and retention of the triclinic lattice in rubrene nanobelts. Note that the lowest fraction (0-0.1k g) of both exfoliated orthorhombic as well as triclinic crystals were composed primarily of unexfoliated rubrene and are therefore omitted from all discussions.

Table 5.2: Low-wavenumber Raman shifts of LPE rubrene (LPE Ortho. Rub., LPE Tri. Rub.) and the corresponding bulk crystals (Ortho. Crys., Tri. Crys.) at an excitation wavelength of 785 nm. The light was incident and the spectra were collected from the ab facet of both orthorhombic as well as triclinic crystals, with the polarization perpendicular to the long axis of the crystals. Adapted with permission from Ref.[283]. Copyright 2021 American Chemical Society.

	LPE Ortho. Rub.			LPE Tri. Rub.			Ortho. Crys.	Tri. Crys.
	0-0.1 k g	0.1-1 k g	1-30 k g	0-0.1 k g	0.1-1 k g	1-30 k g		
Low-Wavenumber Raman Shifts (cm^{-1})	77	78	77	77	78	77	77	76
	88	89	87	95	97	97		96
	106	107	105	122	123	123	106	122
	119	120	119	220	219	220	120	219
	139	140	139				142	
	219	221	220				221	

5.4 Optical Properties of Nanorod and Nanobelt Dispersions

The optical properties of rubrene nanorods and nanobelts were investigated by performing absorbance and emission spectroscopy on the dispersions. A vast amount of literature exists on the optical properties of rubrene solutions and orthorhombic rubrene crystals. There are, however, discrepancies among the reported absorbance and emission spectra in terms of observed peaks, their positions and relative intensities. Irkhin et al. discussed in detail the origin of these variations which they attribute mainly to differences in the incident polarization of light with respect to the crystal axes and facets, and self-absorption of concentrated solutions of rubrene.[294] On the other hand, very little is known about the triclinic crystals of rubrene. Since the emission spectra of rubrene crystals are strongly dependent on the orientation of facets and the polarization of light, exfoliated rubrene dispersions (composed of randomly oriented nanorods and nanobelts) are only compared to dilute rubrene solutions.

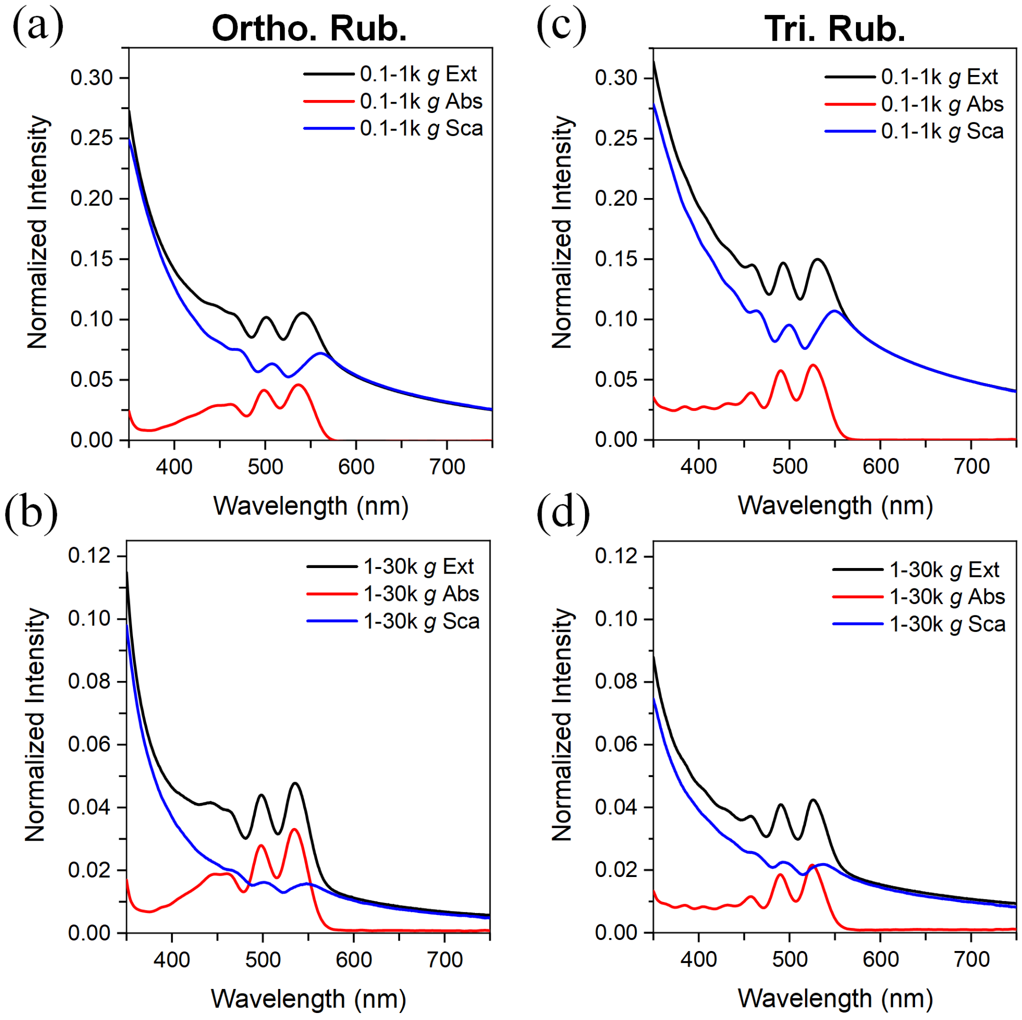

Figure 5.5: Extinction (Ext) and absorbance (Abs) spectra of the (a) intermediate (0.1-1k *g*) and (b) highest (1-30k *g*) fractions of exfoliated orthorhombic rubrene and the same for exfoliated triclinic rubrene in (c) and (d), respectively. Each panel also shows the scattering spectrum (Sca) that was obtained by subtracting the absorbance spectrum from the extinction spectrum. Adapted with permission from Ref.[283]. Copyright 2021 American Chemical Society.

As shown by Irkhin et al. excitation/detection geometry largely influences the absorbance and emission spectra and as such, spectral variations should be carefully interpreted.^{294} Several artefacts were observed in the extinction spectra of exfoliated rubrene dispersions because of the scattering of light, as shown in **Figure 5.5**, due to which their absorbance spectra were recorded using an integrating sphere. It can be seen, especially for the intermediate fraction of both orthorhombic as well as triclinic rubrene (**Figure 5.5(a),(c)**) that the extinction is dominated by scattering. In the non-resonant regime (that is, at wavelengths above the electronic transitions), scattering follows the characteristic power law,[295] whereas in the resonant regime scattering follows absorbance in shape (with a redshift and superimposed on the power law background).

The resulting absorbance of the 0.1-1k *g* and 1-30k *g* fractions of exfoliated orthorhombic rubrene crystal in comparison to a dilute solution of rubrene in chloroform is presented in **Figure 5.6(a)**. All the absorbance peaks of the two fractions appear in the region between 450 and 540 nm, with the usual vibronic progression and nearly indistinguishable spectral features. Only the lowest energy transition of the highest fraction is blueshifted by 2 nm, and its absorbance is slightly lower at shorter wavelengths. **Table 5.3** provides a full list of all the peak positions.

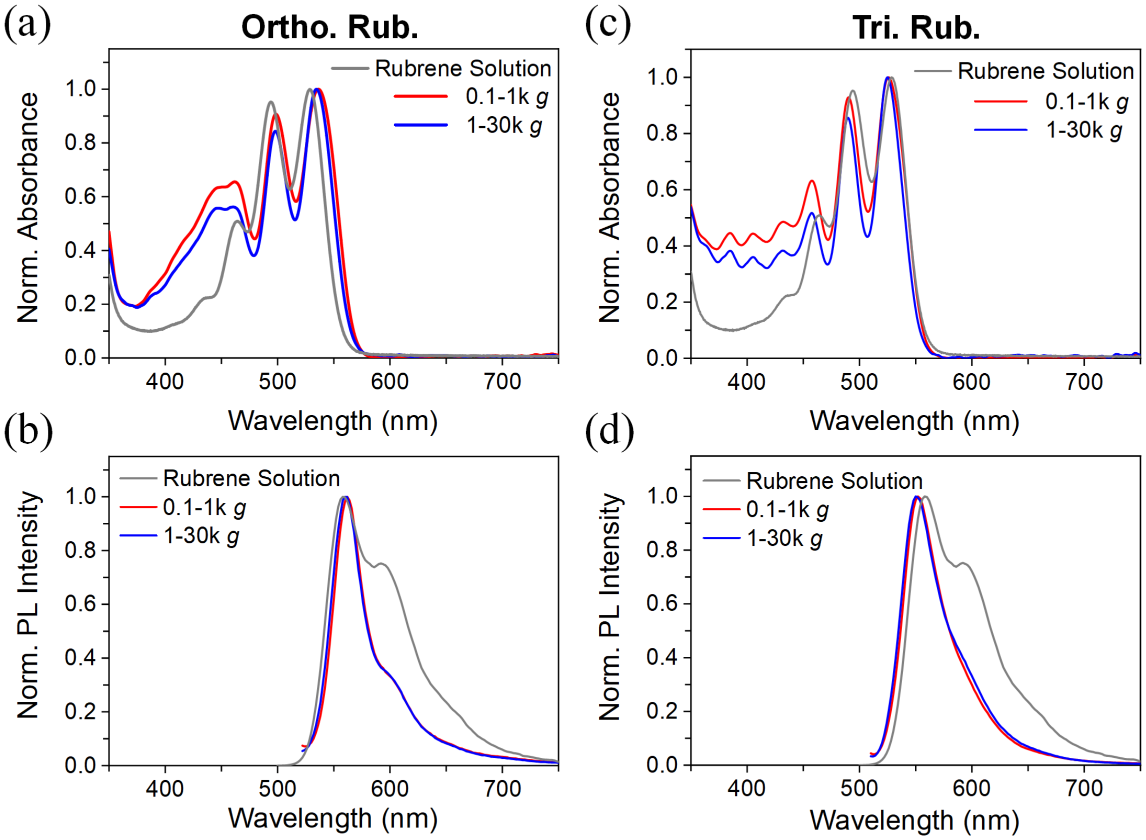

Figure 5.6: Normalized absorbance spectra of the intermediate (0.1-1k *g*) and the highest (1-30k *g*) fractions of exfoliated (a) orthorhombic (ortho.) and (c) triclinic (tri.) rubrene in comparison to that of a dilute solution of rubrene in chloroform. Normalized photoluminescence spectra of the same two fractions of exfoliated (b) orthorhombic and (d) triclinic rubrene. Also shown in the two panels is the normalized photoluminescence spectrum of a dilute solution of rubrene in chloroform. Adapted with permission from Ref.[283]. Copyright 2021 American Chemical Society.

In comparison to the absorbance of rubrene solution, there is a good correspondence in terms of peak shape and relative intensities of the absorption peaks. Clearly, all the optical transitions of both the fractions are redshifted by about 9 nm with respect to the solution, which is an expected offset between solid-state and solution absorption spectra. The broad shoulder that is observed for the two fractions at around 440 nm (2.8 eV) and the higher absorption at shorter wavelengths of the nanorod dispersions compared to the solution might be attributed to the quasi-particle bandgap of crystalline rubrene as proposed by Sai and co-workers.[296]

Figure 5.6(b) shows the photoluminescence (PL) spectra collected from the two fractions (intermediate 0.1-1k *g*, highest 1-30k *g*) of exfoliated orthorhombic rubrene as well as the dilute rubrene solution. The corresponding photoluminescence excitation-emission (PLE) maps and spectra can be found in the Appendix (**Figure A.5**). The emission spectrum of the solution is very sensitive to self-absorption due to the very small Stokes shift of rubrene (see **Figure 5.7(a)**). Hence, the spectrum shown in **Figure 5.6(b)** is that of a very dilute solution whose spectral features remained constant even with further dilution. It shows a very prominent shoulder at 592 nm in comparison to the nanorod dispersions, but the reason is not clear. It could be a result of wavelength-dependent scattering and reabsorption of the emitted light in the dispersions whose Stokes shift is also small, as shown in **Figure 5.7(b)**.

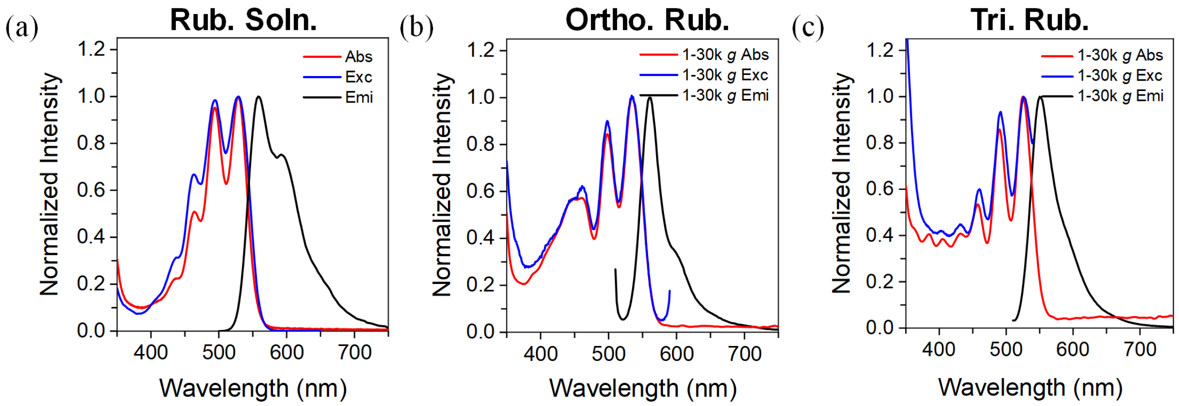

Figure 5.7: Absorbance (Abs), excitation (Exc), and emission (Emi) spectra of (a) a dilute solution of rubrene in chloroform (Rub. Soln.), the highest fraction of exfoliated (b) orthorhombic rubrene (Ortho. Rub.), and (c) triclinic rubrene (Tri. Rub.). Adapted with permission from Ref.[283]. Copyright 2021 American Chemical Society.

The absorbance spectra of the intermediate and the highest fractions of exfoliated triclinic rubrene, shown in **Figure 5.6(c)**, are almost identical except for small changes in peak position (see **Table 5.3**) and slightly lower absorbance of the latter at shorter wavelengths. What is unique is the set of roughly equidistant absorption peaks that are present beyond the vibronic progression of the rubrene solution. This absorption fine structure is also seen in the excitation spectra (see **Figure 5.7(c)**), but its origin is unclear. It is, however, not a consequence of scattering, as established in **Figure 5.5(c),(d)**.

The PL spectra of the 0.1-1k g and the 1-30k g fractions of triclinic rubrene dispersions in comparison to the dilute rubrene solution in chloroform are shown in **Figure 5.6(d)** (see **Figure A.5** of the Appendix for PLE maps). The emission peak of the triclinic rubrene dispersions are blueshifted with respect to the solution (see **Table 5.3**), and the shoulder at 592 nm less pronounced, similar to the previous case. Slight variations in the spectral characteristics may be because of reabsorption and/or scattering effects and not from any particular size-dependent change.

Table 5.3: Absorbance and photoluminescence peak positions of LPE rubrene (LPE Ortho. Rub., LPE Tri. Rub.) and solution of rubrene in chloroform. Adapted with permission from Ref.[283]. Copyright 2021 American Chemical Society.

	LPE Ortho. Rub.			LPE Tri. Rub.			Rubrene Solution
	0-0.1 k g	0.1-1 k g	1-30 k g	0-0.1 k g	0.1-1 k g	1-30 k g	
Absorbance Wavelengths (nm)				385	385	385	
				406	405	405	
	442	446	447	433	432	432	434
	463	462	460	458	458	458	464
	498	498	498	490	490	490	494
	537	537	535	526	526	525	528
PL Position (nm)	566	562	560	554	552	550	558
	604	604	604				592
	λ_{exc} = 500 nm			λ_{exc} = 495 nm			λ_{exc} = 495 nm

The time-resolved PL decay of the same two fractions of exfoliated orthorhombic as well as triclinic rubrene, of the bulk crystals, and of dilute rubrene solution were measured and fitted with either three lifetime components (in the case of dispersions) or a single component (for crystals and solution), as shown in **Figure 5.8**. All the lifetime components of the dispersions are less than half of the PL lifetime of rubrene solution (see **Table 5.4**), but are more comparable to the lifetime of their corresponding parent crystal. The short lifetime component of both exfoliated orthorhombic as well as triclinic rubrene dispersions shows little to no variation across the different fractions. Whereas, the long lifetime component increases from the lowest to the highest fraction in the case of exfoliated orthorhombic rubrene dispersions, but does not follow any trend across the exfoliated triclinic rubrene fractions. It has been suggested that the self-quenching phenomenon observed in solid-state aggregates of red-emissive materials gives rise to the short lifetime component.[106] This may be the case for rubrene nanorods and nanobelts as well but with no specific size-dependent variation.

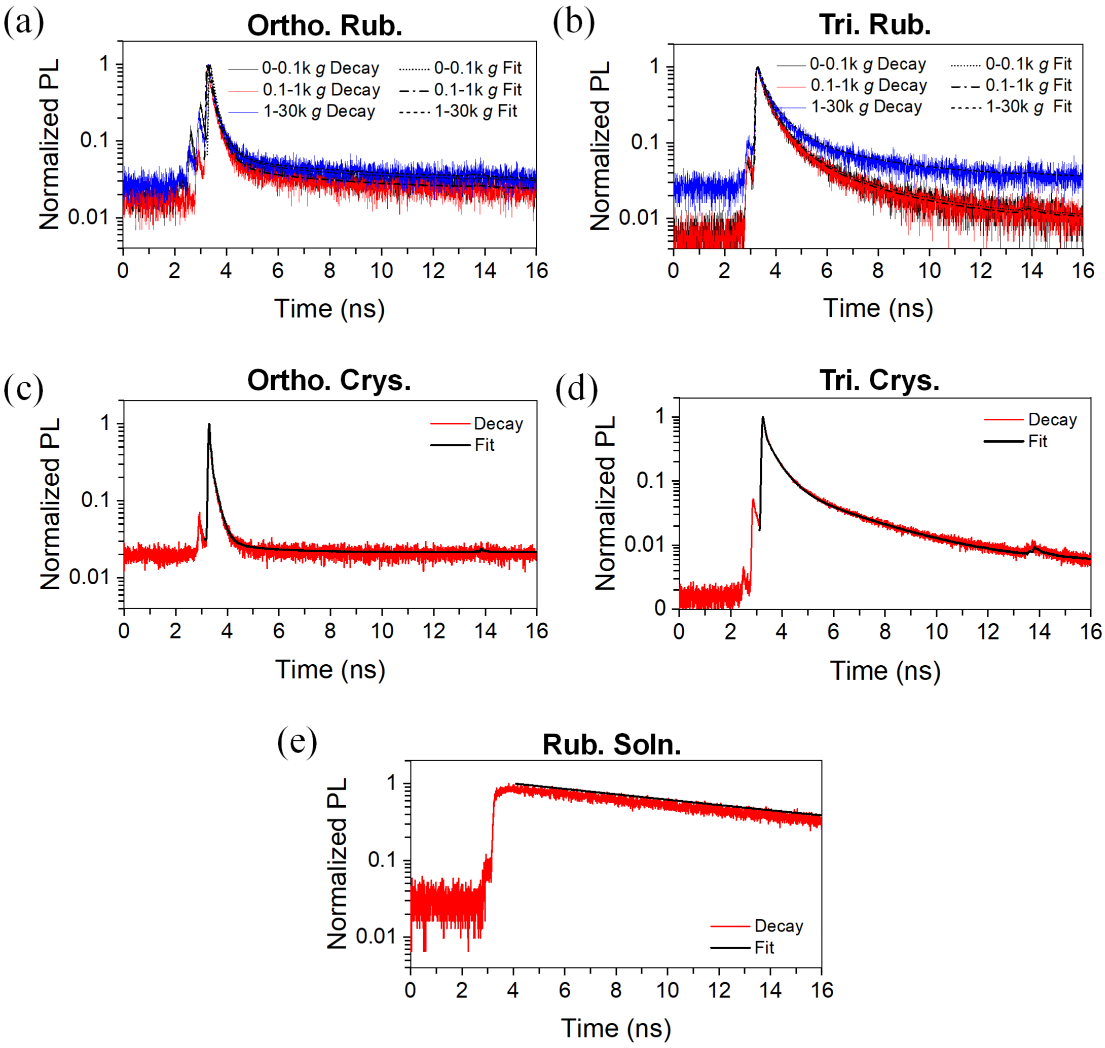

Figure 5.8: Time-resolved photoluminescence decay traces and the single or multiexponential fits of the main emission peak of (a) the three different fractions of exfoliated orthorhombic rubrene, (b) the three different fractions of exfoliated triclinic rubrene, (c) macroscopic orthorhombic crystal, (d) macroscopic triclinic crystal, and (e) dilute solution of rubrene in chloroform. The excitation wavelength for all samples was 493 nm. Adapted with permission from Ref.[283]. Copyright 2021 American Chemical Society.

Table 5.4: Photoluminescence lifetime of the three different fractions of LPE rubrene dispersions, bulk orthorhombic and triclinic crystals, and a dilute solution of rubrene in chloroform. Adapted with permission from Ref.[283]. Copyright 2021 American Chemical Society.

Lifetime (ns) $\lambda_{exc} = 493$ nm	LPE Ortho. Rub.			LPE Tri. Rub.			Ortho. Crys.	Tri. Crys.	Rub. Soln.
	0-0.1 k g	0.1-1 k g	1-30 k g	0-0.1 k g	0.1-1 k g	1-30 k g			
τ_1	0.08	0.08	0.05	0.11	0.11	0.13	0.01	0.03	$\tau = 12$
τ_2	0.56	0.44	0.52	0.70	0.68	0.72	0.19	0.50	
τ_3	3.90	4.10	5.70	3.10	2.80	3.40	1.70	2.80	

5.5 Cleavage Planes of Nanorods and Nanobelts

To get an insight into the possible planes of orthorhombic and triclinic rubrene crystals along which cleavage occurs that results in nanorods and nanobelts, transmission electron microscopy (TEM) and selected-area electron diffraction were employed. Data acquired from these techniques was also used to infer the direction of π-π stacking and orientation of rubrene molecules within the nanostructures. Low electron doses were applied in order to avoid extensive electron irradiation damage of the specimens. A bright-field TEM image of rubrene nanorod exfoliated from the orthorhombic single crystal is shown in **Figure 5.9(a)** with a red circle marking the area of acquisition of the corresponding SAED pattern shown in **Figure 5.9(b)**.

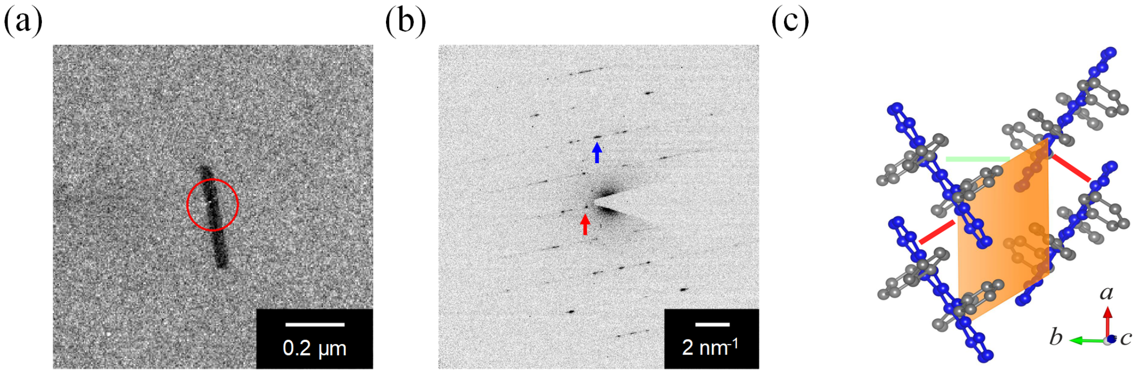

Figure 5.9: (a) Bright-field TEM image of a nanorod with the red circle marking the position of the selected-area aperture. (b) The SAED pattern obtained from (a) with a total electron dose of 3e^{-}/Å^{2}. The red and blue arrows in (b) indicate the 020 reflection at 1.4 nm^{-1} and $\bar{2}06$ reflection at 3.7 nm^{-1}, respectively. (c) The primary cleavage planes with respect to the molecular packing are shown in orange. The red and the green bars represent strong π-π interactions between adjacent molecules and weaker intermolecular interactions, respectively. Images provided by Dr. Haoyuan Qi. Adapted with permission from Ref.[283]. Copyright 2021 American Chemical Society.

The sharp reflections observed in the SAED pattern indicate that crystallinity is preserved in the nanorod after exfoliation. The closest diffraction spots along the high symmetry axes were found to be at 1.4 nm^{-1} and 3.7 nm^{-1}, where the red and blue arrows point, respectively. With the help of a simulated SAED pattern (see **Figure 5.10(b)**) where the closest reflections were found at 1.4 nm^{-1} and 3.6 nm^{-1}, respectively, it was determined that the b-axis is perpendicular to the long axis of the nanorod. From this, it can be deduced that the cleavage occurred mainly parallel to the ac-plane, i.e., (020) plane (see **Figure 5.10(d),(e)**). This is further substantiated by considering the anisotropic intermolecular interactions within the orthorhombic rubrene crystal lattice (see **Figure 5.9(c)**). The strongest interactions are along the π-stacking direction which is along the a-axis.

However, because of the herringbone packing motif, the interactions along the *b*-axis are weaker. Hence, exfoliation parallel to the *ac*-plane is facilitated. If this were the only plane along which exfoliation occurred, nanodisks or nano-platelets would be produced. Since this is not the case, further delamination parallel to the *ab*-plane is expected (i.e., the (002) plane), as the intermolecular interactions along the *c*-axis are also weak, as shown in **Figure 5.10(f)**.

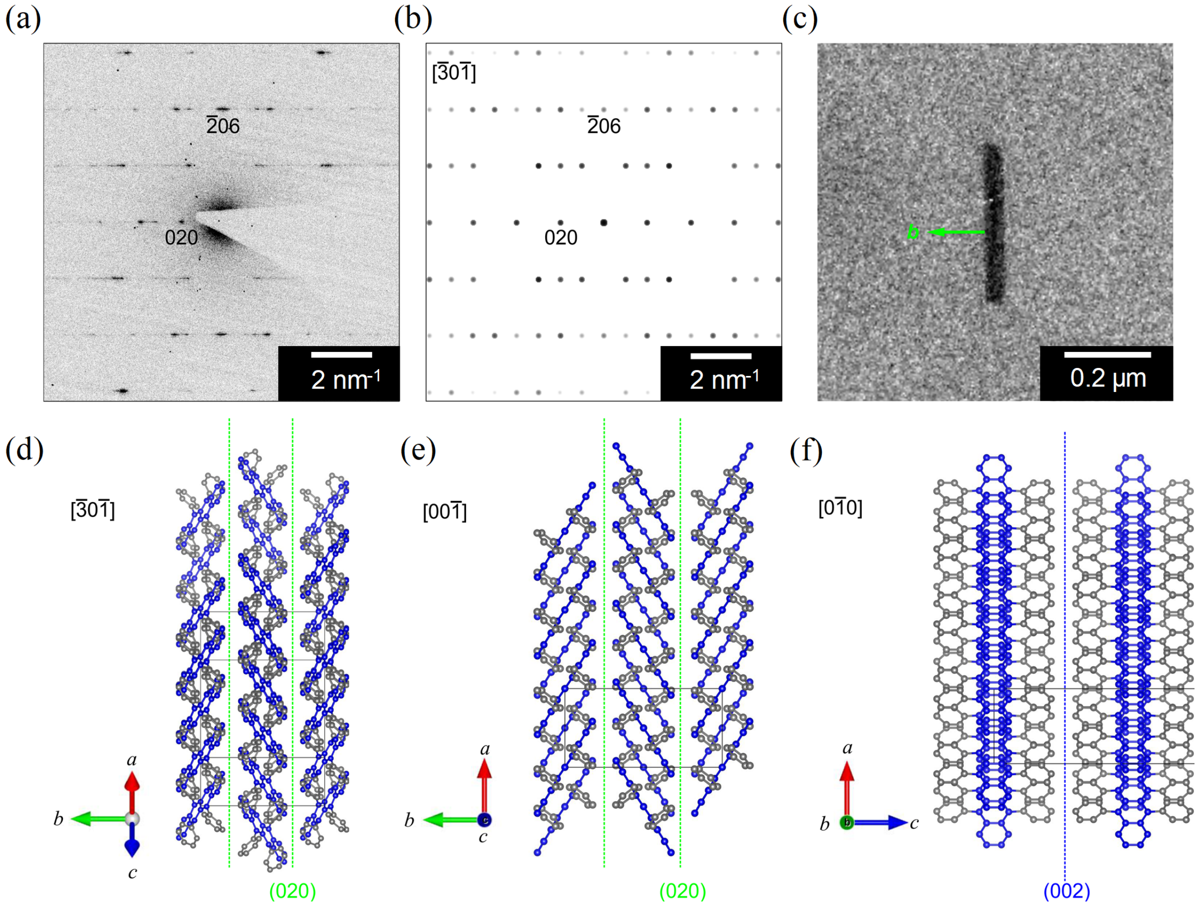

Figure 5.10: (a) Experimental SAED pattern of rubrene nanorod. (b) Simulated SAED pattern of orthorhombic rubrene single crystal along the [$\bar{3}0\bar{1}$] zone axis. (c) Bright-field TEM image of a nanorod from which the SAED pattern in (a) was acquired, indicating (with a green arrow) that the short axis of the nanorod is parallel to the [020] direction, i.e., the *b*-axis ([010] vector). (d) Molecular packing of rubrene in the orthorhombic lattice as viewed in [$\bar{3}0\bar{1}$] projection. The (020) plane (green dashed line) is parallel to the long axis of the nanorod in (c), suggesting that the delamination occurred primarily at the *ac*-plane. (e) Molecular packing of orthorhombic rubrene as viewed in [$00\bar{1}$] projection, showing the herringbone motif with π-stacking along the *a*-axis and weak intermolecular interactions across the *ac*-plane. (f) Molecular packing in orthorhombic rubrene polymorph when viewed in [$0\bar{1}0$] projection, showing weak intermolecular interactions across the *ab*-plane. Therefore, the (002) plane (i.e., the *ab*-plane) denoted by blue dashed line is a plausible second delamination plane. Images provided by Dr. Haoyuan Qi. Adapted with permission from Ref.[283]. Copyright 2021 American Chemical Society.

Important to note is the streaking of the diffraction spots in the experimental SAED pattern of the nanorod (**Figure 5.9(b)**), which could either be an artefact stemming from the limited lateral size of the nanorod or an indication of slight shifts between the molecular layers resulting from the shear force during LPE.

The SAED pattern obtained from a small area of a nanobelt bundle (**Figure 5.11(a)**) that was exfoliated from triclinic rubrene crystals is shown in **Figure 5.11(b)**. Crystallinity of the nanobelts is confirmed by the presence of a diffraction ring, and the lattice spacing of 4 Å can be associated with the intermolecular π-stacking distance in the triclinic rubrene crystals. In contrast to the rigid morphology of the nanorods, the nanobelts appear to be very flexible leading to intertwining and entanglement (see **Figure 5.3**). This further leads to a non-uniform change in the crystal orientation within the selected area due to which a polycrystalline diffraction ring was observed instead of distinct reflections. As a result, correlating the π-stacking direction to the geometry of the nanobelt remains challenging. However, since it is assumed that the nanobelts "peeled-off" from bulk triclinic crystals during LPE, identifying the π-stacking axis and molecular orientation within the pristine crystal may help in determining the same for the nanobelts, in addition to the cleavage planes.

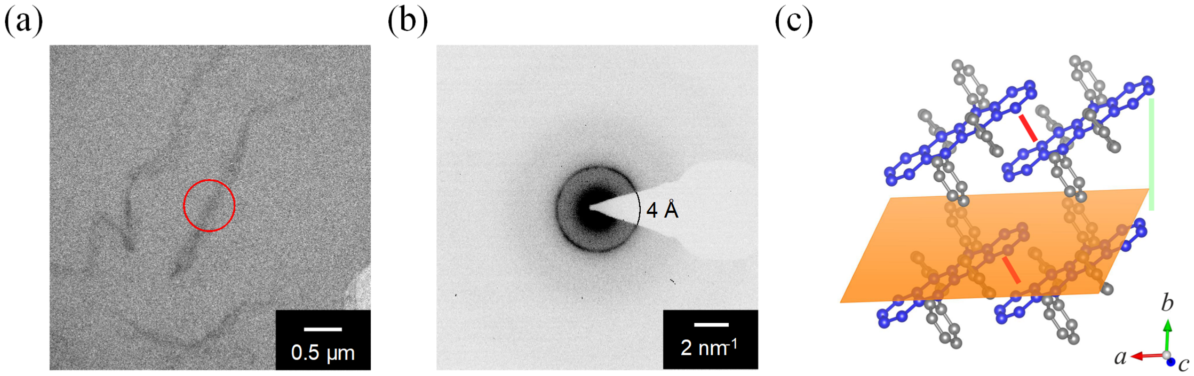

Figure 5.11: (a) Bright-field TEM image of a nanobelt-bundle with the red circle marking the position of the selected-area aperture. (b) The SAED pattern obtained from (a) with a total electron dose of 3e$^-$/Å^2. The diffraction ring in (b) is at 2.5 nm^{-1} or 4 Å. (c) The primary cleavage planes with respect to the molecular packing are shown in orange. The red and the green bars represent strong π-π interactions between adjacent molecules and weaker intermolecular interactions, respectively. Images provided by Dr. Haoyuan Qi. Adapted with permission from Ref.[283]. Copyright 2021 American Chemical Society.

The lattice structure of triclinic rubrene crystals was investigated using continuous rotation electron diffraction (cRED). The reconstructed 3D diffraction pattern is shown in **Figure 5.12(a)**. The unit cell parameters determined using cRED were a = 7.04 Å, b = 8.57 Å, c = 12.21 Å, α = 93.9°, β = 105.8°, γ = 95.4°, which are in excellent agreement with the values reported in literature (a = 7.02 Å, b = 8.54 Å, c = 11.95 Å, α = 93.04°, β = 105.58°, γ = 96.28°).[106] Upon correlation of the reconstructed real-space unit cell with the triclinic rubrene crystal morphology, it was found that the *a*-axis was parallel to the long axis of the needle-shaped crystals (see **Figure 5.12(c)**).

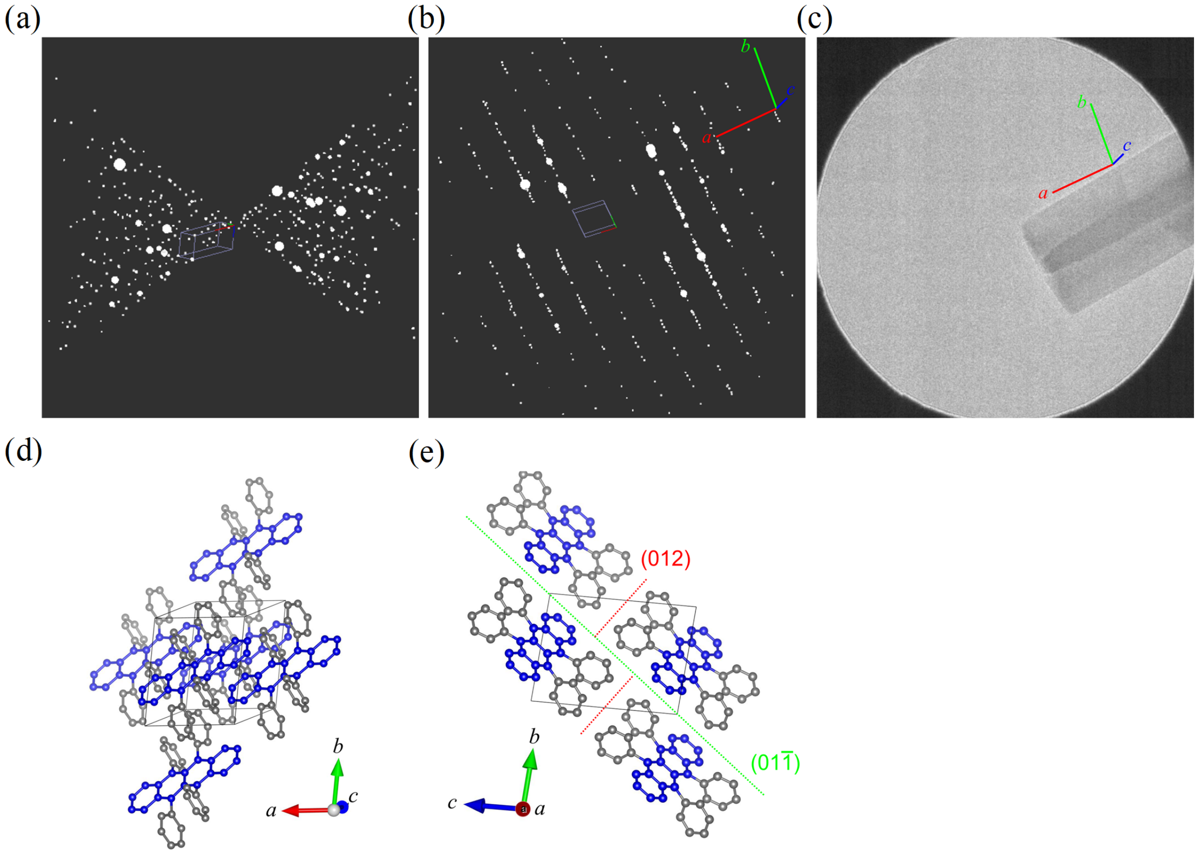

Figure 5.12: (a) Reconstructed 3D electron diffraction pattern of the triclinic unit cell via cRED. The solid red, green, and blue lines represent the reciprocal lattice vectors a^*, b^*, and c^*, respectively. (b) Projection of (a) at a tilt angle of 0°, with the reciprocal unit cell shown in the center and the real lattice vectors in the upper right corner. (c) Bright-field TEM image of a triclinic rubrene crystal at a tilt angle of 0° with the real lattice vectors overlaid. (d) Molecular packing of rubrene in the triclinic lattice with the *a*-axis aligned horizontally. (e) The probable cleavage planes — (00$\bar{1}$) and (012), indicated with dashed green and red lines, respectively, where intermolecular interactions are weak. Images provided by Dr. Haoyuan Qi. Adapted with permission from Ref.[283]. Copyright 2021 American Chemical Society.

Strong intermolecular interactions exist along the *a*-axis since it is the π-stacking direction, as shown in **Figure 5.11(c)**, but are considerably reduced in the direction perpendicular to the *a*-axis. The "peeling off" of the nanobelts is, therefore, supposed to have occurred parallel to the *a*-axis, or in other words, parallel to the (01$\bar{1}$) plane. Following the same line of argument as before for the nanorods, there should be another delamination plane for nanobelts which was found to be the (012) plane. The intermolecular interactions in the direction perpendicular to this plane is also substantially less, as seen in **Figure 5.12(e)**.

5.6 Vibrational Modes of Nanorods and Nanobelts

In **Chapter 4**, nanospectroscopy data of orthorhombic rubrene single crystal was presented. Here, the IR-SNOM is used to investigate the vibrational modes of rubrene nanorods and nanobelts in order to determine the orientation of the molecules. The phase spectrum acquired using the IR-SNOM is compared to the unpolarized FT-IR absorbance spectra of orthorhombic and triclinic crystals.

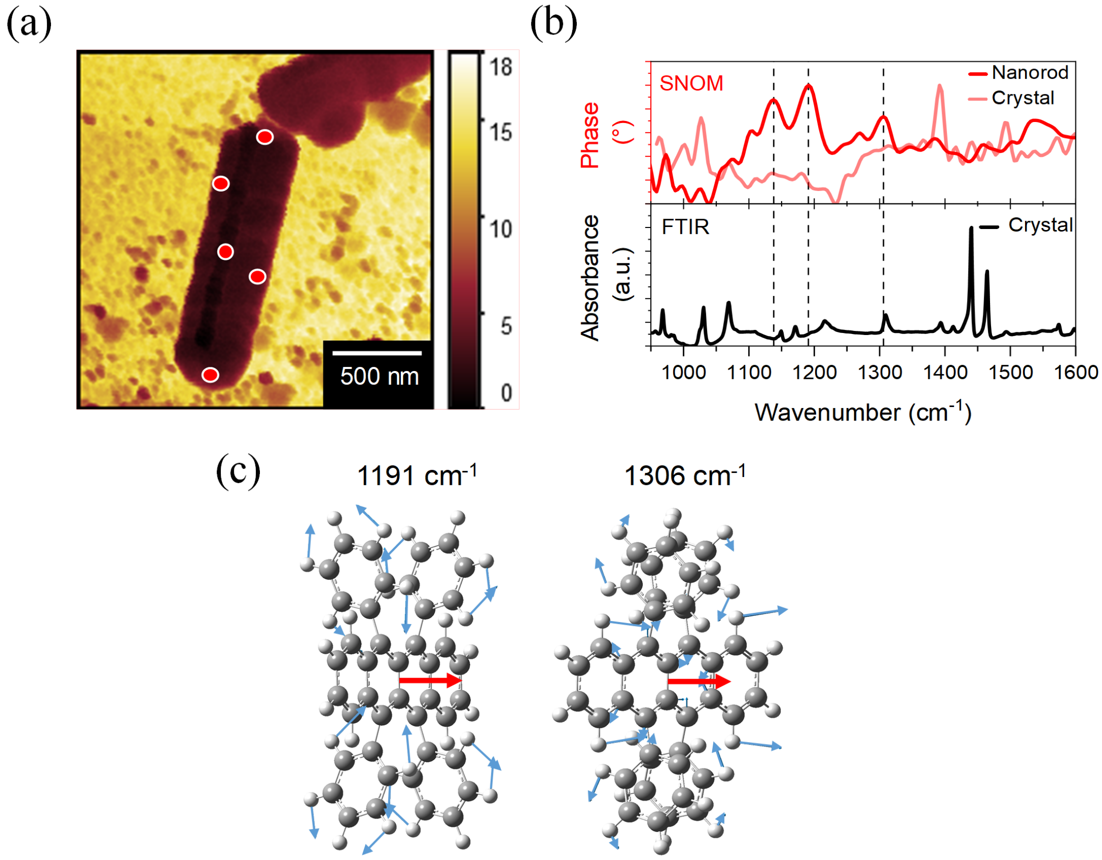

Figure 5.13: (a) White light amplitude image of a rubrene nanorod acquired with an IR-SNOM. (b) Average of IR-SNOM phase spectra collected from points marked in (a). The IR-SNOM phase spectra and the far-field absorbance spectra of the macroscopic orthorhombic rubrene single crystal are also shown. (c) Visualisation of the vibrational modes corresponding to selected absorption peaks of rubrene nanorods. The dipole derivative unit vector is shown with a red arrow (lying in the plane of the paper) and the displacement vectors are in blue. Adapted with permission from Ref.[283]. Copyright 2021 American Chemical Society.

The near-field amplitude image of a single rubrene nanorod is shown in **Figure 5.13(a)**, where the red spots indicate the points from where the phase spectra were measured. The average of all the phase spectra is overlaid on the phase spectrum of orthorhombic rubrene crystal and compared to the far-field unpolarized FT-IR spectrum of the crystal in **Figure 5.13(b)**. The dashed lines mark three weak modes at 1149, 1171, and 1309 cm^{-1} that are observed in the far-field absorbance spectrum of the crystal (black trace) which appear as strongly excited modes at 1138, 1191, and 1306 cm^{-1}, respectively, in the phase spectrum of the nanorods (dark red trace). Interestingly, these modes differ from the strong modes observed in the near-field phase spectrum of the single crystal that appear at 1027, 1392, and 1492 cm^{-1} (light red trace). From the discussion in **Chapter 4**, it is clear that for an IR mode to appear enhanced in the IR-SNOM, a component of its transition dipole moment vector must be aligned with the incident electric field which is oriented parallel to the axis of the tip and perpendicular to the substrate.[147] Taking this into consideration, if the arrangement of the rubrene molecules in the nanorods is the same as in the orthorhombic crystal, then the three aforementioned peaks (at 1138, 1191, and 1306 cm^{-1}) are not expected to be seen because their transition dipole moments lie parallel to the substrate (see **Figure 5.13(c)**). However, these modes are present which suggests that the rubrene nanorod either has a facet different from the *ab* facet parallel to the substrate or there are disordered rubrene molecules at the edges and/or surface of the nanorod. Note that the IR-SNOM signals are highly sensitive to substrate effects,[203] which might have caused the variations reported here.

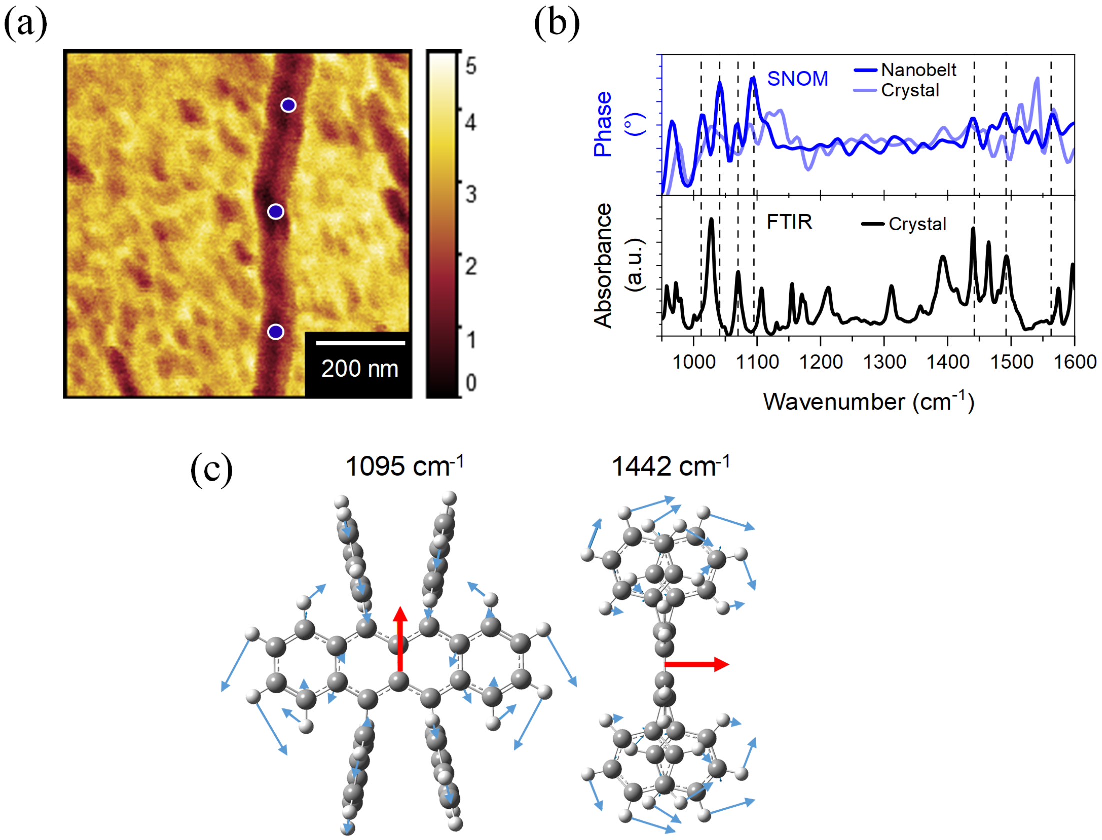

Figure 5.14: (a) White light amplitude image of a rubrene nanobelt acquired with an IR-SNOM. (b) Average of IR-SNOM phase spectra collected from points marked in (a). The IR-SNOM phase spectra and the far-field absorbance spectra of the macroscopic triclinic rubrene single crystal are also shown. (c) Visualisation of the vibrational modes corresponding to selected absorption peaks of rubrene nanobelts. The dipole derivative unit vector is indicated with a red arrow (lying in the plane of the paper) and the displacement vectors are shown in blue. Adapted with permission from Ref.[283]. Copyright 2021 American Chemical Society.

Figure 5.14(a) shows the near-field amplitude image of an individual rubrene nanobelt. The average of the phase spectra recorded from three different points corresponds well to the classical FT-IR absorbance spectrum of the triclinic crystal (see **Figure 5.14(b)**), dashed lines indicate modes that appear in both the spectra), but shows little resemblance to the phase spectrum of the single crystal. The calculated vibrational modes and the corresponding transition dipole moment vectors of peaks at 1095 and 1442 cm^{-1} are shown in **Figure 5.14(c)**. Since the molecules of rubrene are slightly tilted in the triclinic lattice (see **Figure 5.1**), both the modes are expected to be seen in the phase signal of the nanobelt because a component of their transition dipole moment aligns parallel to the incident electric field. As mentioned before, changes in the orientation of the molecules, disorder within the nanobelt or substrate effects may have had an effect on the differences observed between the phase spectra of the nanobelt and the crystal.

5.7 Molecular Orientation in Nanorods and Nanobelts

Based on the experimental data presented in the previous sections, the structural make-up of the nanorods and nanobelts can be inferred. **Figure 5.15** shows an illustration of the proposed molecular packing. From **Figure 5.3(c)**, sodium cholate-stabilized nanorods were found to be about 40 nm thick. Considering the fact that the interlayer distance in the orthorhombic rubrene lattice is around 1.3 nm (see **Figure 5.1**), multiple layers of rubrene molecules are expected in the nanorod as shown in the side-view. With the most probable cleavage planes being the (020) and the (002) planes, the nanorods are expected to cleave from the bulk crystal parallel to these planes.

Furthermore, the long axis of the nanorod is expected to be parallel to a-axis of orthorhombic rubrene since the strongest π-π interactions between rubrene molecules exist in this direction. The IR-SNOM data suggests that there might be layers of rubrene molecules with random orientations resulting from the applied shear forces and interaction with cholate molecules at the edges of the nanorods. This is portrayed in the top-view illustration in **Figure 5.15**.

In rubrene nanobelts, the combined thickness of the adsorbed cholate molecules on the top and bottom faces and the nanobelt itself is only about 3 nm (see **Figure 5.3(f)**). Given that the out-of-plane length of sodium cholate molecule is 0.5 nm, the actual thickness of the nanobelt alone is around 2 nm. Triclinic rubrene's interlayer distance is also roughly 1.1 nm (**Figure 5.1**), from which it can be inferred that the nanobelts represent bilayers, as shown in the side-view of triclinic rubrene in **Figure 5.15**. As discussed in **Section 5.5**, the rubrene molecules are stacked via π-π interactions along the a-axis which coincides with the long axis of the nanobelts. As in the case of orthorhombic rubrene, a layer of disordered molecules can be expected along the edges as illustrated in the top-view representation of the nanobelt. Note that in order to improve the clarity of **Figure 5.15** the surfactant molecules are omitted in the top-view illustrations, while in actuality the entire surface of both the nanostructures are coated with the surfactant molecules for stabilization.

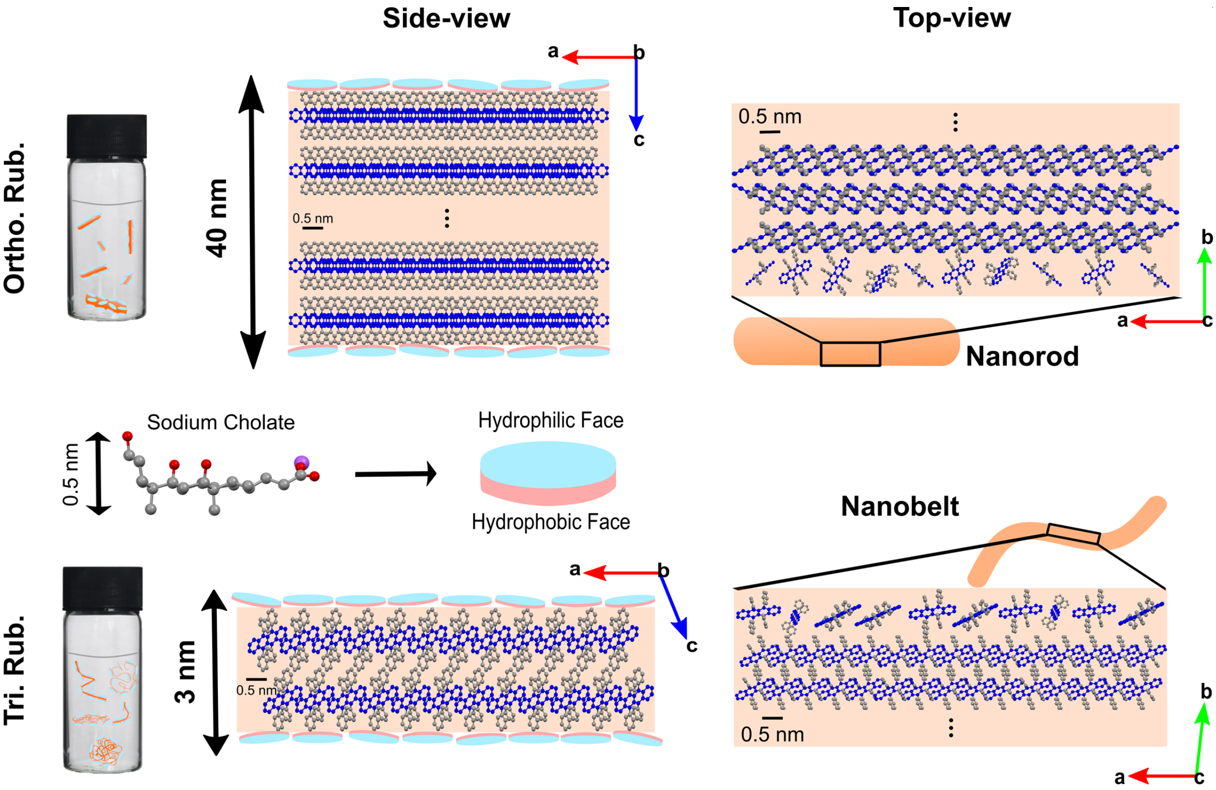

Figure 5.15: Schematic illustration of rubrene nanorods and nanobelts stabilized with sodium cholate and the proposed molecular packing. The side-view of a nanorod (from exfoliated orthorhombic rubrene, Ortho. Rub.) shows multiple stacked layers of rubrene molecules and a nanobelt (from exfoliated triclinic rubrene, Tri. Rub.) shows a rubrene bilayer. The strongest π-π interactions are indicated to be parallel to the crystallographic a-axis or the long-axis of the 1D structures. In the top-view of both the nanostructures, the supposed disordered edge regions are visualised. The surfactant molecules are omitted here for clarity. Scale bars are only approximations. Adapted with permission from Ref.[283]. Copyright 2021 American Chemical Society.

5.8 Conclusion

This study demonstrated for the first time liquid-phase exfoliation of single crystals of a small-molecule organic crystals. The orthorhombic and the triclinic polymorphs of rubrene yielded distinct nanostructures — nanorods and nanobelts, respectively, upon exfoliation via bath sonication. The nanorods and nanobelts could be isolated via liquid cascade centrifugation and stabilized against re-aggregation in aqueous sodium cholate solution.

Lattice phonon Raman spectroscopy suggested that the crystallinity of nano-rubrene was preserved post-exfoliation and the crystal lattice was the same as the corresponding parent crystal. The absorption and photoluminescence spectra of the dispersions resembled that of free rubrene molecules in solution except for the shorter PL lifetimes and additional absorption peaks at lower wavelengths which may have resulted from their crystalline nature. With the help of electron diffraction experiments, the crystallinity of the nanorods and the nanobelts was confirmed. Additionally, the most probable cleavage planes were determined and the direction of π-π stacking could be correlated to the long-axis of both nanorods and nanobelts. The IR-SNOM data further helped establish the molecular packing within the rubrene nanostructures.

The results of this study clearly indicate that even non-covalently bound molecular crystals with strong π-π interactions can be mechanically exfoliated via LPE. It therefore serves as a basis to exfoliate several other small-molecule organic semiconductors, such as pentacene,[287] benzothienobenzothiophene (BTBT),[297] and dinaphthothienothiophene (DNTT)[298] that are known to form layered crystals and thus explore their size-dependent properties. As for further studies on rubrene nanostructures, given that they are crystalline and possess a well-defined π-stacking axis, it would be very interesting to investigate their charge transport behaviour with conductive AFM or by incorporation in short channel transistors.

Chapter 6

Conclusions and Outlook

Prior to this work, studies on a range of materials — polymers, composites, proteins, cells and tissues, had benefited from the use of the AFM-IR. And the alternative method of IR-SNOM which had been tested on inorganic monolayers, polymeric and biological materials had also proved to be useful. Surprisingly, there had been no studies on small organic molecules with the AFM-IR and very few with the IR-SNOM which raised the question of whether the two techniques were applicable to this important class of materials. Moreover, without a comprehensive study examining both the techniques on the same material system, it was hard to determine the advantages and disadvantages of each. It had been well-established that organic crystals exhibit high anisotropy in molecular interactions with strong non-covalent π-π interactions within one crystal plane and much weaker forces acting between different planes. Several small-molecule organic semiconductors were even known to form crystals with distinct layered structures. It was, however, not clear whether the offset between in-plane and out-of-plane interactions was large enough to facilitate the creation of nanostructures by applying mechanical force via, for example, the top-down method of LPE.

A range of small-molecule organic semiconductors were investigated with the AFM-IR and the IR-SNOM. The vibrational modes of single crystals of TIPS-PEN, TIPS-TAP, rubrene and PDIF-CN_2 were examined with the two advanced techniques and compared with the standard FT-IR. A polycrystalline film of PDIF-CN_2 was used to explore the spatial resolution of the AFM-IR and the IR-SNOM as well as the possible information gain through their nanospectroscopy and nanoimaging modes.

Molecular packing and orientation were found to have a strong influence on the excitation of specific modes in the four organic single crystals with the three different techniques. In addition, the direction and polarization of the incident light also played a role in the visibility of certain modes. The oblique incidence of vertically polarized light in the AFM-IR excited modes with both in-plane and out-of-plane components of the transition dipole moment vector, whereas, the IR-SNOM excited only those modes with a component perpendicular to the substrate. This provides information about packing and orientation of molecules, although indirectly. The AFM-IR spectrum of rubrene was found to have an exceptionally good signal-to-noise ratio which was attributed to the presence of distinct molecular layers in the orthorhombic lattice with no interlocking groups between layers that would hinder the thermal expansion perpendicular to the substrate. To have good signals with the IR-SNOM, it is not the thermal expansion that is important but how well the material system can scatter the incident light. For this, the polarizability of the molecule is crucial — higher the polarizability, the better scatterer it is. The structure of PDIF-CN_2 molecule and its orientation in the single crystal are such that it is highly polarizable which would explain its excellent IR-SNOM signal. Overall, the quality of the signals from both the AFM-IR and the IR-SNOM depend strongly on the intrinsic molecular structure and packing of the material system under investigation. Perhaps molecules that arrange themselves into well-separated layers and have high coefficients of thermal expansion in the direction perpendicular to the substrate are more compatible with the AFM-IR. And those that are more polarizable and have their π-conjugated core aligned perpendicular to the substrate and parallel to the direction of electric field enhancement are likely more fitting for investigation with the IR-SNOM.

With the nanospectroscopy and the nanoimaging modes of both AFM-IR and IR-SNOM, local variations in a discontinuous film of PDIF-CN_2 were examined. What could be a variation in the tensile strain between different positions was seen through redshifts in certain vibrational modes and change of relative intensities indicative of differences in molecular orientation were observed in the AFM-IR spectra. These differences were further corroborated by changes in the amplitude between the two regions in the chemical map of the crystallites. Additionally, some non-uniformities in contrast was observed which could be due to various factors, such as differences in thermal expansion or thermal conductance, changes in molecular orientation or simply variations in the thickness. Similar observations were made in the IR-SNOM spectra. The chemical maps, however, were not straightforward to interpret since the amplitude and phase signals are indirectly related to the local complex refractive index. Nevertheless, variations in contrast are indicative of differences in near-field resonances which could have resulted from changes in molecular orientation. Both the techniques enable spectral distinction of local variations, and mapping at specific wavenumbers show clear contrast with good spatial resolution but is difficult to interpret. And the differences between the maps acquired with the AFM-IR and the IR-SNOM can primarily be attributed to the contact mode versus the tapping mode of operation.

In general, both AFM-IR and IR-SNOM were successfully used to study the vibrational modes of small-molecule organic semiconductors. The AFM-IR could provide access to both in-plane as well as out-of-plane modes with excellent spectral resolution and quality.

Polarization dependent spectra could also be acquired. The ease of use and interpretation of data make the AFM-IR a favourable tool to characterize novel organic materials. The IR-SNOM on the other hand, is also suitable to investigate organic materials but is limited by the out-of-plane oscillator strength of the molecules. Interpretation of the spectra is more complicated since the amplitude and phase signals result from complex tip-sample interactions. System specific modelling may be necessary to extract complete information. Chemical maps in both cases are easy to obtain and have high spatial resolution, but the actual cause of differences in contrast is hard to determine since various factors, as mentioned above, may be at play. To decouple them is difficult, which necessitates the use of some complementary techniques.

Going forward, it is first of all important to test the hypothesis on certain organic small-molecules being more compatible with the AFM-IR and some others with the IR-SNOM. Are molecules that arrange themselves into distinct layers in the solid state and have larger coefficients of thermal expansion perpendicular to the substrate more suitable for investigation with the AFM-IR? And, are molecules with higher out-of-plane oscillator strength with their π-conjugated core aligned in the direction of the electric field enhancement better suited for IR-SNOM studies? Molecules such as porphyrin and hexabenzocoronene which adopt 1D herringbone stacking and halogenated TAPPs whose π-conjugated core orients itself either parallel or nearly perpendicular to the substrate based on the deposition method would help answer these questions. The next step would be to examine the structure of films of small organic molecules within a transistor channel using the AFM-IR or the IR-SNOM, and correlate the variations in position-dependent spectra and contrast to the device performance.

In the second part of this work, successful exfoliation of non-covalently bound molecular crystal via LPE was demonstrated for the first time. Exfoliation via bath sonication of orthorhombic and triclinic rubrene crystals, executed separately, yielded nanorods and nanobelts, respectively. They were isolated via LCC and stabilized in aqueous sodium cholate solution. The question of whether crystallinity was preserved in these nanostructures was tackled using different techniques. First, with low-wavenumber Raman spectroscopy the nanorods and the nanobelts were found to have the same lattice phonon modes as their corresponding macroscopic crystal, thus suggesting that the nanostructures were crystalline. Although the absorbance and emission spectra of the dispersions were similar to those of a free rubrene molecule, their PL lifetimes were more comparable to their respective parent crystal which was again indicative of their crystalline nature. Finally, the crystallinity of the nanorods and the nanobelts was confirmed with electron diffraction experiments, which also answered a second question regarding the most probable cleavage planes and the π-stacking direction. With the help of AFM images, electron diffraction patterns, and IR-SNOM spectra, it was possible to establish the likely orientation of rubrene molecules within the nanorods and the nanobelts.

This study clearly shows that non-covalent π-π interactions in organic crystals are strong enough to enable and sustain mechanical exfoliation via LPE. The resulting nanostructures can be stabilized in aqueous surfactant solution and size-selected via LCC. They are crystalline in nature but may show differences in packing and local orientation of molecules in comparison to the parent crystal.

In the future, it would be useful to increase the yield of the nanorods and the nanobelts as well as completely isolate them with the help of methods like density gradient centrifugation. Their charge transport behaviour should be investigated either with conductive AFM or by incorporation into short channel FETs. It would be interesting to test whether other non-covalently bound small-molecule organic semiconducting single crystals can also be exfoliated via LPE and if they show size-dependent properties. Molecules such as pentacene, benzothienobenzothiophene (BTBT), dinaphthothienothiophene (DNTT) that form layered crystals are suitable candidates.

Appendix

A1 DFT-calculated IR spectra

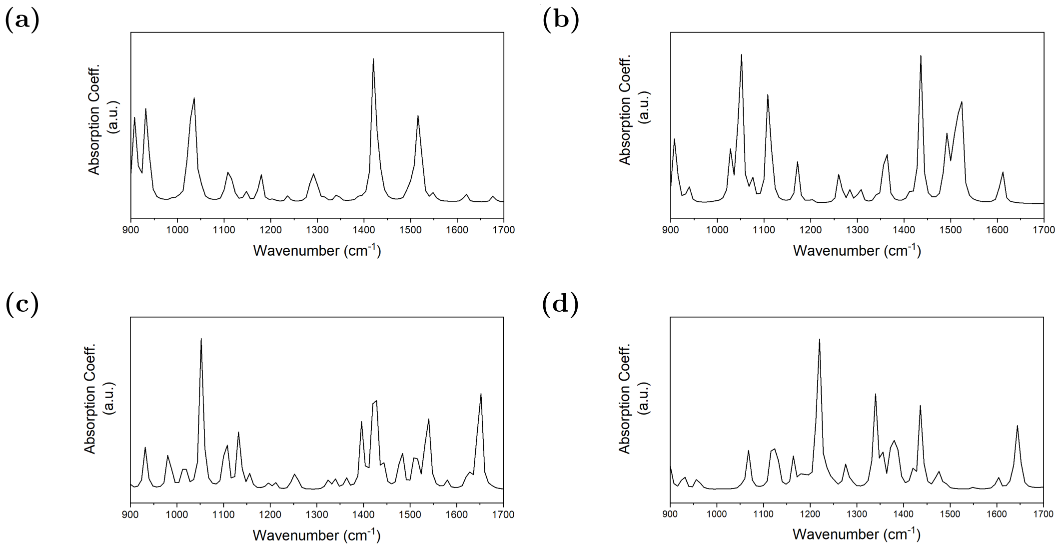

Figure A.1: Calculated IR spectra of (a) TIPS-PEN, (b) TIPS-TAP, (c) Rubrene, and (d) PDIF-CN$_2$. All spectra were broadened using Lorentzian functions with a full-width at half maximum of 4 cm^{-1}. No energy scaling or frequency correction was applied. Adapted with permission from Ref.[147]. Copyright 2020 American Chemical Society.

A2 Near-field amplitude spectra from the IR-SNOM

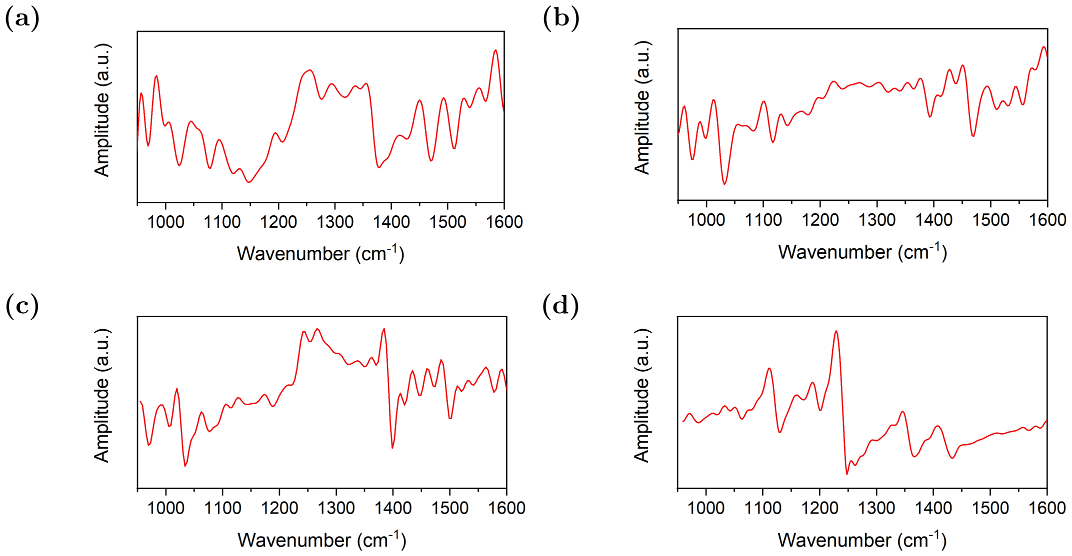

Figure A.2: Near-field amplitude of the second demodulation order of (a) TIPS-PEN, (b) TIPS-TAP, (c) Rubrene, and (d) PDIF-CN$_2$ single crystals. Adapted with permission from Ref.[147]. Copyright 2020 American Chemical Society.

A3 Vibrational modes of PDIF-CN$_2$

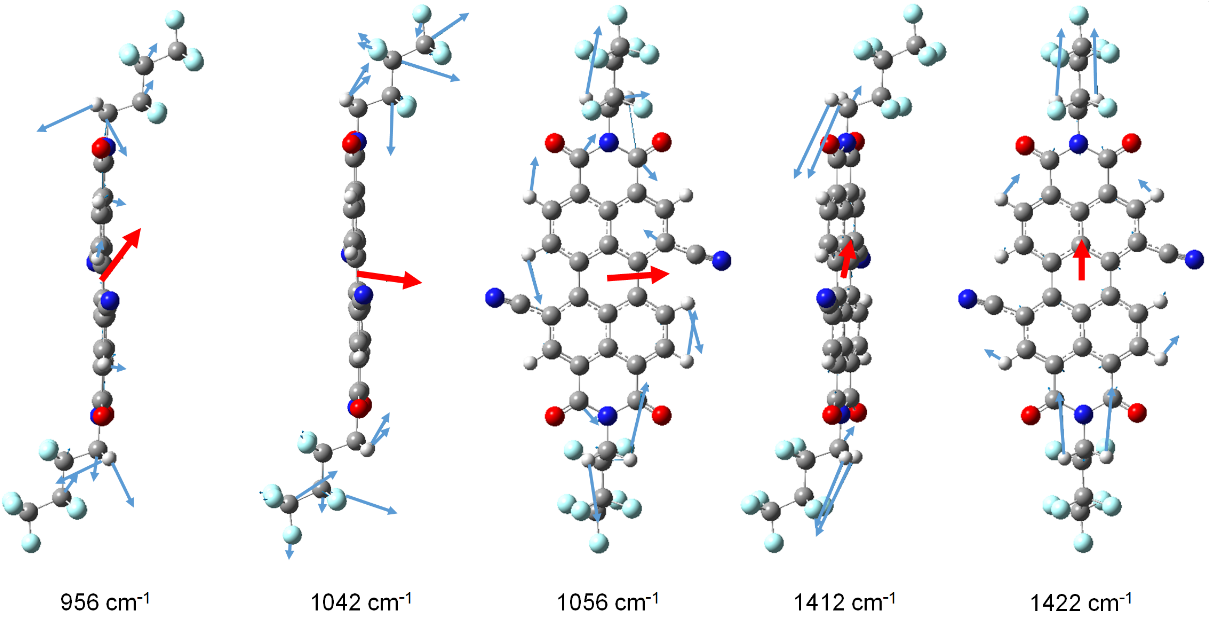

Figure A.3: Vibrational modes corresponding to selected absorption peaks of PDIF-CN$_2$. Blue and red arrows (lying in the plane of the paper and scaled to improve visibility) indicate the displacement vectors and the dipole derivative unit vectors, respectively.

A4 Tables of IR modes

Table A.1: Peak positions in cm^{-1} of all the modes observed for a TIPS-PEN crystal at different polarizations with the three techniques. DFT positions (in cm^{-1}) that were calculated for a single molecule of TIPS-PEN in the gas phase are also included. The intensity of the peaks is indicated with bold font – strong, regular font – medium, in brackets – weak. 'x' indicates that there exists a peak but is not well-resolved; '-' indicates that the corresponding peak is absent. Adapted with permission from Ref.[147]. Copyright 2020 American Chemical Society.

TIPS-PEN	FT-IR	AFM-IR	IR-SNOM	DFT
0°	991	(992)	**992**	908
	1008/1015	x/x	**1014**	933
	(1063)/(1076)	x/x	1069	1053
	1139	(1138)	1137	1111
	1176	1176	-	(1147)
	-	1262	1267	1295
	(1366)/1379	**1370**/1376	**1367**	(1341)
	1461	**1460**	**1460**	**1422**
	(1478)	x	-	(1430)
	1528	**1530**	(1525)	1516
	(1548)	1546	-	(1550)
45°	992	(994)		
	1008/(1014)	x/x		
	(1061)/1075	x/x		
	(1138)	(1138)		
	-	-		
	-	1262		
	1366	**1370**		
	1463	**1460**		
	-	x		
	(1528)	-		
	-	-		

TIPS-PEN	FT-IR	AFM-IR	IR-SNOM	DFT
90°	(992)	992		
	1008/1015	x-x		
	(1061)/1075	x/x		
	(1138)	(1138)		
	(1176)	(1176)		
	-	1262		
	1366	1370/(1380)		
	1463	**1460**		
	-	x		
	1528	1530		
	1547	(1546)		
135°	991	(992)		
	1015	x/x		
	(1061)/(1077)	x/x		
	1138	(1138)		
	1176	(1176)		
	-	1262		
	1379	**1370**/1380		
	1461	**1460**		
	(1478)	x		
	1528	1530		
	(1548)	(1546)		

Table A.2: Peak positions in cm^{-1} of all the modes observed for a TIPS-TAP crystal at different polarizations with the three techniques. DFT positions (in cm^{-1}) that were calculated for a single molecule of TIPS-TAP in the gas phase are also included. The intensity of the peaks is indicated with bold font – strong, regular font – medium, in brackets – weak. 'x' indicates that there exists a peak but is not well-resolved; '-' indicates that the corresponding peak is absent. Adapted with permission from Ref.[147]. Copyright 2020 American Chemical Society.

TIPS-TAP	FT-IR	AFM-IR	IR-SNOM	DFT
0°	994	(994)	992	910
	(1017)/1032	1022/x	**1022**/-	1031/**1053**
	(1067)	(1068)	(1052)/(1079)	1074
	1114	1114	1112	1108
	(1136)	1134	1134	1117
	1179	1178	1179	1172
	-	1228	1227	(1288)
	1315	**1314**	1310	1360
	(1384)	**1384**	**1385**	1417
	1432	**1432**	1432	1434
	1460	**1460**	**1462**	**1438**
	1527	**1526**	**1525**	**1522**
45°	(994)	(990)		
	1023/(1032)	1020/x		
	-	-		
	(1114)	-		
	(1136)	(1134)		
	-	-		
	-	1228		
	-	-		
	(1386)	**1384**		
	(1432)	-		
	1464	**1460**		
	(1527)	(1526)		

TIPS-TAP	FT-IR	AFM-IR	IR-SNOM	DFT
90°	(994)	(992)		
	(1022)/1032	1020/x		
	-	-		
	1114	-		
	-	(1136)		
	(1179)	(1178)		
	-	(1228)		
	(1315)	**1314**		
	(1385)	**1384**		
	1432	(1432)		
	1464	**1460**		
	1527	1526		
135°	(994)	(994)		
	(1016)/**1032**	1016/x		
	(1067)	(1068)		
	1114	(1114)		
	-	1134		
	1179	1178		
	-	1228		
	1315	**1314**		
	(1383)	**1382**		
	1432	**1432**		
	1461	**1460**		
	1527	**1530**		

Table A.3: Peak positions in cm^{-1} of all the modes observed for a rubrene crystal at different polarizations with the three techniques. DFT positions (in cm^{-1}) that were calculated for a single molecule of rubrene in the gas phase are also included. The intensity of the peaks is indicated with bold font – strong, regular font – medium, in brackets – weak. ‘x’ indicates that there exists a peak but is not well-resolved; ‘-’ indicates that the corresponding peak is absent. Adapted with permission from Ref.[147]. Copyright 2020 American Chemical Society.

Rubrene	FT-IR	AFM-IR	IR-SNOM	DFT
0°	(967)	(968)	962	(982)
	1031	**1028**	**1027**	**1053**
	(1069)	(1070)	1070	1105
	-	(1110)	(1109)	(1157)
	-	-	-	(1198)
	-	-	-	(1212)
	(1216)	(1216)	-	(1249)
	1309	(1308)	-	(1338)
	(1393)	**1394**	**1392**	1397
	-	-	1417	**1424**
	1440	**1440**	1442	1481
	1465	**1464**	1467	1512
	(1494)	-	**1492**	**1537**
	-	(1572)	1571	(1580)
45°	968	**968**		
	1031	**1028**		
	(1069)	1068		
	-	(1110)		
	(1149)	(1148)		
	(1171)	(1170)		
	(1216)	-		
	1309	(1308)		
	(1393)	**1394**		
	(1413)	(1412)		
	1441	**1440**		
	1465	**1464**		
	(1494)	-		
	(1574)	1574		

Rubrene	FT-IR	AFM-IR	IR-SNOM	DFT
90°	968	**968**		
	1030	**1028**		
	1068	1068		
	-	(1110)		
	1149	(1148)		
	1171	(1170)		
	-	-		
	(1308)	(1308)		
	(1393)	**1394**		
	(1413)	(1412)		
	1441	**1440**		
	1465	**1464**		
	-	-		
	1575	1574		
135°	968	968		
	1031	**1028**		
	1069	(1068)		
	-	(1110)		
	(1149)	(1148)		
	(1170)	(1170)		
	(1216)	-		
	1309	(1308)		
	(1393)	**1394**		
	(1413)	(1412)		
	1441	**1440**		
	1465	**1464**		
	(1494)	-		
	(1574)	(1572)		

Table A.4: Peak positions in cm^{-1} of all the modes observed for a PDIF-CN$_2$ crystal at different polarizations with the three techniques. DFT positions (in cm^{-1}) that were calculated for a single molecule of PDIF-CN$_2$ in the gas phase are also included. The intensity of the peaks is indicated with bold font – strong, regular font – medium, in brackets – weak. ‘x’ indicates that there exists a peak but is not well-resolved; ‘-’ indicates that the corresponding peak is absent. Adapted with permission from Ref.[147]. Copyright 2020 American Chemical Society.

PDIF-CN$_2$	FT-IR	AFM-IR	IR-SNOM	DFT
0°	(1059)	**1040/1056**	(1039)/(1056)	(1056)/**1068**
	1114/(1124)	**1114/1124**	1123	**1119/1128**
	-	**1194**	1196	(1183)
	1221/1247	**1248**	**1244**	**1214/1220**
	(1352)/1362	**1350/1360**	1356	**1339/1354**
	(1411)/(1427)	**1412/1426**	1421	(1419)/**1437**
45°	(1059)	1040/1058		
	1114/(1124)	1114/1122		
	-	(1194)		
	1221/1247	1248		
	1352/1362	1352/1360		
	(1411)/(1427)	1410/1426		
90°	(1059)	**1040/1056**		
	1124	**1112/1124**		
	-	**1194**		
	(1221)/**1247**	**1246**		
	1351	1350/1358		
	(1413)/(1427)	1412/1426		
135°	(1058)	1042/1056		
	1114/1124	**1112/1124**		
	-	(1194)		
	1221/1247	**1248**		
	1351/1362	1350/1360		
	1413/1427	1412/1426		

A5 Low-wavenumber Raman spectra of rubrene

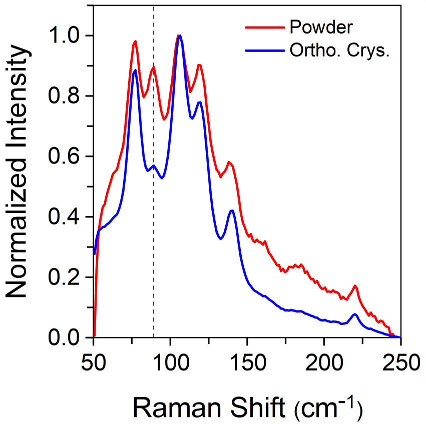

Figure A.4: Normalized low-wavenumber Raman spectra of rubrene powder and a differently oriented orthorhombic rubrene crystal (i.e., laser not incident on the *ab* facet). A weak mode observed in both cases at around 88 cm^{-1} is marked with a black dashed line. Adapted with permission from Ref.[283]. Copyright 2021 American Chemical Society.

A6 PLE maps of rubrene dispersions and solution

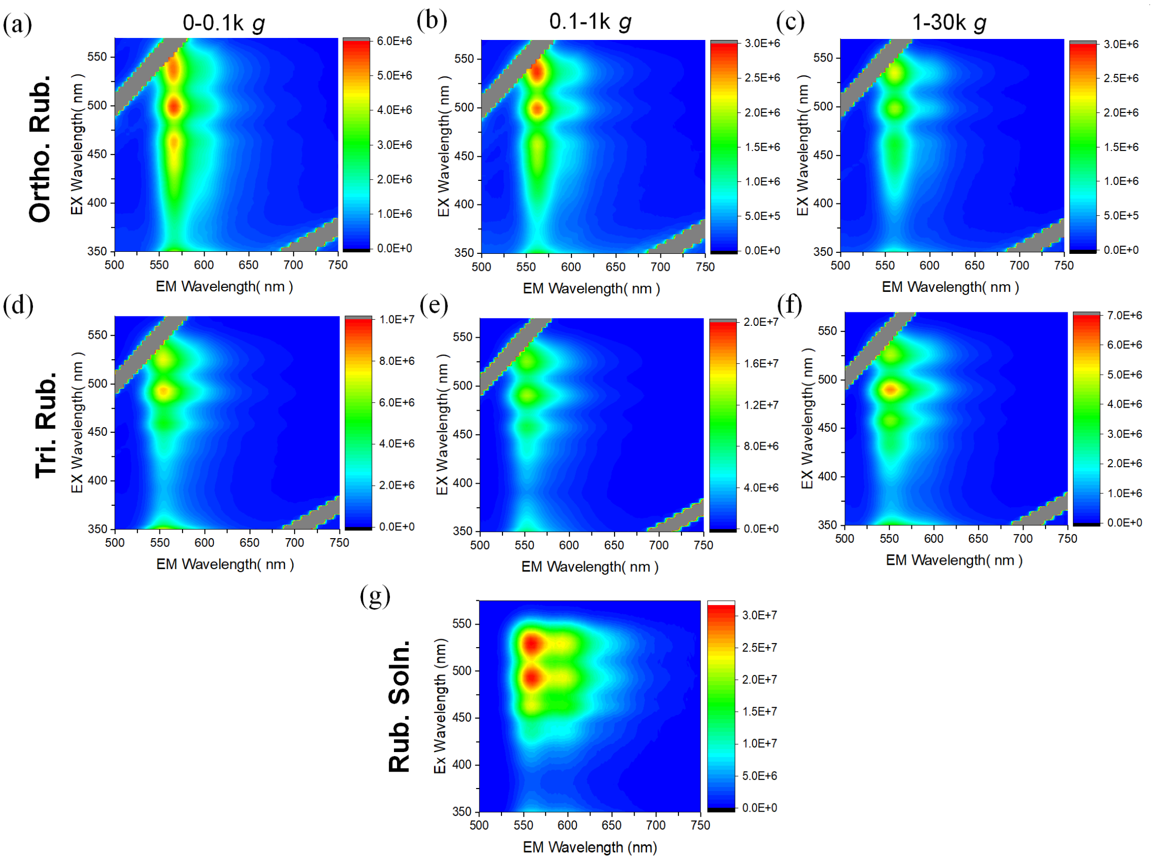

Figure A.5: Photoluminescence excitation-emission maps (PLE maps) of the three different fractions each of exfoliated orthorhombic rubrene (a, b, c) and triclinic rubrene (d, e, f) dispersions, and a dilute rubrene solution in chloroform (g). The grey features in the PLE maps of the dispersions stem from the excitation. Adapted with permission from Ref.[283]. Copyright 2021 American Chemical Society.

Bibliography

(1) Anthony, J. E. Functionalized acenes and heteroacenes for organic electronics. *Chem. Rev.* **2006**, *106*, 5028–5048, DOI: `10.1021/cr050966z`.

(2) Sutton, C.; Risko, C.; Brédas, J.-L. Noncovalent intermolecular interactions in organic electronic materials: implications for the molecular packing vs electronic properties of acenes. *Chem. Mater.* **2016**, *28*, 3–16, DOI: `10.1021/acs.chemmater.5b03266`.

(3) Geim, A. K. Graphene: status and prospects. *Science* **2009**, *324*, 1530–1534, DOI: `10.1126/science.1158877`.

(4) Odom, T. W.; Huang, J.-L.; Kim, P.; Lieber, C. M. Atomic structure and electronic properties of single-walled carbon nanotubes. *Nature* **1998**, *391*, 62–64, DOI: `10.1038/34145`.

(5) Ponomarenko, L. A.; Schedin, F.; Katsnelson, M. I., et al. Chaotic dirac billiard in graphene quantum dots. *Science* **2008**, *320*, 356–358, DOI: `10.1126/science.1154663`.

(6) Wudl, F. Spiers memorial lecture. Organic electronics: an organic materials perspective. *Faraday Discuss.* **2014**, *174*, 9–20, DOI: `10.1039/c4fd00191e`.

(7) Chiang, C. K.; Fincher, C. R.; Park, Y. W., et al. Electrical conductivity in doped polyacetylene. *Phys. Rev. Lett.* **1977**, *39*, 1098–1101, DOI: `10.1103/PhysRevLett.39.1098`.

(8) Warta, W.; Karl, N. Hot holes in naphthalene: high, electric-field-dependent mobilities. *Phys. Rev. B* **1985**, *32*, 1172–1182, DOI: `10.1103/PhysRevB.32.1172`.

(9) Kumar, D.; Sharma, R. C. Advances in conductive polymers. *Eur. Polym. J.* **1998**, *34*, 1053–1060, DOI: `10.1016/S0014-3057(97)00204-8`.

(10) Klauk, H. Organic thin-film transistors. *Chem. Soc. Rev.* **2010**, *39*, 2643–2666, DOI: `10.1039/B909902F`.

(11) Hebard, A. F.; Rosseinsky, M. J.; Haddon, R. C., et al. Superconductivity at 18 K in potassium-doped C60. *Nature* **1991**, *350*, 600–601, DOI: `10.1038/350600a0`.

(12) Fratini, S.; Nikolka, M.; Salleo, A., et al. Charge transport in high-mobility conjugated polymers and molecular semiconductors. *Nat. Mater.* **2020**, *19*, 491–502, DOI: `10.1038/s41563-020-0647-2`.

(13) Gershenson, M. E.; Podzorov, V.; Morpurgo, A. F. Colloquium: electronic transport in single-crystal organic transistors. *Rev. Mod. Phys.* **2006**, *78*, 973–989, DOI: `10.1103/RevModPhys.78.973`.

(14) Sze, S. M.; Li, Y.; Ng, K. K., *Physics of semiconductor devices*; John wiley & sons: 2021.

(15) Lamport, Z. A.; Haneef, H. F.; Anand, S., et al. Tutorial: Organic field-effect transistors: materials, structure and operation. *J. Appl. Phys.* **2018**, *124*, 071101, DOI: `10.1063/1.5042255`.

(16) Choi, H. H.; Cho, K.; Frisbie, C. D., et al. Critical assessment of charge mobility extraction in FETs. *Nat. Mater.* **2018**, *17*, 2–7, DOI: `10.1038/nmat5035`.

(17) Kotadiya, N. B.; Mondal, A.; Blom, P. W. M., et al. A window to trap-free charge transport in organic semiconducting thin films. *Nat. Mater.* **2019**, *18*, 1182–1186, DOI: `10.1038/s41563-019-0473-6`.

(18) Nayak, P. K.; Rosenberg, R.; Barnea-Nehoshtan, L.; Cahen, D. O2 and organic semiconductors: electronic effects. *Org. Electron.* **2013**, *14*, 966–972, DOI: `10.1016/j.orgel.2013.01.020`.

(19) Nicolai, H. T.; Kuik, M.; Wetzelaer, G. A. H., et al. Unification of trap-limited electron transport in semiconducting polymers. *Nat. Mater.* **2012**, *11*, 882–887, DOI: `10.1038/nmat3384`.

(20) Zaumseil, J.; Sirringhaus, H. Electron and ambipolar transport in organic field-effect transistors. *Chem. Rev.* **2007**, *107*, 1296–1323, DOI: `10.1021/cr0501543`.

(21) Jurchescu, O. D.; Baas, J.; Palstra, T. T. M. Effect of impurities on the mobility of single crystal pentacene. *Appl. Phys. Lett.* **2004**, *84*, 3061–3063, DOI: `10.1063/1.1704874`.

(22) Lin, Y.; Gundlach, D. J.; Nelson, S. F.; Jackson, T. N. Stacked pentacene layer organic thin-film transistors with improved characteristics. *IEEE Electron Device Lett.* **1997**, *18*, 606–608, DOI: `10.1109/55.644085`.

(23) Nelson, S. F.; Lin, Y. Y.; Gundlach, D. J.; Jackson, T. N. Temperature-independent transport in high-mobility pentacene transistors. *Appl. Phys. Lett.* **1998**, *72*, 1854–1856, DOI: `10.1063/1.121205`.

(24) Klauk, H.; Halik, M.; Zschieschang, U., et al. High-mobility polymer gate dielectric pentacene thin film transistors. *J. Appl. Phys.* **2002**, *92*, 5259–5263, DOI: `10.1063/1.1511826`.

(25) Dong, H.; Wang, C.; Hu, W. High performance organic semiconductors for field-effect transistors. *Chem. Commun.* **2010**, *46*, 5211–5222, DOI: `10.1039/C0CC00947D`.

(26) Anthony, J. E.; Brooks, J. S.; Eaton, D. L.; Parkin, S. R. Functionalized pentacene: improved electronic properties from control of solid-state order. *J. Am. Chem. Soc.* **2001**, *123*, 9482–9483, DOI: `10.1021/ja0162459`.

(27) Naibi Lakshminarayana, A.; Ong, A.; Chi, C. Modification of acenes for n-channel OFET materials. *J. Mater. Chem. C* **2018**, *6*, 3551–3563, DOI: `10.1039/C8TC00146D`.

(28) Park, S. K.; Jackson, T. N.; Anthony, J. E.; Mourey, D. A. High mobility solution processed 6,13-bis(triisopropyl-silylethynyl) pentacene organic thin film transistors. *Appl. Phys. Lett.* **2007**, *91*, 063514, DOI: `10.1063/1.2768934`.

(29) Lee, S. S.; Kim, C. S.; Gomez, E. D., et al. Controlling nucleation and crystallization in solution-processed organic semiconductors for thin-film transistors. *Adv. Mater.* **2009**, *21*, 3605–3609, DOI: `10.1002/adma.200900705`.

(30) Gundlach, D. J.; Royer, J. E.; Park, S. K., et al. Contact-induced crystallinity for high-performance soluble acene-based transistors and circuits. *Nat. Mater.* **2008**, *7*, 216–221, DOI: `10.1038/nmat2122`.

(31) Goetz, K. P.; Li, Z.; Ward, J. W., et al. Effect of acene length on electronic properties in 5-, 6-, and 7-ringed heteroacenes. *Adv. Mater.* **2011**, *23*, 3698–3703, DOI: `doi.org/10.1002/adma.201101619`.

(32) Tang, M. L.; Okamoto, T.; Bao, Z. High-performance organic semiconductors: asymmetric linear acenes containing sulphur. *J. Am. Chem. Soc.* **2006**, *128*, 16002–16003, DOI: `10.1021/ja066824j`.

(33) Tang, M. L.; Mannsfeld, S. C. B.; Sun, Y.-S., et al. Pentaceno[2,3-b]thiophene, a hexacene analogue for organic thin film transistors. *J. Am. Chem. Soc.* **2009**, *131*, 882–883, DOI: `10.1021/ja808142c`.

(34) Du, C.; Guo, Y.; Liu, Y., et al. Anthra[2,3-b]benzo[d]thiophene: an air-stable asymmetric organic semiconductor with high mobility at room temperature. *Chem. Mater.* **2008**, *20*, 4188–4190, DOI: `10.1021/cm801305f`.

(35) Takimiya, K.; Ebata, H.; Sakamoto, K., et al. 2,7-Diphenyl[1]benzothieno[3,2-b]benzothiophene, a new organic semiconductor for air-stable organic field-effect transistors with mobilities up to 2.0 cm2 V-1 s-1. *J. Am. Chem. Soc.* **2006**, *128*, 12604–12605, DOI: `10.1021/ja064052l`.

(36) Yamamoto, T.; Takimiya, K. Facile synthesis of highly π-extended heteroarenes, Dinaphtho[2,3-b:2',3'-f]chalcogenopheno[3,2-b]chalcogenophenes, and their application to field-effect transistors. *J. Am. Chem. Soc.* **2007**, *129*, 2224–2225, DOI: `10.1021/ja068429z`.

(37) Wawrzinek, R.; Sobus, J.; Chaudhry, M. U., et al. Mobility evaluation of [1]benzothieno[3,2-b][1]benzothiophene derivatives: limitation and impact on charge transport. *ACS Appl. Mater. Interfaces* **2019**, *11*, 3271–3279, DOI: `10.1021/acsami.8b16158`.

(38) Yang, Y. S.; Yasuda, T.; Kakizoe, H., et al. High performance organic field-effect transistors based on single-crystal microribbons and microsheets of solution-processed dithieno[3,2-b:2',3'-d]thiophene derivatives. *Chem. Commun.* **2013**, *49*, 6483–6485, DOI: `10.1039/C3CC42114G`.

(39) Yamaguchi, Y.; Kojiguchi, Y.; Kawata, S., et al. Solution-processable organic semiconductors featuring S-shaped dinaphthothienothiophene (S-DNTT): effects of alkyl chain length on self-organization and carrier transport properties. *Chem. Mater.* **2020**, *32*, 5350–5360, DOI: `10.1021/acs.chemmater.0c01740`.

(40) Ou-Yang, W.; Uemura, T.; Miyake, K., et al. High-performance organic transistors with high-k dielectrics: A comparative study on solution-processed single crystals and vacuum-deposited polycrystalline films of 2,9-didecyl-dinaphtho[2,3-b:2',3'-f]thieno[3,2-b]thiophene. *Appl. Phys. Lett.* **2012**, *101*, 223304, DOI: `10.1063/1.4769436`.

(41) Wang, C.; Dong, H.; Hu, W., et al. Semiconducting π-conjugated systems in field-effect transistors: a material Odyssey of organic electronics. *Chem. Rev.* **2012**, *112*, 2208–2267, DOI: `10.1021/cr100380z`.

(42) Chua, L.-L.; Zaumseil, J.; Chang, J.-F., et al. General observation of n-type field-effect behaviour in organic semiconductors. *Nature* **2005**, *434*, 194–199, DOI: `10.1038/nature03376`.

(43) Anthony, J. E.; Facchetti, A.; Heeney, M., et al. n-Type organic semiconductors in organic electronics. *Adv. Mater.* **2010**, *22*, 3876–3892, DOI: `10.1002/adma.200903628`.

(44) Sakamoto, Y.; Suzuki, T.; Kobayashi, M., et al. Perfluoropentacene and perfluorotetracene: syntheses, crystal structures, and FET characteristics. *Mol. Cryst. Liq. Cryst.* **2006**, *444*, 225–232, DOI: `10.1080/15421400500365011`.

(45) Glöcklhofer, F.; Petritz, A.; Karner, E., et al. Dicyano- and tetracyanopentacene: foundation of an intriguing new class of easy-to-synthesize organic semiconductors. *J. Mater. Chem. C* **2017**, *5*, 2603–2610, DOI: `10.1039/C7TC00143F`.

(46) Bunz, U. H. F.; Engelhart, J. U.; Lindner, B. D.; Schaffroth, M. Large N-heteroacenes: new tricks for very old dogs? *Angew. Chem. Int. Ed.* **2013**, *52*, 3810–3821, DOI: `10.1002/anie.201209479`.

(47) Bunz, U. H. F. The larger linear N-heteroacenes. *Acc. Chem. Res.* **2015**, *48*, 1676–1686, DOI: `10.1021/acs.accounts.5b00118`.

(48) Isoda, K.; Nakamura, M.; Tatenuma, T., et al. Synthesis and characterization of electron-accepting nonsubstituted tetraazaacene derivatives. *Chem. Lett.* **2012**, *41*, 937–939, DOI: `10.1246/cl.2012.937`.

(49) Miao, S.; Appleton, A. L.; Berger, N., et al. 6,13-Diethynyl-5,7,12,14-tetraazapentacene. *Chem. Eur. J.* **2009**, *15*, 4990–4993, DOI: `10.1002/chem.200900324`.

(50) Liang, Z.; Tang, Q.; Mao, R., et al. The position of nitrogen in N-heteropentacenes matters. *Adv. Mater.* **2011**, *23*, 5514–5518, DOI: `10.1002/adma.201103759`.

(51) Xue, G.; Wu, J.; Fan, C., et al. Boosting the electron mobility of solution-grown organic single crystals via reducing the amount of polar solvent residues. *Mater. Horiz.* **2016**, *3*, 119–123, DOI: `10.1039/C5MH00190K`.

(52) Islam, M. M.; Pola, S.; Tao, Y.-T. High mobility n-channel single-crystal field-effect transistors based on 5,7,12,14-tetrachloro-6,13-diazapentacene. *Chem. Commun.* **2011**, *47*, 6356–6358, DOI: `10.1039/C1CC11762A`.

(53) Müller, M.; Beglaryan, S. S.; Koser, S., et al. Dicyano-substituted diazaacenes. *Chem. Eur. J.* **2017**, *23*, 7066–7073, DOI: `10.1002/chem.201700421`.

(54) Reiss, H.; Ji, L.; Han, J., et al. Bromination improves the electron mobility of tetraazapentacene. *Angew. Chem. Int. Ed.* **2018**, *57*, 9543–9547, DOI: `10.1002/anie.201805728`.

(55) Jones, B. A.; Ahrens, M. J.; Yoon, M.-H., et al. High-mobility air-stable n-type semiconductors with processing versatility: dicyanoperylene-3,4:9,10-bis(dicarboximides). *Angew. Chem. Int. Ed.* **2004**, *43*, 6363–6366, DOI: `10.1002/anie.200461324`.

(56) Jung, T.; Yoo, B.; Wang, L., et al. Nanoscale n-channel and ambipolar organic field-effect transistors. *Appl. Phys. Lett.* **2006**, *88*, 183102, DOI: `10.1063/1.2200591`.

(57) Molinari, A. S.; Alves, H.; Chen, Z., et al. High electron mobility in vacuum and ambient for PDIF-CN2 single-crystal transistors. *J. Am. Chem. Soc.* **2009**, *131*, 2462–2463, DOI: `10.1021/ja809848y`.

(58) Podzorov, V.; Pudalov, V. M.; Gershenson, M. E. Field-effect transistors on rubrene single crystals with parylene gate insulator. *Appl. Phys. Lett.* **2003**, *82*, 1739–1741, DOI: `10.1063/1.1560869`.

(59) Podzorov, V.; Sysoev, S.; Loginova, E., et al. Single-crystal organic field effect transistors with the hole mobility ∼8 cm 2/V s. *Appl. Phys. Lett.* **2003**, *83*, 3504–3506, DOI: `10.1063/1.1622799`.

(60) Sundar, V. C.; Zaumseil, J.; Podzorov, V., et al. Elastomeric transistor stamps: reversible probing of charge transport in organic crystals. *Science* **2004**, *303*, 1644–1646, DOI: `10.1126/science.1094196`.

(61) Podzorov, V.; Menard, E.; Borissov, A., et al. Intrinsic charge transport on the surface of organic semiconductors. *Phys. Rev. Lett.* **2004**, *93*, 086602, DOI: `10.1103/PhysRevLett.93.086602`.

(62) Takeya, J.; Goldmann, C.; Haas, S., et al. Field-induced charge transport at the surface of pentacene single crystals: a method to study charge dynamics of two-dimensional electron systems in organic crystals. *J. Appl. Phys.* **2003**, *94*, 5800–5804, DOI: `10.1063/1.1618919`.

(63) De Boer, R. W. I.; Jochemsen, M.; Klapwijk, T. M., et al. Space charge limited transport and time of flight measurements in tetracene single crystals: a comparative study. *J. Appl. Phys.* **2004**, *95*, 1196–1202, DOI: `10.1063/1.1631079`.

(64) Takeya, J.; Tsukagoshi, K.; Aoyagi, Y., et al. Hall effect of quasi-hole gas in organic single-crystal transistors. *Jpn. J. Appl. Phys.* **2005**, *44*, L1393, DOI: `10.1143/JJAP.44.L1393/meta`.

(65) De Boer, R. W. I.; Klapwijk, T. M.; Morpurgo, A. F. Field-effect transistors on tetracene single crystals. *Appl. Phys. Lett.* **2003**, *83*, 4345–4347, DOI: `10.1063/1.1629144`.

(66) Kloc, C.; Simpkins, P. G.; Siegrist, T.; Laudise, R. A. Physical vapor growth of centimeter-sized crystals of α-hexathiophene. *J. Cryst. Growth* **1997**, *182*, 416–427, DOI: `10.1016/S0022-0248(97)00370-9`.

(67) Laudise, R.; Kloc, C.; Simpkins, P.; Siegrist, T. Physical vapor growth of organic semiconductors. *J. Cryst. Growth* **1998**, *187*, 449–454, DOI: `10.1016/S0022-0248(98)00034-7`.

(68) Li, H.; Tee, B. C. K.; Cha, J. J., et al. High-mobility field-effect transistors from large-area solution-grown aligned C60 single crystals. *J. Am. Chem. Soc.* **2012**, *134*, 2760–2765, DOI: `10.1021/ja210430b`.

(69) Uemura, T.; Hirose, Y.; Uno, M., et al. Very high mobility in solution-processed organic thin-film transistors of highly ordered [1]benzothieno[3, 2-b]benzothiophene derivatives. *Appl. Phys. Express* **2009**, *2*, 111501, DOI: `10.1143/APEX.2.111501`.

(70) Soeda, J.; Hirose, Y.; Yamagishi, M., et al. Solution-crystallized organic field-effect transistors with charge-acceptor layers: high-mobility and low-threshold-voltage operation in air. *Adv. Mater.* **2011**, *23*, 3309–3314, DOI: `10.1002/adma.201101027`.

(71) Nakayama, K.; Hirose, Y.; Soeda, J., et al. Patternable solution-crystallized organic transistors with high charge carrier mobility. *Adv. Mater.* **2011**, *23*, 1626–1629, DOI: `10.1002/adma.201004387`.

(72) Diao, Y.; Shaw, L.; Bao, Z.; Mannsfeld, S. C. B. Morphology control strategies for solution-processed organic semiconductor thin films. *Energy Environ. Sci.* **2014**, *7*, 2145–2159, DOI: `10.1039/C4EE00688G`.

(73) Paulus, F.; Engelhart, J. U.; Hopkinson, P. E., et al. The effect of tuning the microstructure of TIPS-tetraazapentacene on the performance of solution processed thin film transistors. *J. Mater. Chem. C* **2016**, *4*, 1194–1200, DOI: `10.1039/C5TC03326H`.

(74) Xue, G.; Fan, C.; Wu, J., et al. Ambipolar charge transport of TIPS-pentacene single-crystals grown from non-polar solvents. *Mater. Horiz.* **2015**, *2*, 344–349, DOI: `10.1039/C4MH00211C`.

(75) Shaw, L.; Bao, Z. The large-area, solution-based deposition of single-crystal organic semiconductors. *Isr. J. Chem.* **2014**, *54*, 496–512, DOI: `10.1002/ijch.201400032`.

(76) Wang, C.; Dong, H.; Jiang, L.; Hu, W. Organic semiconductor crystals. *Chem. Soc. Rev.* **2018**, *47*, 422–500, DOI: `10.1039/C7CS00490G`.

(77) Zhang, X.; Dong, H.; Hu, W. Organic semiconductor single crystals for electronics and photonics. *Adv. Mater.* **2018**, *30*, 1801048, DOI: `10.1002/adma.201801048`.

(78) Sinnokrot, M. O.; Sherrill, C. D. High-accuracy quantum mechanical studies of π-π interactions in benzene dimers. *J. Phys. Chem. A* **2006**, *110*, 10656–10668, DOI: `10.1021/jp0610416`.

(79) Wheeler, S. E. Understanding substituent effects in noncovalent interactions involving aromatic rings. *Acc. Chem. Res.* **2013**, *46*, 1029–1038, DOI: `10.1021/ar300109n`.

(80) Da Silva Filho, D. A.; Kim, E.-G.; Brédas, J.-L. Transport properties in the rubrene crystal: electronic coupling and vibrational reorganization energy. *Adv. Mater.* **2005**, *17*, 1072–1076, DOI: `10.1002/adma.200401866`.

(81) Fratini, S.; Mayou, D.; Ciuchi, S. The transient localization scenario for charge transport in crystalline organic materials. *Adv. Funct. Mater.* **2016**, *26*, 2292–2315, DOI: `10.1002/adfm.201502386`.

(82) Brédas, J. L.; Calbert, J. P.; da Silva Filho, D. A.; Cornil, J. Organic semiconductors: a theoretical characterization of the basic parameters governing charge transport. *Proc. Natl. Acad. Sci. U.S.A.* **2002**, *99*, 5804, DOI: `10.1073/pnas.092143399`.

(83) Moon, H.; Zeis, R.; Borkent, E.-J., et al. Synthesis, crystal structure, and transistor performance of tetracene derivatives. *J. Am. Chem. Soc.* **2004**, *126*, 15322–15323, DOI: `10.1021/ja045208p`.

(84) Park, S. K.; Kim, J. H.; Park, S. Y. Organic 2D optoelectronic crystals: charge transport, emerging functions, and their design perspective. *Adv. Mater.* **2018**, *30*, 1704759, DOI: `10.1002/adma.201704759`.

(85) Anthony, J. E.; Eaton, D. L.; Parkin, S. R. A road map to stable, soluble, easily crystallized pentacene derivatives. *Org. Lett.* **2002**, *4*, 15–18, DOI: `10.1021/ol0167356`.

(86) Inoue, S.; Minemawari, H.; Tsutsumi, J., et al. Effects of substituted alkyl chain length on solution-processable layered organic semiconductor crystals. *Chem. Mater.* **2015**, *27*, 3809–3812, DOI: `10.1021/acs.chemmater.5b00810`.

(87) Minemawari, H.; Tanaka, M.; Tsuzuki, S., et al. Enhanced layered-herringbone packing due to long alkyl chain substitution in solution-processable organic semiconductors. *Chem. Mater.* **2017**, *29*, 1245–1254, DOI: `10.1021/acs.chemmater.6b04628`.

(88) Brillante, A.; Bilotti, I.; Della Valle, R. G., et al. Probing polymorphs of organic semiconductors by lattice phonon Raman microscopy. *CrystEngComm* **2008**, *10*, 937–946, DOI: `10.1039/B804317E`.

(89) Socci, J.; Salzillo, T.; Della Valle, R. G., et al. Fast identification of rubrene polymorphs by lattice phonon Raman microscopy. *Solid State Sci.* **2017**, *71*, 146–151, DOI: `10.1016/j.solidstatesciences.2017.07.015`.

(90) Massaro, F. R.; Moret, M.; Bruno, M.; Aquilano, D. Equilibrium and growth morphology of oligoacenes: periodic bond chains analysis of naphthalene, anthracene, and pentacene crystals. *Cryst. Growth Des.* **2012**, *12*, 982–989, DOI: `10.1021/cg201458g`.

(91) Massaro, F. R.; Moret, M.; Bruno, M.; Aquilano, D. Equilibrium and growth morphology of oligothiophenes: periodic bond chain analysis of quaterthiophene and sexithiophene crystals. *Cryst. Growth Des.* **2013**, *13*, 1334–1341, DOI: `10.1021/cg301868m`.

(92) Allen, C. F. H.; Gilman, L. A Synthesis of Rubrene. *J. Am. Chem. Soc.* **1936**, *58*, 937–940, DOI: `10.1021/ja01297a028`.

(93) Strickler, S.; Berg, R. A. Relationship between absorption intensity and fluorescence lifetime of molecules. *J. Chem. Phys.* **1962**, *37*, 814–822, DOI: `10.1063/1.1733166`.

(94) Takeya, J.; Yamagishi, M.; Tominari, Y., et al. Very high-mobility organic single-crystal transistors with in-crystal conduction channels. *Appl. Phys. Lett.* **2007**, *90*, 102120, DOI: `10.1063/1.2711393`.

(95) Löhmannsröben, H.-G. Photophysical properties and laser performance of rubrene. *Appl. Phys. B* **1988**, *47*, 195–199, DOI: `10.1007/BF00684088`.

(96) Kanagasekaran, T.; Shimotani, H.; Shimizu, R., et al. A new electrode design for ambipolar injection in organic semiconductors. *Nat. Commun.* **2017**, *8*, 1–7, DOI: `10.1038/s41467-017-01047-9`.

(97) Oyamada, T.; Uchiuzou, H.; Akiyama, S., et al. Lateral organic light-emitting diode with field-effect transistor characteristics. *J. Appl. Phys.* **2005**, *98*, 074506, DOI: `10.1063/1.2060932`.

(98) Zhao, B.; Miao, Y.; Wang, Z., et al. Highly efficient orange fluorescent OLEDs based on the energy transfer from bilayer interface exciplex. *Org. Electron.* **2016**, *37*, 1–5, DOI: `10.1016/j.orgel.2016.06.016`.

(99) Hung, W.-Y.; Chiang, P.-Y.; Lin, S.-W., et al. Balance the carrier mobility to achieve high performance exciplex OLED using a triazine-based acceptor. *ACS Appl. Mater. Interfaces* **2016**, *8*, 4811–4818, DOI: `10.1021/acsami.5b11895`.

(100) Nagata, R.; Nakanotani, H.; Potscavage Jr, W. J.; Adachi, C. Exploiting singlet fission in organic light-emitting diodes. *Adv. Mater.* **2018**, *30*, 1801484, DOI: `10.1002/adma.201801484`.

(101) Su, W.-C.; Lee, C.-C.; Li, Y.-Z.; Liu, S.-W. Influence of singlet and charge-transfer excitons on the open-circuit voltage of rubrene/fullerene organic photovoltaic device. *ACS Appl. Mater. Interfaces* **2016**, *8*, 28757–28762, DOI: `10.1021/acsami.6b08363`.

(102) Ndjawa, G. O. N.; Graham, K. R.; Mollinger, S., et al. Open-circuit voltage in organic solar cells: the impacts of donor semicrystallinity and coexistence of multiple interfacial charge-transfer bands. *Adv. Energy Mater.* **2017**, *7*, 1601995, DOI: `10.1002/aenm.201601995`.

(103) Cong, S.; Yang, H.; Lou, Y., et al. Organic small molecule as the underlayer toward high performance planar perovskite solar cells. *ACS Appl. Mater. Interfaces* **2017**, *9*, 2295–2300, DOI: `10.1021/acsami.6b12268`.

(104) Shim, J.; Raman, K.; Park, Y., et al. Large spin diffusion length in an amorphous organic semiconductor. *Phys. Rev. Lett.* **2008**, *100*, 226603, DOI: `10.1103/PhysRevLett.100.226603`.

(105) Zhang, X.; Ma, Q.; Suzuki, K., et al. Magnetoresistance effect in rubrene-based spin valves at room temperature. *ACS Appl. Mater. Interfaces* **2015**, *7*, 4685–4692, DOI: `10.1021/am508173j`.

(106) Huang, L.; Liao, Q.; Shi, Q., et al. Rubrene micro-crystals from solution routes: their crystallography, morphology and optical properties. *J. Mater. Chem.* **2010**, *20*, 159–166, DOI: `10.1039/B914334C`.

(107) Jurchescu, O. D.; Meetsma, A.; Palstra, T. T. Low-temperature structure of rubrene single crystals grown by vapor transport. *Acta Crystallogr. B* **2006**, *62*, 330–334, DOI: `10.1107/S0108768106003053`.

(108) Ullah, A.; Micolich, A.; Cochrane, J.; Hamilton, A., *The effect of temperature and gas flow on the physical vapour growth of mm-scale rubrene crystals for organic FETs*; SPIE Microelectronics, MEMS, and Nanotechnology, Vol. 6800; SPIE: 2008.

(109) Lee, H. M.; Moon, H.; Kim, H.-S., et al. Abrupt heating-induced high-quality crystalline rubrene thin films for organic thin-film transistors. *Org. Electron.* **2011**, *12*, 1446–1453, DOI: `10.1016/j.orgel.2011.05.015`.

(110) Fielitz, T. R.; Holmes, R. J. Crystal morphology and growth in annealed rubrene thin films. *Cryst. Growth Des.* **2016**, *16*, 4720–4726, DOI: `10.1021/acs.cgd.6b00783`.

(111) Fusella, M. A.; Schreiber, F.; Abbasi, K., et al. Homoepitaxy of crystalline rubrene thin films. *Nano Lett.* **2017**, *17*, 3040–3046, DOI: `10.1021/acs.nanolett.7b00380`.

(112) Jo, P. S.; Duong, D. T.; Park, J., et al. Control of rubrene polymorphs via polymer binders: Applications in organic field-effect transistors. *Chem. Mater.* **2015**, *27*, 3979–3987, DOI: `10.1021/acs.chemmater.5b00884`.

(113) Stassen, A.; De Boer, R.; Iosad, N.; Morpurgo, A. Influence of the gate dielectric on the mobility of rubrene single-crystal field-effect transistors. *Appl. Phys. Lett.* **2004**, *85*, 3899–3901, DOI: `10.1063/1.1812368`.

(114) Hulea, I. N.; Fratini, S.; Xie, H., et al. Tunable Fröhlich polarons in organic single-crystal transistors. *Nat. Mater.* **2006**, *5*, 982–986, DOI: `10.1038/nmat1774`.

(115) Takeya, J.; Yamagishi, M.; Tominari, Y., et al. Very high-mobility organic single-crystal transistors with in-crystal conduction channels. *Appl. Phys. Lett.* **2007**, *90*, 102120, DOI: `10.1063/1.2711393`.

(116) Podzorov, V.; Menard, E.; Rogers, J.; Gershenson, M. Hall effect in the accumulation layers on the surface of organic semiconductors. *Phys. Rev. Lett.* **2005**, *95*, 226601, DOI: `10.1103/PhysRevLett.95.226601`.

(117) Takahashi, T.; Takenobu, T.; Takeya, J.; Iwasa, Y. Ambipolar organic field-effect transistors based on rubrene single crystals. *Appl. Phys. Lett.* **2006**, *88*, 033505, DOI: `10.1063/1.2166698`.

(118) Takenobu, T.; Takahashi, T.; Takeya, J.; Iwasa, Y. Effect of metal electrodes on rubrene single-crystal transistors. *Appl. Phys. Lett.* **2007**, *90*, 013507, DOI: `10.1063/1.2408642`.

(119) Wang, Y.; Kumashiro, R.; Nouchi, R., et al. Influence of interface modifications on carrier mobilities in rubrene single crystal ambipolar field-effect transistors. *J. Appl. Phys.* **2009**, *105*, 124912, DOI: `10.1063/1.3153946`.

(120) Bisri, S. Z.; Takenobu, T.; Takahashi, T.; Iwasa, Y. Electron transport in rubrene single-crystal transistors. *Appl. Phys. Lett.* **2010**, *96*, 90, DOI: `10.1063/1.3419899`.

(121) Uemura, T.; Yamagishi, M.; Okada, Y., et al. Monolithic complementary inverters based on organic single crystals. *Adv. Mater.* **2010**, *22*, 3938–3941, DOI: `10.1002/adma.201000480`.

(122) Yomogida, Y.; Pu, J.; Shimotani, H., et al. Ambipolar organic single-crystal transistors based on ion gels. *Adv. Mater.* **2012**, *24*, 4392–4397, DOI: `10.1002/adma.201200655`.

(123) Kanagasekaran, T.; Shimotani, H.; Shimizu, R., et al. A new electrode design for ambipolar injection in organic semiconductors. *Nat. Commun.* **2017**, *8*, 1–7, DOI: `10.1038/s41467-017-01047-9`.

(124) He, X.; Chow, W.; Liu, F., et al. MoS2/rubrene van der waals heterostructure: toward ambipolar field-effect transistors and inverter circuits. *Small* **2017**, *13*, 1602558, DOI: `10.1002/smll.201602558`.

(125) Park, C.-J.; Park, H. J.; Lee, J. Y., et al. Photovoltaic field-effect transistors using a MoS2 and organic rubrene van der Waals hybrid. *ACS Appl. Mater. Interfaces* **2018**, *10*, 29848–29856, DOI: `10.1021/acsami.8b11559`.

(126) Lee, M. Y.; Park, J.; Oh, J. H. High-performance ambipolar organic phototransistors based on core–shell p–n junction organic single crystals. *ACS Appl. Electron. Mater.* **2019**, *2*, 9–18, DOI: `10.1021/acsaelm.9b00588`.

(127) Fusella, M. A.; Yang, S.; Abbasi, K., et al. Use of an underlayer for large area crystallization of rubrene thin films. *Chem. Mater.* **2017**, *29*, 6666–6673, DOI: `10.1021/acs.chemmater.7b01143`.

(128) Pernstich, K. P.; Rössner, B.; Batlogg, B. Field-effect-modulated Seebeck coefficient in organic semiconductors. *Nat. Mater.* **2008**, *7*, 321–5, DOI: `10.1038/nmat2120`.

(129) Blülle, B.; Troisi, A.; Häusermann, R.; Batlogg, B. Charge transport perpendicular to the high mobility plane in organic crystals: bandlike temperature dependence maintained despite hundredfold anisotropy. *Phys. Rev. B* **2016**, *93*, 035205, DOI: `10.1103/PhysRevB.93.035205`.

(130) Ma, L.; Zhang, K.; Kloc, C., et al. Singlet fission in rubrene single crystal: direct observation by femtosecond pump–probe spectroscopy. *Phys. Chem. Chem. Phys.* **2012**, *14*, 8307–8312, DOI: `10.1039/C2CP40449D`.

(131) Najafov, H.; Lee, B.; Zhou, Q., et al. Observation of long-range exciton diffusion in highly ordered organic semiconductors. *Nat. Mater.* **2010**, *9*, 938–943, DOI: `10.1038/nmat2872`.

(132) Irkhin, P.; Biaggio, I. Direct imaging of anisotropic exciton diffusion and triplet diffusion length in rubrene single crystals. *Phys. Rev. Lett.* **2011**, *107*, 017402, DOI: `10.1103/PhysRevLett.107.017402`.

(133) Irkhin, P.; Ryasnyanskiy, A.; Koehler, M.; Biaggio, I. Absorption and photoluminescence spectroscopy of rubrene single crystals. *Phys. Rev. B* **2012**, *86*, 085143, DOI: `10.1103/PhysRevB.86.085143`.

(134) Tavazzi, S.; Borghesi, A.; Papagni, A., et al. Optical response and emission waveguiding in rubrene crystals. *Phys. Rev. B* **2007**, *75*, 245416, DOI: `10.1103/PhysRevB.75.245416`.

(135) Sheng, X.; Peng, A.; Fu, H., et al. Modulation of a fluorescence switch based on photochromic spirooxazine in composite organic nanoparticles. *Nanotechnology* **2007**, *18*, 145707, DOI: `10.1088/0957-4484/18/14/145707`.

(136) Piland, G. B.; Burdett, J. J.; Kurunthu, D.; Bardeen, C. J. Magnetic field effects on singlet fission and fluorescence decay dynamics in amorphous rubrene. *J. Phys. Chem. C* **2013**, *117*, 1224–1236, DOI: `10.1021/jp309286v`.

(137) Ryasnyanskiy, A.; Biaggio, I. Triplet exciton dynamics in rubrene single crystals. *Phys. Rev. B* **2011**, *84*, 193203, DOI: `10.1103/PhysRevB.84.193203`.

(138) Jankus, V.; Snedden, E. W.; Bright, D. W., et al. Competition between polaron pair formation and singlet fission observed in amorphous rubrene films. *Phys. Rev. B* **2013**, *87*, 224202, DOI: `10.1103/PhysRevB.87.224202`.

(139) Stuart, B., *Infrared spectroscopy: fundamentals and applications*; Chichester, West Sussex, England ; Hoboken, NJ : J. Wiley, 2004: 2004, DOI: `10.1002/0470011149`.

(140) Centrone, A. Infrared imaging and spectroscopy beyond the diffraction limit. *Annu. Rev. Anal. Chem.* **2015**, *8*, 101–126, DOI: `10.1146/annurev-anchem-071114-040435`.

(141) Atkins, P.; de Paula, J., *Atkins' physical chemistry*, 8th; Oxford University Press: Oxford; New York, 2006.

(142) Wilson, E. B.; Decius, J. C.; Cross, P. C., *Molecular vibrations: the theory of infrared and Raman vibrational spectra*; Courier Corporation: 1980.

(143) Porter, M. D.; Bright, T. B.; Allara, D. L.; Chidsey, C. E. Spontaneously organized molecular assemblies. 4. Structural characterization of n-alkyl thiol monolayers on gold by optical ellipsometry, infrared spectroscopy, and electrochemistry. *J. Am. Chem. Soc.* **1987**, *109*, 3559–3568, DOI: `10.1021/ja00246a011`.

(144) Laibinis, P. E.; Nuzzo, R. G.; Whitesides, G. M. Structure of monolayers formed by coadsorption of two n-alkanethiols of different chain lengths on gold and its relation to wetting. *J. Phys. Chem.* **1992**, *96*, 5097–5105, DOI: `10.1021/j100191a065`.

(145) Goetz, K. P.; Tsutsumi, J.; Pookpanratana, S., et al. Polymorphism in the 1:1 charge-transfer complex DBTTF–TCNQ and its effects on optical and electronic properties. *Adv. Electron. Mater.* **2016**, *2*, 1600203, DOI: `10.1002/aelm.201600203`.

(146) Capria, E.; Benevoli, L.; Perucchi, A., et al. Infrared investigations of 4-hydroxycyanobenzene single crystals. *J. Phys. Chem. A* **2013**, *117*, 6781–6788, DOI: `10.1021/jp405058h`.

(147) Rao, V. J.; Matthiesen, M.; Goetz, K. P., et al. AFM-IR and IR-SNOM for the characterization of small molecule organic semiconductors. *J. Phys. Chem. C* **2020**, *124*, 5331–5344, DOI: `10.1021/acs.jpcc.9b11056`.

(148) Levin, I. W.; Bhargava, R. Fourier transform infrared vibrational spectroscopic imaging: integrating microscopy and molecular recognition. *Annu. Rev. Phys. Chem.* **2005**, *56*, 429–474, DOI: `10.1146/annurev.physchem.56.092503.141205`.

(149) Reddy, R. K.; Walsh, M. J.; Schulmerich, M. V., et al. High-definition infrared spectroscopic imaging. *Appl. Spectrosc.* **2013**, *67*, 93–105.

(150) Nasse, M. J.; Walsh, M. J.; Mattson, E. C., et al. High-resolution Fourier-transform infrared chemical imaging with multiple synchrotron beams. *Nat. Methods* **2011**, *8*, 413–416, DOI: `10.1038/nmeth.1585`.

(151) Phillips, M. C.; Hô, N. Infrared hyperspectral imaging using a broadly tunable external cavity quantum cascade laser and microbolometer focal plane array. *Opt. Express* **2008**, *16*, 1836–1845, DOI: `10.1364/OE.16.001836`.

(152) Bassan, P.; Weida, M. J.; Rowlette, J.; Gardner, P. Large scale infrared imaging of tissue micro arrays (TMAs) using a tunable Quantum Cascade Laser (QCL) based microscope. *Analyst* **2014**, *139*, 3856–3859, DOI: `10.1039/C4AN00638K`.

(153) Toporski, J.; Dieing, T.; Hollricher, O., *Confocal Raman microscopy*; Springer: 2018; Vol. 66.

(154) Brillante, A.; Della Valle, R. G.; Farina, L., et al. Raman phonon spectra of pentacene polymorphs. *Chem. Phys. Lett.* **2002**, *357*, 32–36, DOI: `10.1016/S0009-2614(02)00441-4`.

(155) Brillante, A.; Bilotti, I.; Biscarini, F., et al. Polymorphs of –sexithiophene probed by lattice phonon Raman microscopy. *Chem. Phys.* **2006**, *328*, 125–131, DOI: `10.1016/j.chemphys.2006.06.018`.

(156) Troisi, A.; Orlandi, G. Charge-transport regime of crystalline organic semiconductors: diffusion limited by thermal off-diagonal electronic disorder. *Phys. Rev. Lett.* **2006**, *96*, 086601, DOI: `10.1103/PhysRevLett.96.086601`.

(157) Fratini, S.; Ciuchi, S.; Mayou, D., et al. A map of high-mobility molecular semiconductors. *Nat. Mater.* **2017**, *16*, 998–1002, DOI: `10.1038/nmat4970`.

(158) Sosorev, A. Y.; Maslennikov, D. R.; Kharlanov, O. G., et al. Impact of low-frequency vibrations on charge transport in high-mobility organic semiconductors. *Phys. Status Solidi RRL* **2019**, *13*, 1800485, DOI: `10.1002/pssr.201800485`.

(159) Schweicher, G.; D'Avino, G.; Ruggiero, M. T., et al. Chasing the "killer" phonon mode for the rational design of low-disorder, high-mobility molecular semiconductors. *Adv. Mater.* **2019**, *31*, 1902407, DOI: `10.1002/adma.201902407`.

(160) Asher, M.; Angerer, D.; Korobko, R., et al. Anharmonic lattice vibrations in small-molecule organic semiconductors. *Adv. Mater.* **2020**, *32*, 1908028, DOI: `10.1002/adma.201908028`.

(161) Hammiche, A.; Pollock, H. M.; Reading, M., et al. Photothermal FT-IR spectroscopy: a step towards FT-IR microscopy at a resolution better than the diffraction limit. *Appl. Spectrosc.* **1999**, *53*, 810–815.

(162) Dazzi, A.; Prazeres, R.; Glotin, F.; Ortega, J. M. Local infrared microspectroscopy with subwavelength spatial resolution with an atomic force microscope tip used as a photothermal sensor. *Opt. Lett.* **2005**, *30*, 2388–2390, DOI: `10.1364/OL.30.002388`.

(163) Dazzi, A.; Prazeres, R.; Glotin, F.; Ortega, J. M. Subwavelength infrared spectromicroscopy using an AFM as a local absorption sensor. *Infrared Phys. Technol.* **2006**, *49*, 113–121, DOI: `10.1016/j.infrared.2006.01.009`.

(164) Dazzi, A.; Prazeres, R.; Glotin, F.; Ortega, J. M. Analysis of nano-chemical mapping performed by an AFM-based ("AFMIR") acousto-optic technique. *Ultramicroscopy* **2007**, *107*, 1194–1200, DOI: `10.1016/j.ultramic.2007.01.018`.

(165) Dazzi, A.; Prater, C. B.; Hu, Q., et al. AFM-IR: combining atomic force microscopy and infrared spectroscopy for nanoscale chemical characterization. *Appl. Spectrosc.* **2012**, *66*, 1365–84, DOI: `10.1366/12-06804`.

(166) Lahiri, B.; Holland, G.; Centrone, A. Chemical imaging beyond the diffraction limit: experimental validation of the PTIR technique. *Small* **2013**, *9*, 439–445, DOI: `10.1002/smll.201200788`.

(167) Dazzi, A.; Prater, C. B. AFM-IR: Technology and applications in nanoscale infrared spectroscopy and chemical imaging. *Chem. Rev.* **2017**, *117*, 5146–5173, DOI: `10.1021/acs.chemrev.6b00448`.

(168) Dazzi, A.; Glotin, F.; Carminati, R. Theory of infrared nanospectroscopy by photothermal induced resonance. *J. Appl. Phys.* **2010**, *107*, 124519, DOI: `10.1063/1.3429214`.

(169) Lu, F.; Jin, M.; Belkin, M. A. Tip-enhanced infrared nanospectroscopy via molecular expansion force detection. *Nat. Photonics* **2014**, *8*, 307–312, DOI: `10.1038/nphoton.2013.373`.

(170) Morsch, S.; Lyon, S.; Edmondson, S.; Gibbon, S. Reflectance in AFM-IR: implications for interpretation and remote analysis of the buried interface. *Anal. Chem.* **2020**, *92*, 8117–8124, DOI: `10.1021/acs.analchem.9b05793`.

(171) Mathurin, J.; Deniset-Besseau, A.; Dazzi, A. Advanced infrared nanospectroscopy using photothermal induced resonance technique, AFMIR: new approach using tapping mode. *Acta Phys. Pol. A* **2020**, *137*, DOI: `10.12693/APhysPolA.137.2`.

(172) Mathurin, J.; Pancani, E.; Deniset-Besseau, A., et al. How to unravel the chemical structure and component localization of individual drug-loaded polymeric nanoparticles by using tapping AFM-IR. *Analyst* **2018**, *143*, 5940–5949, DOI: `10.1039/C8AN01239C`.

(173) Piergies, N.; Dazzi, A.; Deniset-Besseau, A., et al. Nanoscale image of the drug/metal mono-layer interaction: tapping AFM-IR investigations. *Nano Res.* **2020**, *13*, 1020–1028, DOI: `10.1007/s12274-020-2738-4`.

(174) Tuteja, M.; Kang, M.; Leal, C.; Centrone, A. Nanoscale partitioning of paclitaxel in hybrid lipid–polymer membranes. *Analyst* **2018**, *143*, 3808–3813, DOI: `10.1039/C8AN00838H`.

(175) Eby, T.; Gundusharma, U.; Lo, M., et al. Reverse engineering of polymeric multilayers using AFM-based nanoscale IR spectroscopy and thermal analysis. *Spectrosc. Eur.* **2012**, *24*, 18.

(176) Kelchtermans, M.; Lo, M.; Dillon, E., et al. Characterization of a polyethylene–polyamide multilayer film using nanoscale infrared spectroscopy and imaging. *Vib. Spectrosc* **2016**, *82*, 10–15, DOI: `10.1016/j.vibspec.2015.11.004`.

(177) Ye, J.; Midorikawa, H.; Awatani, T., et al. Nanoscale infrared spectroscopy and AFM imaging of a polycarbonate/acrylonitrile-styrene/butadiene blend. *Microsc. Anal.* **2012**, *26*, 24–27.

(178) Tang, F.; Bao, P.; Su, Z. Analysis of nanodomain composition in high-impact polypropylene by atomic force microscopy-infrared. *Anal. Chem.* **2016**, *88*, 4926–4930, DOI: `10.1021/acs.analchem.6b00798`.

(179) Gong, L.; Chase, D. B.; Noda, I., et al. Discovery of β-form crystal structure in electrospun poly[(R)-3-hydroxybutyrate-co-(R)-3-hydroxyhexanoate] (PHBHx) nanofibers: from fiber mats to single fibers. *Macromolecules* **2015**, *48*, 6197–6205, DOI: `10.1021/acs.macromol.5b00638`.

(180) Clède, S.; Lambert, F.; Sandt, C., et al. Detection of an estrogen derivative in two breast cancer cell lines using a single core multimodal probe for imaging (SCoMPI) imaged by a panel of luminescent and vibrational techniques. *Analyst* **2013**, *138*, 5627–5638, DOI: `10.1039/C3AN00807J`.

(181) Policar, C.; Waern, J. B.; Plamont, M. A., et al. Subcellular IR imaging of a metal-carbonyl moiety using photothermally induced resonance. *Angew. Chem. Int. Ed. Engl.* **2011**, *50*, 860–4, DOI: `10.1002/anie.201003161`.

(182) Marcott, C.; Lo, M.; Kjoller, K., et al. Nanoscale infrared (IR) spectroscopy and imaging of structural lipids in human stratum corneum using an atomic force microscope to directly detect absorbed light from a tunable IR laser source. *Exp. Dermatol.* **2013**, *22*, 419–421, DOI: `10.1111/exd.12144`.

(183) Ruggeri, F. S.; Longo, G.; Faggiano, S., et al. Infrared nanospectroscopy characterization of oligomeric and fibrillar aggregates during amyloid formation. *Nat. Commun.* **2015**, *6*, 7831, DOI: `10.1038/ncomms8831`.

(184) Yuan, Y.; Chae, J.; Shao, Y., et al. Photovoltaic switching mechanism in lateral structure hybrid perovskite solar cells. *Adv. Energy Mater.* **2015**, *5*, 1500615, DOI: `10.1002/aenm.201500615`.

(185) Felts, J. R.; Law, S.; Roberts, C. M., et al. Near-field infrared absorption of plasmonic semiconductor microparticles studied using atomic force microscope infrared spectroscopy. *Appl. Phys. Lett.* **2013**, *102*, 152110, DOI: `10.1063/1.4802211`.

(186) Houel, J.; Sauvage, S.; Boucaud, P., et al. Ultraweak-absorption microscopy of a single semiconductor quantum dot in the midinfrared range. *Phys. Rev. Lett.* **2007**, *99*, 217404, DOI: `10.1103/PhysRevLett.99.217404`.

(187) Sauvage, S.; Driss, A.; Réveret, F., et al. Homogeneous broadening of the S to P transition in InGaAs/GaAs quantum dots measured by infrared absorption imaging with nanoscale resolution. *Phys. Rev. B* **2011**, *83*, 035302, DOI: `10.1103/PhysRevB.83.035302`.

(188) Houel, J.; Homeyer, E.; Sauvage, S., et al. Midinfrared absorption measured at a $\lambda/400$ resolution with an atomic force microscope. *Opt. Express* **2009**, *17*, 10887–10894, DOI: `10.1364/OE.17.010887`.

(189) Lo, M. K.; Dazzi, A.; Marcott, C. A., et al. Nanoscale chemical-mechanical characterization of nanoelectronic low-k dielectric/Cu interconnects. *ECS J. Solid State Sci. Technol.* **2015**, *5*, P3018, DOI: `10.1149/2.0041604jss`.

(190) Latour, G.; Robinet, L.; Dazzi, A., et al. Correlative nonlinear optical microscopy and infrared nanoscopy reveals collagen degradation in altered parchments. *Sci. Rep.* **2016**, *6*, 26344, DOI: `10.1038/srep26344`.

(191) Mei, Y.; Diemer, P. J.; Niazi, M. R., et al. Crossover from band-like to thermally activated charge transport in organic transistors due to strain-induced traps. *Proc. Natl. Acad. Sci. U.S.A.* **2017**, *114*, E6739–E6748, DOI: `10.1073/pnas.1705164114`.

(192) Keilmann, F.; Hillenbrand, R. Near-field microscopy by elastic light scattering from a tip. *Philos. Trans. R. Soc.* **2004**, *362*, 787–805, DOI: `10.1098/rsta.2003.1347`.

(193) Hermann, R. J.; Gordon, M. J. Nanoscale optical microscopy and spectroscopy using near-field probes. *Annu. Rev. Chem. Biomol. Eng.* **2018**, *9*, 365–387, DOI: `10.1146/annurev-chembioeng-060817-084150`.

(194) Chen, X.; Hu, D.; Mescall, R., et al. Modern scattering-type scanning near-field optical microscopy for advanced material research. *Adv. Mater.* **2019**, *31*, 1804774, DOI: `10.1002/adma.201804774`.

(195) Muller, E. A.; Pollard, B.; Raschke, M. B. Infrared chemical nano-imaging: accessing structure, coupling, and dynamics on molecular length scales. *J. Phys. Chem. Lett.* **2015**, *6*, 1275–1284, DOI: `10.1021/acs.jpclett.5b00108`.

(196) Xiao, L.; Schultz, Z. D. Spectroscopic imaging at the nanoscale: technologies and recent applications. *Anal. Chem.* **2018**, *90*, 440–458, DOI: `10.1021/acs.analchem.7b04151`.

(197) Huth, F.; Govyadinov, A.; Amarie, S., et al. Nano-FTIR absorption spectroscopy of molecular fingerprints at 20 nm spatial resolution. *Nano Lett.* **2012**, *12*, 3973–3978, DOI: `10.1021/nl301159v`.

(198) Huth, F. Nano-FTIR-nanoscale infrared near-field spectroscopy, Thesis, 2015.

(199) Ocelic, N.; Huber, A.; Hillenbrand, R. Pseudoheterodyne detection for background-free near-field spectroscopy. *Appl. Phys. Lett.* **2006**, *89*, 101124, DOI: `10.1063/1.2348781`.

(200) Taubner, T.; Hillenbrand, R.; Keilmann, F. Nanoscale polymer recognition by spectral signature in scattering infrared near-field microscopy. *Appl. Phys. Lett.* **2004**, *85*, 5064–5066, DOI: `10.1063/1.1827334`.

(201) Stiegler, J. M.; Abate, Y.; Cvitkovic, A., et al. Nanoscale infrared absorption spectroscopy of individual nanoparticles enabled by scattering-type near-field microscopy. *ACS Nano* **2011**, *5*, 6494–6499, DOI: `10.1021/nn2017638`.

(202) Cvitkovic, A.; Ocelic, N.; Hillenbrand, R. Analytical model for quantitative prediction of material contrasts in scattering-type near-field optical microscopy. *Opt. Express* **2007**, *15*, 8550–8565, DOI: `10.1364/OE.15.008550`.

(203) Mastel, S.; Govyadinov, A. A.; de Oliveira, T. V. A. G., et al. Nanoscale-resolved chemical identification of thin organic films using infrared near-field spectroscopy and standard Fourier transform infrared references. *Appl. Phys. Lett.* **2015**, *106*, 023113, DOI: `10.1063/1.4905507`.

(204) Fei, Z.; Rodin, A. S.; Gannett, W., et al. Electronic and plasmonic phenomena at graphene grain boundaries. *Nat. Nanotechnol.* **2013**, *8*, 821–825, DOI: `10.1038/nnano.2013.197`.

(205) Chen, J.; Nesterov, M. L.; Nikitin, A. Y., et al. Strong plasmon reflection at nanometer-size gaps in monolayer graphene on SiC. *Nano Lett.* **2013**, *13*, 6210–6215, DOI: `10.1021/nl403622t`.

(206) Dai, S.; Fei, Z.; Ma, Q., et al. Tunable phonon polaritons in atomically thin van der Waals crystals of boron nitride. *Science* **2014**, *343*, 1125, DOI: `10.1126/science.1246833`.

(207) Barcelos, I. D.; Cadore, A. R.; Campos, L. C., et al. In *18th Brazilian Workshop on Semiconductor Physics*.

(208) Patoka, P.; Ulrich, G.; Nguyen, A. E., et al. Nanoscale plasmonic phenomena in CVD-grown MoS2 monolayer revealed by ultra-broadband synchrotron radiation based nano-FTIR spectroscopy and near-field microscopy. *Opt. Express* **2016**, *24*, 1154–1164, DOI: `10.1364/OE.24.001154`.

(209) Babicheva, V. E.; Gamage, S.; Zhen, L., et al. Near-field surface waves in few-layer MoS2. *ACS Photonics* **2018**, *5*, 2106–2112, DOI: `10.1021/acsphotonics.7b01563`.

(210) Liu, R.; Liao, B.; Guo, X., et al. Study of graphene plasmons in graphene–MoS2 heterostructures for optoelectronic integrated devices. *Nanoscale* **2017**, *9*, 208–215, DOI: `10.1039/C6NR07081G`.

(211) Németh, G.; Datz, D.; Tóháti, H. M., et al. Nanoscale characterization of individual horizontally aligned single-walled carbon nanotubes. *Phys. Status Solidi B* **2017**, *254*, 1700433, DOI: `10.1002/pssb.201700433`.

(212) Tian, X.; Gu, Q.; Duan, J., et al. Improving Luttinger-liquid plasmons in carbon nanotubes by chemical doping. *Nanoscale* **2018**, *10*, 6288–6293, DOI: `10.1039/C8NR00310F`.

(213) Wang, S.; Zhao, S.; Shi, Z., et al. Nonlinear Luttinger liquid plasmons in semiconducting single-walled carbon nanotubes. *Nat. Mater.* **2020**, *19*, 986–991, DOI: `10.1038/s41563-020-0652-5`.

(214) Pollard, B.; Muller, E. A.; Hinrichs, K.; Raschke, M. B. Vibrational nano-spectroscopic imaging correlating structure with intermolecular coupling and dynamics. *Nat. Commun.* **2014**, *5*, 3587, DOI: `10.1038/ncomms4587`.

(215) Amenabar, I.; Poly, S.; Goikoetxea, M., et al. Hyperspectral infrared nanoimaging of organic samples based on Fourier transform infrared nanospectroscopy. *Nat. Commun.* **2017**, *8*, 14402, DOI: `10.1038/ncomms14402`.

(216) Wiens, R.; Findlay, C. R.; Baldwin, S. G., et al. High spatial resolution (1.1 µm and 20 nm) FTIR polarization contrast imaging reveals pre-rupture disorder in damaged tendon. *Faraday Discuss.* **2016**, *187*, 555–573, DOI: `10.1039/C5FD00168D`.

(217) Khatib, O.; Wood, J. D.; McLeod, A. S., et al. Graphene-based platform for infrared near-field nanospectroscopy of water and biological materials in an aqueous environment. *ACS Nano* **2015**, *9*, 7968–75, DOI: `10.1021/acsnano.5b01184`.

(218) Muller, E. A.; Pollard, B.; Bechtel, H. A., et al. Infrared vibrational nanocrystallography and nano-imaging. *Sci. Adv.* **2016**, *2*, e1601006, DOI: `10.1126/sciadv.1601006`.

(219) Westermeier, C.; Cernescu, A.; Amarie, S., et al. Sub-micron phase coexistence in small-molecule organic thin films revealed by infrared nano-imaging. *Nat. Commun.* **2014**, *5*, 4101, DOI: `10.1038/ncomms5101`.

(220) Novoselov, K. S.; Geim, A. K.; Morozov, S. V., et al. Electric field effect in atomically thin carbon films. *Science* **2004**, *306*, 666–669, DOI: `10.1126/science.1102896`.

(221) Golberg, D.; Bando, Y.; Huang, Y., et al. Boron nitride nanotubes and nanosheets. *ACS Nano* **2010**, *4*, 2979–2993, DOI: `10.1021/nn1006495`.

(222) Wang, Q. H.; Kalantar-Zadeh, K.; Kis, A., et al. Electronics and optoelectronics of two-dimensional transition metal dichalcogenides. *Nat. Nanotechnol.* **2012**, *7*, 699–712, DOI: `10.1038/nnano.2012.193`.

(223) Osada, M.; Sasaki, T. Exfoliated oxide nanosheets: new solution to nanoelectronics. *J. Mater. Chem.* **2009**, *19*, 2503–2511, DOI: `10.1039/B820160A`.

(224) Ma, R.; Sasaki, T. Nanosheets of oxides and hydroxides: ultimate 2D charge-bearing functional crystallites. *Adv. Mater.* **2010**, *22*, 5082–5104, DOI: `10.1002/adma.201001722`.

(225) Hanlon, D.; Backes, C.; Doherty, E., et al. Liquid exfoliation of solvent-stabilized few-layer black phosphorus for applications beyond electronics. *Nat. Commun.* **2015**, *6*, 1–11, DOI: `10.1038/ncomms9563`.

(226) Hernandez, Y.; Nicolosi, V.; Lotya, M., et al. High-yield production of graphene by liquid-phase exfoliation of graphite. *Nat. Nanotechnol.* **2008**, *3*, 563–8, DOI: `10.1038/nnano.2008.215`.

(227) Nicolosi, V.; Chhowalla, M.; Kanatzidis, M. G., et al. Liquid exfoliation of layered materials. *Science* **2013**, *340*, DOI: `10.1126/science.1226419`.

(228) Paton, K. R.; Varrla, E.; Backes, C., et al. Scalable production of large quantities of defect-free few-layer graphene by shear exfoliation in liquids. *Nat. Mater.* **2014**, *13*, 624–630, DOI: `10.1038/nmat3944`.

(229) Lin, Y.; Williams, T. V.; Xu, T.-B., et al. Aqueous dispersions of few-layered and monolayered hexagonal boron nitride nanosheets from sonication-assisted hydrolysis: critical role of water. *J. Phys. Chem. C* **2011**, *115*, 2679–2685, DOI: `10.1021/jp110985w`.

(230) Coleman, J. N.; Lotya, M.; O'Neill, A., et al. Two-dimensional nanosheets produced by liquid exfoliation of layered materials. *Science* **2011**, *331*, 568–571, DOI: `10.1126/science.1194975`.

(231) Boland, J. B.; Harvey, A.; Tian, R., et al. Liquid phase exfoliation of MoO2 nanosheets for lithium ion battery applications. *Nanoscale Adv.* **2019**, *1*, 1560–1570, DOI: `10.1039/C8NA00241J`.

(232) Hanlon, D.; Backes, C.; Higgins, T. M., et al. Production of molybdenum trioxide nanosheets by liquid exfoliation and their application in high-performance supercapacitors. *Chem. Mater.* **2014**, *26*, 1751–1763, DOI: `10.1021/cm500271u`.

(233) Harvey, A.; He, X.; Godwin, I. J., et al. Production of Ni(OH)2 nanosheets by liquid phase exfoliation: from optical properties to electrochemical applications. *J. Mater. Chem. A* **2016**, *4*, 11046–11059, DOI: `10.1039/C6TA02811J`.

(234) McAteer, D.; Godwin, I. J.; Ling, Z., et al. Liquid exfoliated Co(OH)2 nanosheets as low-cost, yet high-performance catalysts for the oxygen evolution reaction. *Adv. Energy Mater.* **2018**, *8*, 1702965, DOI: `10.1002/aenm.201702965`.

(235) Dangol, R.; Dai, Z.; Chaturvedi, A., et al. Few-layer NiPS3 nanosheets as bifunctional materials for Li-ion storage and oxygen evolution reaction. *Nanoscale* **2018**, *10*, 4890–4896, DOI: `10.1039/C7NR08745D`.

(236) Harvey, A.; Backes, C.; Gholamvand, Z., et al. Preparation of gallium sulfide nanosheets by liquid exfoliation and their application as hydrogen evolution catalysts. *Chem. Mater.* **2015**, *27*, 3483–3493, DOI: `10.1021/acs.chemmater.5b00910`.

(237) Petroni, E.; Lago, E.; Bellani, S., et al. Liquid-phase exfoliated indium–selenide flakes and their application in hydrogen evolution reaction. *Small* **2018**, *14*, 1800749, DOI: `10.1002/smll.201800749`.

(238) Brent, J. R.; Lewis, D. J.; Lorenz, T., et al. Tin(II) sulfide (SnS) nanosheets by liquid-phase exfoliation of herzenbergite: IV–VI main group two-dimensional atomic crystals. *J. Am. Chem. Soc.* **2015**, *137*, 12689–12696, DOI: `10.1021/jacs.5b08236`.

(239) Zhang, P.; Zhao, F.; Long, P., et al. Sonication-assisted liquid-phase exfoliated α-GeTe: a two-dimensional material with high Fe3+ sensitivity. *Nanoscale* **2018**, *10*, 15989–15997, DOI: `10.1039/C8NR03091J`.

(240) Lange, R. Z.; Synnatschke, K.; Qi, H., et al. Enriching and quantifying porous single layer 2D polymers by exfoliation of chemically modified van der Waals crystals. *Angew. Chem. Int. Ed.* **2020**, *59*, 5683–5695, DOI: `10.1002/anie.201912705`.

(241) Das, G.; Biswal, B. P.; Kandambeth, S., et al. Chemical sensing in two dimensional porous covalent organic nanosheets. *Chem. Sci.* **2015**, *6*, 3931–3939, DOI: `10.1039/C5SC00512D`.

(242) Leubner, S.; Bengtsson, V. E. G.; Synnatschke, K., et al. Synthesis and exfoliation of a new layered mesoporous Zr-MOF comprising hexa- and dodecanuclear clusters as well as a small organic linker molecule. *J. Am. Chem. Soc.* **2020**, *142*, 15995–16000, DOI: `10.1021/jacs.0c06978`.

(243) Backes, C.; Campi, D.; Szydlowska, B. M., et al. Equipartition of energy defines the size–thickness relationship in liquid-exfoliated nanosheets. *ACS Nano* **2019**, *13*, 7050–7061, DOI: `10.1021/acsnano.9b02234`.

(244) Backes, C.; Szydłowska, B. M.; Harvey, A., et al. Production of highly monolayer enriched dispersions of liquid-exfoliated nanosheets by liquid cascade centrifugation. *ACS Nano* **2016**, *10*, 1589–1601, DOI: `10.1021/acsnano.5b07228`.

(245) Bonaccorso, F.; Bartolotta, A.; Coleman, J. N.; Backes, C. 2D-crystal-based functional inks. *Adv. Mater.* **2016**, *28*, 6136–6166, DOI: `10.1002/adma.201506410`.

(246) Backes, C.; Higgins, T. M.; Kelly, A., et al. Guidelines for exfoliation, characterization and processing of layered materials produced by liquid exfoliation. *Chem. Mater.* **2017**, *29*, 243–255, DOI: `10.1021/acs.chemmater.6b03335`.

(247) Paton, K. R.; Varrla, E.; Backes, C., et al. Scalable production of large quantities of defect-free few-layer graphene by shear exfoliation in liquids. *Nat. Mater.* **2014**, *13*, 624–30, DOI: `10.1038/nmat3944`.

(248) Zhi, C.; Bando, Y.; Tang, C., et al. Larges-scale fabrication of boron nitride nanosheets and their utilization in polymeric composites with improved thermal and mechanical properties. *Adv. Mater.* **2009**, *21*, 2889–2893, DOI: `10.1002/adma.200900323`.

(249) Smith, R. J.; King, P. J.; Lotya, M., et al. Large-scale exfoliation of inorganic layered compounds in aqueous surfactant solutions. *Adv. Mater.* **2011**, *23*, 3944–3948, DOI: `10.1002/adma.201102584`.

(250) Ciesielski, A.; Samorì, P. Graphene via sonication assisted liquid-phase exfoliation. *Chem. Soc. Rev.* **2014**, *43*, 381–398, DOI: `10.1039/C3CS60217F`.

(251) Derjaguin, B.; Landau, L. Theory of the stability of strongly charged lyophobic sols and of the adhesion of strongly charged particles in solutions of electrolytes. *Prog. Surf. Sci.* **1993**, *43*, 30–59, DOI: `10.1016/0079-6816(93)90013-L`.

(252) Verwey, E. J. W. Theory of the stability of lyophobic colloids. *J. Phys. Chem.* **1947**, *51*, 631–636, DOI: `10.1021/j150453a001`.

(253) Myers, D., *Surfactant science and technology*; John Wiley & Sons: 2020.

(254) Napper, D. H. Steric stabilization. *J. Colloid Interface Sci.* **1977**, *58*, 390–407, DOI: `10.1016/0021-9797(77)90150-3`.

(255) Clogston, J. D.; Patri, A. K. In *Characterization of nanoparticles intended for drug delivery*, McNeil, S. E., Ed.; Humana Press: Totowa, NJ, 2011, pp 63–70, DOI: `10.1007/978-1-60327-198-1_6`.

(256) Kang, J.; Seo, J.-W. T.; Alducin, D., et al. Thickness sorting of two-dimensional transition metal dichalcogenides via copolymer-assisted density gradient ultracentrifugation. *Nat. Commun.* **2014**, *5*, 5478, DOI: `10.1038/ncomms6478`.

(257) Zhu, J.; Kang, J.; Kang, J., et al. Solution-processed dielectrics based on thickness-sorted two-dimensional hexagonal boron nitride nanosheets. *Nano Lett.* **2015**, *15*, 7029–7036, DOI: `10.1021/acs.nanolett.5b03075`.

(258) Green, A. A.; Hersam, M. C. Solution phase production of graphene with controlled thickness via density differentiation. *Nano Lett.* **2009**, *9*, 4031–6, DOI: `10.1021/nl902200b`.

(259) Backes, C.; Paton, K. R.; Hanlon, D., et al. Spectroscopic metrics allow in situ measurement of mean size and thickness of liquid-exfoliated few-layer graphene nanosheets. *Nanoscale* **2016**, *8*, 4311–4323, DOI: `10.1039/C5NR08047A`.

(260) Batchelor, G. K., *An introduction to fluid dynamics*; Cambridge University Press: 2000.

(261) Lebowitz, J.; Lewis, M. S.; Schuck, P. Modern analytical ultracentrifugation in protein science: a tutorial review. *Protein Sci.* **2002**, *11*, 2067–2079, DOI: `10.1110/ps.0207702`.

(262) Gorelik, T. E.; Habermehl, S.; Shubin, A. A., et al. Crystal structure of copper perchlorophthalocyanine analysed by 3D electron diffraction. *Acta Crystallogr. B* **2021**, *77*, DOI: `10.1107/S2052520621006806`.

(263) Gong, L.; Chase, D. B.; Noda, I., et al. Discovery of β-form crystal structure in electrospun poly[(R)-3-hydroxybutyrate-co-(R)-3-hydroxyhexanoate] (PHBHx) nanofibers: from fiber mats to single fibers. *Macromolecules* **2015**, *48*, 6197–6205, DOI: `10.1021/acs.macromol.5b00638`.

(264) Ghosh, S.; Ramos, L.; Remita, S., et al. Conducting polymer nanofibers with controlled diameters synthesized in hexagonal mesophases. *New J. Chem.* **2015**, *39*, 8311–8320, DOI: `10.1039/C5NJ00826C`.

(265) Coletta, C.; Cui, Z.; Dazzi, A., et al. A pulsed electron beam synthesis of PEDOT conducting polymers by using sulfate radicals as oxidizing species. *Radiat. Phys. Chem.* **2016**, *126*, 21–31, DOI: `10.1016/j.radphyschem.2016.05.003`.

(266) Berweger, S.; Nguyen, D. M.; Muller, E. A., et al. Nano-chemical infrared imaging of membrane proteins in lipid bilayers. *J. Am. Chem. Soc.* **2013**, *135*, 18292–18295, DOI: `10.1021/ja409815g`.

(267) Dai, S.; Ma, Q.; Liu, M. K., et al. Graphene on hexagonal boron nitride as a tunable hyperbolic metamaterial. *Nat. Nanotechnol.* **2015**, *10*, 682–686, DOI: `10.1038/nnano.2015.131`.

(268) Patoka, P.; Ulrich, G.; Nguyen, A. E., et al. Nanoscale plasmonic phenomena in CVD-grown MoS 2 monolayer revealed by ultra-broadband synchrotron radiation based nano-FTIR spectroscopy and near-field microscopy. *Opt. Express* **2016**, *24*, 1154–1164, DOI: `10.1364/OE.24.001154`.

(269) Shi, Z.; Bechtel, H. A.; Berweger, S., et al. Amplitude- and phase-resolved nanospectral imaging of phonon polaritons in hexagonal boron nitride. *ACS Photonics* **2015**, *2*, 790–796, DOI: `10.1021/acsphotonics.5b00007`.

(270) Liu, M. K.; Wagner, M.; Abreu, E., et al. Anisotropic electronic state via spontaneous phase separation in strained vanadium dioxide films. *Phys. Rev. Lett.* **2013**, *111*, 096602, DOI: `10.1103/PhysRevLett.111.096602`.

(271) Pollard, B.; Muller, E. A.; Hinrichs, K.; Raschke, M. B. Vibrational nano-spectroscopic imaging correlating structure with intermolecular coupling and dynamics. *Nat. Commun.* **2014**, *5*, 3587, DOI: `10.1038/ncomms4587`.

(272) Mrkyvkova, N.; Cernescu, A.; Futera, Z., et al. Nanoimaging of orientational defects in semiconducting organic films. *J. Phys. Chem. C* **2021**, *125*, 9229–9235, DOI: `10.1021/acs.jpcc.1c00059`.

(273) Minder, N. A.; Ono, S.; Chen, Z., et al. Band-like electron transport in organic transistors and implication of the molecular structure for performance optimization. *Adv. Mater.* **2012**, *24*, 503–508, DOI: `10.1002/adma.201103960`.

(274) He, T.; Stolte, M.; Burschka, C., et al. Single-crystal field-effect transistors of new Cl2-NDI polymorph processed by sublimation in air. *Nat. Commun.* **2015**, *6*, 5954, DOI: `10.1038/ncomms6954`.

(275) Izawa, T.; Miyazaki, E.; Takimiya, K. Molecular ordering of high-performance soluble molecular semiconductors and re-evaluation of their field-effect transistor characteristics. *Adv. Mater.* **2008**, *20*, 3388–3392, DOI: `10.1002/adma.200800799`.

(276) Miyata, Y.; Yoshikawa, E.; Minari, T., et al. High-performance organic field-effect transistors based on dihexyl-substituted dibenzo[d,d']thieno[3,2-b;4,5-b']dithiophene. *J. Mater. Chem.* **2012**, *22*, 7715–7717, DOI: `10.1039/C2JM30840A`.

(277) Riehm, T.; De Paoli, G.; Konradsson, A. E., et al. Tetraazaperopyrenes: a new class of multifunctional chromophores. *Chem. Eur. J.* **2007**, *13*, 7317–7329, DOI: `10.1002/chem.200700383`.

(278) Hahn, L.; Maaß, F.; Bleith, T., et al. Core halogenation as a construction principle in tuning the material properties of tetraazaperopyrenes. *Chem. Eur. J.* **2015**, *21*, 17691–17700, DOI: `10.1002/chem.201503484`.

(279) Geib, S.; Zschieschang, U.; Gsänger, M., et al. Core-brominated tetraazaperopyrenes as n-channel semiconductors for organic complementary circuits on flexible substrates. *Adv. Funct. Mater.* **2013**, *23*, 3866–3874, DOI: `10.1002/adfm.201203600`.

(280) Che, C.-M.; Xiang, H.-F.; Chui, S. S.-Y., et al. A high-performance organic field-effect transistor based on platinum (II) porphyrin: peripheral substituents on porphyrin ligand significantly affect film structure and charge mobility. *Chem. Asian J.* **2008**, *3*, 1092–1103, DOI: `10.1002/asia.200800011`.

(281) Goddard, R.; Haenel, M. W.; Herndon, W. C., et al. Crystallization of large planar polycyclic aromatic hydrocarbons: the molecular and crystal structures of hexabenzo [bc,ef,hi,kl,no,qr] coronene and Benzo [1,2,3-bc:4,5,6-b'c'] dicoronene. *J. Am. Chem. Soc.* **1995**, *117*, 30–41, DOI: `10.1021/ja00106a004`.

(282) Tzschoppe, M.; Huck, C.; Günther, B., et al. Deposition-dependent morphology and infrared vibrational spectra of brominated tetraazaperopyrene layers. *J. Phys. Chem. C* **2019**, *124*, 769–779, DOI: `10.1021/acs.jpcc.9b10155`.

(283) Rao, V. J.; Qi, H.; Berger, F. J., et al. Liquid Phase Exfoliation of Rubrene Single Crystals into Nanorods and Nanobelts. *ACS Nano* **2021**, DOI: `10.1021/acsnano.1c08965`.

(284) Backes, C.; Smith, R. J.; McEvoy, N., et al. Edge and confinement effects allow in situ measurement of size and thickness of liquid-exfoliated nanosheets. *Nat. Commun.* **2014**, *5*, 4576, DOI: `10.1038/ncomms5576`.

(285) Kaur, H.; Tian, R.; Roy, A., et al. Production of quasi-2D platelets of nonlayered iron pyrite (FeS2) by liquid-phase exfoliation for high performance battery electrodes. *ACS Nano* **2020**, *14*, 13418–13432, DOI: `10.1021/acsnano.0c05292`.

(286) Gibaja, C.; Rodríguez-San-Miguel, D.; Paz, W. S., et al. Exfoliation of alpha-germanium: a covalent diamond-like structure. *Adv. Mater.* **2021**, *33*, 2006826, DOI: `10.1002/adma.202006826`.

(287) Siegrist, T.; Besnard, C.; Haas, S., et al. A polymorph lost and found: the high-temperature crystal structure of pentacene. *Adv. Mater.* **2007**, *19*, 2079–2082, DOI: `10.1002/adma.200602072`.

(288) Haas, S.; Batlogg, B.; Besnard, C., et al. Large uniaxial negative thermal expansion in pentacene due to steric hindrance. *Phys. Rev. B* **2007**, *76*, 205203, DOI: `10.1103/PhysRevB.76.205203`.

(289) Reyes-Martinez, M. A.; Ramasubramaniam, A.; Briseno, A. L.; Crosby, A. J. The intrinsic mechanical properties of rubrene single crystals. *Adv. Mater.* **2012**, *24*, 5548–5552, DOI: `10.1002/adma.201201749`.

(290) Yamamura, A.; Fujii, H.; Ogasawara, H., et al. Sub-molecular structural relaxation at a physisorbed interface with monolayer organic single-crystal semiconductors. *Commun. Phys.* **2020**, *3*, 20, DOI: `10.1038/s42005-020-0285-7`.

(291) Briseno, A. L.; Mannsfeld, S. C. B.; Reese, C., et al. Perylenediimide nanowires and their use in fabricating field-effect transistors and complementary inverters. *Nano Lett.* **2007**, *7*, 2847–2853, DOI: `10.1021/nl071495u`.

(292) El Helou, M.; Medenbach, O.; Witte, G. Rubrene microcrystals: a route to investigate surface morphology and bulk anisotropies of organic semiconductors. *Cryst. Growth Des.* **2010**, *10*, 3496–3501, DOI: `10.1021/cg1003758`.

(293) Sinwani, M.; Tischler, Y. R. Raman and photoluminescence properties of red and yellow rubrene crystals. *J. Phys. Chem. C* **2014**, *118*, 14528–14533, DOI: `10.1021/jp5032338`.

(294) Irkhin, P.; Ryasnyanskiy, A.; Koehler, M.; Biaggio, I. Absorption and photoluminescence spectroscopy of rubrene single crystals. *Phys. Rev. B* **2012**, *86*, 085143, DOI: `10.1103/PhysRevB.86.085143`.

(295) Harvey, A.; Backes, C.; Boland, J. B., et al. Non-resonant light scattering in dispersions of 2D nanosheets. *Nat. Commun.* **2018**, *9*, 4553, DOI: `10.1038/s41467-018-07005-3`.

(296) Sai, N.; Tiago, M. L.; Chelikowsky, J. R.; Reboredo, F. A. Optical spectra and exchange-correlation effects in molecular crystals. *Phys. Rev. B* **2008**, *77*, 161306, DOI: `10.1103/PhysRevB.77.161306`.

(297) Ebata, H.; Izawa, T.; Miyazaki, E., et al. Highly soluble [1]benzothieno[3,2-b]benzothiophene (BTBT) derivatives for high-performance, solution-processed organic field-effect transistors. *J. Am. Chem. Soc.* **2007**, *129*, 15732–15733, DOI: `10.1021/ja074841i`.

(298) Xie, W.; Willa, K.; Wu, Y., et al. Temperature-independent transport in high-mobility dinaphtho-thieno-thiophene (DNTT) single crystal transistors. *Adv. Mater.* **2013**, *25*, 3478–3484, DOI: `10.1002/adma.201300886`.

Eidesstattliche Versicherung

Eidesstattliche Versicherung gemäß §8 der Promotionsordnung für die Naturwissenschaftlich-Mathematische Gesamtfakultät der Universität Heidelberg

1. Bei der eingereichten Dissertation zu dem Thema *Vibrational Spectroscopy of Macroscopic and Liquid-Phase Exfoliated Organic Crystals* handelt es sich um meine eigenständig erbrachte Leistung.

2. Ich habe nur die angegebenen Quellen und Hilfsmittel benutzt und mich keiner unzulässigen Hilfe Dritter bedient. Insbesondere habe ich wörtlich oder sinngemäß aus anderen Werken übernommene Inhalte als solche kenntlich gemacht.

3. Die Arbeit oder Teile davon habe ich nicht an einer Hochschule des In- oder Auslands als Bestandteil einer Prüfungs- oder Qualifikationsleitung vorgelegt.

4. Die Richtigkeit der vorstehenden Erklärungen bestätige ich.

5. Die Bedeutung der eidesstattlichen Versicherung und die strafrechtlichen Folgen einer unrichtigen oder unvollständigen eidesstattlichen Versicherung sind mir bekannt.

Ich versichere an Eides statt, dass ich nach bestem Wissen die reine Wahrheit erklärt und nichts verschwiegen habe.

10. Dezember 2021, Heidelberg

Vaishnavi Jayathirtha Rao